UNIVERSITY OF ADELAIDE

DOCTORAL THESIS

Development of an Integrated Stochastic Model for the Evaluation of the Impact of Microscopic Extension on Tumour Clonogen Survival in Heterogeneous Hypoxic Glioblastoma Multiforme

---

LEYLA MOGHADDASI

Supervisor: Prof. Eva Bezak
Co-Supervisors: Prof. Loredana Marcu (until 2012) &
Dr. Wendy Harriss-Phillips (2013-2016)

A thesis submitted in fulfilment of the requirements
for the degree of Doctor of Philosophy

in the

School of Physical Sciences
University of Adelaide

September 2016

Declaration of Authorship

I, Leyla Moghaddasi, certify that this thesis titled, 'Development of an Integrated Stochastic Model for the Evaluation of the Impact of Microscopic Extension on Tumour Clonogen Survival in Heterogeneous Hypoxic Glioblastoma Multiforme ' and the work presented in it are my own. I confirm that:

- This work contains no material which has been accepted for the award of any other degree or diploma in any university or other tertiary institution to Leyla Moghaddasi and, to the best of my knowledge and belief, contains no material previously published or written by another person, except where due reference has been made in the text.
- I give consent to this copy of my thesis, when deposited in the University Library, being made available for loan and photocopying, subject to the provisions of the Copyright Act 1968.
- The author acknowledges that copyright of published works contained within this thesis resides with the copyright holder(s) of those works.
- I also give permission for the digital version of my thesis to be made available on the internet, visa the University's digital research repository, the Library catalogue, the Australasian Digital Theses Program (ADTP) and also through web search engines, unless permission has been granted by the University to restrict access for a period of time.

Signed: ______________________________

Date: ______________________________

Peer Reviewed Publications

Published

1. Moghaddasi, L., E. Bezak, and L.G. Marcu, "In Silico Modelling of Tumour Margin Diffusion and Infiltration: Review of Current Status," *Computational and Mathematical Methods in Medicine*, vol. 2012, Article ID 672895, 16 pages, 2012. doi:10.1155/2012/672895.
2. Moghaddasi, L., E. Bezak, and L.G. Marcu, Current challenges in clinical target volume definition: Tumour margins and microscopic extensions. *Acta Oncol*, 2012. 51(8): p. 984-95.
3. Moghaddasi, L., E. Bezak, and W. Harris-Phillips, Evaluation of current clinical target volume definitions for Glioblastoma using cell-based dosimetry stochastic methods. *Br J Radiol* 2015; 88: 20150155.
4. Moghaddasi, L., E. Bezak, and W. Harris-Phillips, Monte Carlo model development for evaluation of current clinical target volume definition for heterogeneous and hypoxic glioblastoma. *Phys. Med. Biol.* 61 (2016) 3407–3426.

Submitted for Publication

1. Moghaddasi, L., E. Bezak, and W. Harris-Phillips, Development and verification of a Geant4 beam model for Boron Neutron Capture Therapy, *Computational and Mathematical Methods in Medicine*, 2016 (Submitted Sep 2016).
2. Moghaddasi, L., E. Bezak, and W. Harris-Phillips, Development of an integrated Monte Carlo model for glioblastoma multiforme treated with boron neutron capture therapy, *Physics in Medicine and Biology*, 2016 (Submitted Aug 2016).

Grants and Scholarships

- ACPSEM EPSM 2012 Scholarship.

Conference Presentations and Awards

National

1. Moghaddasi, L., E. Bezak, Marcu, L. (2012), Geant4 beam model development for mathematical modelling of tumour microscopic extension (The quest for CTV for Brain Glioma), Oral Presentation, Engineering and Physics sciences in Medicine Conference. Gold Coast, Australia.

2. Moghaddasi, L., E. Bezak, (2013) mathematical model development for evaluation of current clinical target volume (CTV) definition of glioblastoma using Geant4, Oral Presentation, Engineering and Physics sciences in Medicine Conference. Perth, Australia.

3. Moghaddasi, L., E. Bezak, W. Harris-Phillips, (2014) Monte Carlo model development for evaluation of current clinical target volume (CTV) definition for glioblastoma (GBM), Oral Presentation, Combined Scientific Meeting (CSM). Melbourne, Australia.

4. Moghaddasi, L., E. Bezak, W. Harris-Phillips, (2014) Monte Carlo model development for evaluation of current clinical target volume definition for glioblastoma using Boron neutron capture therapy, Oral Presentation, Micro-Mini and Nanodosimetry (MMND). Port Douglas, QLD, Australia.

International

1. Moghaddasi, L., E. Bezak, (2013), mathematical model development for evaluation of current clinical target volume (CTV) definition of glioblastoma using Geant4, Oral Presentation, Radiation Research Society Conference, New Orleans, USA.

2. Moghaddasi, L., E. Bezak, W. Harris-Phillips, (2014) Monte Carlo model development for evaluation of current clinical target volume (CTV) definition for glioblastoma, Poster and poster discussion session presentation, ESTRO33. Vienna, Austria.

3. Moghaddasi, L., E. Bezak, W. Harris-Phillips, (2014) Monte Carlo assessment of glioblastoma (GBM) clinical target volume (CTV) efficacy based on calculated cell survival following external beam radiotherapy for heterogeneous and hypoxic

GBM tumours, Poster Presentation, Radiation Research Society (RRS) Conference, LasVegas, USA.

4. Moghaddasi, L., E. Bezak, W. Harris-Phillips, (2015) Monte Carlo model development for evaluation of glioblastoma CTV using Boron neutron capture therapy, Oral Presentation, World Congress on Medical Physics and Biomedical Engineering, Toronto, Ontario Canada.

5. Moghaddasi, L., E. Bezak, W. Harris-Phillips, (2016) Monte Carlo model development for evaluation of current clinical target volume definitions for glioblastoma using boron neutron capture therapy, accepted for Poster Presentation, Radiation Research Society (RRS) Conference, Hawaii, USA.

6. Moghaddasi, L., E. Bezak, (2016)An integrated Monte Carlo model for heterogeneous glioblastoma multiforme treated with boron neutron capture therapy, accepted for Oral Presentation, International Conference in Medical Physics (ICMP), Bangkok, Thailand.

I believe in intuition and inspiration. Imagination is more important than knowledge. For knowledge is limited, whereas imagination embraces the entire world, stimulating progress, giving birth to evolution. It is, strictly speaking, a real factor in scientific research.

Albert Einstein

Abstract

Determination of an optimal Clinical Target Volume (CTV) margin is generally challenging since the exact extent of microscopic disease to be encompassed by the CTV cannot be fully visualized using current imaging techniques and therefore remains uncertain.

The aim of this work was to establish a treatment-modelling framework for evaluation of current CTV practices in terms of tumour clonogen survival fraction following treatment. An integrated radiobiological model has been developed for this purpose, using the Monte Carlo (MC) toolkit Geant4. In order to determine the tumour site with high discrepancy/uncertainty in terms of the CTV margin definition, a comprehensive literature review was conducted. As a result, Glioblastoma Multiforme (GBM) was identified to be the subject of this research work.

Model Development

The architecture of the MC model consists of three main components: 1) simulation of a GBM tumour with diffusions of tumour cells beyond the limit of the CTV, called Microscopic Extension Probability (MEP) model; 2) irradiation of the GBM model; and 3) cell survival calculation.

GBM treatment modelling using 6 MV conventional X-ray therapy

A model of GBM and its microscopic extension was developed using MATLAB® (MathWork® Natick, MA). The input parameters required for the simulation were obtained from published clinical literature data. The MC toolkit Geant4 was used for the second component of the model. The input code enabled simulation of geometry (i.e. the GBM model), the radiation beam , and detailed transport of each particle tracked throughout the geometry until coming to rest. As a result absorbed dose was calculated in individual cells. In the third component of the model, predicting survival probability for each individual tumour cell within the *in silico* model, was achieved using a combination of Matlab codes developed in this work and Geant4 outputs imported into Matlab. The Linear Quadratic (LQ) model was used to calculate cell survival probabilities.

Homogeneous and normoxic GBM

The first study considered a simplified model of GBM consisting of a population of cells with homogeneous radiosensitivities represented in terms of α and β parameters of the LQ model. At this stage of the study, hypoxic cells were not considered. A Geant4 cellular model was developed to calculate the absorbed dose in individual cells represented by cubic voxels of 20 μm sides. The system was irradiated with opposing 6MV X-ray beams. The beams encompassed planning target volumes corresponding to 2.0 and 2.5 cm CTV margins. As a result, Survival Fraction (SFs) following x-ray EBRT were calculated for various simulation set-ups including different cellular p53 gene status, CTV margin extensions and ME propagations in regions of interest.

Heterogeneous and hypoxic GBM

The next stage of the project focused on expanding the GBM model to incorporate other radiobiological parameters affecting cellular radiosensitivities. Oxygenation and heterogeneous radiosensitivity profiles were incorporated into the GBM model. The genetic heterogeneity was modelled using a range of α/β values associated with different GBM cell lines, obtained from published clinical data. Cellular oxygen pressure taken from a sample weighted to literature-based profiles was randomly distributed. Three types of GBM models were analysed: homogeneous-normoxic, heterogeneous-normoxic, and heterogeneous-hypoxic. The SF in different regions of the tumour model and the effect of the CTV margin extension from 2.0 – 2.5 cm on SFs were investigated for three MEP models.

The results of this study for a virtual GBM model suggested that radiobiological damage caused by x-ray beams may not be sufficient to kill or sterilize GBM cell populations, and the tumour is most likely to relapse in the treatment volume. Therefore, the ultimate aim of the x-ray therapy of these tumours may be extension of time to recurrence rather than cure. This conclusion led the direction of the study to another modality which could potentially offer more promising treatment outcome for GBM.

GBM treatment modelling using Boron Neutron Capture Therapy

Recent technological advances have enabled other modalities to be developed, including charged particle radiation and targeted therapies, to be developed. Boron Neutron Capture Therapy (BNCT) is a biochemically-targeted type of radiotherapy where thermal neutrons are captured by ^{10}B, resulting in the emission of high Linear Energy Transfer (LET) α-particles and re-coiling ^{7}Li nucleus. This is a binary modality in which a suitable ^{10}B agent is taken up preferentially by malignant cells. The clustered damage produced by high LET radiation could selectively destroy cancer cells dispersed in normal tissue, with minimal normal tissue toxicity. This makes BNCT an appropriate modality for infiltrative GBM.

A realistic neutron beam model was developed in Geant4 and verified against published data. The system was defined as a cubic phantom divided to 20 μm side voxels (the average size of glioma cells) and irradiated with an epithermal neutron beam. Typical ^{10}B concentrations in GBM and normal brain cells were obtained from literature. Each cell was then assigned a ^{10}B concentration depending on its MEP status. Nested parameterisation method was used, to assign each cell with its corresponding material, which was built in Geant4 using brain composition with added boron atoms. Results from the cell-based dosimetry model and the MEP models were combined to evaluate SFs for CTV margins of 2.0 & 2.5 cm, and different infiltration distributions in regions of interest.

Conclusion

A novel Monte Carlo-based approach has been employed by this project aiming to address a clinically important question. The integrated GBM radiobiological model is a tool to quantitatively evaluate the impact of different CTV margins for GBM on cancer cell survival. It is believed that the information acquired during this research will be useful for clinicians to optimize treatment prescription for glioblastoma multiforme patients using x-ray therapy and boron neutron capture therapy.

Acknowledgements

It is a pleasant task to express my thanks to all those who contributed in many ways to the success of this study and made it an unforgettable experience for me. This thesis has been kept on track and been seen through to completion with the support and encouragement of many special people. I would first like to thank my loving, and encouraging husband, Mojtaba Moosavi, and sons, Ali and Mohammad, for sticking with me through all the good times and difficult, and helping to keep me sane. Words fail to express my deep sense of gratitude towards Mojtaba for his genuine and unconditional love, who has selflessly supported me in whatever way he could during my pursuits.

I would like to take this opportunity to thank my parents for raising me to become a loving and caring person. They themselves have been a true model of it. I will always be grateful to my mum who has made an untold number of sacrifices for the entire family and myself. I thank her for nurturing me and for her love and devotion. And dad, I have always been inspired by your exceptional character, your resilience, intelligence, generosity and broad mindedness. When things turned difficult, I was able to persevere when I reminded myself that I am your daughter. Mum and dad, I deeply wish as you go through this manuscript, you feel proud of the person I have become. This PhD marks a new beginning of my life which I endeavour to devote to cancer research.

I would like to acknowledge the administrative physics department staff at the University of Adelaide, for their support, particularly Katie Burton who has always been very welcoming and cheerful to all students including myself. In addition, I would like to thank Ramona Adorjan for her assistance in computer software and hardware support. They were essential for timely completion of this research work which was mostly computational-based.

I am very grateful to eRSA high performance supercomputers staff, particularly Mr. Andrew Hill for his great support, allocating 96 cores of the Tizard supercomputer for 10 weeks for my simulations to run.

Thank you to the ACPSEM for selecting me for the scholarship to attend the EPSM 2012 conference on the Gold Coast.

Special thanks to Dr. Manuel Graeber for taking his time to discuss in regards to the model assumptions related to genetic heterogeneity. Undoubtedly, reasonably accurate results cannot be achieved unless biologically meaningful input parameters are used.

I gratefully acknowledge all the staff in the Medical Physics department at the Royal Adelaide Hospital. My time in Australia and working at the Royal Adelaide Hospital, was made enjoyable in large part due to the many friends and groups that became a part of my life. I loved working with all of you throughout these years and I appreciate the love and support I received from you during the time my life hit one of the most difficult stages. I expand my special thanks to Miss Christine Robinson, our office manager, for organizing conferences, travel documents and many more which helped me to present this work nationally and internationally.

My time at RAH was also enriched by my great fellow PhD students for the stimulating discussions and all the fun we have had over the past four years. Thanks to Dr. Scott Penfold, our postgraduate coordinator, for being such a great and knowledgeable mentor from the very beginning of my research work. Thank you for patiently addressing my questions in regards to Geant4 until I stood up on my own feet. I hope we can collaberate together in the future.

My thanks goes in particular to my office room mates and fellow PhD students then, Dr. Michael Douglass and Dr. Alexandre Santos for their great company and scientific discussions on a variety of topics in the field. A very special thank to them for proofreading parts of my thesis.

A big thank you to Dr. Michael Douglass for helping me with Geant4 programming when I started and so many rounds of enjoyable discussions with him on my project. I admire his distinguished talent and look forward to collaborating with him in future research work.

My special thanks goes to my co-supervisors Prof. Loredana Marcu and Dr. Wendy Harriss-Phillips.

Many thanks to Prof. Loredana Marcu who has been a constant source of encouragement and motivation when she was my co-supervisor in Adelaide and even after she left to Europe. Her broad knowledge and insight enriched my ideas when I started as a newbie in the field. I hope we can work together on other projects in the future.

Thank you to Dr. Wendy Harriss-Phillips for her support in proofreading my publications, presentations and her helpful comments and suggestions. I am looking forward to learning more from her in the field of clinical medical physics as part of TEAP training.

Last and foremost I would like to express my heartfelt thanks to my supervisor Prof. Eva Bezak. She has been by far the greatest supervisor and mentor I could ever have

wished for. There were many times where I reached dead ends and each time she was there to steer me towards the right path. She supported me unconditionally and frankly I could not have not possibly come this far to accomplish this research, had she not supported and encouraged me in my difficult times. She was prepared to sit and listen to my troubles and always made me feel welcome. She has taught me, both consciously and unconsciously, how good research work is done. I would like to thank her for her patience to spend endless hours proofreading my thesis. I have learnt a great deal from her on improving my academic writing skills through her invaluable comments on my thesis and research papers. I appreciate all her contributions of selfless time, noble ideas, immense knowledge and intelligence, her contagious enthusiasm to make my PhD experience productive, stimulating, and memorable. I want to thank her for facilitating funding for me to present my research in several national and international conferences. Words are not enough to express my deep sense of gratitude, and I can only say I am truly grateful and indebted to her. I would be honoured if I could continue working with her on so many useful and cutting-edge research works to come ...

Contents

List of Figures

List of Tables

Abbreviations

BNCT	**B**oron **N**eutron **C**apture **T**herapy
CPU	**C**entral **P**rocessing **U**nit
CT	**C**omputer **T**omography
CTV	**C**linical **T**arget **V**olume
DNA	**D**eoxyribo**n**ucleic **A**cid
DSB	**D**ouble **S**trand **B**reak
EBRT	**E**xternal **B**eam **R**adio**t**herapy
GEANT	**Ge**ometry **an**d **T**racking
GPU	**G**raphics **P**rocessing **U**nit
GTV	**G**ross **T**umour **V**olume
IGRT	**I**ntensity **G**ated **R**adio**t**herapy
IMAT	**I**ntensity **M**odulated **A**rc **t**herapy
IMRT	**I**ntensity **M**odulated **R**adio**t**herapy
LET	**L**inear **E**nergy **T**ransfer
LPL	**L**ethal **P**otentially **L**ethal
LQ	**L**inear **Q**uadratic
MC	**M**onte **C**arlo
MRI	**M**angetic **R**essonance **I**maging
OER	**O**xygen **E**nhancement **R**atio
PC	**P**ersonal **C**omputer
PDF	**P**robability **D**ensity **F**unctions
PET	**P**ositron **E**mission **T**omography
PTV	**P**lanning **T**arget **V**olume
RAM	**R**andom **A**ccess **M**emory

RBE	**R**elative **B**iological **E**ffectiveness

Physical Constants

Speed of Light $c = 2.997\ 924\ 58 \times 10^{8}\ \mathrm{ms}^{-1}$

Gravitational Constant $G = 6.673\ 84 \times 10^{-11}\ \mathrm{m}^{3}\ \mathrm{kg}^{-1}\ \mathrm{s}^{-2}$

Plank's Constant $h = 6.626\ 069\ 57 \times 10^{-34}\ \mathrm{m}^{2}\ \mathrm{kg}\ \mathrm{s}^{-1}$

Fine Structure Constant $\alpha = 7.297\ 352 \times 10^{-3}$

Electron Rest Mass Energy $m_e = 510.99\ \mathrm{keV}$

Proton Rest Mass Energy $m_p = 938.27\ \mathrm{MeV}$

Neutron Rest Mass Energy $m_n = 939.56\ \mathrm{MeV}$

Alpha Particle Rest Mass Energy $m_\alpha = 3727.37\ \mathrm{MeV}$

Charge of an Electron $e = 1.6021 \times 10^{-19}\ \mathrm{C}$

Classical Electron Radius $r_e = 2.817\ 940 \times 10^{-15}\ \mathrm{m}$

Bohr Radius $a_0 = 0.529177 \times 10^{-10}\ \mathrm{m}$

Compton Wavelength $\lambda_C = 2.426 \times 10^{-12}\ \mathrm{m}$

Stefan-Boltzmann Constant $\sigma = 5.670\ 373 \times 10^{-8}\ \mathrm{W\ m}^{-2}\ \mathrm{K}^{-4}$

Boltzmann Constant $k = 1.380\ 658 \times 10^{-23}\ \mathrm{J\ K}^{-1}$

Rydberg Constant $\mathfrak{R} = 10\ 973\ 731.568 \times 10^{-1}\ \mathrm{m}^{-1}$

Avogadro's constant $N_A = 6.0221 \times 10^{23}\ \mathrm{mol}^{-1}$

Permittivity of Free Space $\epsilon_0 = 8.8541 \times 10^{-12}\ \mathrm{F\ m}^{-1}$

Permeability of Free Space $\mu_0 = 12.566\ 370 \times 10^{-7}\ \mathrm{N\ A}^{-2}$

Gas Constant $R = 8.3144\ \mathrm{J\ K}^{-1}\ \mathrm{mol}^{-1}$

Symbols

D	Absorbed radiation dose	Gy
P	Power	Watts
SF	Survival fraction	(dimensionless)
E	Particle energy	MeV
σ	Interaction cross section	cm^{-1}
Z	Atomic number	(dimensionless)
T	Kinetic energy	MeV
B	Binding energy	eV

Dedicated to my beloved late aunt, Fatemeh Borghei, whose accomplished life was cut short too soon by lung cancer. She was a brilliant astrophysicist and her beautiful mind is what inspired me to become a scientist. Her incredible patience to answer my never-ending questions, our quiet moments looking through her telescope into the night sky trying to see different constellations, and so much more, shaped me as a female scientist. She did what she came here to do, and I recovered from my grief only to pick up where she left off- to devote the rest of my life to cancer care and research.

May her stardust soul rest in peace...

Chapter 1

Introduction

Cancer is a major health problem estimated to affect one in three and one in four Australian men and women before the age of 75, respectively (Australian Institute of Health and Welfare, 2015). This statistics is the same for the population of the United States (Siegel et al., 2013). Due to substantial improvements in treatment approaches, the mortality to incidence ratio (i.e. number of deaths from cancer divided by the number of new cancer incidences in a given year), which is a rough measure of cancer fatality, declined by 26% from 1990 to 2011. This ratio was evaluated to be 0.37 and 0.36 for Australian males and females, respectively (Australian Institute of Health and Welfare, 2015).

Radiation therapy alone or in combination with surgery and chemotherapy has been applied in cancer treatment for over 100 years. The two most common radiotherapy modalities are: 1) External Beam Radiation Therapy (EBRT) utilizing primarily megavoltage x-rays, electrons, charged particles, and neutrons; and 2) brachytherapy, which is more effective than EBRT in delivering a localised dose to the tumour volume but can be invasive and also can only be implemented for certain tumour types.

Treatment of deep-seated tumours became possible following a sequence of key advances beginning with the development of ^{60}Co machines and their implementation of the first treatment in 1950, London, Ontario, followed by the first treatment using a linear accelerator (linac) in 1953, London, UK. In the past six decades, ongoing research has been conducted, and as a result, the reliability of linacs has greatly improved. Complex beam delivery systems have been designed for better radiation field conformality, and new functionalities (e.g. portal imaging and Cone Beam Computed Tomography (CBCT)) have been incorporated to enable image guided therapy.

Recent technological and pharmaceutical advances have enabled other radiotherapy modalities to be developed. The two most major advances are heavy ion therapy (e.g. protons and carbon ions) and targeted therapy. These modalities have several physical and biological advantages over megavoltage x-rays partly due to the fact that the treatment is delivered by high Linear Energy Transfer (LET)[1] particles. Targeted therapy modalities, such as Targeted Alpha Therapy (TAT) and Boron Neutron Capture Therapy (BNCT), are designed to target cancer cells and deliver localized dose from high LET particles preferentially to tumour cells and provide a superior normal tissue sparing as compared to conventional EBRT (Allen, 2006, Barth et al., 2004).

1.1 Radiation Therapy of Cancer Cells

In radiotherapy, ionizing radiation emerging either from an accelerator (i.e. EBRT) or internal sources (i.e. brachytherapy and targeted therapy) strikes the cells along its path, resulting in a sequence of ionizing events and molecular bond breakage. This eventually leads to double/single strand DNA breaks and cell death. Biological damage caused by ionizing radiation results from two different types of processes: direct and indirect. In direct action, which is dominant for high LET particles, such as protons and alpha particles, an ionizing event occurs directly within DNA molecules. Indirect action, the dominant effect for low LET particles including x-ray, electron and neutron beams, is a term referred to a process where a secondary electron liberated by ionizing radiation interacts with a water molecule to produce free radicals. Highly reactive free radicals have a high probability to form DNA adducts, resulting in DNA damage. The processes involved in the interaction of radiation with cells can be broken down into five stages with time durations ranging from $\sim 10^{-6}\ s$ for physical stage (i.e. ionisation) up to years for the biological stage (i.e. cell death/induction of cancer), as shown in figure 1.1 (for indirect

---

[1] LET is the rate of energy loss by incident ionizing radiation per unit length: $LET = \frac{dE}{dx}(keV/\mu m)$

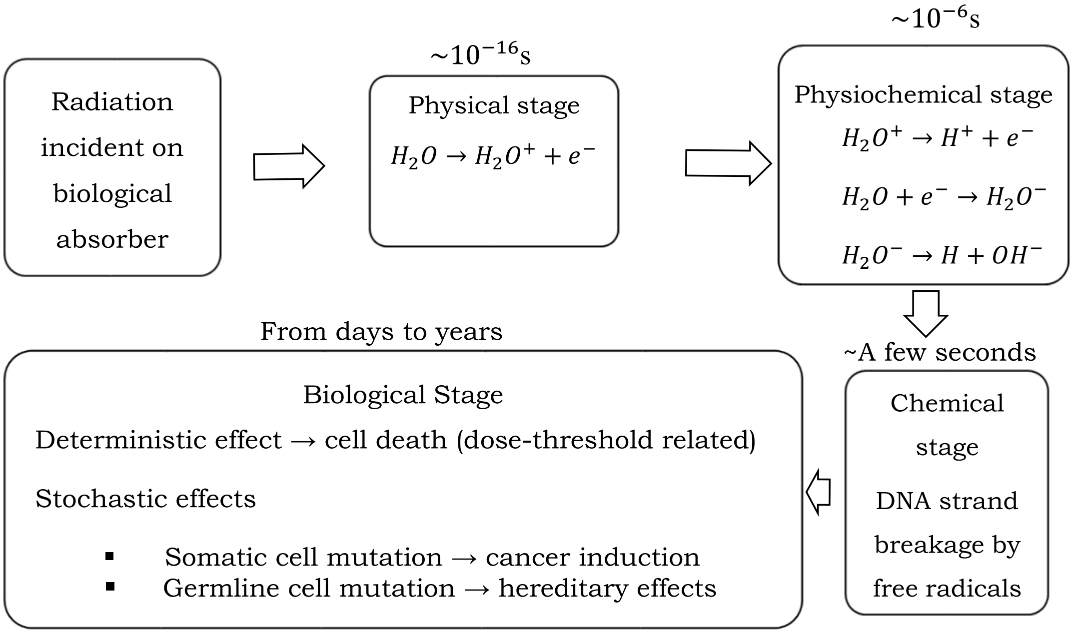

Figure 1.1: Various stages of indirect ionizing radiation interaction with biological tissue from exposure, up until the biological endpoint. The number above each box is the duration time for the respective stage.

damage). In a normal progression through cell division, cells undergo signalling pathways to recognize DNA damage and initiate its repair. Any DNA lesion identified at cell cycle checkpoints is directed to repair pathways where repair is attempted or else signalled to undergo cell death via apoptosis. In terms of repair pathways, radiation-produced DNA damage can be categorized as (Marcu et al., 2012):

1. Lethal damage which is irrepairable leading to mitotic cell death via apoptosis.
2. Sublethal Damage (SLD) is a damage that can be repaired unless additional damage occurs.
3. Potentially Lethal Damage (PLD) which is a type of damage that is normally non-lethal but may become lethal depending on the post-irradiation environment.

However, for cells with abnormal cell cycle progression characteristics due to mutant/non-existent cell cycle checkpoints (e.g. ensuing a series of DNA mutations), DNA lesions can escape cell cycle check points causing cells to lose self-elimination capability and form an abnormal aggregation of cells with chromosomal aberrations, called a neoplasm or a tumour. The term neoplasm/tumour can refer to benign (usually curable) or malignant (cancerous) growths. Due to the fact that energy deposition by ionizing radiation is a stochastic process, the cellular response to ionizing radiation, occurring either by direct or indirect action of radiation, may result in (ICRP, 1991):

1. Lethal damage to cells or prevention of cell division leading to depletion of cell population within the site of the corresponding tumour. These are called early or deterministic effects which are dependent on the delivered dose.
2. Stochastic damage resulting in non-lethal mutations in cells. If mutations occur in somatic cells it may result in cancer induction and if germ cells are mutated, heritable effects may occur.

The main objective of radiotherapy is to maximise the dose to the tumour volume while sparing as much of the surrounding healthy tissue as possible from radiation morbidity. This is to achieve the highest probability of tumour control while reducing the severity of side effects and the probability of developing second cancers. In order to evaluate the efficacy of radiotherapy treatment the biological effect of ionizing radiation needs to be determined (Marcu et al., 2012).

1.2 Radiobiological modelling

Mathematical and computational models are frequently used in clinical radiobiology. They have been used to understand complex biophysical radiation damage processes and attempt to relate the physical absorbed dose to chemo-biological cellular damage since the early 1970 (Chadwick and Leenhouts, 1973). Radiobiological effect of radiation is commonly measured by the so-called cell survival curve, that is, the relationship between the absorbed dose and the fraction of cells surviving the irradiation. The first mathematical formula, derived from the target theory principles (i.e. assuming double hits on a single DNA target are required to kill the cell) which was in good agreement with then

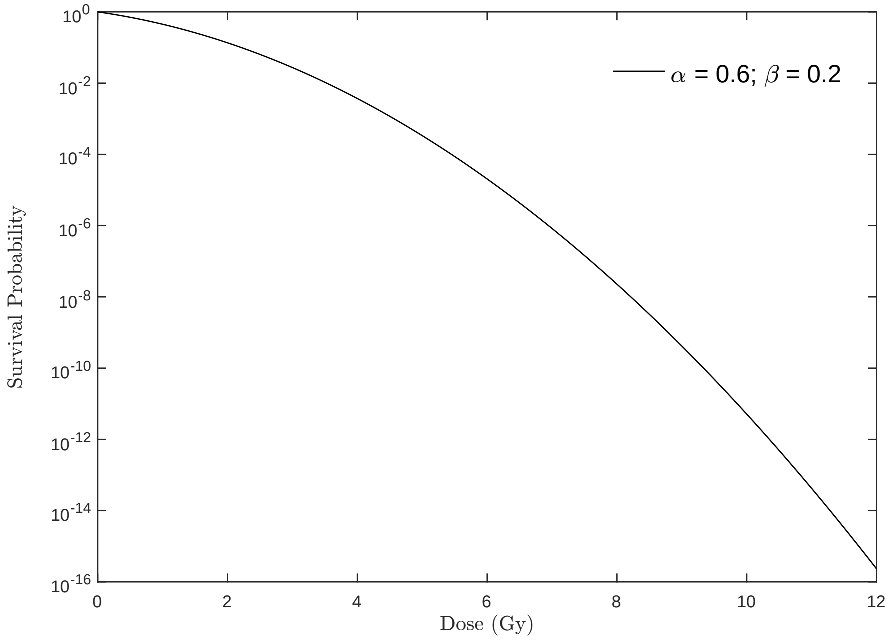

FIGURE 1.2: Cell survival probability based on the LQ model after a single dose of radiation for a tumour with the LQ parameters of $\alpha = 0.6$ and $\beta = 0.2$.

experimental data, was proposed by Chadwick (Chadwick and Leenhouts, 1973). This model, which is still used in clinics, is called the Linear Quadratic (LQ) model and relates macroscopic dose deposition to radiation-induced damages in the cell population. The LQ model predicts the survival probability of a tumour for a given α and β values and a given radiation dose D according to equation 1.1 and is plotted in figure 1.2. α and β parameters of the LQ model are the first and the second slope of the survival probability curve, respectively, and their ratio is commonly used as an estimate of fractionation sensitivity of a specific tumour. Survival is then calculated as:

$$S = e^{-\alpha D - \beta D^2} \tag{1.1}$$

where S is the cell survival fraction probability for cells receiving radiation dose D.

In current clinical radiobiology, the efficacy of radiation therapy is commonly evaluated by dose-response relationship parameters Tumour Control Probability (TCP) and Normal Tissue Complication Probability (NTCP). TCP is the probability of zero surviving clonogenic cells. The Poisson distribution in equation 1.2 (Zaider and Hanin, 2011) analytically approximates TCP which is a function of cell survival probability, which may be calculated or predicted using the LQ or other models.:

$$\begin{aligned} TCP &= e^{-n(D)} \\ n(D) &= n(0)S(D) \end{aligned} \tag{1.2}$$

where $n(D)$ is the expected number of clonogens (i.e. a cell that has the potential to proliferate and give rise to a colony of cells) surviving the absorbed dose D and $n(0)$ is the initial number of clonogenic cells. Unlike TCP, NTCP is hard to model due to varying radiosensitivity levels of different organs and due to varying proximity of the irradiated tumour volume to organs at risks. One of the commonly used models for NTCP that has been in good agreement with early clinical data is the Lyman model, equation 1.3 (Lyman, 1985):

$$\begin{aligned} NTCP &= \frac{1}{\sqrt{2\pi}} \int_{-\infty}^{1} exp^{(-t^2/2)} dt \\ t &= \frac{D - TD_{50}(V)}{m} TD_{50}(V) \end{aligned} \tag{1.3}$$

where $TD(V)$ is the tolerance dose for a given partial volume V, $TD_{50}(V)$ is the absorbed dose that results in 50% NTCP in a given partial volume V and m is a tissue specific parameter. The balance between TCP and NTCP is a measure of therapeutic ratio of the treatment which generally refers to the ratio of TCP and NTCP at a specified absorbed dose (Lyman, 1985). Most of the model parameters described above have been derived from the report of Emami *et al.* (Emami et al., 1991).

With the advent of new treatment techniques, e.g. Intensity Modulated Radiation Therapy (IMRT) and Image Guided Radiation Therapy (IGRT), and improving precision of dose measurements (including *in-vivo* dosimetry), increasing number of studies of tissue tolerance have been published which have rendered a large amount of the Emami data (Emami et al., 1991) outdated. As a result, the currently available 3D dose–volume/outcome were summarized with the aim to develop a practical guideline for clinicians to reasonably balance normal tissue toxicity versus prescribed dose, a committee of experts developed updated guidelines on Quantitative Analysis of Normal Tissue Effects in the Clinic (QUANTEC) (Bentzen et al., 2010).

In later years the LQ model was further extended and incorporated the effects of fractionation, hypoxia and accelerated fractionation. In 1986 Curtis presented a more accurate model to predict cell survival probability, called Lethal and Potentially Lethal (LPL) model (Curtis, 1986), accounting for dose, dose rate, LET, repair and interaction kinetics of biological lesions (i.e. lethal and potentially lethal lesions). LPL model, which is a more accurate representation of cellular radiobiology and cell survival probability, is based on microscopic parameters (e.g. DNA lesions formed by ionisation events) rather than macroscopic used in the LQ model. At low doses, LPL model reduces to the familiar LQ model.

In an effort to improve upon LPL and other previous models, Stewart developed the Two Lesion Kinetic (TLK) model, predicting cell survival probability/cell death as a function of DNA Double Strand Break (DSB) formation, biochemical repair and misrepair (Stewart, 2001, Douglass et al., 2015a). TLK and LPL models can be integrated with computational models (i.e. to calculate ionisation events) for even a more robust estimation of radiation damage.

With powerful computers becoming widely available enabling parallel Central Processing Unit (CPU) and Graphics Processing Unit (GPU) programming, current and future radiobiological modelling used to predict cell survival probability has moved toward stochastic computational models using particle tracking Monte Carlo (MC) packages such as Geant4 (Agostinelli et al., 2003) and RITRACKS (Plante and Cucinotta, 2011). The physics models and cross section libraries of these packages allow to simulate the complete particle track structure and hence model DNA damage directly (Douglass et al., 2015b). Ongoing research is being performed to expand cross section libraries to various materials and particle energies and to improve on modelling of geometrical structure of DNA molecule (Plante and Cucinotta, 2008, Bernal et al., 2015).

1.3 Target Volume Definitions

Technological advances over the past decades have led to development of modern treatment techniques, e.g. IMRT, IGRT and Intensity Modulated Arc Therapy (IMAT). These techniques offer the advantage of decreasing the volume of normal tissue irradiated by x-rays as a result of more conformal dose distribution to irradiated target volumes. However, whether these advances have translated to improved TCP, is subject of discussion.

Several successive steps have to be taken to determine and optimize radiation prescription parameters (including volumes, dose and fractionation) in the course of treatment planning before radiotherapy is delivered. The first step consists of delineation of the relevant target volume to be irradiated. According to the International Commission on Radiation Units and Measurements (ICRU no.50) (Jones, 1994), Gross Tumour Volume (GTV) is the visible extent and location of the tumour which is delineated by a radiation oncologist based upon visible tumour representation using a variety of imaging techniques available today. The GTV, however, is only a proportion of the whole disease. In order to treat the disease successfully, the entire population of clonogenic cells within the gross tumour and its Microscopic Extension (ME), i.e. parts of subclinical tumour which are not detected within the resolution or sensitivities of imaging techniques, have to be eradicated. According to the ICRU report 50, ”the Clinical Target Volume (CTV) is a volume encompassing visible Gross Tumour Volume (GTV) and subclinical malignant disease” (Jones, 1994). Following the CTV determination, to ensure that the CTV receives the prescribed dose, the Planning Target Volume (PTV) is drawn to account for target position uncertainties due to organ motion and daily set-up variations. The schematic diagram of radiotherapy target volumes are shown in figure 1.3.

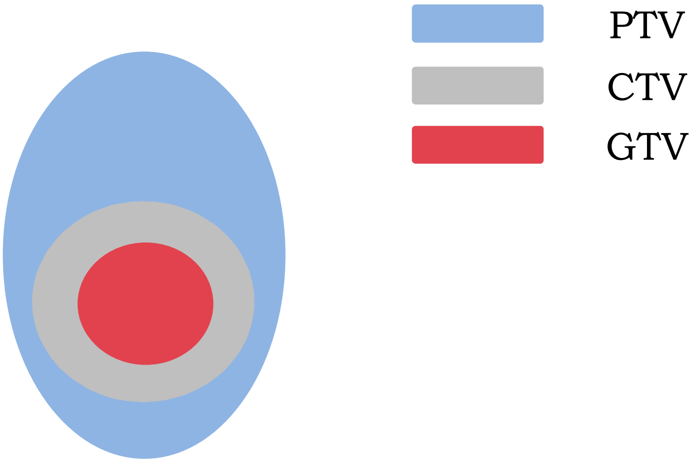

FIGURE 1.3: Schematic diagram of radiotherapy target volumes as defined by ICRU (Jones, 1994).

1.3.1 Imaging techniques and detection of Microscopic Extensions

Computerized Tomography (CT) and Magnetic Resonance Imaging (MRI) are currently the primary imaging techniques used for definition of target volumes in particular for the precise delineation of GTV. Nevertheless, their intrinsic resolution limits identification of the real extent of the tumour in the form of individual malignant cells or cell clusters.

Positron Emission Tomography (PET) is a diagnostic imaging technique which employs positron emitting radionuclides labelled with appropriate pharmaceuticals to assess the metabolic and functional activity of lesions. Many pathological conditions cause alteration of metabolic rates of specific substances (labelled by radionuclides) in the affected regions. PET's ability to identify viable tumour cells based on differential uptake of radiopharmaceuticals reflecting their metabolic rates has been widely studied and reported (Picard, 1999, Cherry et al., 2012, Padma et al., 2003, Liu et al., 2007, Dong et al., 2009). The superiority of PET to CT/MRI in revealing suspicious lesions even prior to observable anatomical changes was demonstrated in several clinical studies (Mosskin et al., 1989, Murakami et al., 2006, Aguirre et al., 2007, Matsuo et al., 2012, Sharma et al., 2012).

In the study of Matsuo *et al.* (Matsuo et al., 2012), carbon-11-labelled Methionine PET images of patients with Glioblastoma (GBM) were considered gold standards to assess CTV margins defined on MRI images.

While PET can identify malignant lesions not detectable by CT/MRI, it provides little information about their exact location within the organ due to its inferior spatial resolution, which ranges from 2-4 mm for an 80 cm diameter system typical for human imaging (Levin and Hoffman, 1999). This shortcoming can be compensated partly by co-registration of functional PET images with corresponding CT/MRI images. Co-registration of separately acquired PET and morphologic CT/MRI images, however, is clinically limited due to complexity of fusion algorithms, inaccuracies caused by patient repositioning and movement of internal organs and long acquisition times (Patton et al., 2000, Bar-Shalom et al., 2003). To overcome these problems, hybrid PET/CT and PET/MR scanners (a CT or MR and a PET scanner integrated and located within a single unit with a common patient table) have been developed (Patton et al., 2000, Bar-Shalom et al., 2003, Yong et al., 2010, Histed et al., 2012, Schwenzer et al., 2012). The hybrid scanners provide simultaneous acquisition of PET and CT/MR data which is fused into a single image set within the system to provide anatomical localization of lesions with different metabolism (Gordin et al., 2007). In addition, the combined PET/CT system provides more accurate anatomical maps to be used for attenuation corrections of PET scans (with appropriate scaling for 511 keV photons) prior to registration on the transmission image (CT scan) (Bar-Shalom et al., 2003). Therefore, PET/CT and PET/MR, offering both anatomical and functional data, are perhaps the most accurate modalities in diagnostic imaging for cancer. However, PET/CT and PET/MR techniques are still incapable of accurately detecting microscopic extension of a tumour since spatial resolution of this system is limited (1.8-2.4 mm for PET-CT) due to several factors such as non-colinearity and positron range (Wienhard et al., 1992).

As a result, the exact incidence and the extent of microscopic disease remains uncertain and the delineation of a CTV that contains the original lesion including any possible invasion beyond gross tumour or nodal microscopic spread is empirical in most instances. There is no consensus on whether CTV margins are unnecessarily generous (associated with toxicity of normal tissue and increased NTCP) or inadequate (associated with poor treatment efficacy and therefore reduced TCP). Therefore, both large and tight margins could yield undesirable results and an optimal CTV that keeps NTCP and TCP in balance is required. Hence, CTV represents a challenging volume to be defined.

1.3.2 CTV definition and modern radiotherapy techniques-what are we targeting?

Current radiotherapy treatment modalities, utilizing newer technologies like IGRT and IMAT, have been developed aimed to increase the precision of organ position determination and conformity of dose delivery which in turn results in minimization of set-up errors allowing the PTV margin to be reduced. Despite these advances in treatment modalities and imaging techniques, the uncertainty regarding microscopic extension incorporated within the CTV margin limits further reduction of irradiated volumes since the risk of missing a part or even a few cells of malignant disease is increased, as illustrated in figure 1.4. To have an estimation of the extent of the risk, it is worth noting that the Poisson distribution model of TCP (Zaider and Hanin, 2011) suggests that one single cell surviving radiation therapy will reduce TCP to 37%. While this definition is a crude approach to TCP assessment, as it does not consider the host contribution to eradication of the last few cells (such as immune response, bystander effect, and vascular damage), it is the most widely accepted cell-survival model for clinical use. As a result, to take the advantage of current treatment modalities and their capacity to reduce irradiation target volumes, the pattern of microscopic extension of a tumour is a crucial piece of information required when determining the CTV margin for these advanced techniques which restrict the high dose regions to defined irradiation volumes. An editorial note presented by Van Herk (Van Herk, 2008) has addressed this issue mentioning that smaller margins due to increased precision provided by IGRT could lead to the loss of tumour control. As pointed out in this report, more generous margins could eradicate subclinical disease which cannot be detected by current imaging tools. The reduction of margins should not be warranted based only on the reduced uncertainties in treatment delivery (e.g. provided by IGRT) and biological uncertainties (e.g. microscopic extension) should not be underestimated (Van Herk, 2008, 2004). Several clinical studies have demonstrated

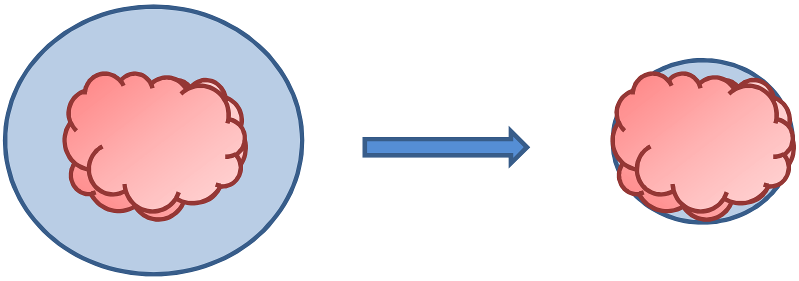

Figure 1.4: Schematic diagram of CTV and PTV correlation for conventional treatment techniques, on the left, as compared to modern treatment techniques, on the right. CTV is indicated by the red contour and the blue contour defines the PTV. As shown, significant reduction of PTV may result in missing a part of microscopic disease resulting in poorer treatment efficacy.

that application of smaller margins, depending on the precision of treatment delivery by modern radiotherapy techniques, may deteriorate clinical outcomes and result in early tumour progression and regional spread deemed to be associated with microscopic disease (Heemsbergen et al., 2013, Witte et al., 2010, Engels et al., 2009).

A comprehensive review of histopathological studies evaluating microscopic extension of tumours demonstrated that the issue of the CTV margin definition persists in the majority of tumour sites. Large discrepancies exist between the outcomes of different studies for a number of tumour sites (e.g. brain) in contrast to other organs (e.g. breast and prostate) that show a better consistency in proposed/applied margins (Moghaddasi et al., 2012b).

1.4 Challenges in radiotherapy of Gliobastoma

Gliomas are the most common primary brain tumors. Glioblastoma Multiforme (GBM) is derived from astrocytes and is the most malignant (i.e. grade IV) astrocytic tumour (Li et al., 2013). The median overall survival is $\sim$ 20 months, despite treatment schedules combining surgery, external beam radiotherapy, and chemotherapy (Louvel et al., 2016). The technological advances in x-ray external radiotherapy in terms of increased precision of dose delivery has not led to patient cure in the case of GBM. This raises the need to acquire an understanding of the dynamics and features of GBM, which have caused all current treatment regimens to be ineffective. This knowledge could help to design radiotherapy treatment plans which are more adequate to defeat this type of tumour, and improve the treatment efficacy as a result. GBM features characteristics which are different from other tumours and include:

1. A very high mobility, growing infiltratively into normal brain tissue rather than forming a solid tumour mass with defined boundaries (Unkelbach et al., 2014). The diffusive characteristics of GBM cells and their rapid peripheral expansion cause the CTV delineation of this type of tumour to be problematic. In a review study of histopathological findings of GBM patients, it was concluded that there is limited consensus between institutes and studies in terms of the extent of high grade glioma cell infiltration into normal brain tissue and the CTV margin applied as a result (Moghaddasi et al., 2012b).
2. High intrinsic radio-resistance with genetic heterogeneity and complexity (Graeber, 2010, Taghian et al., 1992).
3. Extensive intra and peri-tumoural hypoxia (Collingridge et al., 1999).

1.4.1 How to approach these challenges?

While megavoltage x-rays remain the dominant treatment modality due to their reliability, availability and efficacy in the treatment of many forms of cancer, recent technological advances have enabled other radiotherapy modalities to be developed.

Targeted therapies that use high LET particles, TAT and BNCT for example, are designed to target cancer cells and deliver localized dose selectively to tumour cells and provide a superior normal tissue sparing as compared to conventional EBRT (Van Dyk, 1999). BNCT, in particular, may be useful in radiotherapy of GBM. BNCT is based on thermal neutron capture by stable ^{10}B resulting in emission of high LET particles through a fission reaction. This is a binary modality in which a suitable ^{10}B agent is taken up preferentially by malignant cells (Van Dyk, 1999). The clustered damage produced by high LET radiation beam can therefore selectively destroy cancer cells dispersed in normal tissue, with minimal normal tissue toxicity. BNCT is theoretically a suitable modality for GBM as it provides resolution for both infiltrative and radioresistance (i.e. due to intrinsic radioresistance of GBM cells and hypoxia) features of this disease.

1.5 Mathematical and computational models

Computational and biomathematical modelling are valuable tools in providing qualitative and quantitative predictions of oncogenesis and treatment outcomes for a variety of circumstances, for instance, the application of different CTV margins or therapeutic regimens. In a previous report (Moghaddasi et al., 2012a), a comprehensive review was presented on mathematical models developed for tumour growth and invasion and response to radiotherapy regimens. Two approaches are generally used for modelling: analytical and stochastic. Analytical models are mostly capable of describing tumour behaviour at the macroscopic level and fail to provide predictions at the cellular and subcellular (i.e. microscopic) scale. Recent analytical models, however, have attempted to describe microscopic damage, e.g. local effect model (Friedrich et al., 2013). In addition, intrinsically probabilistic nature of radiobiological and physical processes involved in radiation interactions with matter cannot be simulated by deterministic models where biological phenomena are represented by mathematical equations and the solutions of the equations remain the same for the same set of input parameters.

Monte Carlo, in general, is a very useful method to model sophisticated phenomena with significant variations such as biological systems. In MC techniques, inputs are selected randomly from a probability distribution over the domain of possible inputs (e.g. interaction processes that a given particle with a specific energy can undergo). The results are produced by analytical computation performed on the inputs. Several MC codes, for example, EGSnrc (Kawrakow, 2000) for the simulation of photon and electron electromagnetic processes, and GEANT4 (Agostinelli et al., 2003), MCNP/MCNPX (Briesmeister et al., 2000), PARTRACK (Friedland et al., 2011), and RITRACKS (Plante and Cucinotta, 2011) including hadronic processes have been developed. Complex experimental set-ups (e.g. detector geometry or cell component and DNA structure) can be simulated using these MC packages which makes them an invaluable tool in the field of radiation dosimetry and radiobiological modelling.

1.6 Aims of the Current Work

The aim of the current work was to develop a comprehensive and flexible radiobiological modelling framework of GBM radiation treatment for evaluation of current CTV margin practices in terms of surviving tumour clonogen following radiotherapy. The architecture of the MC model consists of:

1. Simulation of a GBM tumour with diffusions of tumor cells beyond the limit of the Clinical Target Volume (CTV), called Microscopic Extension Probability (MEP) model.
2. Irradiation of the GBM model.
3. Cell survival calculation.
4. Compare the number of surviving clonogens as a function of microscopic extension geometry, tumour radiobiological parameters, CTV margin and treatment modality.

MATLAB® (MathWork®, Natick, MA) will be used to develop the first component of the model, a model of GBM and its microscopic extension. The literature will be reviewed to identify appropriate input parameters required for the model. The MC toolkit Geant4 (Agostinelli et al., 2003) will be used for the second component of the model. An algorithm will be developed in MATLAB for the third component of the model, calculating survival fraction of the *in-silico* tumour, using a combination of MATLAB codes to be developed in the first part and Geant4 outputs.

A novel Monte Carlo approach will be taken in this project aiming to address a clinically important question of the optimal CTV for GBM using two treatment modalities. It is believed that the information acquired while performing this research work can be useful for clinicians to optimize treatment prescription for glioblastoma multiforme patients using external beam photon therapy and boron neutron capture therapy.

1.7 Thesis Outline

Chapter 2 presents a review of histopathological studies addressing the extent of sub-clinical disease and its possible correlation with tumour characteristics in various tumour sites. The aggregation of published data for different tumour sites will reveal tumour sites for which the consensus on the extension of the CTV margin is limited and therefore requires further investigation.

Chapter 3 is a critical review of current status of mathematical and computational models with an emphasis on models developed for GBM of the brain. The major limitations of each model will be discussed.

Chapter 4 begins with a brief discussion of the structure of Geant4 MC particle tracking toolkit and continues with the description development and verification of the Geant4 6 MV x-ray EBRT beam model developed in the current work.

Chapter 5 describes the development of MEP models and cell-based dosimetry Geant4 model to calculate absorbed dose in individual cells. The integration of cell-based Geant4 model and MEP model to form the GBM model will then be discussed. The application of the integrated GBM model to predict individual cell survival probabilities will be demonstrated for a simplified scenario of a GBM model with homogeneous population of cells with normal oxygenation.

The effect of incorporating other radiobiological properties of GBM cells including heterogeneous cellular radiosensitivities and varying oxygenations (i.e. hypoxia) on cell survival is investigated and presented in Chapter 6.

Following chapter 6, and in the light of information obtained for treatment outcome for a semi-realistic GBM model using conventional x-ray EBRT, the study focuses on an alternative treatment modality for GBM, called BNCT. Chapter 7 outlines the fundamentals of this treatment technique and describes the development and verification of a Geant4 BNCT beam model in the current work.

Chapter 8 describes the architecture of the GBM model for BNCT treatment modality. The detailed particle tracking including the individual simulation of each emitted particle from several fission reactions resulting in several dose components corresponding to each reaction are described and the results are presented. The investigation of the efficacy of BNCT for GBM treatment using the GBM model is presented for a simplified model of GBM consisting of homogeneous population of cell and isotropic infiltration distribution. The impact of different CTV margin extensions on cell survival fraction in BNCT treatment is also studied.

Chapter 9 expands on the model presented in chapter 8 by incorporation of genetic heterogeneity in terms of radiation sensitivity and using anisotropic microscopic disease extensions. The results of BNCT in both chapter 8 and 9 are compared with x-ray EBRT.

Chapter 10 concludes the thesis with a summary of the major achievements of the models developed in this work for glioblastoma multiforme. The plans for extending the model in the future are also discussed.

Chapter 2

The Quest for Clinical Target Volume

The publication [P1] forms the basis of this chapter.

Moghaddasi, L., E. Bezak, and L.G. Marcu, Current challenges in clinical target volume definition: Tumour margins and microscopic extensions. *Acta Oncol*, 2012. 51(8): p. 984-95.

2.1 Introduction and motivation

The emergence of new technologies in radiotherapy, such as Intensity Modulated Radiotherapy (IMRT), Image Guided Radiotherapy (IGRT), gating and Intensity Modulated Arc Therapy (IMAT), aimed to increase the precision of dose delivery and reduce the Planning target Volume (PTV) margins, has raised the need for optimal irradiation target volume determination. However, the reduction of irradiated volumes could increase the risk of missing a part or even a few cells of malignant disease, and potentially result in treatment failure. This is due to the fact that the exact incidence and extent of microscopic disease to be encompassed in the Clinical Target Volume (CTV) [1] cannot be

---

[1] According to ICRU report 50, the "Clinical Target Volume (CTV) is a volume encompassing visible Gross Tumour Volume (GTV) and subclinical malignant disease" (ICRU, 1999).

visualized by any current imaging techniques and therefore, this margin is determined empirically and is subject to uncertainty.

A a review of histopathological studies addressing the extent of subclinical disease is presented in this chapter. This is to identify tumour sites for which the consensus on the extension of the CTV margin is limited and, therefore requires further investigation.

2.2 Statement of Contribution

2.2.1 Conception

The idea to conduct a review of published clinical data to seek microscopic extension of different tumour sites was first conceptualised by Eva Bezak. The search methodology in which to collect comprehensive data was conceptualised by Leyla Moghaddasi, Eva Bezak and Loredana Marcu.

2.2.2 Realisation

The critical review was performed by Leyla Moghaddasi. General supervision and guidance was provided by Eva Bezak, and Loredana Marcu. The manuscript was then evaluated by Eva Bezak and Loredana Marcu in terms of data accuracy, critical appraisal, conclusions reached, and general structure and flow.

2.2.3 Documentation

This paper was primarily written by Leyla Moghaddasi. Editing was performed by all authors.

Statement of Authorship

Title of Paper	Current challenges in clinical target volume definition: Tumour margins and microscopic extensions
Publication Status	☑ Published ☐ Accepted for Publication ☐ Submitted for Publication ☐ Publication Style
Publication Details	Moghaddasi, L., E. Bezak, and L.G. Marcu, *Acta Oncol*, 2012. 51(8): p. 984-95.

Principal Author

Name of Principal Author (Candidate)	Leyla Moghaddasi		
Contribution to the Paper	Conducted the literature review, and wrote the manuscript and acted as corresponding author.		
Overall percentage (%)	70%		
Signature		Date	22/06/2016

Co-Author Contributions

By signing the Statement of Authorship, each author certifies that:

i. the candidate's stated contribution to the publication is accurate (as detailed above);

ii. permission is granted for the candidate in include the publication in the thesis; and

iii. the sum of all co-author contributions is equal to 100% less the candidate's stated contribution.

Name of Co-Author	Prof. Eva Bezak		
Contribution to the Paper	Initial idea, general guidance and supervision, and manuscript revision.		
Overall percentage (%)	15%		
Signature		Date	22/06/2016

Name of Co-Author	Prof. Loredana Marcu		
Contribution to the Paper	Initial idea, general guidance and supervision, and manuscript revision.		
Overall percentage (%)	15%		
Signature		Date	22/06/2016

Moghaddasi, L., Bezak, E. & Marcu, L.G. (2012). Current challenges in clinical target volume definition: Tumour margins and microscopic extensions.
Acta Oncologica, 51(8), 984-995.

2.3 Additional remarks

Target treatment volume definitions for glioblastoma of the brain, the CTV margin in particular continues to be a major concern in radiotherapy and consequently has been the subject of numerous clinical investigations in recent years (Niyazi et al., 2016, Fiorentino et al., 2013, Wee et al., 2015, Berberat et al., 2014, Rosenschold et al., 2014, Yan et al., 2014). Treatment volumes used for GBM have varied significantly between different trials and institutions (Niyazi et al., 2016). There is no clear consensus on what imaging modality should be used or whether the CTV is applied to the GTV or whether it should include oedema (i.e. T2-MRI). The Radiation Therapy Oncology group (RTOG) recommends that initial CTV margins encompasses the entire T2-MRI (i.e. including peritumoral edema) plus a 2.0 cm margin. The standard irradiation schedule should be followed by a boost dose delivered to T1-MRI plus a 2.5 cm margin (Gilbert et al., 2014). In contrast, EORTC recommends that the CTV should encompass the T1-MRI and surgical cavity plus a 2 cm (i.e. The CTV should be modified if anatomical corrections are necessary) (Niyazi et al., 2016).

Fiorentino (Fiorentino et al., 2013) compared CTV margin definitions based on Magnetic Resonance Imagining-Computed Tomography (MRI-CT) fusion and CT only images by performing analysis on 120 CT and MRI images of GBM patients. It was concluded that MRI-CT fusion provided more information and CTV based only on CT was not adequate, as up to 20% of MRI target was missed (Fiorentino et al., 2013). Some studies used diffusion tensor imaging (DTI) to improve the precision of target volumes delineation, and demonstrated that DTI can individualize margin delineation and could potentially reduce the size of the CTV for specific cases (Berberat et al., 2014). Rosenschold (Rosenschold et al., 2014) suggested Positron Emission Tomography (PET)-guided radiation therapy planning for definition of GTV and CTV and concluded that the technique is most useful for patients with grade IV glioma or above. Yan developed an algorithm based on geodesic distance calculation to reduce inter-observariation for the CTV margin delineation of GBM patients (Yan et al., 2014).

Having identified the tumour site to be considered in this research work, which was GBM of the brain, the literature was reviewed further to seek quantitative data of microscopic extension for high-grade glioma or glioblastoma (i.e. in addition to the data presented in the supplementary appendix table). The published data in regards to brain glioblastoma specifically has been summarized in table 2.1. Burger *etal.* (Burger et al., 1988) compared CT scans and histological specimens of 15 GBM patients. The microscopic disease was found up to 5 cm from the visible tumour on a CT scan, with 20% of patients presenting with 2-3 cm infiltration, and 13% with 3-5 cm infiltration. Another CT versus histopatholgical specimen comparison of 11 GBM patients suggested a 3.0 cm CTV margin would have encompassed the entire disease in all cases (Halperin et al., 1989). Several studies investigating the recurrence pattern of GBM patients reported in varying ranges of microscopic disease beyond the visible tumour: 0.0-4.0 cm (Gaspar et al., 1992), 0.0-9.3 cm (Wallner et al., 1989), and 0.0-4.8 cm (Aydın et al., 2001). Hess *etal.* (Hess et al., 1994) analysed the failure pattern of GBM patients as compared to their pre-irradiation CT scans. 14% of the patients included in the study recurred outside or marginally outside the treatment volume. Study of Lee (Lee et al., 2009) showed 43% non-central recurrences when a margin of 1.5 cm was applied to T1-MR.

Several mathematical models, using parameters obtained from clinical patient data, also evaluated/predicted optimal treatment margins in GBM (Trépanier et al., 2012, Unkelbach et al., 2014, Bondiau et al., 2011). Bondiau (Bondiau et al., 2011) applied a virtual model of glioma growth developed by Clatz (Clatz et al., 2005) on actual patient data and compared the tumour growth pattern derived from the model with current radiotherapy margins. Tumour growth was studied in two scenarios: high diffusion-low proliferation (HD-LP) and high proliferation-low diffusion (HP-LD) tumours. It was concluded that for a 2 cm CTV margin, 2.1% and 15.1% of microscopic invasive tumour cells fell outside the margin for LD-HP and HD-LP tumours respectively. In contrast, the mathematical model developed by Trepanier (Trépanier et al., 2012) suggested that 44.0% of recurrences occurred outside treatment volume.

Table 2.1: A summary of clinical findings on microscopic extension of glioblastoma multiforme.

Year/ Author	Patient number	Conventional CTV margin	Proposed CTV margin	ME range	ME mean
(Burger et al., 1988)	15	CT + 2 cm	NP	0-5 cm	NP
(Halperin et al., 1989)	15	CT + 1 cm	Edema + 3 cm	0-3 cm	NP
(Wallner et al., 1989)	34	CT + 3-4 cm	NP	0-9 cm	3 cm
(Gaspar et al., 1992)	70	CT + 2 cm	CT + 4 cm	0-4 cm	NP
(Hess et al., 1994)	68	CT + 2 cm	NP	NP	NP
(Aydın et al., 2001)	46	CT + 2-3 cm	CT + 3 cm	0.2-4.8 cm	1.9 cm
(Chang et al., 2007)	48	NP	T-1MR + 2 cm	NP	NP
(Lee et al., 2009)	16	T1-MR + 1.5 cm	NP	NP	NP
(McDonald et al., 2011)	62	T2-MR + 2 cm	T2-MR + 0.5 cm	NP	NP

2.4 Discussion and conclusion

A comprehensive review was performed of studies evaluating the quantitative extent of microscopic disease in various tumour sites. The results were summarized in the supplementary appendix table of the paper. While the issue of CTV uncertainty continues to be one of the reasons for treatment failure even after technological advances in RT, the number of studies addressing the ME is either very limited (e.g. ovarian, bladder, and liver cancer) or non-existent for several cancer sites (e.g. colon and rectum). Reasonable number of studies were found for breast, lung, prostate and brain malignancies. As listed in the supplementary appendix table, there is a better consistency in proposed margins for several organs (e.g. lung and prostate) in contrast to other organs where there are large discrepancies between studies and institutions (e.g. brain and breast).

It was shown that the consensus on the extent of histological disease is very limited for high grade gliomas, particularly Glioblastoma Multiforme (GBM). This is evident from table 2.1 which provides additional information to the supplementary table for GBM of the brain. Glioblastoma of the brain will be the tumour site investigated in this work. The data collected in this study will be used in a mathematical model to be developed.

Chapter 3

In-Silico Modelling of Tumour Margin Diffusion and Infiltration: Review of Current Status

The publication [P2] forms the basis of this chapter.

Moghaddasi, L., E. Bezak, and L.G. Marcu, *In-Silico* Modelling of Tumour Margin Diffusion and Infiltration: Review of Current Status. *Computational and mathematical methods in medicine*, 2012 Jul 11; 2012.

3.1 Introduction and motivation

Computational and mathematical modelling based on biological data has been long recognized a valuable tool to simulate biological systems and, in case of radiotherapy to provide predictions of the probable response of a tumour to therapeutic regimens for different tumour conditions such as the tumour microenvironment, oxygenation, radiosensitivity and different treatment techniques. A comprehensive review of mathematical modelling for tumour growth and its invasion to the surrounding healthy tissue, with the emphasis on glioblastoma modelling is presented in this chapter. Modelling approaches published in literature, including analytical, stochastic and hybrid, are critically reviewed. Gaps in literature are identified and the modelling approach to be taken in this research (i.e. development of a radiobiological framework for a simulated microscopic-scale GBM model) will be determined.

3.2 Statement of Contribution

3.2.1 Conception

The idea to conduct a review of the current status of mathematical and computational models with an emphasis on models developed for GBM of the brain was first conceptualised by Eva Bezak. The search strategy and data collection was conceptualised by Leyla Moghaddasi, Eva Bezak and Loredana Marcu.

3.2.2 Realisation

The critical review was performed by Leyla Moghaddasi. General supervision and guidance was provided by Eva Bezak, and Loredana Marcu. The manuscript was then evaluated by Eva Bezak and Loredana Marcu in terms of critical appraisal, data accuracy, conclusions reached, and general structure and flow.

3.2.3 Documentation

This paper was primarily written by Leyla Moghaddasi. Editing was performed by all authors.

Statement of Authorship

Title of Paper	In Silico Modelling of Tumour Margin Diffusion and Infiltration: Review of Current Status
Publication Status	☑ Published ☐ Accepted for Publication ☐ Submitted for Publication ☐ Publication Style
Publication Details	Moghaddasi, L., E. Bezak, and L.G. Marcu, *Computational and Mathematical Methods in Medicine,* Volume 2012, Article ID 672895, 16 pages

Principal Author

Name of Principal Author (Candidate)	Leyla Moghaddasi		
Contribution to the Paper	Conducted the literature review, and wrote the manuscript and acted as corresponding author.		
Overall percentage (%)	70%		
Signature		Date	22/06/2016

Co-Author Contributions

By signing the Statement of Authorship, each author certifies that:

i. the candidate's stated contribution to the publication is accurate (as detailed above);

ii. permission is granted for the candidate in include the publication in the thesis; and

iii. the sum of all co-author contributions is equal to 100% less the candidate's stated contribution.

Name of Co-Author	Prof. Eva Bezak		
Contribution to the Paper	Initial idea, general guidance and supervision, and manuscript revision.		
Overall percentage (%)	15%		
Signature		Date	22/06/2016

Name of Co-Author	Prof. Loredana Marcu		
Contribution to the Paper	Initial idea, general guidance and supervision, and manuscript revision.		
Overall percentage (%)	15%		
Signature		Date	22/06/2016

Hindawi Publishing Corporation
Computational and Mathematical Methods in Medicine
Volume 2012, Article ID 672895, 16 pages
doi:10.1155/2012/672895

Review Article

In Silico Modelling of Tumour Margin Diffusion and Infiltration: Review of Current Status

Fatemeh Leyla Moghaddasi,[1,2] Eva Bezak,[1,2] and Loredana Marcu[1,2,3]

[1] *Department of Medical Physics, Royal Adelaide Hospital, North Terrace, Adelaide, SA 5000, Australia*
[2] *School of Chemistry and Physics, The University of Adelaide, North Terrace, Adelaide, SA 5000, Australia*
[3] *Faculty of Sciences, University of Oradea, Oradea, Romania*

Correspondence should be addressed to Fatemeh Leyla Moghaddasi, fatemeh.moghaddasi@adelaide.edu.au

Received 13 February 2012; Accepted 11 April 2012

Academic Editor: Scott Penfold

As a result of advanced treatment techniques, requiring precise target definitions, a need for more accurate delineation of the Clinical Target Volume (CTV) has arisen. Mathematical modelling is found to be a powerful tool to provide fairly accurate predictions for the Microscopic Extension (ME) of a tumour to be incorporated in a CTV. In general terms, biomathematical models based on a sequence of observations or development of a hypothesis assume some links between biological mechanisms involved in cancer development and progression to provide quantitative or qualitative measures of tumour behaviour as well as tumour response to treatment. Generally, two approaches are taken: deterministic and stochastic modelling. In this paper, recent mathematical models, including deterministic and stochastic methods, are reviewed and critically compared. It is concluded that stochastic models are more promising to provide a realistic description of cancer tumour behaviour due to being intrinsically probabilistic as well as discrete, which enables incorporation of patient-specific biomedical data such as tumour heterogeneity and anatomical boundaries.

1. Introduction

Advanced radiotherapy techniques like 3D Conformal Radiotherapy (3D-CRT), Intensity-Modulated Radiation Therapy (IMRT), and Image-guided Radiation Therapy (IGRT) restrict the high dose region to defined target volumes to spare adjacent normal tissue. The margins are generally reduced for modern radiotherapy techniques due to (a) more accurate organ specification with the use of daily image guidance that results in minimization of set up error, and (b) superior conformity of dose distribution to irradiation target volumes. However, a successful implementation of these techniques, that is, achieving an acceptable Tumour Control Probability (TCP) and Normal Tissue Complication Probability (NTCP), requires very accurate target volume delineation. According to ICRU report 50, the "Clinical Target Volume (CTV) is a volume encompassing visible Gross Tumour Volume (GTV) and subclinical malignant disease" [1]. Since subclinical disease cannot be detected by imaging technologies, in contrast to gross tumour volume, which is the visible extent and location of malignant disease [1], CTV needs to be estimated. To ensure that CTV receives the prescribed dose, the Planning Target Volume (PTV) is drawn to account for several possible uncertainties. These uncertainties are due to both physiologic movements which are not controllable (e.g. patient's respiration) and to daily set-up variations. PTV is then the volume for which dose calculation is performed and ensures that the whole of CTV will receive the full prescribed radiation dose. Figure 1 schematically illustrates radiotherapy irradiation volumes and their respective uncertainties regarding volume delineation.

Among radiotherapy target volumes, delineation of the Clinical Target Volume (CTV) is the most controversial. To date, there is no consensus regarding the extent of histological disease, thus the question of how far CTV is extended beyond GTV is mostly left to the discretion of radiation oncologists based on their experience, depending on patient's

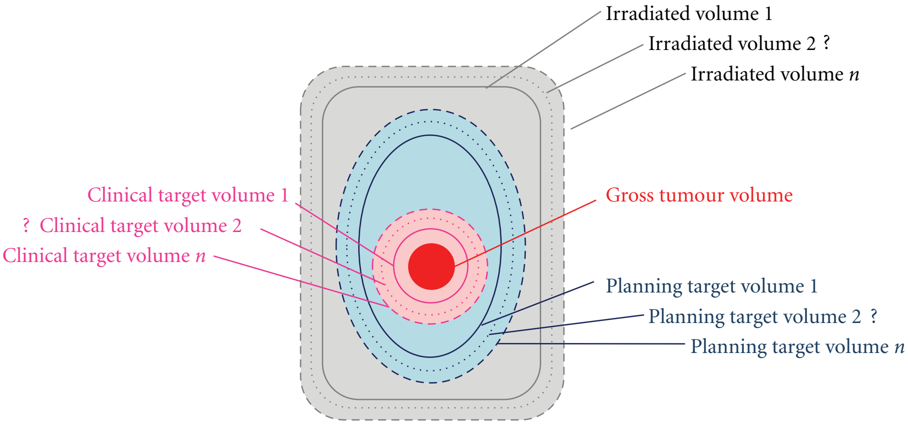

FIGURE 1: Schematic diagram of radiotherapy irradiation volumes.

histopathological data. The uncertainty in CTV represents a limitation on reduction of the irradiated target volume. When the irradiated target volume is reduced due to dose conformity of new treatment modalities, NTCP is improved. On the other hand, the issue of CTV fuzziness becomes a cause of concern because any PTV reduction enhances the risk of missing a part or a few cells of subclinical disease, as illustrated in Figure 2. It is worth mentioning that missing one single cell reduces TCP to 37%. (The Poisson distribution definition for TCP: TCP $= e^{-n(D)}$, where $n(D)$ is the expected number of surviving clonogens.) Therefore, in order to confidently reduce the irradiated target volume, as is the trend with current treatment techniques, the pattern of microscopic extension needs to be known or predicted.

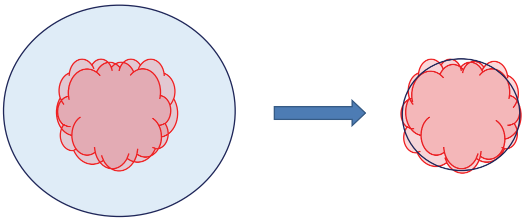

FIGURE 2: Schematic diagram of CTV and PTV correlation for conventional treatment techniques, on the left, as compared to modern treatment techniques, on the right. CTV is indicated by red contour and blue contour defines the PTV. As shown, the reduction of PTV may result in missing a part of microscopic disease that leads to poor treatment efficacy.

1.1. Biological Background. Normal growth and regeneration of an organ requires cells to undergo cell division and to proliferate. The rate of proliferation, however, is systematically regulated to ensure the balance between cell proliferation and cell loss as well as integrity and functionality of each organ. This regulation occurs at cell cycle check points where progression to a subsequent phase is prevented unless prerequisites are satisfied. DNA lesions are recognized at check points that lead onto repair pathways [4]. Normally, cells with unrepaired DNA cannot continue their cycle and are led to apoptosis (programmed cell death). Any uncontrolled proliferation of cells, ensuing a series of DNA mutations, results in abnormal aggregation of cells called a tumour. An evolving tumour population undergoes two stages, namely, *avascular phase* and *vascular phase* and transition between these two phases requires angiogenesis, a process which involves development and recruitment of blood vessels to supply tumour cells with nutrients [5, 6]. Tumour commences its growth primarily via cell proliferation in an avascular phase. Further in its growth, individual tumour cells secrete a substance called Tumour Angiogenesis Factor (TAF) that initiates angiogenesis [6]. At this stage, that is, the beginning of a vascular phase, tumour acquires the capability to invade locally in the adjacent normal tissue, and later tumour cells can detach themselves from the primary mass and migrate through blood or lymphatic system to other sites in the body to produce new colonies (i.e., metastasis) [6–9].

The Extracellular Matrix (ECM) is the external part of tissue on which cells reside. It provides structural support to the cells, regulates intercellular communications and so forth. The ECM also imposes spatial constraint on tumour proliferation. On the other hand, the tumour invasion is known to be facilitated by gradients in the ECM density (i.e., an ECM gradient is a directional rise in ECM density, and its magnitude determines how fast the ECM density rises in that direction). These gradients cause the cells in the outer layer of a tumour to break away from the primary tumour mass and move along the gradient, a phenomenon called *haptotaxis* [9]. It is known that, Matrix Degrading Enzymes (MDEs) produced by cancer cells degrade the surrounding ECM resulting in development of ECM gradients [9].

Apart from proliferation and haptotaxis, other factors like cell-cell adhesion, cell-matrix adhesion, and ECM density also affect cell motility in the course of tumour invasion [6].

In summary, tumour evolution is an interrelated multistage process that starts from a series of cancer-associated gene mutations leading to formation of a colony that could further invade adjacent tissues and finally metastasize in distant organs. Better understanding of biological mechanisms of cancer development helps to anticipate the behaviour of the tumour that undoubtedly leads to a better treatment efficacy.

1.2. Mathematical Modelling. Mathematical modelling is a suitable tool to generate algorithms to correlate information acquired from imaging techniques to the pattern of growth and tumour invasion. In a typical course of model development, biological phenomena are represented in mathematical equations. The solutions of the equations, in return, provide predictions of tumour evolution, tumour aggressiveness in a given patient, and so forth. The validity of a model is then examined by comparison with available actual data, and iteration is performed until an adequate match is reached and thus a plausible model is obtained. A semirealistic model developed in this manner provides an insight into biological mechanisms of tumour growth and invasion under a variety of circumstances. It also allows for assessment of potential treatment regimens. The model could be useful for clinicians in clinical tumour volume definition.

Oncogenesis can be modelled at three levels: (1) subcellular level, (2) cellular and microscopic level that concerns individual cell behaviour while taking into account cell-extracellular matrix (ECM) interactions, and (3) macroscopic level that is related to the evolution of tumour in terms of cell density and mostly is based upon reaction-diffusion equations [10].

In this paper, some of the recent computational and mathematical models developed for tumour growth and invasion are reviewed. Two approaches used for modelling, analytical and stochastic, are discussed individually in the following sections.

2. Deterministic Models

2.1. Analytical Models. Analytical modelling of tumour growth has been typically done based on the reaction-diffusion equations in the literature. Swanson et al. [11] reviewed some recent models developed for glioma of the brain. The problem was initially formulated as a conservation equation by Murray's group [12–14] as: the rate at which tumour cell population changes is equal to diffusion (motility) of tumour cells plus proliferation of tumour cells. For untreated glioma, this can be represented in a mathematical form as [11, 15]

$$\frac{\partial c}{\partial t} = -\nabla \cdot J + \rho c, \tag{1}$$

where $c(x,t)$ denotes the density of tumour at location x and time t, $\nabla \cdot J$ is the diffusion component (i.e., outflow of material out of the system), and ρc is proliferation component (inflow of material in the system), where ρ is the proliferation coefficient. Using the Fick's first law that assumes the diffusive flux flows from high-concentration regions to low-concentration regions, the diffusion component is related to tumour cell density as follows:

$$J = -D\frac{\partial c}{\partial x} \xrightarrow{\text{in 3D}} J = -D\nabla c. \tag{2}$$

Thus (1) takes the form

$$\frac{\partial c}{\partial t} = \nabla \cdot (D\nabla c) + \rho c, \tag{3}$$

where D is diffusion coefficient representing active motility of cancer cells and ∇ denotes spatial gradient operator. The first term, the diffusion component, is related to the periphery of the tumour while the second term, the proliferation component, pertains to active part of tumour core and is described by cellular proliferation laws (e.g., exponential growth) [10]. The assumptions considered in this model were the following.

(i) Brain tissue is homogeneous thus diffusion coefficient, D, is constant throughout the brain.

(ii) Tumour growth is generally exponential thus ρc is constant.

(iii) Boundary condition: $c(x,0) = f(x)$, where$f(x)$ is initial profile of the tumour and there is no migration beyond brain boundaries.

Thus (3) reduces to

$$\frac{\partial c}{\partial t} = D\nabla^2 c + \rho c. \tag{4}$$

One of the consequences of (4) is that tumour density distribution, c, is a function of the ratio of ρ/D thus two different tumours whose different combinations of ρ and D result in the same ratio of ρ/D, appear the same at a single observation time. Hence, just a single MRI/CT image is not sufficient to estimate CTV correctly without knowing the pattern of tumour cell density distribution.

A more realistic approach was taken by Swanson et al. [2, 17]who introduced the geometry of the brain into the model, thus in the revised form of the model, the following assumptions were considered.

(i) Complex geometry of brain is introduced, thus diffusion coefficient, D, is not uniform and is a function of location in the brain tissue.

(ii) Equation (3) is applied to describe the pattern of growth in diffusive models with D being a function of x as follows:

$$D(x) = \begin{cases} D_W, & \text{(diffusion coefficientin white matter of the brain)}, \\ D_G, & \text{(diffusion coefficient in gray matter of the brain)}, \end{cases} \tag{5}$$

$$\text{where } D_W > D_G.$$

To determine the model parameters, 12 serial CT scans of a patient, diagnosed with astrocytoma, during his terminal year were examined to derive estimations for velocities of tumour margin advance through grey and white matter, ν_G and ν_W, respectively. Fisher's approximation ($D = \nu^2/4\rho$)

was then applied to correlate velocity, v, of detectable tumour margin with proliferation rate and diffusion coefficients. According to CT scans of the right hemisphere (predominantly grey matter), v_G was identified to be 0.008 cm/day, thus Fisher approximation gives $D_G = 0.0013\,\text{cm}^2/\text{day}$, and D_W being almost five times of D_G becomes $0.0065\,\text{cm}^2/\text{day}$. To assign diffusion coefficients to corresponding brain cells, spatial distribution of white and grey matter was adopted from the brain web database [31]. Applying these determined parameters in the simulation based on (3) describing virtual gliomas growth, two-dimensional plots of tumour cell density on coronal, sagittal and axial planes were generated, as shown in Figure 3. Using these plots, they determined the part of tumour volume that can be visualized using MRI technique. Enhanced MRI technique has a detection threshold of $400\,\text{cells/mm}^2$. This means that any part of tumour having a concentration below this threshold is not detectable on a MRI image. The comparison between detectable part and simulated profile provides an insight into how far and at what concentration microscopic disease is invaded beyond visible tumour. This model that derived the behaviour of glioma according to two factors ("D" and "ρ") demonstrates that the distribution of ME in invasive gliomas does not follow an isotropic pattern that is invariably assumed by clinicians for definition of CTV.

The biomathematical modelling based on (3) in conjunction with serial pre-treatment MRI images of the patient also provides a tool to quantify patient-specific proliferation and diffusion rates. Wang et al. [32] examined two pretreatment MRI images of each of a population of 32 patients diagnosed with Glioblastoma (GBM) to quantify patient-specific kinetic rates of glioma cells (net proliferation and diffusion rates). These parameters are used to predict the course of disease and, more importantly, to assess the efficacy of different treatment plans for each individual patient through a survival analysis. In the survival analysis, the effectiveness of any treatment was measured via the ratio of actual survival time after respective therapy to the calculated survival time (by the model) without therapy.

The evolution of mathematical modelling to gain insight into the mechanism of GBM growth and invasion initiated by Swanson et al. [11, 17] was followed by Stein et al. [20] who developed a continuum model and compared the outcome of the model with 3D *in vitro* experiments on the three dimensional pattern of growth of GBM spheroids. It was concluded that GBM spheroids consist of two classes of cells, namely, proliferating core cells and peripheral migrating cells. This finding was later included in other models like the model of Thalhauser et al. [22] in which three dependent variables, namely, the concentration of migrating cells, proliferating cells and oxygen (mmHg) were correlated in three partial differential equations for tumour development around a central blood microvessel. Analysis of the density distribution profiles of these two classes of cells led to a hypothesis regarding emergence of metastatic phenotype to occur for population of cells containing highly motile cells. This hypothesis is based on the evidence that populations of motile cells grow to lower densities compared to aggressive growers (mobile cells), and hence they are unlikely to cause vascular network collapse since they cause less compressive pressure on microvessel walls. In a more recent progress, Eikenberry et al. [8] incorporated haptotaxis in GBM models and also extended the model stochastically to form a deterministic-stochastic system for modelling. The mathematical model was developed based on four dependent variables: the concentration of migrating cells, proliferating cells, ECM, and matrix degrading enzyme. The system of partial differential equations was discretized to allow for stochastic estimation of the transition probability between proliferating and migrating class of cells at each grid point. The stochastic nature of the model allows for applying patient-specific geometry of brain and location of tumour inside the brain during simulation. The simulation was performed for an actual clinical case of a GBM patient undergoing a course of treatment including surgical resection, gamma knife, and chemotherapy. The model qualitatively reproduced the actual tumour growth of the patient. However, the model failed to simulate the deformation of surgical cavity.

The spatial-temporal evolution of the brain tumour in the presence of chemotherapy was investigated by Tracqui et al. [2, 12]. Twelve successive CT scans during the terminal year of a patient diagnosed with astrocytoma were studied. The patient received two courses of chemotherapy during 12 months before death, thus (3) can be modified as

$$\frac{\partial c}{\partial t} = \nabla \cdot (D \nabla c) + f(c) - g(c), \tag{6}$$

where $g(c)$ is the cell loss due to chemotherapy and defined as

$$g(c) = [K_1(t) + K_2(t)]c \tag{7}$$

with

$$K_1(t) = \begin{cases} k_1, & \text{during the time the first course} \\ & \text{of drug was delivered,} \\ 0, & \text{during the time the second course} \\ & \text{of drug was delivered,} \end{cases}$$
$$K_2(t) = \begin{cases} 0, & \text{during the time the first course} \\ & \text{of drug was delivered,} \\ k_2, & \text{during the time the second course} \\ & \text{of drug was delivered,} \end{cases} \tag{8}$$

where k_1 and k_2 are positive constants.

The proliferation term, $f(c)$, is typically taken as a linear function of c (exponential proliferation) or a nonlinear function of c (logistic proliferation) when the proliferation is limited, since cell density is close to its maximum:

$$f(c) = \begin{cases} \rho c, & \text{exponential proliferation,} \\ \rho c(1 - c), & \text{logistic proliferation.} \end{cases} \tag{9}$$

The area of tumour was evaluated at each successive CT scan and then the data was compared to the values derived from (6). The comparison between time evolution of

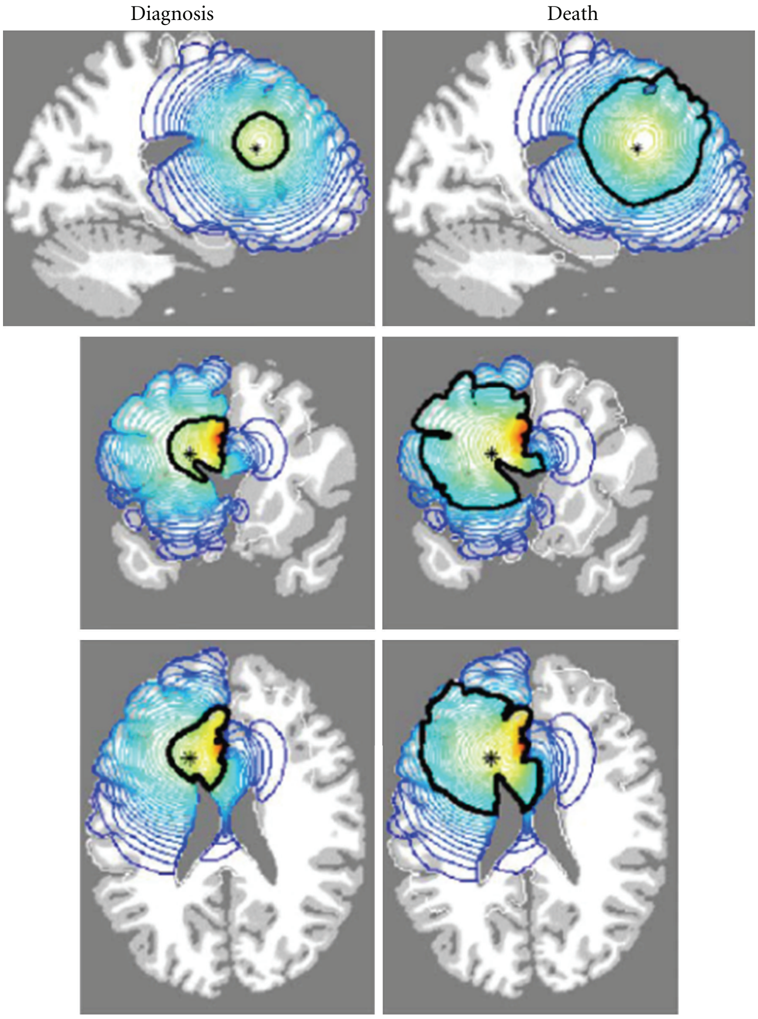

Figure 3: The left column corresponds to the tumour at diagnosis and right column corresponds to tumour at death. The dark black contour defines the detectable edge of tumour by (MRI), red contour indicates high density of tumour cells, and blue contour denotes low-density disease. Courtesy of Swanson et al. [2].

simulated tumour area and tumour areas acquired from CT scans showed a distinctive discrepancy, particularly before the end of the first course of chemotherapy. Consequently, the assumptions were revised and it was postulated that there is a second cell density $c_2(x, y, t)$ present which is resistant to the first course of chemotherapy but sensitive to the second course. The insensitivity of the second population was considered to be due to mutations from the radiotherapy administered three years earlier. Given this condition, the system was described mathematically as follows:

$$\begin{aligned} \frac{\partial c_1}{\partial t} &= \nabla \cdot (D\nabla c_1) + \rho_1 c_1 (1-c) - [K_1(t) + K_2(t)]c_1 \\ \frac{\partial c}{\partial t} &= \nabla \cdot (D\nabla c) + \rho_1 c_1 (1-c) + \rho_2 c_2 (1-c) - K_1(t) c_1 \\ &\quad - K_2(t) c, \end{aligned} \tag{10}$$

where ρ_1 and ρ_2 are proliferation rates corresponding to the first and second cell density, respectively, and variable c represents the total density of tumour cells ($c = c_1 + c_2$).

After optimization and identification of unknown parameters, the identified values were found to be in agreement with known biological data (e.g., $D = 1.2 \times 10^{-7}\ \mathrm{cm}^2/\mathrm{s}$ which is comparable with estimation of glioma cell migration rate obtained from *in vitro* experiments [33]).

Woodward et al. [15, 34] modified Tracqui's model for the same case study in terms of initial conditions related to distribution of type one and two of cancerous cells. In contrast to Tracqui's model that assumed an approximate initial distribution of 90% of type one and 10% of type two cancerous cells, Woodward included another parameter as the number of type one cells remaining after surgery followed by X-ray therapy 1000 days before the first scan and also assumed that type two cancerous cells are the result of mutations of type one cells three years earlier. This allowed for prediction of distribution of each type of cells at the time of diagnosis (rather than making a rough estimation) and at any time during the terminal year. Furthermore, the simulated evolution of the tumour was used to retrospectively evaluate different courses of treatments (e.g., different extent of surgical resections instead of chemotherapy) in terms of their respective subclinical recurrence.

Swanson et al. [11, 35] investigated the incorporation of cell loss due to chemotherapy in a more general formulation by defining $g(c)$ to be a periodic function such that for the time periods chemotherapy is on, $g(c)$ is equal to a specific positive constant, k (indicating the rate of cell loss due to chemotherapy), and otherwise is zero. The model was originally formulated assuming homogeneous drug delivery and further developed to take into account heterogeneity in drug delivery, whereby drug delivery is expected to be less in white matter compared to that in gray matter. The experimental observation of shrinkage of gliomas in specific areas together with persistent growth in other areas of the brain following chemotherapy was explained by this model.

Clatz et al. [10] developed a numerical model to simulate the three-dimensional pattern of growth and invasion of Glioblastomas. To account for different diffusion coefficients which are dependent on the brain tissue, the anatomical atlas of the brain in conjunction with Diffusion Tensor Image (DTI) were employed. The algorithm comprised of four steps. First, the patient MRI images were registered on the brain atlas on which gross volumes were delineated by a radiation oncologist. In the second step, the image registered on atlas was used to produce patient's tetrahedral mesh of brain in which diffusion coefficients respective to each voxel were specified using brain atlas and DTI of the patient. Simulation was performed in the third step by applying reaction-diffusion equation on initial tetrahedral mesh of brain. Ultimately, to measure the validity of the model, the simulated profile was compared with brain deformation seen on the patient MRI images in six months later.

Bondiau et al. [36] applied the virtual model of glioma growth developed by Clatz on actual data of a single patient and compared tumour growth pattern derived from the model with current radiotherapy margins. Tumour growth was studied in two scenarios, namely, high diffusion-low proliferation (HD-LP) and high proliferation-low diffusion (HP-LD) tumours. It was observed that, with 2 cm margin, 2.1% and 15.1% of microscopic invasive tumour cells fall outside margin in HP-LD and HD- LP tumours, respectively. Also 53.5% and 55.5% of cells inside margin in HP-LD and HD- LP, respectively, are normal brain cells. Therefore, it was concluded that uniform clinical margins may not be adequate to cover whole tumour neither to spare normal tissue. Although this conclusion is supported by many other studies, the rationale of this comparison is argued on the basis that a model which is based on a single patient clinical data, though sophisticated, cannot be considered as a criterion to assess clinical margins. It first needs to be validated against some actual clinical data (e.g., recurrence rate) in a statistically sufficient number of patients.

The effect of external beam radiation therapy was incorporated in the reaction-diffusion model in the study of Rockne et al. [23]. Therefore, the conservation of cells (3) can be modified as:

$$\begin{aligned}\frac{\partial c}{\partial t} = {} & \underbrace{\nabla\cdot(D\nabla c)}_{\text{Diffusion of glioma cells}} + \underbrace{\rho c\left(1-\frac{c}{k}\right)}_{\text{Logistic proliferation}} \\ & + \underbrace{R(x,t,\text{Dose})c\left(1-\frac{c}{k}\right)}_{\text{Cell loss due to radiotherapy}}, \\ R(x,t,\text{Dose}) = {} & \begin{cases} 0, & \text{for } t\notin \text{therapy},\\ \left(1-e^{-(\alpha D+\beta D^2)}\right), & \text{for } t\in \text{therapy},\end{cases}\end{aligned} \tag{11}$$

where D and k denote the dose and tumour carrying capacity, respectively. $R(x,t,\text{Dose})$ is the probability of death of cancer cells (one minus cell survival fraction given by the linear-quadratic model of cell survival ($S=e^{-(\alpha D+\beta D^2)}$)) due to radiotherapy.

In previous models, passive translocation of cells due to ECM-cell interactions and active cell migration were overlooked. Retaining reaction-diffusion formula as the framework, Tracqui [16] introduced the effects of passive translocation of cells due to ECM-cell interactions and active cell migration up to adhesivity gradient. The variables u, ρ, and c were designated for mechanical displacement of cell-ECM composite, density of ECM, and cell density, respectively. The parameter r denotes the proliferation rate of cancer cells. Thus the reaction-diffusion formula (cell conservation equation) takes the bllowing form:

$$\begin{aligned}\frac{\partial c}{\partial t} &= -\nabla\cdot(J_c+J_d+J_h)+rc(1-c),\\ J_d &= -D\nabla c \text{ (diffusion term)},\\ J_c &= \frac{c\partial u}{\partial t} \text{ (convection term)},\\ J_h &= hc\nabla\rho.\end{aligned} \tag{12}$$

The convection term addresses ECM displacement due to cells convection with velocity $\partial u/\partial t$. Equation (12) indicates that the two new terms inhibit tumour growth. Moreover, the conservation of ECM density reads as

$$\frac{\partial\rho}{\partial t} = \underbrace{-\nabla\cdot\left(\frac{\rho\partial u}{\partial t}\right)}_{\text{convection}} + \underbrace{S(c,p)}_{\text{ECM biosynthesis}} - \underbrace{G(c,p)}_{\text{ECM degradation}}, \tag{13}$$

where $S(c,p)$ and $G(c,p)$ denote the rate of formation and loss of ECM, respectively. For the sake of simplicity, ECM turnover was neglected, that is, $S(c,p)=G(c,p)=0$. Thus (12) and (13) together with the equation regarding viscoelastic response of ECM to cells' traction force formed a set of differential equations for modelling. Nonhomogeneous and nonsymmetric profile at the tumour surface was obtained by the model. To validate the model, it was suggested to compare growth pattern generated by the model with that acquired from *in vitro* experiments. To our knowledge, no article addressing such a comparison associated with this model has been found. Synthesis and degradation of ECM which was neglected in primary calculation could be further included.

More recently, the interactions of cell-cell and cell-ECM were considered in a more elaborate way in reaction-diffusion models. Gerisch and Chaplain [6] developed an analytical Partial Differential Equation (PDE) model to simulate tumour growth and invasion both one and two dimensionally. In the study of Gerisch, firstly a local continuum model was formulated based on the system of reaction-diffusion equations proposed by Anderson et al. [21]. It was assumed that the movement of the cells is due to random motility with constant diffusion coefficient D_1 (assuming constant ECM density), and haptotactic response to the ECM gradient. As a matter of fact, cancer cell motility depends on both ECM gradient and density, thus this was a simplifying assumption. The series of differential equations constituting the model are as follows:

$$\begin{aligned}
\frac{\partial c}{\partial t} &= \nabla \cdot \left[D_1 \nabla c - \chi c \nabla v\right] + \mu_1 c(1 - \vartheta_1 c - \vartheta_2 v),\\
\frac{\partial v}{\partial t} &= -\gamma m v + \mu_2 (1 - \vartheta_1 c - \vartheta_2 v),\\
\frac{\partial m}{\partial t} &= \nabla \cdot [D_3 \nabla m] + \alpha c - \lambda m,
\end{aligned} \tag{14}$$

where $c(x,t)$, $v(x,t)$, $m(x,t)$ denote the cancer cell density, the ECM density and the concentration of Matrix Degrading Enzyme (MDE), respectively. The parameters ϑ_1 and ϑ_2 are fractions of unit volume occupied by cancer cells and ECM, respectively. μ_1, μ_2, γ, D_3, α and λ denote proliferation rate of cancer cells, remodelling rate of ECM, degradation rate of ECM, MDE diffusion coefficient, the rate of release, and removal of MDE, respectively. Finally, χ is designated for haptotactic function. Equation (14) differs from that of Anderson in two aspects: Employing logistic proliferation and applying modified haptotactic function to prevent cellular overcrowding at boundaries. There is also a slight difference in definition of Initial Conditions (IC) associated with ECM.

In the second step, Gerisch modified this model (14) to a nonlocal continuum model to include cell-cell and cell-ECM adhesion. To this end, the haptotactic term was substituted with a nonlocal flux term in (14). The nonlocal term represents the velocity of cancer cells due to cellular adhesion (cell-cell adhesion) and to the ECM (cell-ECM adhesion). The growth profile was simulated for both local and nonlocal models and surprisingly the detachment of a cluster of cells that degrades ECM on its way and migrates was obtained.

Within the realm of continuum modelling, the approach that regards a tumour as a continuum medium whose overall dynamic and morphology is dependent on the microenvironment material concentration is reflected in some other works in literature [37–46]. In these models, the concentration of microenvironment materials such as nutrition supply, like oxygen and glucose, and growth inhibitor, which is either anticancer drugs or chemicals produced by immune system, is assumed to influence individual cells phenotype.

2.2. Hybrid Models. The above-addressed models, both deterministic reaction-diffusion equations whose solutions is in the form of invading travelling waves of cancer cells and mechano-cellular formalism (e.g., Tracqui, 1995 [16]) provide spatio-temporal spread of tumour at macroscopic level. However, the behaviour of tumours at cellular and sub-cellular levels, which becomes important when individual cell effects dominate in the course of tumour growth and invasion, such as the spatio-temporal evolution of tumour cell heterogeneity, cannot be predicted by these modelling approaches [47, 48]. Therefore, the continuum modelling is appropriate for studying systems at a large scale. Discrete modelling can overcome this limitation since it can track individual cells and update their states at each time step. Thus it is an appropriate tool to investigate the interaction between cells and ECM, phenotypic transitions of cells which leads to a nonlinear cancer system to another state that in return affects the overall behaviour and morphology of tumours and so forth. The important drawback of discrete modelling is its increasingly high computational demands as the number of cells being modelled increases. An alternative to these scale-specific models is a multiscale approach that refers to the models that contain more than one spatial and temporal scale to take into account cross-scale mechanisms in the course of tumour growth and evolution [49]. This approach is classified as "hybrid" modelling. A hybrid model comprises of a continuum deterministic part that controls the concentration of ECM and chemicals, and a stochastic discrete part governing cell migration and interactions.

Such a hybrid model of tumour growth and invasion was developed by Anderson [19]. The formalism of hybrid modelling enables to simulate specific cell processes (e.g. proliferation and cell-cell adhesion) and also inclusion of different tumour cell phenotypes at cellular level in a continuum chemical/ECM surrounding. The model parameters consisted of concentration distributions of tumour cell (n), ECM (f), MDE (m), and oxygen (c). The interaction of these parameters was represented in a set of differential equations, as follows:

$$\begin{aligned}
\frac{\partial c}{\partial t} &= \overbrace{D_c \nabla^2 c}^{\text{oxygen diffusion}} + \overbrace{\beta f}^{\text{oxygen production}} - \overbrace{\gamma n}^{\text{oxygen uptake}}\\
&\quad - \overbrace{\alpha c}^{\text{oxygendecay}},\\
\frac{\partial m}{\partial t} &= \overbrace{D_m \nabla^2 m}^{\text{MDE diffusion}} + \overbrace{\mu n}^{\text{MDE production}} - \overbrace{\lambda m}^{\text{MDE decay}},\\
\frac{\partial f}{\partial t} &= \overbrace{-\delta m f}^{\text{ECM degrdation}},\\
\frac{\partial n}{\partial t} &= \overbrace{D_n \nabla^2 n}^{\text{random motility}} - \overbrace{\chi \nabla \cdot (n \nabla f)}^{\text{haptotaxix}}.
\end{aligned} \tag{15}$$

As indicated in the first line of (15), oxygen is diffused into the ECM, consumed by tumour and decayed naturally at rates γ and α, respectively. The hybrid model, that follows the path of each individual cell, requires discretising the system of differential equation based on finite difference method in a given time and space steps [21]. Each point on the grid is correlated to neighbouring grids via coefficients indicating the probability of transition from that grid to another. For example, tumour cell density is expressed as

$$n_{i,j}^{q+1} = n_{i,j}^{q} P_0 + n_{i+1,j}^{q} P_1 + n_{i-1,j}^{q} P_2 + n_{i,j+1}^{q} P_3 + n_{i,j-1}^{q} P_4, \tag{16}$$

where indices i and j represent the location and q specifies the time. The coefficients $P_0, P_1, \ldots, P_4$ are probabilities of transition from the grid in question to the respective neighbouring grids. Unlike purely continuum modelling, the hybrid model, being intrinsically multiscale, allows for investigation of the effect of tumour cell heterogeneity on the morphology and phenotypic diversity of invading vascular tumours (e.g., capturing the emergent property of invasive cells) [50]. In the more recent studies of Anderson et al. [51, 52], the hybrid model was used to simulate the shape of a growing tumour under homogeneous and heterogeneous matrix distribution and a phenotypically heterogeneous tumour cell population. Also, the impact of nutrient availability during tumour development on tumour morphology was examined. The models predicted that harsh microenvironment conditions lead to a tumour mass with invasive morphology (fingering margins) dominated with a few aggressive phenotypes. Other studies independently conducted *in vivo* and *in vitro* experiments to examine the role of harsh environment (e.g., hypoxia) in the invasive morphology of tumours [18, 53]. The results of their investigations corresponded to those predicted by the hybrid model. However, neither of them examined phenotypic composition of the resulting tumours, thus these experiments just partially validate the hybrid model.

Malignant tumour invasion, driven by haptotaxis, both in the form of travelling waves (continuum models) [54–56] and hybrid models [57–59], has been also modelled by others. The model developed by Anderson and Chaplain [58] was mathematically analysed by Kubo [60] to investigate asymptotic profiles of solutions. The simulated tumour cell distribution illustrated that a cluster of cells detaches from the original tumour mass and migrates further away from the tumour as the time evolves. The simulated tumour cell distribution shows an explicit detachment of a cluster of cells and qualitatively corresponds to the results of Gerisch's study [6].

The most recent work in the continuum deterministic framework is the study of Swanson [61]. In this study the Proliferation-Invasion (PI) model was developed to produce a Proliferation Invasion Hypoxia Necrosis Angiogenesis (PIHNA) model incorporating the mechanisms related to angiogenesis cascade. Three different cellular types, namely, proliferative, hypoxic, and necrotic were described mathematically in a form of three partial differential equations in which conversions of each type to others due to microenvironmental changes were included. It is known that, while tumour cells grow and invade according to their respective proliferation and diffusion rates, the microenvironment becomes harsh and leads to the production of Tumour Angiogenic Factor (TAF) by proliferative and hypoxic cells in response to the metabolic demands of tumour. It is worth noting that the rate of production of TAF by hypoxic cells is significantly higher compared to that by proliferative cells. The presence of TAF in tumour microenvironment stimulates vascularisation. These two processes were also represented in two differential equations that formed a system of five equations for modelling. The *in silico* prediction of malignant progression of tumour corresponded well with imaging (MRI) and histologic data of three GBM patients who had approximately similar size of tumour but different hypoxic and necrotic ratios on their MR images. In the context of microscopic extension, this model can predict local invasion. However, it cannot visualize those microscopic clusters of cells detached from main mass of tumour, since it overlooks migration (via haptotaxis).

Table 1 Summarizes the major analytical models of tumour proliferation and diffusion reported in the literature.

Analytical modelling based on conservation of cells has evolved from basic models such as the one proposed by Murray's group [12–14] to very sophisticated models considering many biological mechanisms involved in tumour growth and invasion (e.g., Gerisch and Chaplain [6]). Some significant achievements regarding prediction of tumour behaviour in the course of its progression can also be obtained using this class of modelling. However, in order to obtain a realistic model, other critical characteristics of tumour cell growth are yet to be taken into account. The heterogeneity of diffusion coefficients and multilayer nature of tumours (necrotic, hypoxic, and proliferative layers) brought about by nutrient gradient exemplify the overlooked parameters. Moreover, purely analytical (continuum) modelling seems to be too inflexible to represent the biological phenomena which are intrinsically probabilistic. Therefore, what is actually favoured is not one single precise solution for a given situation provided by analytical models, but rather a probability distribution which better describes the behaviour of such systems.

3. Stochastic Models

Stochastic models are guided by probability distribution. The various techniques used in stochastic modelling are dominated by Monte Carlo and Markov approaches which are generally employed in the simulation of biological systems.

3.1. Markov Model. Markov models are stochastic models which simulate the state of systems with time-dependent random variables possessing Markov property. A stochastic process has Markov property (or memoryless property), if the probability distribution of future states depends only on the present state and not on the preceding sequence of events. This reads mathematically as

$$\begin{aligned} &P(X_{n+1} = x \mid X_1 = x_1, X_2 = x_2, \ldots, X_n = x_n) \\ &\quad = P(X_{n+1} = x \mid X_n = x_n), \end{aligned} \tag{17}$$

Table 1: A summary of analytical models of tumour proliferation and diffusion.

Type	Site of modelling	Incorporated mechanisms	Model validation and results	Comments	Reference
Continuum	Glioma	Random motility with uniform diffusion; exponential proliferation	N/A	Prediction of basic behaviour of gliomas (e.g., tumour cell density is a function of ρ/D)	Cruywagen et al. 1995 [14]
Continuum	Astrocytoma	Random motility with uniform diffusion; logistic proliferation; cell loss due to chemotherapy	12 CT images of a patient/agreement between model parameters and experimental data	The model is applicable for a specific course of treatment	Tracqui et al. 1995 [12]
Mechano-chemical	Multisite	Uniform diffusion; logistic proliferation; ECM-cell adhesion; haptotaxis	N/A	While important mechanisms in tumour invasion are considered, the behaviour of tumour at cellular level cannot be predicted	Tracqui 1995 [16]
Continuum	Glioma	Random motility with nonuniform diffusion; exponential proliferation	Virtual MRI image/obtaining nonisotropic invasion pattern	Rough prediction of the extent and concentration of local invasion. Applicable for tumours >1 $(\mathrm{mm})^3$	Swanson et al. 2002, 2000 [2, 17]
Continuum	Glioblastoma	Nonuniform diffusion; exponential proliferation; mass effect	MR images/capable to simulate complex tumour behaviour	Migration and departure of cells not taken into account	Clatz et al. 2005 [10]
Continuum-Stochastic	Multisite	Random motility with uniform diffusion; haptotaxis; three-population tumour cells; heterogeneous ECM	Model predictions consistent with clinical findings [18]	Stochastic nature of the model allows to predict avascular invading tumour morphology by following individual cells with different phenotypes at each time and space step	Anderson 2005 [19]
Continuum	Glioma	Random motility with uniform diffusion; logistic proliferation; radially biased motility; shedding of invasive cell at tumour surface	The model reproduces *in vitro* experiments data	Assuming two-population tumour cells, proliferative (core) and invasive (periphery), and modelling invasive cells. Applicable for tumours <1 $(\mathrm{mm})^3$	Stein et al. 2007 [20]
Continuum	Multisite	Random motility with uniform diffusion; logistic proliferation; ECM-cell adhesion; haptotaxis, Cell-cell adhesion	Comparison to simulation results of Anderson et al. [21]	Simplifying assumptions: uniform diffusion and that haptotaxis is independent of ECM density; the simulation is 2D	Gerisch and Chaplain 2008 [6]

Table 1: Continued.

Type	Site of modelling	Incorporated mechanisms	Model validation and results	Comments	Reference
Continuum	multisite	Random motility with uniform diffusion; logistic proliferation; two-population tumour cells; oxygen concentration	*In vivo* tumour growth observation	Assumption: cells could either proliferate or migrate where transition between these two classes is environment-dependent; haptotaxis not considered	Thalhauser et al. 2009 [22]
Continuum-Stochastic	Glioma	Random motility with nonuniform diffusion; logistic proliferation; two-population tumour cells; haptotaxis	The model predicts the tumour growth pattern of a clinical case	Stochastic step of the model allows for introduction of patient-specific parameters (e.g., tumour location)	Eikenberry et al. 2009 [8]
Continuum	Glioma	Random motility with nonuniform diffusion; logistic proliferation; radiotherapy	The biopsies of nine patients/the model reproduces RT response	In contrast with imaging-based RT response, this model incorporates patient-specific tumour growth kinetics to quantify RT outcome	Rockne et al. 2010 [23]

where X_is are random variables having Markov property. A Markov chain is the simplest Markov model which is a chainlike random process that transforms from one state (i) to another (j) by a transition matrix whose elements are described as

$$p_{ij} = P(X_{n+1} = j \mid X_n = i). \quad (18)$$

Benson et al. [3] produced a theoretical model to predict the microscopic spread of tumour to regional lymph nodes based on anatomical information adopted from the Foundational Model of Anatomy (FMA) in the head and neck cancer. A computational rule-based model was previously proposed in this area, based on clinical data rather than anatomical principles, by Kalet et al. [62]. FMA provides information regarding an almost complete set of drainage pathways or lymph chains which is known to be followed by subclinical spread [63]. The information acquired from FMA was supplemented by clinical data pertaining to lymph chains that span multiple regions. The inputs to the model were primary tumour location and T-stage. In FMA every primary site is associated with its respective lymphatic chains, thus lymphatic chains with subparts corresponding to the primary tumour location were derived from FMA. A sequence of Markov models were developed such that each hidden Markov model was assigned to one position in the pathway where position "0" was labelled for the original tumour. The validity of the model was examined by comparing the model results with two surgical data. Overall, the model overpredicted the metastasis in specific regions, requiring certain modifications such as revising supplementary data added to FMA. The procedure starting from model inputs to model validation followed by iteration is diagrammatically shown in Figure 4.

3.2. Monte Carlo Model. Monte Carlo (MC) models are widely used in the field of cancer biology and treatment since this method is particularly useful for simulating systems with considerable uncertainty in parameters.

The earliest developed MC models of tumour growth date back to early 80's, for example the work of Duchting and vogelsaenger [64] for small tumours which took into account nutritional needs of tumours. Aiming to investigate the pattern of *in vivo* cancer development, Qi [65] simulated the distribution of cancer cells in a given biochemical environment as a two dimensional cellular automaton on a square lattice. Qi et al. [66] later advanced the model to take into account proliferation of cancer cells, nutrition supply, mechanical pressure, and the cytotoxic behaviour of immune system and reproduced Gompertz model which is typically used to describe the growth of cancer tumour volume (Gompertz model of cancer tumour volume growth is $V = V_0 \exp(A/B(1 - \exp(1 - Bt))$, where V is the volume of tumour at time t and V_0 is the initial volume. A and B are parameters). Smolle and Stettner [67] considered a two-dimensional tumour growth model and correlated macroscopic behaviour of tumour (tumour morphology) with the functionality of tumour cells at microscopic level (e.g., interaction of tumour cells with microenvironment).

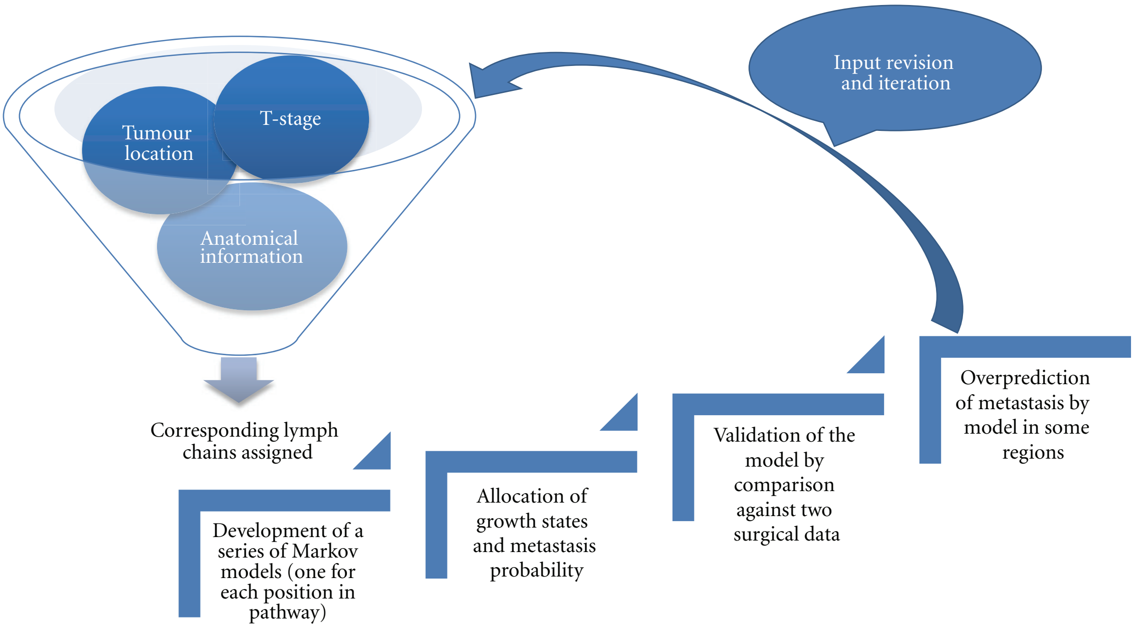

FIGURE 4: Schematic diagram of the Markov model developed by Benson et al. [3].

Later, the invasiveness of tumour in the absence of active motility was studied in a stochastic cellular automata by Smolle et al. [68]. Aimed to provide an algorithm to predict the extent and direction of spread of a brain tumour, another elegant approach was presented in a patient-specific *in vivo* brain tumour growth model which was developed by Wasserman et al. [69]. The model involved a variety of forces associated with microenvironmental (e.g., nutrient and growth inhibitor distributions) and mechanical factors (e.g., cell adhesiveness and resistance of brain parenchyma to expansion) and was implemented via the finite element method. To validate, the model was implemented on a patient MRI data to retrospectively predict the extension of tumour with respect to time. An approximate agreement between simulated tumour extension and MRI image was achieved. It is worth noting that this model explicitly addresses the problem of subclinical boundaries (CTV) in irradiation target definitions.

One of the common approaches in stochastic modelling is the Cellular Automaton (CA) method which employs a grid lattice, with each site in the grid accommodating a finite number of cells in specific states, to grow a tumour from a few cells to macroscopic stages. When the time is incremented by one, the defined biological rules determine the updated states of cells in terms of their current states and microenvironment. A 3D cellular automaton model of untreated brain tumour was developed by Kansal et al. [24, 70]. The site of tumour growth was modelled as a Delaney lattice, made of Voronoi network by connecting those sites whose polyhedra share a common face. Therefore, the density of lattice varied continuously with the radius of tumour, being greater in the centre and reduced towards the surface of the tumour. The tessellation lattice was isotropic, thus it precluded the anisotropies encountered in the models in which cubic lattice was adopted (e.g., the model presented by Duchting and Vogelsaenger [64]). However, a purely random distribution could result in some regions with either very high or very low cell density corresponding to small and large Voronoi cells, respectively. To preclude biologically unreasonable variations in size of cells, a technique called Random Sequential Addition (RSA) was used. In this technique, during the generation of random points, they are checked for not being within a given distance from neighbouring points. The tumour was proposed to be as a self-organising and ideally spherical biosystem with three different layers (necrotic, nonproliferative, and proliferative) whose thicknesses are governed by nutrition supply gradient diffusing into inner layers. This hypothesis was later supported by an *in vitro* study conducted by Deisboeck et al. [71] and was used in the model developed by Yang and Torquato [72], whereby the effect of microenvironment heterogeneity on morphology of invasive tumours was investigated. Four time-dependent variables investigated in the Kansal's model consist of overall tumour radius, proliferative and nonproliferative thickness, and probability of division. Once the lattice was generated, the initial set up was designated whereupon proliferation algorithm was applied. In the algorithm, the probability of transition of cells between nonproliferative and necrotic was considered to be a function of distance from the edge of tumour (nutrient supply) such that nonproliferative cells located at more than a specific distance from the surface of tumour were turned to necrotic. In addition, the transition between proliferative to non-proliferative occurs when there is no sufficient space for the new cell to be generated by a dividing cell. These transitions were considered stochastic in the 2D cellular automata model presented by Qi [66]. In the same framework, clonal competition (emerging a more rapidly growing tumour from a more slowly growing parent) was also quantitatively analysed by introducing another set of inputs in the model after a specific time [73].

Aimed to simulate untreated tumour growth and also the response of tumour to different schemes of radiotherapy, a four dimensional, patient-specific, *in vivo* stochastic model was developed by Stamatakos et al. [25, 74, 75]. The model is outlined as a 3D discretising cubic mesh structure in which each mesh accommodates a specific Number of Biological Cells (NBCs) which is called a Geometric Cell (GC). In addition, different phases of tumour cell cycles have been taken into account according to the cytokinetic model proposed by Duchting et al. [76], as illustrated in Figure 5. Three metabolic subregions were considered: proliferating cell regions, resting G_0 cell regions and dead cell regions. The metabolic state of each GC was determined depending on the distribution of its contained cells in different phases. The initial NBC distribution is derived from imaging and histopathological data of each individual patient, whereby the tumour region is apportioned to three metabolic layers: proliferating, resting, and necrotic. Time is discretized and at the end of each time step the GC mesh is updated such that transitions between different metabolic states are estimated and applied (e.g., M cells in a GC for which the mitosis time is over are transited to G_0 or G_1 with the probability depending on the subregion they belong). The time was incremented at the end of each scan and the process iterated. In order to investigate the radiotherapy effect on tumour shrinkage, the Linear Quadratic (LQ) model of surviving fraction ($S = e^{-\alpha D-\beta D^2}$) is employed. Three sets of radio sensitivity parameters (α and β) were assumed corresponding to proliferative, necrotic, and resting states and the tumour regression was simulated for three specific cases: standard fractionation/radiosensitive tumour, standard fractionation/moderately radiosensitive, and hyper fractionation scheme/radiosensitive tumour [77]. The simulations of tumour shrinkage under various therapeutic regimens qualitatively reproduced the clinical observations.

The model was gradually improved to take into account possible parameters involved in tumour growth and response to radiotherapy to achieve a more biologically realistic description of cancer biology and treatment. Antipas et al. [26] studied the effect of hypoxia in radio sensitivity of tumours by introducing Oxygen Enhancement Ratio (OER) parameter and investigated the influence of OER as well as parameters corresponding to cell cycle duration on tumour growth and shrinkage under standard and accelerated fractionation regimens. The model was applied to two GBM cases, a qualitative agreement between simulation results and clinical experience was achieved. In addition, the effect of oxygen on tumour behaviour appeared to conceptually correspond to that derived by Anderson et al. [19, 50, 51]. More recently, Stamatakos et al. [27] introduced the role of neoangiogenesis distribution in a 4D model of *in vivo* tumour growth and response to radiation. In the same framework, Dionysiou et al. [78, 79] conducted parametric studies to investigate the effect of varying parameters on the radiotherapy treatment outcome with emphasis on genetic profile of tumour. Though the model includes some simplifying assumptions or may lack some parameters (since biological mechanisms in cancer are not fully understood), the discrete and modulated nature of the model allows for inclusion of further improvements. While this approach, initiated by Stamatakos et al. [25, 74] and refined later by his team [26, 27, 75, 77–79], was aimed to simulate tumour growth and response to radiotherapy, it has the potential to be improved to take into account infiltration of a malignant tumour (e.g., by introducing haptotaxis and cell-cell adhesion). This is enabled due to the discrete and modular character of the model which allows incorporation of further mechanisms without extensive modifications.

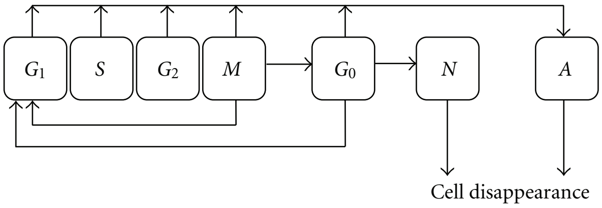

FIGURE 5: The pathway of cells through cell cycle: G_1 phase (gap 1); S phase (DNA synthesis); G_2 phase (gap 2); M phase (mitosis); G_0 phase (if nutrition and oxygen is not sufficient, the cell enters this phase for a limited time); N phase (the cell enters necrotic phase, if it does not receive nutrition until the resting time is expired, otherwise it enters G_1); A phase (apoptotic).

Individual-Based Modelling (IBM), which has gained popularity for modelling of biological processes, is another class of stochastic modelling [80]. In IBM approach, the biosystem population is regarded as being composed of individual cells whose sets of traits which determines their interaction with microenvironment vary. The IBM allows for explicit inclusion of variations in specifications of individual cells (heterogeneity). Aiming to investigate cancer invasion and the effect of microenvironment on growing tumour morphology and phenotype a novel IBM model was developed and further extended by Gerlee et al. [9, 30, 81, 82]. The model was constructed on a two-dimensional grid representing ECM, with each point possessing ECM, nutrition and oxygen concentration respective to that point in the ECM. Each point on the grid could either be occupied by a cancer cell or be empty. It was assumed that the cell's behaviour or phenotype is determined based on its interaction with neighbouring cells and microenvironment. Hence, a forward neural network fed with microenvironment variables as inputs to give the response of the cell (phenotype) was established. Three layers were considered for this network: (1) input layer which receives input microenvironment parameters (e.g., number of neighbours, oxygen, glucose consumption and ECM gradient); (2) hidden layer which is connected to the input layer via connection matrix consisting of regulatory genes which control the behaviour of cells via weighting factors (w) of the connection matrix; (3) output layer which is connected to the hidden layer via connection matrix (W) and determines the phenotype (e.g., metabolism, proliferation, quiescence, haptotaxis). The

Table 2: Summaries of stochastic models of tumour growth and invasion.

Type	Site of modelling	Incorporated mechanisms	Model validation and results	Comments	Reference
Monte Carlo (cellular automaton model)	Brain	3D tessellation lattice grid, three-population tumour, nutrition gradient, clonal competition, intercellular mechanical stress	N/A	Since active motility is not taken into account, the tumour invasion cannot be investigated	Kansal et al. 2000 [24]
Monte Carlo	multisite	Different phases of cell cycle, three-population tumour cells, shrinkage of tumour due to radiotherapy, cubic grid	Application of the model to small cell lung cancer/qualitative correspondence to *in vitro* experiments	The microscopic extension cannot be predicted since each grid element is almost 1 mm^3 accommodating 10^6 cells	Stamatakos 2001 [25]
Monte Carlo	Multisite	Different phases of cell cycle, three-population tumour cells, shrinkage of tumour due to radiotherapy, cubic grid, hypoxia	Application of the model to two GBM cases/qualitative correspondence to clinical observations	The possibility to optimize radiotherapy fractionation regimens, unable to depict microscopic spread	Antipas et al. 2004 [26]
Monte Carlo	Multisite	Different phases of cell cycle, three-population tumour cells, shrinkage of tumour due to radiotherapy, cubic grid, hypoxia, neo-angiogenesis	Parametric validation against two different categories of GBM/qualitative correspondence to experiments	Generally, the discrete nature of these models allows for inclusion of other parameters	Stamatakos et al. 2006 [27]
Markov model	Head and Neck	Lymphatic drainage pathway, T-stage, tumour location	Comparison to two surgical data/over prediction of metastasis	Quantitative prediction of microscopic spread was found to be feasible	Benson et al. 2006 [3]
Monte Carlo (individual-based model)	Multisite	Three-population tumour, 2D grid, nutrition and oxygen concentration, different phases of cell cycle	Comparison to the study of Anderson [19] and also experimental results [28, 29]/good agreement	Haptotaxis is not taken into account thus tumour invasion is not depicted	Gerlee and Anderson 2007 [30]
Monte Carlo (individual-based model)	Multisite	Three-population tumour, 2D grid, nutrition and oxygen concentration, different phases of cell cycle, haptotaxis	Comparison to the study of Anderson [19] and also experiment results/good agreement	The influence of evolution of tumour cell phenotype in response to microenvironment on tumour development and progression is an important conclusion to be used in the study of microscopic extension	Gerlee and Anderson 2009 [9]

nutrition concentrations were modelled by reaction diffusion equations according to which concentrations were calculated for each grid at every time step (10^{-1} cell cycle). The emergence of glycolytic phenotype associated with anaerobic metabolism pathway of cells was investigated in subsequent extension of the model [81], and more recently haptotaxis was taken into account [9]. The effect of haptotaxis was included in the model by a differential equation describing degradation of ECM at grid points. Accordingly, cells take the direction with maximum ECM gradient, and when there is no gradient, the existing cells go into proliferation mode until the gradient is sufficient to move. The switch between proliferation and haptotaxis was also depended on the number of vacant neighbours. The more number of vacancies, the more probable the cell stays in proliferation mode. Finally, it was demonstrated that with the emergence of haptotaxis, tumour growth is altered showing different morphologies (compact or branched) depending on the oxygen and ECM concentration. This outcome was supported by other analyses of the model [82, 83] and conceptually corresponded to the simulation results of the hybrid IBM model of Anderson et al. [19, 51].

To summarize, in clinical situations, physicians propose CTVs based on their experience of the extent of malignant tumours growth. Therefore, the ability to accurately model the tumour extension at microscopic scale is highly desirable.

Within the realm of stochastic modelling, a significant number of research works has been developed to contribute to the understanding of the tumour growth and invasion via a variety of classes of Monte Carlo models. However, irrespective of the class, these studies aim to gain insight into either the biology of cancer growth in general terms or the response of tumour to radiotherapy rather than the microscopic extension of tumour which is to be incorporated in CTV. Hence, there is room for investigation in this respect, in the light of information acquired from these studies. Table 2 summarizes a few major models of tumour growth and invasion which represent various classes of Monte Carlo models.

4. Conclusion

An infiltrating neoplasm undergoes several stages in the course of its growth and progression and understanding of the mechanisms governing the evolution of tumour is required to deliver an appropriate therapy which results in optimal tumour control and reduced normal tissue side effects. Mathematical modelling is recognized as a great tool to facilitate this understanding. Furthermore, mathematical models provide predictions of the probable response of tumour to therapeutic regimens in a variety of circumstances, different in terms of factors such as the tumour microenvironment, and stage. In this paper, we have reviewed the evolution of mathematical modelling of tumour growth and invasion in both analytical and stochastic approaches. Analytical models are capable to describe the behaviour of tumour at macroscopic level for specific conditions; however, they fail to provide predictions at microscopic (cellular and subcellular) level. In addition, the ongoing research to enhance the limited insight into complex and dynamic cancer systems may reveal some further parameters which have to be included in models. However, analytical models are not flexible for these modifications. On the other hand, stochastic models efficiently depict the characteristic and behaviour of tumour as this class of modelling enables introducing new parameters as well as specific anatomical boundaries. Finally, we came to believe that while none of the above-mentioned models address explicitly the microscopic extension of tumour, they have the potential to be used to deduce the extent of subclinical disease which is not detected by imaging techniques. To serve this purpose, however, models have to be further modified, applying the relevant biological parameters, to become site-specific. The tumour sites that have a relatively high histopathological data available, such as prostate and gliomas can be potentially modelled and validated faster than those having little or no clinical data related to their microscopic extension.

References

[1] International Commission of Radiation Units and Measurements, "Prescribing, Recording, and Reporting Photon Beam Therapy," Report 50, ICRU, 1993.

[2] K. R. Swanson, E. C. Alvord Jr., and J. D. Murray, "Virtual brain tumours (gliomas) enhance the reality of medical imaging and highlight inadequacies of current therapy," *British Journal of Cancer*, vol. 86, no. 1, pp. 14–18, 2002.

[3] N. Benson, M. Whipple, and I. J. Kalet, "A Markov model approach to predicting regional tumor spread in the lymphatic system of the head and neck," in *Proceedings of the AMIA Annual Symposium*, pp. 31–35, 2006.

[4] J. K. A. Jameel, V. S. R. Rao, L. Cawkwell, and P. J. Drew, "Radioresistance in carcinoma of the breast," *Breast*, vol. 13, no. 6, pp. 452–460, 2004.

[5] A. J. F. Griffits, W. M. Miller, and R. C. Lewontin, *Modern Genetic Analysis*, W. H. Freeman, Newyork, NY, USA, 1999.

[6] A. Gerisch and M. A. J. Chaplain, "Mathematical modelling of cancer cell invasion of tissue: local and non-local models and the effect of adhesion," *Journal of Theoretical Biology*, vol. 250, no. 4, pp. 684–704, 2008.

[7] E. J. Hall and A. J. Giaccia, *Radiobiology for the Radiologist*, Lippincott Williams & Wilkins, 6th edition, 2006.

[8] S. E. Eikenberry, T. Sankar, M. C. Preul, E. J. Kostelich, C. J. Thalhauser, and Y. Kuang, "Virtual glioblastoma: growth, migration and treatment in a three-dimensional mathematical model," *Cell Proliferation*, vol. 42, no. 4, pp. 511–528, 2009.

[9] P. Gerlee and A. R. A. Anderson, "Evolution of cell motility in an individual-based model of tumour growth," *Journal of Theoretical Biology*, vol. 259, no. 1, pp. 67–83, 2009.

[10] O. Clatz, M. Sermesant, P. Y. Bondiau et al., "Realistic simulation of the 3-D growth of brain tumors in MR images coupling diffusion with biomechanical deformation," *IEEE Transactions on Medical Imaging*, vol. 24, no. 10, pp. 1334–1346, 2005.

[11] K. R. Swanson, C. Bridge, J. D. Murray, and E. C. Alvord, "Virtual and real brain tumors: using mathematical modeling to quantify glioma growth and invasion," *Journal of the Neurological Sciences*, vol. 216, no. 1, pp. 1–10, 2003.

[12] P. Tracqui, G. C. Cruywagen, D. E. Woodward, G. T. Bartoo, J. D. Murray, and E. C. Alvord, "A mathematical model of glioma growth: the effect of chemotherapy on spatio-temporal growth," *Cell Proliferation*, vol. 28, no. 1, pp. 17–31, 1995.

[13] J. D. Murray, *Mathematical Biology*, Springer, New York, NY, USA, 3rd edition, 2002.

[14] G. C. Cruywagen, D. E. Woodward, P. Tracui, G. T. Bartoo, J. D. Murray, and E. C. Alvord, "The modeling of diffusive tumours," *Journal of Biological Systems*, vol. 3, no. 4, pp. 937–945, 1995.

[15] H. L. P. Harpold, E. C. Alvord Jr., and K. R. Swanson, "The evolution of mathematical modeling of glioma proliferation and invasion," *Journal of Neuropathology and Experimental Neurology*, vol. 66, no. 1, pp. 1–9, 2007.

[16] P. Tracqui, "From passive diffusion to active cellular migration in mathematical models of tumour invasion," *Acta Biotheoretica*, vol. 43, no. 4, pp. 443–464, 1995.

[17] K. R. Swanson, E. C. Alvord Jr., and J. D. Murray, "A quantitative model for differential motility of gliomas in grey and white matter," *Cell Proliferation*, vol. 33, no. 5, pp. 317–329, 2000.

[18] O. Casanovas, D. J. Hicklin, G. Bergers, and D. Hanahan, "Drug resistance by evasion of antiangiogenic targeting of VEGF signaling in late-stage pancreatic islet tumors," *Cancer Cell*, vol. 8, no. 4, pp. 299–309, 2005.

[19] A. R. A. Anderson, "A hybrid mathematical model of solid tumour invasion: the importance of cell adhesion," *Mathematical Medicine and Biology*, vol. 22, no. 2, pp. 163–186, 2005.

[20] A. M. Stein, T. Demuth, D. Mobley, M. Berens, and L. M. Sander, "A mathematical model of glioblastoma tumor spheroid invasion in a three-dimensional in vitro experiment," *Biophysical Journal*, vol. 92, no. 1, pp. 356–365, 2007.

[21] A. R. Anderson, M. A. J. Chaplain, E. L. Newman, R. J. C. Steele, and A. M. Thampson, "Mathematical modelling of tumour invasion and metastasis," *Computational and Mathematical Methods in Medicine*, vol. 2, no. 2, pp. 129–154, 2000.

[22] C. J. Thalhauser, T. Sankar, M. C. Preul, and Y. Kuang, "Explicit separation of growth and motility in a new tumor cord model," *Bulletin of Mathematical Biology*, vol. 71, no. 3, pp. 585–601, 2009.

[23] R. Rockne, J. K. Rockhill, M. Mrugala et al., "Predicting the efficacy of radiotherapy in individual glioblastoma patients in vivo: a mathematical modeling approach," *Physics in Medicine and Biology*, vol. 55, no. 12, pp. 3271–3285, 2010.

[24] A. R. Kansal, S. Torquato, G. R. Harsh, E. A. Chiocca, and T. S. Deisboeck, "Simulated brain tumor growth dynamics using a three-dimensional cellular automaton," *Journal of Theoretical Biology*, vol. 203, no. 4, pp. 367–382, 2000.

[25] G. S. Stamatakos, "In vivo tumor growth and response to radiation therapy: a novel algorithmic description," *International Journal of Radiation Oncology, Biology, Physics*, vol. 51, no. 3, p. 240, 2001.

[26] V. P. Antipas, G. S. Stamatakos, N. K. Uzunoglu, D. D. Dionysiou, and R. G. Dale, "A spatio-temporal simulation model of the response of solid tumours to radiotherapy in vivo: parametric validation concerning oxygen enhancement ratio and cell cycle duration," *Physics in Medicine and Biology*, vol. 49, no. 8, pp. 1485–1504, 2004.

[27] G. S. Stamatakos, V. P. Antipas, N. K. Uzunoglu, and R. G. Dale, "A four-dimensional computer simulation model of the in vivo response to radiotherapy of glioblastoma multiforme: studies on the effect of clonogenic cell density," *British Journal of Radiology*, vol. 79, no. 941, pp. 389–400, 2006.

[28] T. G. Graeber, C. Osmanian, T. Jacks et al., "Hypoxia-mediated selection of cells with diminished apoptotic potential in solid tumours," *Nature*, vol. 379, no. 6560, pp. 88–91, 1996.

[29] C. Y. Kim, M. H. Tsai, C. Osmanian et al., "Selection of human cervical epithelial cells that possess reduced apoptotic potential to low-oxygen conditions," *Cancer Research*, vol. 57, no. 19, pp. 4200–4204, 1997.

[30] P. Gerlee and A. R. A. Anderson, "An evolutionary hybrid cellular automaton model of solid tumour growth," *Journal of Theoretical Biology*, vol. 246, no. 4, pp. 583–603, 2007.

[31] D. L. Collins, A. P. Zijdenbos, V. Kollokian et al., "Design and construction of a realistic digital brain phantom," *IEEE Transactions on Medical Imaging*, vol. 17, no. 3, pp. 463–468, 1998.

[32] C. H. Wang, J. K. Rockhill, M. Mrugala et al., "Prognostic significance of growth kinetics in newly diagnosed glioblastomas revealed by combining serial imaging with a novel biomathematical model," *Cancer Research*, vol. 69, no. 23, pp. 9133–9140, 2009.

[33] M. R. Chicoine and D. L. Silbergeld, "Assessment of brain tumor cell motility in vivo and in vitro," *Journal of Neurosurgery*, vol. 82, no. 4, pp. 615–622, 1995.

[34] D. E. Woodward, J. Cook, P. Tracqui, G. C. Cruywagen, J. D. Murray, and E. C. Alvord, "A mathematical model of glioma growth: the effect of extent of surgical resection," *Cell Proliferation*, vol. 29, no. 6, pp. 269–288, 1996.

[35] K. R. Swanson, E. C. Alvord, and J. D. Murray, "Quantifying efficacy of chemotherapy of brain tumors with homogeneous and heterogeneous drug delivery," *Acta Biotheoretica*, vol. 50, no. 4, pp. 223–237, 2002.

[36] P. Y. Bondiau, E. Konukoglu, O. Clatz, H. Delingette, M. Frenay, and P. Paquis, "Biocomputing: numerical simulation of glioblastoma growth and comparison with conventional irradiation margins," *Physica Medica*, vol. 27, no. 2, pp. 103–108, 2011.

[37] H. M. Byrne and M. A. Chaplain, "Growth of nonnecrotic tumors in the presence and absence of inhibitors," *Mathematical Biosciences*, vol. 130, no. 2, pp. 151–181, 1995.

[38] H. M. Byrne and M. A. J. Chaplain, "Growth of necrotic tumors in the presence and absence of inhibitors," *Mathematical Biosciences*, vol. 135, no. 2, pp. 187–216, 1996.

[39] H. M. Byrne and M. A. J. Chaplain, "Free boundary value problems associated with the growth and development of multicellular spheroids," *European Journal of Applied Mathematics*, vol. 8, no. 6, pp. 639–658, 1997.

[40] N. Bellomo and L. Preziosi, "Modelling and mathematical problems related to tumor evolution and its interaction with the immune system," *Mathematical and Computer Modelling*, vol. 32, no. 3-4, pp. 413–452, 2000.

[41] V. Cristini, J. Lowengrub, and Q. Nie, "Nonlinear simulation of tumor growth," *Journal of Mathematical Biology*, vol. 46, no. 3, pp. 191–224, 2003.

[42] R. P. Araujo and D. L. S. McElwain, "A history of the study of solid tumour growth: the contribution of mathematical modelling," *Bulletin of Mathematical Biology*, vol. 66, no. 5, pp. 1039–1091, 2004.

[43] V. Cristini, H. B. Frieboes, R. Gatenby, S. Caserta, M. Ferrari, and J. Sinek, "Morphologic instability and cancer invasion," *Clinical Cancer Research*, vol. 11, no. 19, pp. 6772–6779, 2005.

[44] P. Macklin and J. Lowengrub, "Evolving interfaces via gradients of geometry-dependent interior Poisson problems: application to tumor growth," *Journal of Computational Physics*, vol. 203, no. 1, pp. 191–220, 2005.

[45] P. Macklin and J. Lowengrub, "Nonlinear simulation of the effect of microenvironment on tumor growth," *Journal of Theoretical Biology*, vol. 245, no. 4, pp. 677–704, 2007.

[46] S. Sanga, H. B. Frieboes, X. Zheng, R. Gatenby, E. L. Bearer, and V. Cristini, "Predictive oncology: a review of multidisciplinary, multiscale in silico modeling linking phenotype, morphology and growth," *NeuroImage*, vol. 37, supplement, no. 1, pp. S120–S134, 2007.

[47] R. A. Gatenby, A. S. Silva, R. J. Gillies, and B. R. Frieden, "Adaptive therapy," *Cancer Research*, vol. 69, no. 11, pp. 4894–4903, 2009.

[48] T. S. Deisboeck, "Multiscale cancer modeling," *Annual Review of Biomedical Engineering*, vol. 13, pp. 127–155, 2011.

[49] D. C. Walker and J. Southgate, "The virtual cell—a candidate co-ordinator for 'middle-out' modelling of biological systems," *Briefings in Bioinformatics*, vol. 10, no. 4, pp. 450–461, 2009.

[50] A. R. A. Anderson and V. Quaranta, "Integrative mathematical oncology," *Nature Reviews Cancer*, vol. 8, no. 3, pp. 227–234, 2008.

[51] A. R. A. Anderson, A. M. Weaver, P. T. Cummings, and V. Quaranta, "Tumor morphology and phenotypic evolution driven by selective pressure from the microenvironment," *Cell*, vol. 127, no. 5, pp. 905–915, 2006.

[52] A. R. A. Anderson, K. A. Rejniak, P. Gerlee, and V. Quaranta, "Microenvironment driven invasion: a multiscale multimodel investigation," *Journal of Mathematical Biology*, vol. 58, no. 4-5, pp. 579–624, 2009.

[53] J. T. Erler, K. L. Bennewith, M. Nicolau et al., "Lysyl oxidase is essential for hypoxia-induced metastasis," *Nature*, vol. 440, no. 7088, pp. 1222–1226, 2006.

[54] B. P. Marchant, J. Norbury, and A. J. Perumpanani, "Traveling shock waves arising in a model of malignant invasion," *SIAM Journal on Applied Mathematics*, vol. 60, no. 2, pp. 463–476, 2000.

[55] B. P. Marchant, J. Norbury, and J. A. Sherratt, "Travelling wave solutions to a haptotaxis-dominated model of malignant invasion," *Nonlinearity*, vol. 14, no. 6, pp. 1653–1671, 2001.

[56] B. P. Marchant, J. Norbury, and H. M. Byrne, "Biphasic behaviour in malignant invasion," *Mathematical Medicine and Biology*, vol. 23, no. 3, pp. 173–196, 2006.

[57] A. R. A. Anderson and M. A. J. Chaplain, "A mathematical model for capillary network formation in the absence of endothelial cell proliferation," *Applied Mathematics Letters*, vol. 11, no. 3, pp. 109–114, 1998.

[58] A. R. A. Anderson and M. A. J. Chaplain, "Continuous and discrete mathematical models of tumor-induced angiogenesis," *Bulletin of Mathematical Biology*, vol. 60, no. 5, pp. 857–899, 1998.

[59] H. B. Frieboes, J. S. Lowengrub, S. Wise et al., "Computer simulation of glioma growth and morphology," *NeuroImage*, vol. 37, no. 1, supplement, pp. S59–S70, 2007.

[60] A. Kubo, "Mathematical analysis of a model of tumour invasion and simulations," *International Journal of Mathematical Models and Methods in Applied Sciences*, vol. 4, no. 3, pp. 187–194, 2010.

[61] K. R. Swanson, "Quantifying the role of angiogenesis in malignant progression of gliomas: in silico modeling integrates imaging and histology," *Cancer Research*, vol. 71, no. 24, pp. 7366–7375, 2011.

[62] I. J. Kalet, M. Whipple, S. Pessah, J. Barker, M. M. Austin-Seymour, and L. G. Shapiro, "A rule-based model for local and regional tumor spread," in *Proceedings of the AMIA Annual Symposium*, pp. 360–364, 2002.

[63] C. Rosse, L. G. Shapiro, and J. F. Brinkley, "The digital anatomist foundational model: principles for defining and structuring its concept domain," in *Proceedings of the AMIA Annual Symposium*, pp. 820–824, 1998.

[64] W. Duchting and T. Vogelsaenger, "Recent progress in modelling and simulation of three-dimensional tumor growth and treatment," *BioSystems*, vol. 18, no. 1, pp. 79–91, 1985.

[65] A. S. Qi, "Multiple solutions of a model describing cancerous growth," *Bulletin of Mathematical Biology*, vol. 50, no. 1, pp. 1–17, 1988.

[66] A. S. Qi, "A cellular automaton model of cancerous growth," *Journal of Theoretical Biology*, vol. 161, no. 1, pp. 1–12, 1993.

[67] J. Smolle and H. Stettner, "Computer simulation of tumour cell invasion by a stochastic growth model," *Journal of Theoretical Biology*, vol. 160, no. 1, pp. 63–72, 1993.

[68] J. Smolle, R. Hofmann-Wellenhof, and R. Fink-Puches, "Cellular invasion without cellular motility in a stochastic growth model," *Analytical Cellular Pathology*, vol. 10, no. 1, pp. 37–43, 1996.

[69] R. Wasserman, R. Acharya, C. Sibata, and K. H. Shin, "A patient-specific in vivo tumor model," *Mathematical Biosciences*, vol. 136, no. 2, pp. 111–140, 1996.

[70] A. R. Kansal, S. Torquato, G. R. Harsh IV, E. A. Chiocca, and T. S. Deisboeck, "Cellular automaton of idealized brain tumor growth dynamics," *BioSystems*, vol. 55, no. 1–3, pp. 119–127, 2000.

[71] T. S. Deisboeck, M. E. Berens, A. R. Kansal, S. Torquato, A. O. Stemmer-Rachamimov, and E. A. Chiocca, "Pattern of self-organization in tumour systems: complex growth dynamics in a novel brain tumour spheroid model," *Cell Proliferation*, vol. 34, no. 2, pp. 115–134, 2001.

[72] Y. Jiao and S. Torquato, "Emergent behavior from a cellular automaton model for invasive tumor growth in heterogeneous microenvironments," *PLoS Computational Biology*, vol. 7, no. 12, 2011.

[73] A. R. Kansal, S. Torquato, E. A. Chiocca, and T. S. Deisboeck, "Emergence of a subpopulation in a computational model of tumor growth," *Journal of Theoretical Biology*, vol. 207, no. 3, pp. 431–441, 2000.

[74] G. S. Stamatakos, E. I. Zacharaki, M. I. Makropoulou et al., "Modeling tumor growth and irradiation response in vitro—a combination of high-performance computing and web-based technologies including VRML visualization," *IEEE Transactions on Information Technology in Biomedicine*, vol. 5, no. 4, pp. 279–289, 2001.

[75] G. S. Stamatakos, D. D. Dionysiou, E. I. Zacharaki, N. A. Mquravliansky, K. S. Nikita, and N. K. Uzunoglu, "In silico radiation oncology: combining novel simulation algorithms with current visualization techniques," *Proceedings of the IEEE*, vol. 90, no. 11, pp. 1764–1777, 2002.

[76] W. Duchting, T. Ginsberg, and W. Ulmer, "Modeling of radiogenic responses induced by fractionated irradiation in malignant and normal tissue," *Stem Cells*, vol. 13, no. 1, pp. 301–306, 1995.

[77] D. D. Dionysiou, G. S. Stamatakos, N. K. Uzunoglu, K. S. Nikita, and A. Marioli, "A four-dimensional simulation model of tumour response to radiotherapy in vivo: parametric validation considering radiosensitivity, genetic profile and fractionation," *Journal of Theoretical Biology*, vol. 230, no. 1, pp. 1–20, 2004.

[78] D. D. Dionysiou, G. S. Stamatakos, N. K. Uzunoglu, and K. S. Nikita, "A computer simulation of in vivo tumour growth and response to radiotherapy: new algorithms and parametric results," *Computers in Biology and Medicine*, vol. 36, no. 5, pp. 448–464, 2006.

[79] D. D. Dionysiou, "Critical parameters determining standard radiotherapy treatment outcome for glioblastoma multiforme: a computer simulation," *The Open Biomedical Engineering Journal*, vol. 2, pp. 43–51, 2008.

[80] A. R. Anderson, M. A. J. Chaplain, and K. A. Rejniak, *Single-Cell-Based Models in Biology and Medicine*, Berkhauser, Basel, Switzerland, 2007.

[81] P. Gerlee and A. R. A. Anderson, "A hybrid cellular automaton model of clonal evolution in cancer: the emergence of the glycolytic phenotype," *Journal of Theoretical Biology*, vol. 250, no. 4, pp. 705–722, 2008.

[82] P. Gerlee and A. R. A. Anderson, "Modelling evolutionary cell behaviour using neural networks: application to tumour growth," *BioSystems*, vol. 95, no. 2, pp. 166–174, 2009.

[83] P. Gerlee and A. R. A. Anderson, "Stability analysis of a hybrid cellular automaton model of cell colony growth," *Physical Review E*, vol. 75, no. 5, Article ID 051911, 2007.

3.3 Discussion and conclusion

As discussed in the paper, deterministic/analytical modelling based on conservation of cells originally formulated by Murray (Murray, 2002), has evolved to sophisticated models incorporating biological mechanisms such as hypoxia, haptotaxis and more. This approach has been since adopted in other works predicting the pattern of GBM infiltration (Unkelbach et al., 2014, Martínez-González et al., 2012). Valuable achievements with respect to predicting tumour behaviour in the course of its progression have been obtained using this class of model. Nevertheless, deterministic models can anticipate tumour behaviour at a macroscopic level and fail to provide predictions at cellular and subcellular (i.e. microscopic) levels.

Stochastic modelling (e.g. Monte Carlo (MC)) enables simulation of radiation treatment of a population of cells with various radiobiological characteristics at microscopic (i.e. cellular) and sub-cellular levels. Furthermore, stochastic approaches, due to being driven by probability distributions, is more appropriate to model the probabilistic nature of radiobiological processes and stochastic nature of elementary particle interactions with matter.

"Monte Carlo is a numerical method to solve equations or calculate integrals based on random number sampling" (Fippel, 2013). MC, in general, is a very useful method to model sophisticated phenomena with significant variations such as biological systems. MC particle tracking simulations have been widely used in the field of Medical Physics to predict the individual track histories of every particle (primaries and secondaries) to calculate the dose in a patient/phantom by integrating the energy losses of each particle along their tracks within each voxel of specified size. Every MC particle tracking package requires the following components:

1. A random number generator and a sampling method from a Probability Density Function (PDF).
2. A method to design the geometry of the medium to be traversed by primary particles.

3. A method to describe primary particles properties.
4. A method to store histories of particles and any quantity of interest.
5. The technique by which cross sections related to each interaction and each particle are calculated. These cross sections typically include two types of transport algorithms (i.e. libraries): photon transport and charged particle transport.

Several MC codes, for example, EGSnrc (Kawrakow, 2000) for the simulation of electromagnetic processes, and GEANT4 (Agostinelli et al., 2003), MCNP/MCNPX (Briesmeister et al., 2000), and RITRACKS (Plante and Cucinotta, 2011) that include hadronic processes, have been developed. Complex experimental set-ups (e.g. detector geometry or cell component and DNA structure) can be simulated using these MC packages, with many applications in radiation dosimetry and radiobiological modelling. Geant4 is a freely available MC toolkit to simulate the interactions of energetic particles in matter in complicated geometries and in a variety of applications ranging from high-energy astrophysics, nuclear and accelerator physics to medical physics.

In 2001 Fix *et al.* (Fix et al., 2001) developed a Geant4 MC application to calculate the dose from a 6 MV x-ray beam in $1.0 \times 1.0 \times 0.1\ cm^3$ voxels. The code incorporated linac head components. Energy spectrum and angular distribution of incident particles were also implemented. The model was used for detailed characterization of a 6 MV beam from Varian Clinac 2300. While the model was able to successfully reproduce measured data (within 1.5%), it lacks the ability to calculate the dose at a cellular level (i.e. micro-scale), hence, it is useful for macroscopic applications only.

For the first time, cell-based dosimetry calculation was performed by Incerti *et al.* (Incerti et al., 2009) in a single cell with its realistic geometry and material composition using Geant4 MC toolkit. The simulation code included the entire microbeam line for cellular irradiation with 3 MeV incident alpha particles. This model demonstrated the versatility of Geant4 toolkit to simulate complicated geometry at a very fine scale (e.g. cell components such as cytoplasm and nucleus were also modelled), transport particles through this geometry and to accurately obtain the dose at cellular or subcellular levels for various treatment modalities.

Douglass *et al.* (Douglass et al., 2012) developed an algorithm for growing a macroscopic tumour volume from individual randomised cells. The main physical and chemical components of the cell (e.g. nucleus, membrane and cytoplasm) were modelled. The tumour model was then imported into Geant4 to simulate ionisation track structure within each cell region in order to predict radiation induced cell death (Douglass et al., 2015a).

Each of these models have progressively improved the ability to accurately predict absorbed dose and radiobiological effects of radiation (e.g. cell death) by moving from a macroscopic to a microscopic scale. This has become possible due to ongoing enhancements developed by the worldwide Geant4 collaboration group (e.g. the expansion of cross section libraries to include data relating to low energy radiation track structure) as well as development in the field of cellular biology. Despite these developments, to our knowledge, there is no published work reporting an integrated stochastic tumour model with MC cell-based dosimetry application to evaluate radiotherapy treatment outcome for glioblastoma of the brain. The work presented in this thesis aims to utilize Geant4 toolkit to develop a comprehensive stochastic radiobiological model for the glioblastoma of the brain.

Chapter 4

Development and Verification of a Geant4 Model for Varian Clinac iX 6 MV X-ray Beam

In this chapter, the development of the first stage of the radiobiological model, i.e. 6 MV Varian Clinac iX beam model, is described. The beam model development is consisted of:

- Development of a 6 MV x-ray beam model produced by Varian Clinac iX linear accelerator (Varian® Medical System, Palo Alto, CA).
- Using the beam model to investigate the effect of various detector set-ups and materials, including heterogeneous slab phantoms, and several mono-energetic x-ray beams, 300 keV, 2 MeV, and 6 MeV, on the dose distribution .
- Quantitative and qualitative verification of simulation results to insure the accuracy of dose calculations by testing the model in a variety of conditions.

4.1 Introduction

As discussed in chapter 3, bio-mathematical and computational modelling is a great tool to provide qualitative and quantitative predictions of treatment outcome for a range of radiotherapy regimens and techniques.

A mathematical model to represent an External Beam Radiation Therapy (EBRT) technique should consist of three key components: 1) a beam model as the source of external radiation therapy, 2) a tumour and its microscopic extension embedded in healthy tissue, and 3) a list of interaction cross section libraries for particle transport through matter to calculate dose deposition in the tumour. To begin with, a beam model should be developed and verified against experimental data. In this study a Geant4 beam model for Varian Clinac iX 6 MV diverging x-ray beam with its realistic energy spectrum was developed. The available photon beam models, provided by International Atomic Energy Agency (IAEA) (*https://www.nds.iaea.org/phsp/photon1*) were not be used as it was intended to validate the beam model against the in-house measured data from Varian Clinac iX accelerator, Royal Adelaide Hospital.

4.1.1 Structure of Geant4

Geant4 (Agostinelli et al., 2003) is a powerful object-oriented MC particle tracking toolkit written in C++ language. The Geant4 framework is composed of building blocks called classes, each encapsulating a complete set of data and methods (i.e. functions containing instructions for building its "objects") describing the component it is representing. This feature of Geant4 allows development of a simulated experimental set-up including particle sources, geometry and detectors by using objects of their corresponding classes which can be tailored to a particular detector set-up. In a Geant4 application, four essential user-defined concrete classes, derived from Geant4 abstract classes, are required to describe the most basic experimental set-up:

- Define the geometrical set-up including material and volume.
- Define the source of primary particles.

- Define physics to be involved including particles, physics models and production thresholds.
- Track and extract information required.

One may also consider to visualize geometry, trajectories and physics output; use User Interfaces (UI) and so forth. The components used need to be registered in a manager/run controller class (i.e. G4RunManager) and an interface must be established from each component to other components if they are meant to be linked. Figure 4.1 shows these key classes and the way they are related. To specify relevant characteristics of a class while building a concrete class, several other Geant4 classes may be required, e.g. for each mandatory class in figure 4.1 a few relevant classes and methods are listed. In most cases, however, these few classes will not be sufficient to describe a suitable physics simulation and additional classes must be included.

Geant4 does not provide a main source file and it needs to be created by the user. As the name suggests, in the main file, a run manager (i.e. derived from G4RunManger base class) is constructed and the mandatory classes and any other user action classes are registered in the defined run manager. The main source file also includes initialization of the run manager, random seed number method and the mode the simulation should be run in (i.e. batch or interactive mode).

4.1.1.1 Geometry and scoring

Geant4 adopts a hierarchical approach (parent–child tree structure) for geometry construction and each geometry item is called an object. An object in the simulation geometry has three volumes associated with it: a solid volume to define the size and shape of the object, a logical volume defining material; and a physical volume defining spatial positioning of the object with respect to its mother volume. All geometry items must be enclosed within a laboratory frame (i.e. the world volume) and all objects (geometry items) within the world volume must be defined by their position, orientation, size and material composition as well as other characteristics including whether or not particles can interact with such a volume or scoring needs to be done in these volumes. Figure 4.2

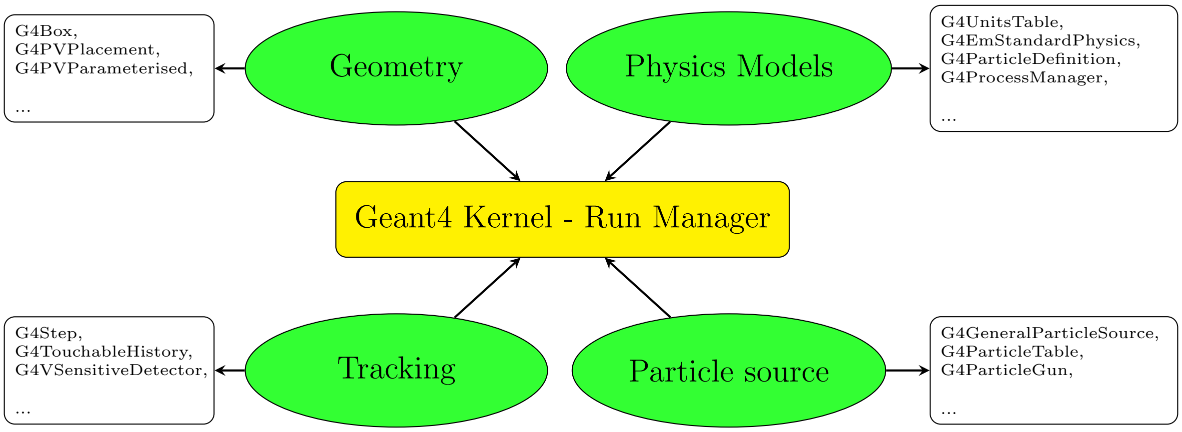

FIGURE 4.1: Schematic diagram showing the essential Geant4 classes to describe a basic experimental set-up. More advanced models require implementation of other classes as well. The concrete classes built by an application developer, including mandatory classes (green) and any other user-defined classes, must be registered to the run manager class which is responsible for controlling the flow of the program and manages a run.

shows a geometry consisting of three objects (i.e. numbered 1, 2, and 3), one of which has a daughter volume (i.e. number 1). The world volume, enclosing all geometry items is at the top of the hierarchy tree, figure 4.3.

To define the geometry, Geant4 provides a base class called *G4VUserDetectorConstruction* from which an object (i.e. defined by a user of an application) inherits its attributes.

It is often required to divide a geometry item to identical or non-identical voxels to extract physics information, e.g. absorbed dose, energy flux and so forth. To construct a geometry configuration consisting of multiple identical copies of a single logical volume repeated in specified rotational or translational order, the physical volume can be defined using Replicas method from the repeated volume technique. In the case the repeated volumes are different in shape, size or materials, the parametrized volume technique can be used. The limitation of parametrized volumes is that these volumes cannot have daughter volumes, and as a result division of the detector to voxels of specific sizes to score the dose is not possible. To overcome this limitation, parallel geometry or Readout Geometry (RO geometry) method has been provided in the toolkit. The idea is to create a geometry consisting of a world volume, a phantom identical in material and size to the world volume, and the mother volume of parametrised volume in the real geometry, respectively. The phantom in virtual geometry can be divided to voxels for scoring purposes. This volume acts as a virtual tracking geometry, through which

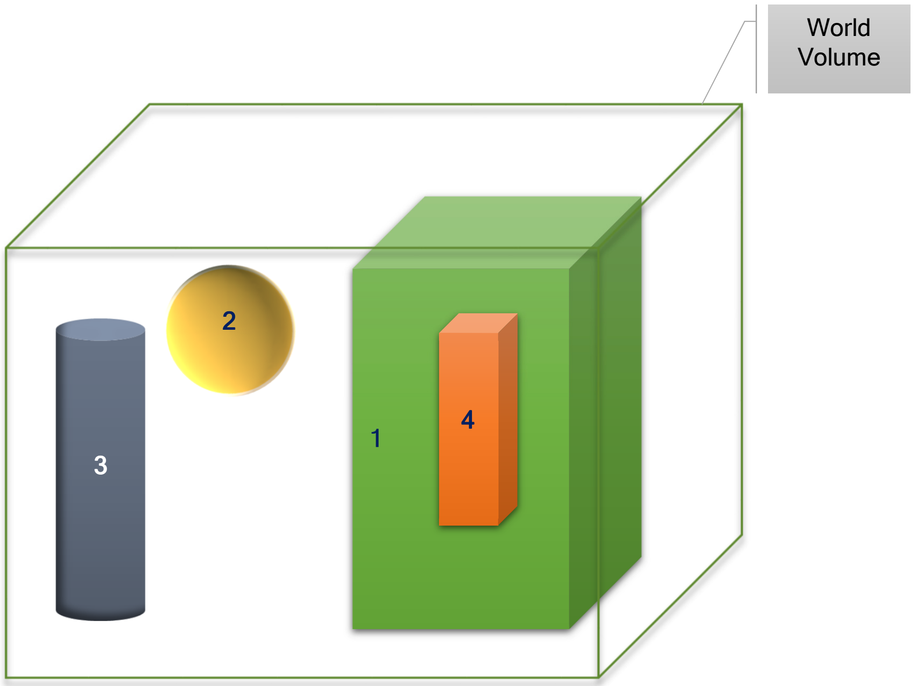

Figure 4.2: An example of a Geant4 geometry: The world volume contains three mother volumes, a green cube (No. 1), a yellow sphere (No. 2) and a dark blue cylinder (No. 3). Object number 1 has a daughter, which is an orange rectangular cube (No. 4).

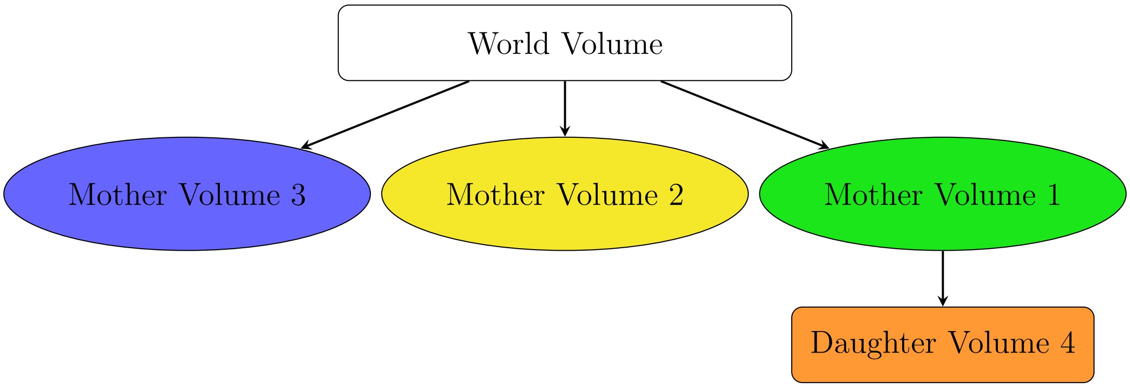

Figure 4.3: The hierarchy tree associated with the geometry volume shown in figure 4.2. The colour code in this figure is in accordance with those in figure 4.2.

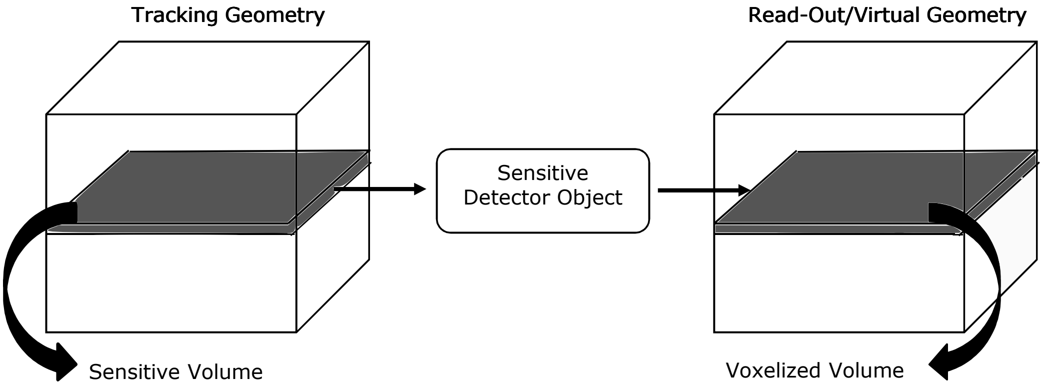

FIGURE 4.4: Association of tracking geometry with dummy parallel geometry.

the real geometry could be scanned. The schematic diagram in figure 4.4 illustrates the association between real and RO geometries.

In Geant4, materials can be defined in a number of ways. Materials are composed of molecular components called elements and each element can be made of several isotopes. The molecular components of a particular composite material can be created using the *G4Element* and *G4Isotope* classes, respectively. The material is then defined by adding respective elements as a *G4Material* object. An alternative is to use Geant4 Material Database, National Institute of Standards and Technology (NIST) Listings, "Compositions of Materials used in STAR Databases" webpage: *http://physics.nist.gov/cgi-bin/Star/compos.pl?matno=123*. It is also possible to define a new material based on materials in the NIST through overwriting properties which need to be changed in the base material.

The simulation in Geant4 is performed "silently", that is, the required physics information should be extracted by the user. In Geant4 terminology, three basic concepts, with respect to particle tracking, are: event, track and step. A particle history is called an event, which is the basic unit of a Geant4 simulation. Track is a snapshot of a particle's history, containing physical quantities of current instance. Step, whose size can be defined by the user, has two points and contains delta information of a particle, e.g. total absorbed dose in the step, time-of-flight spent by the step. The status of a track is updated at the end of each step. The user has several options to retrieve information (e.g. total absorbed dose) about particle history, as follows:

1. Command-Based Scoring: Through interactive commands, the user defines a 3D scoring mesh which forms a parallel world volume through which navigation across the detector is performed. The scoring is done by a number of scorers defined for each individual physical quantity meant to be scored.

2. Creating scoring maps of each physical quantity for each event (i.e. particle history): *G4MultiFunctionalDetector* which is assigned to one or more logical volumes, creates a collection (i.e. map) of physical quantities for an event. The scorers respective to each quantity are derived from the Geant4 base class *G4VPrimitiveScorer* and are registered to *G4MultiFunctionalDetector*.

3. Creating a sensitive detector: When a logical volume is assigned with an object derived from the class *G4VSensitiveDetector*, the volume becomes sensitive, that is, if during processing of a particle track, a step occurs in this logical volume, the sensitive detector object is activated by this step. This results in construction of hits (i.e. a hit/hit maps is built to store information extracted from a step) from information extracted from the steps along the particle track. The collections of hits for each event is stored in a container class called *G4HCofThisEvent*. The hits collection from each event (contained in *G4HCofThisEvent* object associated with the respective event) is passed to user *RunAction* class to be accumulated for all events.

4.1.1.2 Primary particle generation

In order to generate primary particles, a user concrete class, in which beam specifications such as energy, momentum direction and so forth are specified, must be derived from *G4VUserPrimaryGeneratorAction* base class of Geant4. Then the actual generation of primaries can be implemented using any of the three classes: *G4ParticleGun*, *G4GeneralParticleSource* and *G4HEPEvtInterface* (Collaboration, 2012).

General Particle Source (GPS) has a large degree of flexibility to allow specification of more sophisticated sources, particularly beams with energy spectrum, and randomized spatial and angular distributions, through a fairly simple implementation. Using GPS, the properties of primary particles are defined in macro files and the code must be run in an interactive mode, or alternatively the particle generation can be controlled at user interface (UI) terminal.

4.1.1.3 Physics models

There are two types of particle transport in MC particle tracking packages: photon interactions and charged particle (e.g. electron and proton) interactions.

When a photon of energy E is incident on the surface of a homogeneous medium, the probability of interaction $p(r)$ after travelling an infinitesimal depth dr into the medium is calculated using equation 4.1 (Marcu et al., 2012), where $\mu(E)$ is the linear attenuation coefficient for a photon of energy E in the medium it is traversing:

$$p(r)dr = \mu(E)e^{-\mu(E)r}dr \tag{4.1}$$

The primary photon interactions in radiation therapy energy range are: photoelectric interaction, Compton scattering and pair production. Thus, the total linear attenuation coefficients is (Marcu et al., 2012):

$$\mu = \tau + \sigma + \kappa \tag{4.2}$$

where μ, τ, σ, and κ are total, photoelectric, Compton scattering, and pair production attenuation coefficients, respectively.

Charged particles undergo two types of interactions when traversing a medium: elastic and inelastic. Radiobiological cell damage is mostly caused by inelastic interactions (including ionisation and excitation processes). In elastic interactions a particle experiences a change of its trajectory angle and energy change (rest mass and kinetic energies) of the particle and the atomic number of the medium). Charged particles undergo a large number of interactions when travelling through a medium which makes their tracking very computationally expensive. The method of particle transport in MC simulations is called

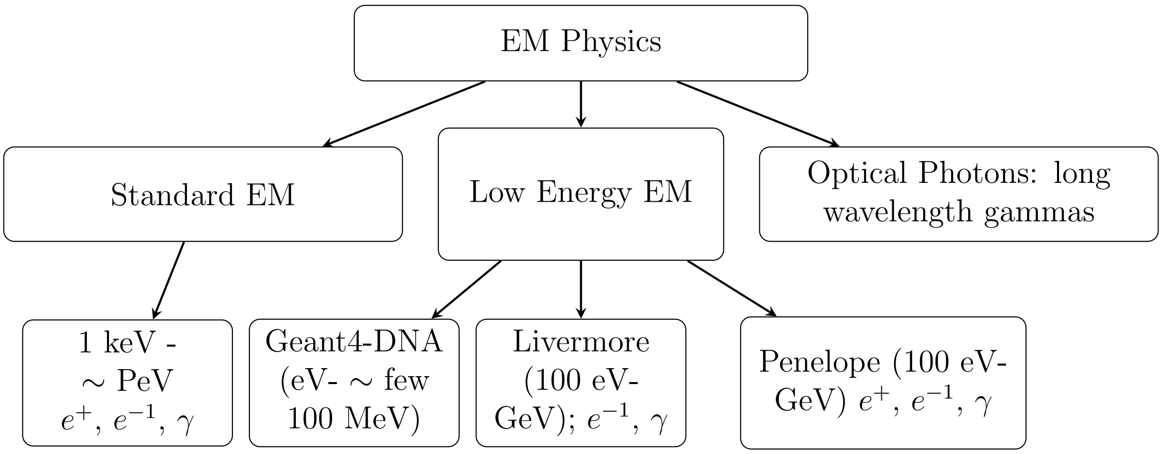

FIGURE 4.5: The energy ranges of different electromagnetic physics provided by Geant4 (Collaboration, 2012).

condensed history transport in which the changes in the trajectory angles are condensed into a single deflection angle, on the grounds that they are small and negligible.

Geant4 physics processes are categorized into three main classes: Electromagnetic (EM), Hadronic and Decay & Parametrized. No application requires all physics processes that Geant4 provides and depending on the requirements of a G4 application, the user should define appropriate physics and particles (Collaboration, 2012). Understanding of the physics involved in an application is of essential importance in determination of a suitable physics list, due to the fact that physics list should be sufficiently comprehensive to ensure the precision of calculation while maintaining the computation time in practical range.

Electromagnetic processes are classified into three classes, which are shown in the diagram in figure 4.5. The rationale for developing low energy EM processes is to extend the coverage of EM physics list down to very low energies (eV) by introducing more detailed atomic shell structures.

Three different methods are provided by Geant4 to set up a physics list for an application: 1) reference or pre-packaged physics lists which include various choices of EM and hadronic physics that are instantiated directly in the main source file; 2) set up a *G4VUserPhysicsList* in the application in which all processes, to be used, are defined and associated with their respective particles. All particles which are used in the application as well as physics modules (e.g. EM, hadronic and etc.) should be constructed. The drawback of such a list is that it can become too lengthy and complicated; and 3) implement a *G4VModularPhysList*, which contains desired combinations of selected particles and related processes, hence it is a more convenient way to define the physics. A large selection of modular physics lists is available in the Geant4 toolkit that have been verified against experimental data. These physics lists can simply be called by the user's application saving a significant amount of time and ambiguity.

The production threshold for secondary particles is a known concept in MC simulation. Due to Central Processing Unit (CPU) computation time limitation, the particles cannot be tracked down to zero energy through discrete energy loss because some processes (e.g. infrared divergence) increase CPU time enormously. In order to avoid this problem, in every Geant4 application a threshold is defined below which no secondaries are produced (i.e. discrete energy loss stops when the energy of particle becomes smaller or equal to threshold) and then the particle is tracked down to zero using continuous energy loss formalism. This threshold should be sufficiently low to satisfy the precision required in the application but not so low that it increases the CPU time unnecessarily. Another problem which arises here is that this threshold is particle and material dependent and thus thresholds should be defined for each single particle and be adjusted for every material the particle traverses through. The Geant4 solution to this issue is to define the threshold as a distance, called cut-off range, which is internally converted to energy for each particle type and material.

4.2 Materials and Methods

Geant4 MC toolkit was used to develop a 6 MV x-ray beam model in this work. The GPS was used as the primary radiation particle generator to describe primary particles properties (e.g. start position, initial energy and distance from the phantom). The reason is that the GPS system provides greater customisation in terms of defining particle properties such as energy spectra, angular distribution and so forth. The beam energy spectrum was obtained from the $Pinnacle3^{TM}$ treatment planning system v.9.0 (Philips Medical System, Milpitas, CA) for a 6 MV x-ray beam from a Varian Clinac iX linear accelerator. The realistic energy spectrum of the beam, shown in figure 4.6, was simulated

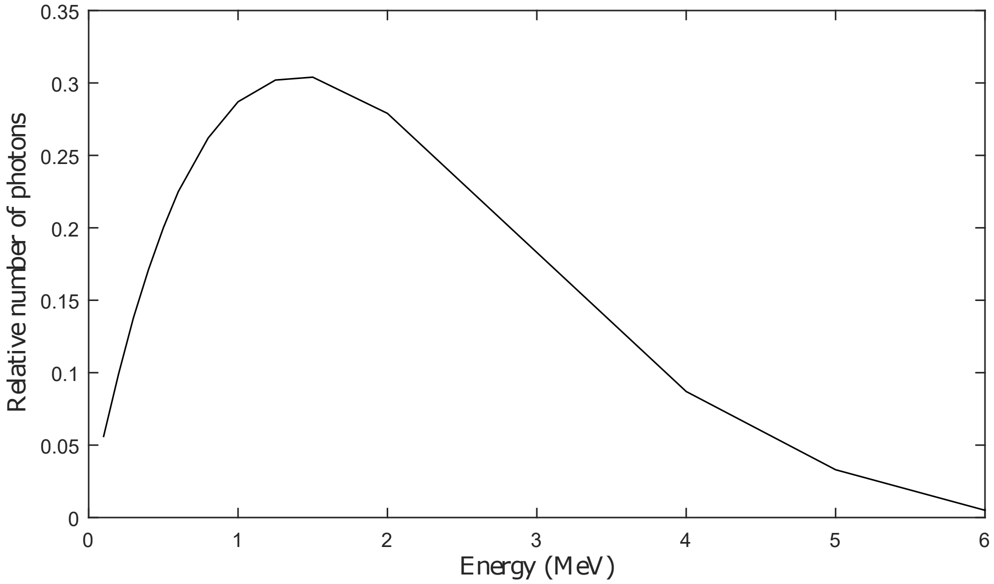

FIGURE 4.6: Photon energy distribution of a 6 MV beam, obtained from the *Pinnacle*^{3TM} treatment planning system v.9.0 (Philips Medical System, Milpitas, CA) produced by Varian Clinac iX linear accelerator (Varian® Medical System, Palo Alto, CA).

in the form of a histogram with linear interpolation. The beam was defined as a point source where the diameter of the beam was adjusted by setting the minimum and the maximum values for Theta and Phi angles (i.e. spherical coordinates), resulting in a circular conical beam. A 5 cm diameter conical beam, with 100 cm Source to Surface Distance (SSD) and isotropic angular distributions was modelled, see figure 4.7. Cartesian coordinates were used with z as the beam direction, and x and y as the lateral directions. The linac head components were not simulated in the present work.

At this stage of simulation, the detector was defined in such a way to represent the reference conditions set-up, as defined by TRS-398 (Andreo et al., 2000) for dose determination in a water phantom irradiated by megavoltage x-ray beams from a Varian Clinac iX, so that the verification of the beam model was possible. The detector was a $20 \times 20 \times 20$ cm^3 water phantom located at the centre of the world volume, made of air and encompassing the entire geometry of $110 \times 110 \times 110$ cm^3. The phantom was irradiated with a 6 MV x-ray beam described above.

In this simulation the sensitive detector method was implemented for scoring the total

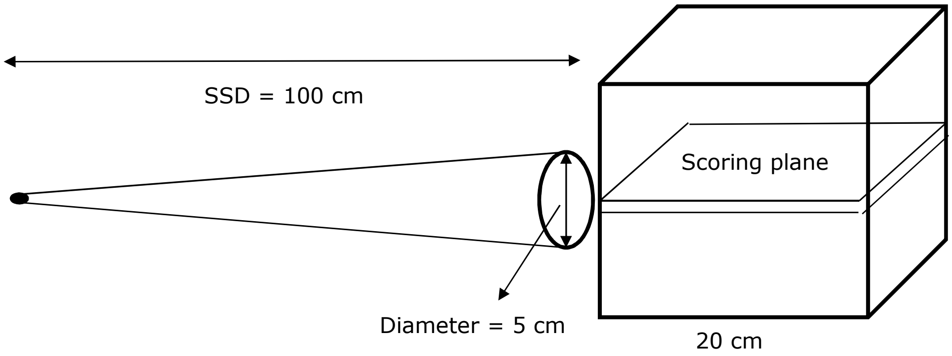

Figure 4.7: A schematic diagram showing the simulation set-up: a conical spectrum of 6 MV x-ray beam, at 100 SSD, fired into a 20 × 20 × 20 cm^3 water phantom and the middle scoring slice 20 × 20 × 0.1 cm^3 along the beam axis.

absorbed dose. The central x-z plane of the water phantom with 1 mm thickness was divided into 1 mm^3 voxels, representing sensitive volume for scoring purposes. As a result, an array of 200 × 200 voxels of the calculated absorbed dose was obtained.

The modular physics list method was implemented using Penelope low energy electromagnetic physics model, capable of simulating hard collisions in which secondary particles are generated down to 250 eV (Cirrone et al., 2010). The convention for the cut-off range value is from one tenth to one half of the smallest detector size (i.e. voxel). For this particular simulation, where the CPU time was not an issue, the cut-off value and step size were set to one tenth of the voxel size (i.e. 0.1 mm). Parallel simulation using Geant4 code v. 4.9.5.p02 on an 8-CPU 64 bit Linux computer cluster was performed for a total of 4×10^8 particles. Finally, the dose distribution at the central plane along the beam direction was obtained. It should be noted that to achieve a typical therapeutic dose (i.e. $\sim$ 2 Gy), a simulation should run for days to weeks depending on user-defined precision defined in the code. One may therefore consider terminating the simulation after reasonable statistics has been acquired, and the distribution can be either scaled up or added up to the required dose using various algorithms to minimize the noise amplification.

The accuracy of MC simulations and beam models need to be validated with respect to experimental data. In this work, the Geant4 calculated dose distribution was exported to MATLAB® for data analysis and several beam characteristics, including percentage depth dose (PDD) curves and off-axis profiles, were obtained. The array was normalized to the maximum dose to obtain PDD curves which correlates the doses at various depths within a phantom. In order to verify the validity of the beam model, the calculated PDD for a 5 cm diameter x-ray beam was compared with corresponding PDD data, obtained from commissioning data acquired in a water phantom using ionization chamber CC13, 6 MV x-ray produced by Varian Clinac iX, Royal Adelaide Hospital. The agreement between calculated and measured PDDs was assessed.

For qualitative verifications, separate simulations were run for different beam sizes, namely, 2, 10, and 20 cm diameters, to confirm the accuracy of the scattered dose calculation. To further examine the accuracy of the model's dose calculation, the Geant4 simulation was performed for four beam energies (300 keV, 2 MeV, 6 MeV, and 6 MV), as well as various materials including cortical bone ($\rho = 1.92$ g/cm^3), skeleton ($\rho = 1.486$ g/cm^3), and lung ($\rho = 0.2$ g/cm^3). Simulations were performed for each scenario and resulting PDDs were qualitatively compared with expected physical behaviours. The skeleton material was defined by adding its respective elements using the *G4Element* to a *G4Material* object. The cortical bone and lung materials were specified using NIST database, where for lung the density of the corresponding NIST compound (i.e. $\rho = 1.05$ g/cm^3) was overwritten to $\rho = 0.2$ g/cm^3.

4.2.1 Diverging Photon Beam in a Heterogeneous Phantom

As a proof of principle, the dose distributions in inhomogeneous media were investigated to study the dose at various interfaces. In this part of simulation, the detector was designed as a three-layer geometry using parametrized volume method. The three-layer geometry was designed as $4 \times 20 \times 20$ cm^3 of bone or lung enclosed by $8 \times 20 \times 20$ cm^3 tissue on both sides. In this case, the code incorporated an object of *ROGeom* class and its associated dummy sensitive detector class along with the real geometry and its associated sensitive detector class. The central plane along the z axis in the water phantom of the virtual geometry was divided into 1 mm^3 voxels. The parallel and tracking geometries were designed to communicate with virtual/RO geometry through passing the pointer of the tracking (i.e. real) geometry to the sensitive detector and then interfacing the sensitive detector class to the RO geometry, see Figure 4.8.

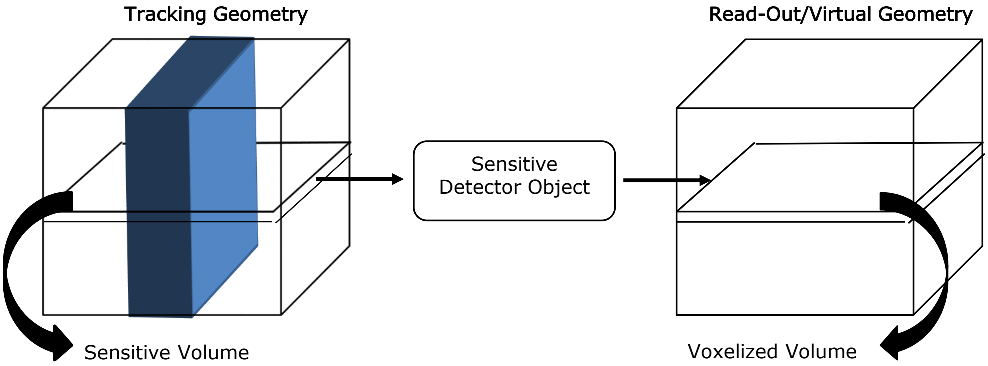

FIGURE 4.8: The simulated geometry for interface investigation. In the real geometry on the left the material was parametrized into a slab of cortical bone/skeleton/lung (blue) enclosed water on both sides.

Parallel simulation using Geant4 code v. 4.9.5.p02 on an 8-CPU 64 bit Linux computer cluster was performed for the total of 4×10^8 particles. As a result, the dose distributions for the lung and bone interfaces were investigated: water-bone-water and water-lung-water and the resulting PDDs were compared with PDDs obtained for homogeneous water phantom and the differences were explained.

4.3 Results and Discussion

Figure 4.9 shows a visualization of the simulated detector, rendered using Geant4, with scoring plane located mid-plane along the beam axis.

The 3D and 2D views of the calculated dose distribution for a diverging 6 MV x-ray beam of 5 cm diameter are shown in figure 4.10(a) and figure 4.10(b), respectively. The divergence of the beam is apparent in figure 4.10(b).

With respect to quantitative beam model verification, the Geant4 calculated PDDs for 2, 5, 10, and 20 cm diameter beams agreed with measured PDDs with an average difference of $0.96 \pm 0.4\%$ (beyond build-up region). The agreement was considered reasonable and comparable with that achieved by other MC studies. For example, the Geant4 calculated dose distribution was within 1% averaged difference from measured data (with an ionization chamber (CC13, Scanditronix–wellhofer) in the study of Okamoto *et al.* (Okamoto

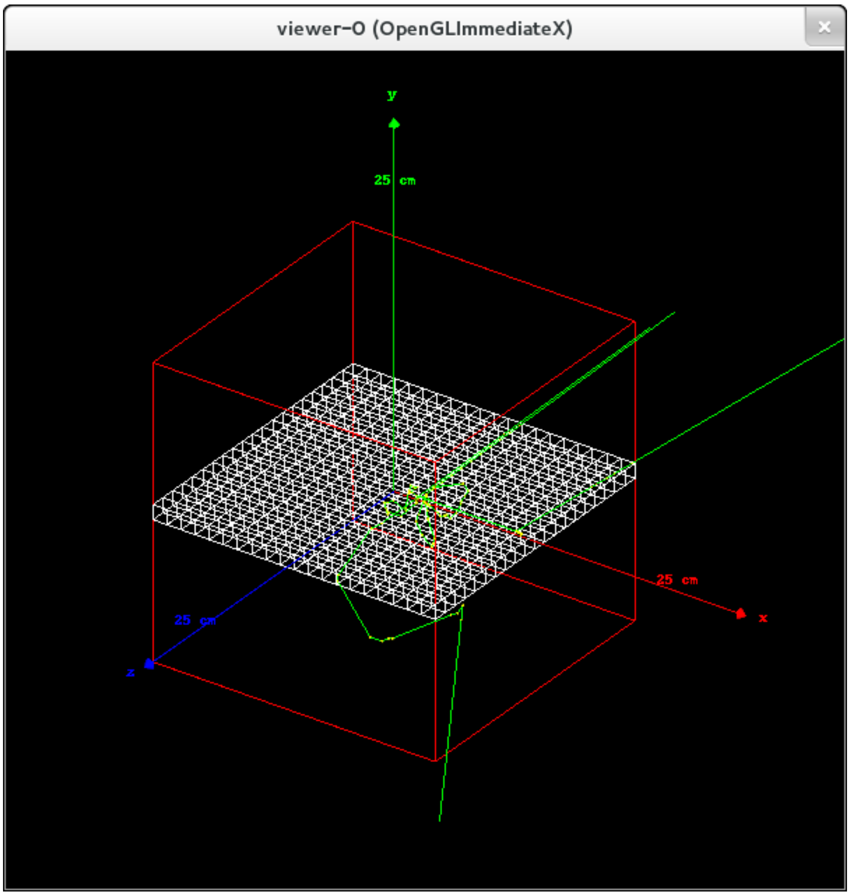

FIGURE 4.9: Illustration of the detector geometry from a 45° angle; the water phantom and the sensitive detector are shown in red and white, respectively. Photons tracks are shown in green and only one photon, fired along +z axis is visualized.

et al., 2011), where linac head components were also taken into account. Figure 4.11 (a) and (b) shows the comparison of the PDDs calculated in this simulation for 5 and 10 cm diameter beams with measured data. It should be noted that, the measured data were obtained for square fields, whereas simulation results were calculated for circular fields. Although this influences profiles, it does not affect PDDs significantly. Additionally, underestimation of calculated dose in the build-up region is due to the fact that the linac head components, which contribute to scatter dose in this region, have not been considered in this model. Nevertheless, as far as the purpose of this project is concerned, this issue does not have an adverse effect on the accuracy of the work in this thesis, since only the dose deposition beyond the build-up region has been used.

The qualitative verifications of the beam model included off-axis profiles, PDDs for various beam energies and phantom materials. The simulated data reproduced the trends

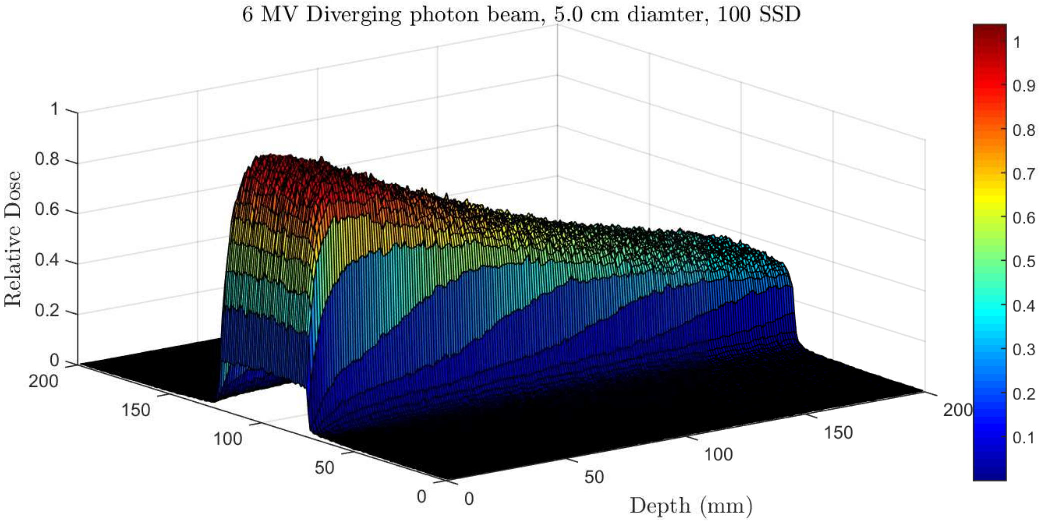

(a)

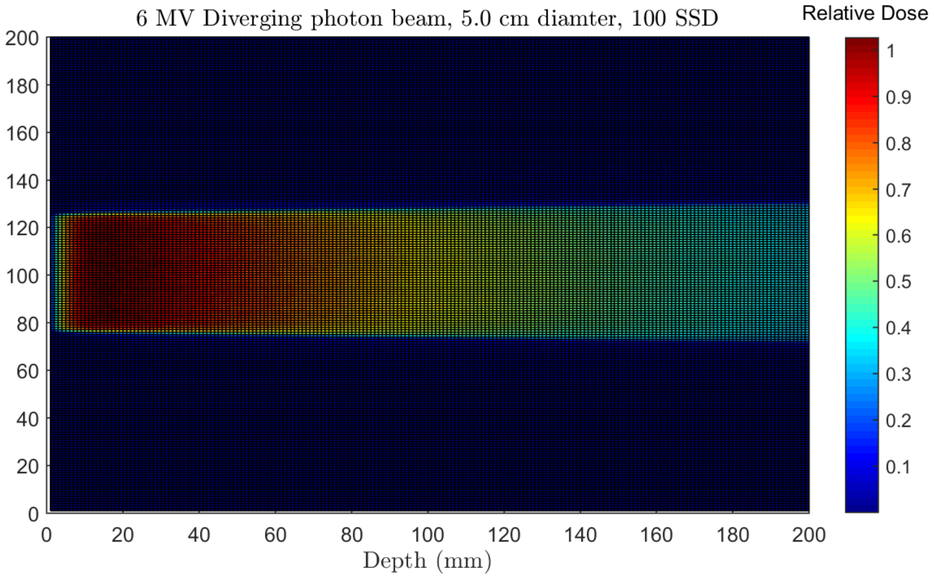

(b)

FIGURE 4.10: Calculated dose profile in mid-plane for conical/diverging 6 MV x-ray beam of 5 cm diameter at 100 cm SSD; a) 3D view; b) 2D Lateral view. The statistical uncertainty in the calculated results was on average ±0.8%.

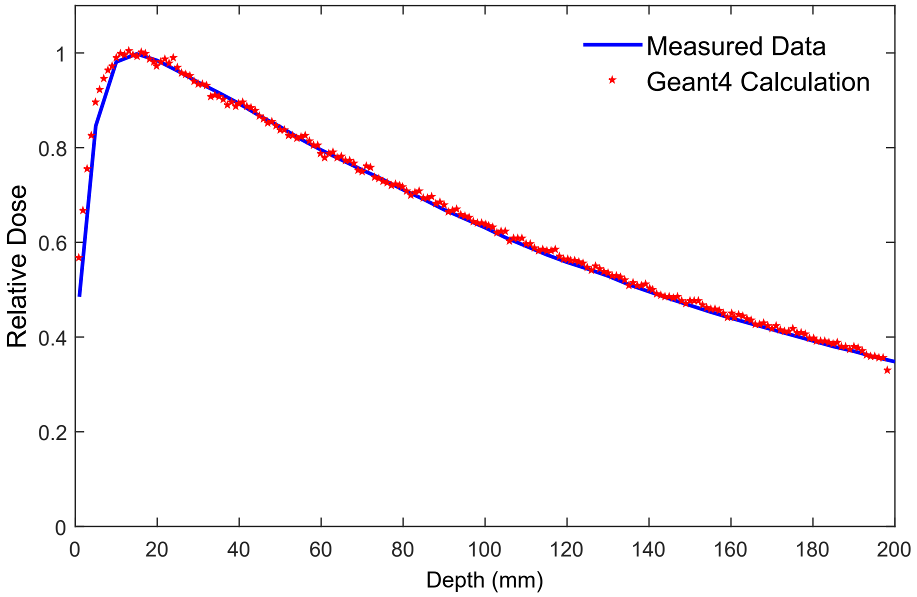

(a)

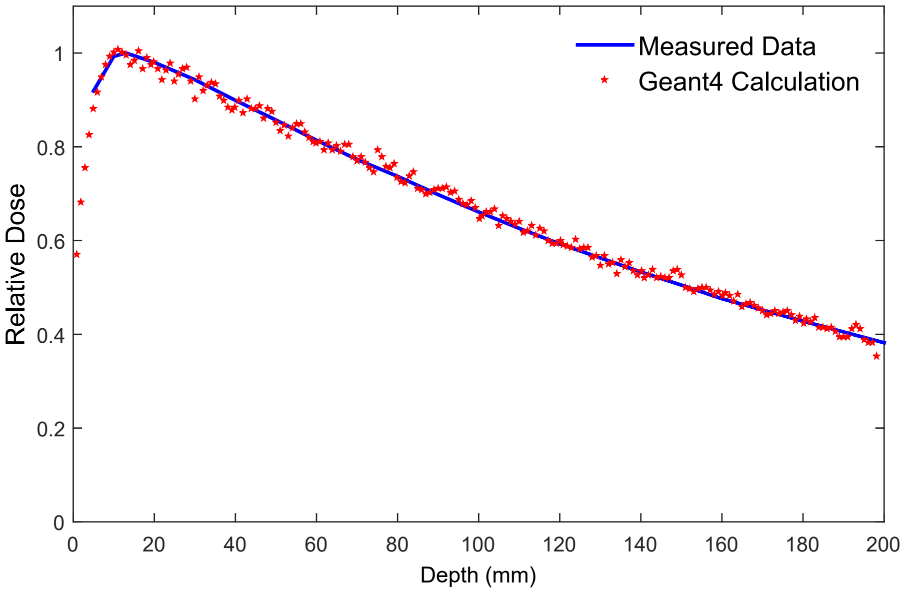

(b)

FIGURE 4.11: Comparison between calculated and measured (i.e. commissioning data acquired in a water phantom using CC13 ionization chamber for 6 MV x-ray beam from a Varian Clinac iX accelerator, Royal Adelaide Hospital) and calculated percentage depth dose (PDD) data for: a) a 5 cm diameter; and b) a 10 cm diameter fields for a simulated 6 MV x-ray beam. The statistical errors for a simulated 6 MV x-ray beam were ±0.8% and ±2.1% respectively.

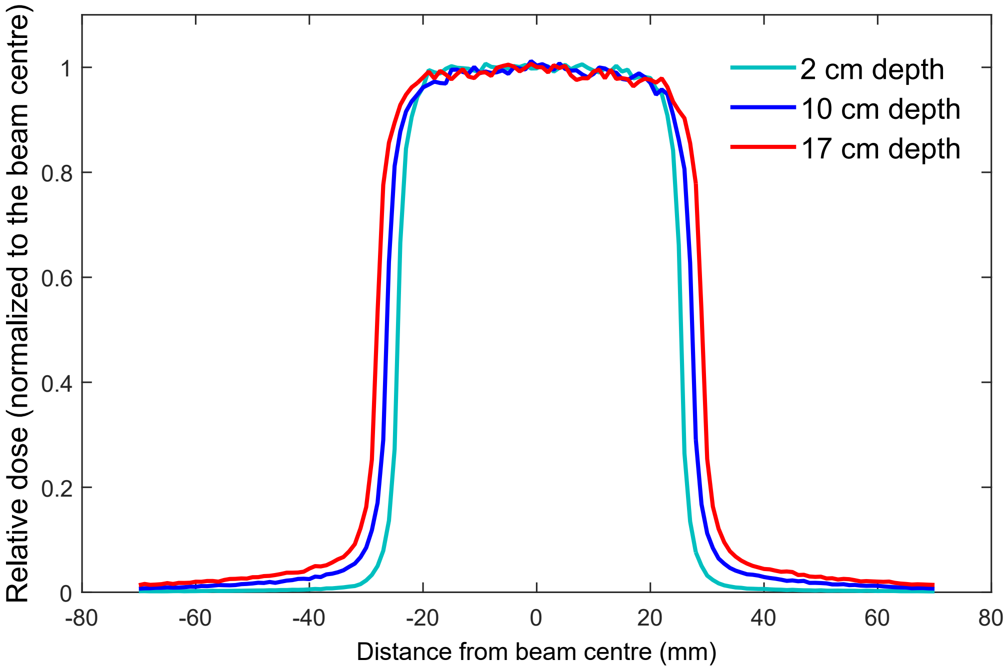

FIGURE 4.12: Calculated off-axis profiles of a 6 MV diverging x-ray beam of 5 cm diameter at 2, 10, and 17 cm depths from the water phantom surface.

observed in experimental data. The calculated off-axis profiles of the same diameter beam at three different depths from the phantom surface and normalized to the beam central axis at 2 cm depth are shown in figure 4.12. The model predicts the widening of the penumbra at larger depths in the phantom (the trend is attributed to increased off-axis scatter at larger depths), is in accordance with the trend observed in experimental measurements (Cheung et al., 2006).

Figure 4.13 shows agreement between simulation results and experimental data from a Varian Clinac iX linear accelerator for a 6 MV x-ray beam, for PDD verification as a function of beam size. As demonstrated for the same beam energy, the dose at a depth below the surface increases as the field size is increased which is due to the fact that while the dose from primary radiation remains the same for the same beam energy, the lateral scatter radiation contributing to the dose on the central axis (CAX) increases as the field size is increased. The increase in PDD is greater at larger depths as a result the increased scatter.

Calculated PDDs for four different beam energies, 2 MeV, 6 MeV, 300 keV and 6 MV, with 5 cm diameter beam at 100 cm SSD are compared in figure 4.14. As expected

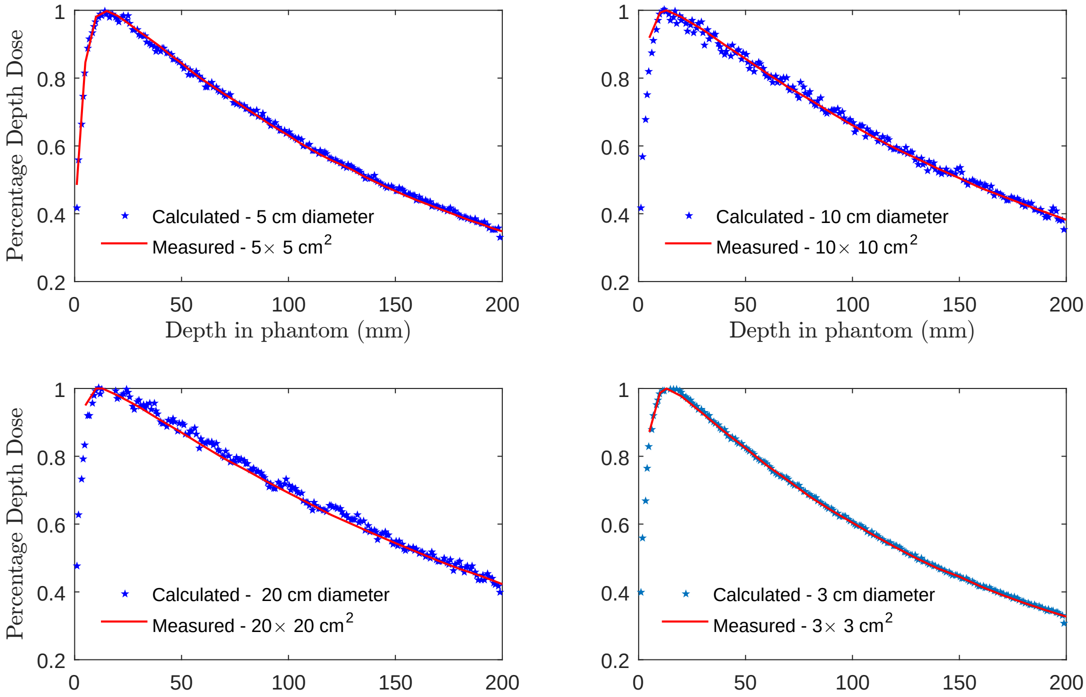

FIGURE 4.13: Geant4 calculated and measured (from a Varian Clinac iX linear accelerator) PDD curves of a 6 MV diverging x-ray beam for different field sizes. The relative error in calculated data ranged from 0.6% for 3.0 cm radius beam to 4% for 20 cm radius beam.

from experimental observations, x-ray beam PDDs increase with increasing energy. The depths of maximum dose were found to be approximately 1 mm, 11 mm, 15 mm, and 30 mm for 300 keV, 2 MeV, 6 MV and 6 MeV, respectively. These findings compare well with typical depths of maximum dose being 0 mm and 15 mm for 300 keV and 6 MV, respectively, as reported by Podgorsak (Podgorsak, 2005), and about 28 mm for 6 MeV x-ray beam as reported by Purdy *et al.* (Purdy et al., 2012). A complete quantitative verification cannot be made as the position of the depth of maximum dose is not only the function of the beam energy, but also depends on the design of the treatment head of a specific machine and the field size. The shift in the depth of maximum dose for the same energy on different machines results mostly from electron scattering through collimator and scattering filters.

A comparison of percentage depth dose profiles in various media including water, cortical

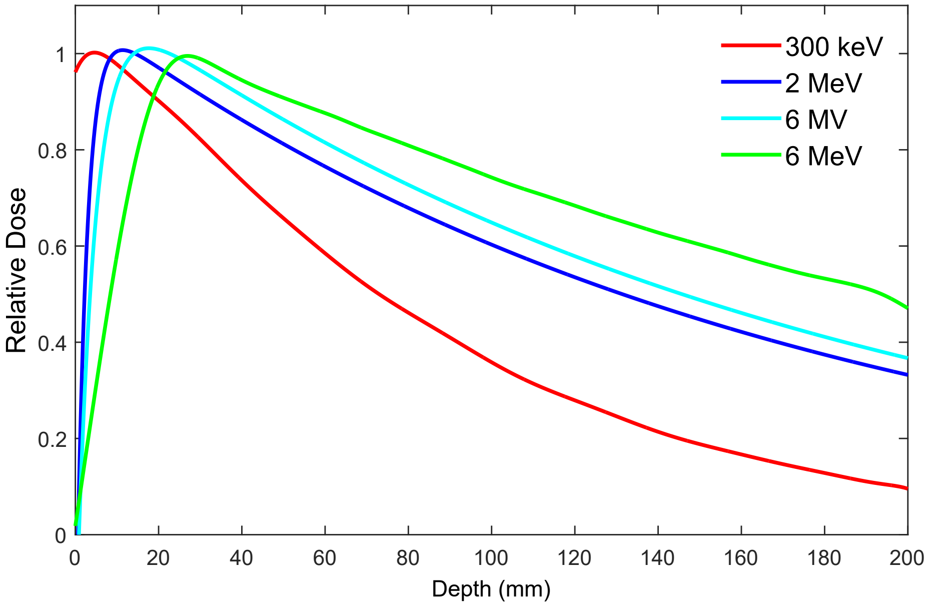

Figure 4.14: Geant4-calculated PDD curves of diverging x-ray beam with four different energies, 5 cm diameter, 100 cm SSD .

bone, skeleton and lung is presented in figure 4.15. The statistical uncertainties in the calculated results were ±0.8%, ±0.5%, ±0.5% and ±4.8% for water, cortical bone, skeleton and lung, respectively. As shown in figure 4.15, as the density of the absorber increases, the dose decreases as a function of depth for the same beam energy. This observation implies that the beam attenuation is higher in materials with higher densities. This trend is as expected, as the attenuation coefficient is proportional to density. Therefore, the Geant4 beam model results have qualitatively met the expected physical behaviour with respect to the depth dose deposition behaviour in materials with different densities.

The resulting PDDs of a 6 MV x-ray beam for water-bone-water phantom and in a water phantom only, are plotted in figure 4.16. The predominant interaction in this photon energy range is Compton scattering where the cross sections are approximately independent of absorber's atomic number, therefore, there is no increase in dose in bone material as compared to water. Also, beyond the water-bone interface, the depth dose is lower due to the fact that the attenuation of x-ray beam is higher in materials with higher densities (i.e. higher attenuation in bone as compared to water) and thus the PDD curve for a water-bone-water phantom falls below the curve for a water phantom from the first interface. As shown, immediately before the water-bone interface there is a cold

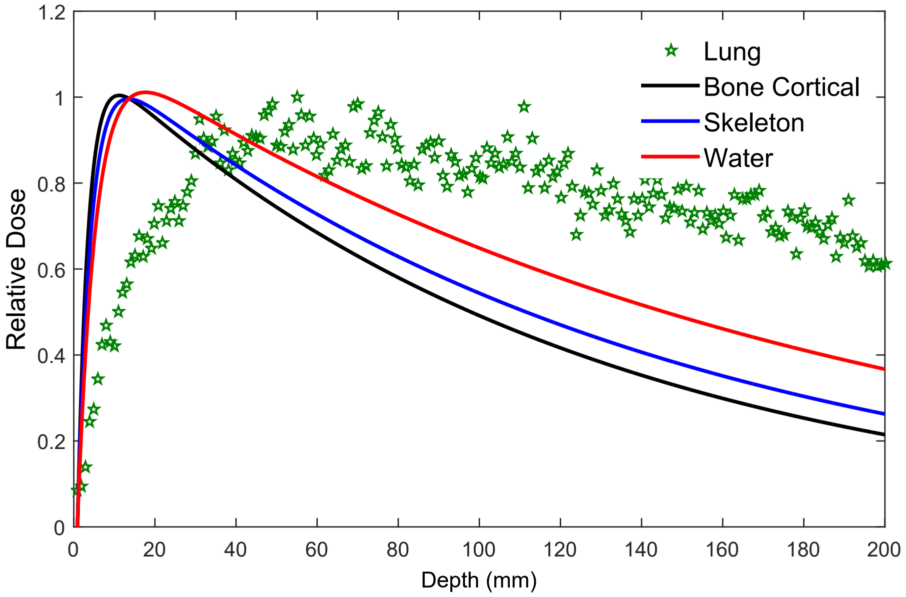

Figure 4.15: PDD curves diverging 6 MV x-ray beam of 5 cm diameter in various media.

spot, followed by a hot spot (in the first voxel in bone). This is as a result of the shorter range of secondary electrons in bone compared to water. The backscattered electrons produced in bone, immediately beyond the interface, deposit their energies in bone and do not reach the water before the interface. As a result, the dose in water adjacent to the bone interface becomes significantly less as it lacks the contribution of backscattered electrons. Consequently the dose in bone at the interface has a peak since it includes the dose deposition of those backscattered electrons. In conclusion, while there is noise in the calculated results for the PDD curve of the beam model for a water-bone-water phantom qualitatively reflects the expected behaviour of such a x-ray beam at these interfaces. The trend of dose deposition obtained from this simulation matches with the outcome of other MC calculations for PDDs of 6 MV x-ray in heterogeneous slab phantoms (Carrasco et al., 2007, Han et al., 2011).

Figure 4.17 illustrates the comparison between PDD curves of 6 MV x-ray beam obtained for a water-lung-water phantom and a water phantom. As mentioned above, the Compton scattering is the predominant interaction at this x-ray energy and thus no significant decrease in dose in lung tissue is expected. As shown in Figure 4.17, this expectation is met and the dose is slightly less in lung tissue as compared to water. However, the

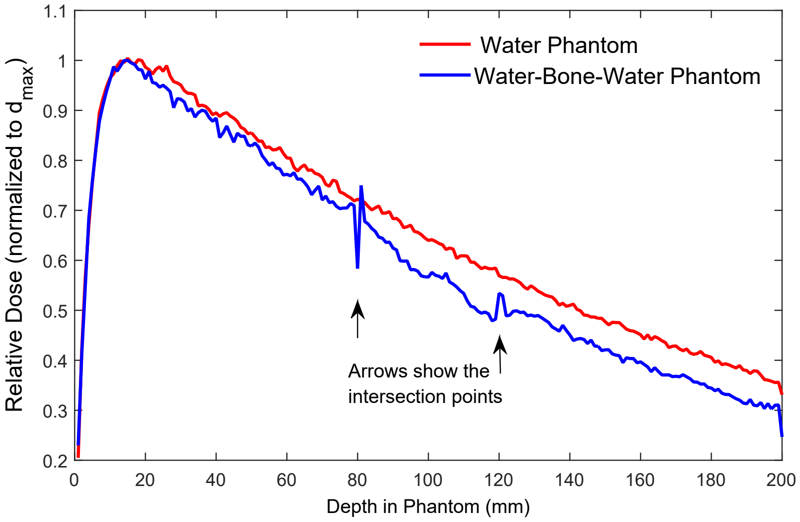

FIGURE 4.16: The comparison of Geant4-calculated PDD curves from 6 MV diverging x-ray beam, 100 cm SSD in a water phantom with that in a water-bone-water phantom. The locations of interfaces are shown with arrows. The statistical uncertainty of the calculated results was on average ±0.7%.

depth dose is higher after the second interface (i.e. lung-water) which is attributed to the lower attenuation of the x-ray beam in materials with lower densities (i.e. lesser photon attenuation in lung than water). At interfaces, the situation is quite different to the water-bone-water phantom; however, the reason behind the peaks is still the difference in the range of electrons in different materials with different densities. The backscattered electrons produced in lung after the water-lung interface deposit their energy in water as they can travel longer distances in lung and reach the water (i.e. the range of electrons in lung is much longer than that in water) giving rise to a sharp peak in dose in the water adjacent to the interface. At the lung-water interface, the situation is similar to water-bone interface. The backscattered electrons in water deposit their energy in water before reaching the lung, resulting in a cold spot in lung and a hot spot in water adjacent to the interface. In conclusion, the qualitative agreement of the simulation results with expected physical behaviour as well as with other MC calculations for similar conditions (Carrasco et al., 2007, Han et al., 2011) is a further verification of the beam model developed in this work.

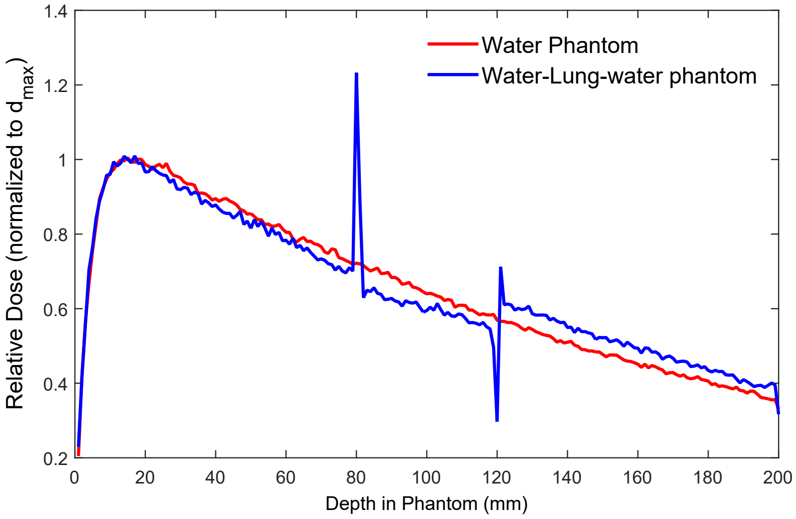

FIGURE 4.17: The comparison of PDD curves of a 6 MV diverging x-ray beam, 100 cm SSD in a water phantom with that of water-bone-water phantom. Interface locations are at 80 and 120 mm. The statistical uncertainty of the calculated results was on average ±1.0%.

4.4 Conclusion

A Geant4 beam model was developed for a 6 MV diverging x-ray beam from a Varian Clinac iX linear accelerator to be used as the source of radiation in subsequent chapters of the thesis. Comprehensive verification of the beam model was performed to assure the precision of the dosimetry/microdosimetry results and consequently the validity of the conclusions drawn in this project. The beam model quantitatively (i.e. within $0.96\pm0.4\%$ for PDDs obtained for different beam sizes) and qualitatively agreed with measured data and expected physical behaviours.

Chapter 5

Evaluation of current clinical target volume definitions for glioblastoma using cell-based dosimetry stochastic methods

The publication [P3] forms the basis of this chapter.

Moghaddasi, L., E. Bezak, and W. Harris-Phillips, Evaluation of current clinical target volume definitions for Glioblastoma using cell-based dosimetry stochastic methods. *Br J Radiol* 2015; 88: 20150155.

5.1 Introduction and motivation

In this chapter the development of an integrated Glioblastoma (GBM) treatment model to evaluate current Clinical Target Volume (CTV) definitions in terms of cell kill efficacy will be described. This is to address an important clinical issue related to GBM which grows in an infiltrative pattern rather than forming a solid tumour mass, causing the CTV margin definition to be especially problematic. The development of the code consists of the following stages:

- Development of a beam model for a 6 MV x-ray beam produced by Varian iX linear accelerator (Varian® Medical System, Palo Alto, CA) as described in chapter 4.
- Development of a microscopic-scale GBM model simulating the GBM tumour and its subclinical infiltration with homogeneous population of cells uniform radiosensitivity and normal oxygenation.
- Development of a Survival Fraction (SF) algorithm to translate the physical dose delivered to individual cells to biological endpoint, which in this work is the probability that cell will survive the radiation damage.

5.2 Statement of Contribution

5.2.1 Conception

The initial idea of the architecture of the integrated Monte Carlo model was first conceptualised by Eva Bezak. The method to design individual components of the model was conceptualised by Leyla Moghaddasi and Eva Bezak.

5.2.2 Realisation

The integrated MC model was fully developed by Leyla Moghaddasi. General supervision and guidance was provided by Eva Bezak. The manuscript was evaluated by Eva Bezak in terms of accuracy and interpretation of calculated results, conclusions reached, and general structure and flow.

5.2.3 Documentation

This paper was primarily written by Leyla Moghaddasi. Editing was performed by all authors.

Statement of Authorship

Title of Paper	Evaluation of current clinical target volume definitions for glioblastoma using cell-based dosimetry stochastic methods
Publication Status	☑ Published ☐ Accepted for Publication ☐ Submitted for Publication ☐ Publication Style
Publication Details	Moghaddasi, L., E. Bezak, and W. Harris-Phillips, *Br J Radiol, 2015; 88: 20150155*

Principal Author

Name of Principal Author (Candidate)	Leyla Moghaddasi		
Contribution to the Paper	Developed the model, analysed the results of calculations, and wrote the manuscript and acted as corresponding author.		
Overall percentage (%)	80%		
Signature		Date	24/06/2016

Co-Author Contributions

By signing the Statement of Authorship, each author certifies that:

i. the candidate's stated contribution to the publication is accurate (as detailed above);

ii. permission is granted for the candidate in include the publication in the thesis; and

iii. the sum of all co-author contributions is equal to 100% less the candidate's stated contribution.

Name of Co-Author	Prof. Eva Bezak		
Contribution to the Paper	Initial idea, general guidance and supervision, and manuscript revision.		
Overall percentage (%)	15%		
Signature		Date	24/06/2016

Name of Co-Author	Dr. Wendy Harris-Phillips		
Contribution to the Paper	Manuscript revision and editing.		
Overall percentage (%)	5%		
Signature		Date	24/06/2016

Moghaddasi, L., Bezak, E. & Harriss-Phillips, W. (2015). Evaluation of current clinical target volume definitions for glioblastoma using cell-based dosimetry stochastic methods.
British Journal of Radiology, *88*(1053), 1-14

5.3 Conclusion

An innovative approach was taken in this work to establish a cellular-scale modelling framework for GBM treatment using a 6 MV x-ray beam. The GBM treatment outcome was evaluated in terms of cellular Survival Fraction (SF). Figure 5.1 shows schematically the simulated treatment modelling set-up including the tumour structure irradiated by two opposing x-ray beams.

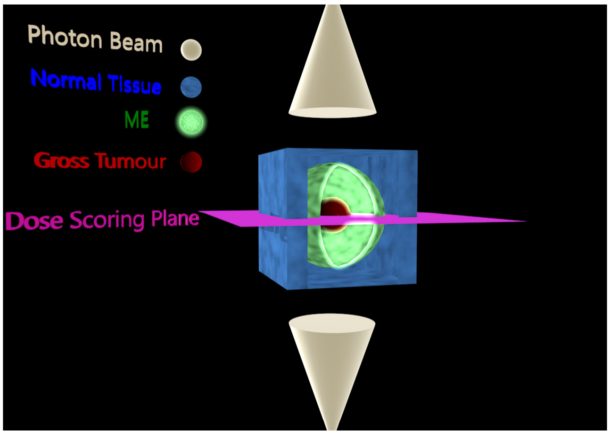

FIGURE 5.1: Schematic diagram showing the simulated treatment set-up. The GTV (red) is enclosed by a microscopic extension, shown in fuzzy green to represent the uncertainty, embedded in normal tissue (blue). The system is irradiated by two opposing circular 6 MV x-ray beams.

Two main novelties of the model are:

1. The code provides a useful quantitative tool for evaluation of CTV margins for different infiltration patterns which can provide guidance for clinicians in their decision on selection of an optimal CTV margin.
2. The flexible cellular platform established allows for incorporation of other biological characteristics of a tumour that affect cellular radiosensitivity. The code can also be used to model other treatment modalities and regimens.

It was concluded that while x-ray therapy remains ineffective for GBM patients, a 0.5 cm CTV margin increase (from 2.0 to 2.5 cm) may be beneficial to extend time to recurrence for patients with GBM. This was based on simulation results showing a reduction of SF by approximately four times when the CTV margin was extended for a GBM consisting of cells expressing mutant p53 tumour suppressor gene (i.e. correlated to increased radioresistance as compared to wild type p53). We acknowledge that this study has utilized a simplified model of GBM (i.e. homogeneous radiosensitivity and normal oxygenation) and the conclusions drawn should be interpreted with care. The next chapter will describe the expansion of this model to incorporate genetic heterogeneity and hypoxia in the GBM treatment modelling framework.

Chapter 6

Monte Carlo model development for evaluation of current clinical target volume definition for heterogeneous and hypoxic glioblastoma

The publication [P4] forms the basis of this chapter.

Moghaddasi, L., E. Bezak, and W. Harris-Phillips, Monte Carlo model development for evaluation of current clinical target volume definition for heterogeneous and hypoxic glioblastoma. *Phys. Med. Biol.* 61 (2016) 3407–3426.

6.1 Introduction and motivation

In this chapter the expansion of the code developed in chapter 5 is described. The GBM model is further developed to incorporate biological parameters that affect cellular radiosensitivity, including genetic heterogeneity (in terms of varying α & β values) and cellular oxygenation. As a result, the code developed represents a more realistic model of GBM which often presents clinically with extensive hypoxia, genetic heterogeneities and complexities.

Similar to chapter 5, the tumour cell survival fraction following x-ray therapy will be investigated in regions of interest for the semi-realistic GBM model for various infiltration distributions and application of two CTV margin extensions (2.0 and 2.5 cm).

6.2 Statement of Contribution

6.2.1 Conception

The initial idea of designing a cell-based Monte Carlo model platform to enable further expansion of the model, such as cellular oxygenation and heterogeneous radiosensitivity which is the subject of the work presented in this chapter, was first conceptualised by Leyla Moghaddasi. The method to incorporate these cellular parameters into the MC model was conceptualised by Leyla Moghaddasi, and Eva Bezak.

6.2.2 Realisation

The literature review to identify model parameters and expansion of the code to incorporate these parameters was conducted by Leyla Moghaddasi. General supervision and guidance was provided by Eva Bezak. The manuscript was evaluated by Eva Bezak in terms of accuracy and interpretation of calculated results, conclusions reached, and general structure and flow.

6.2.3 Documentation

This paper was primarily written by Leyla Moghaddasi. Editing was performed by all authors.

Statement of Authorship

Title of Paper	**Monte-Carlo model development for evaluation of current clinical target volume definition for heterogeneous and hypoxic glioblastoma**
Publication Status	☑ Published ☐ Accepted for Publication ☐ Submitted for Publication ☐ Publication Style
Publication Details	Moghaddasi, L., E. Bezak, and W. Harris-Phillips, *Phys. Med. Biol.* **61** (2016) 3407–3426

Principal Author

Name of Principal Author (Candidate)	Leyla Moghaddasi		
Contribution to the Paper	Developed the model, analysed the results of calculations, and wrote the manuscript and acted as corresponding author.		
Overall percentage (%)	80%		
Signature		Date	24/06/2016

Co-Author Contributions

By signing the Statement of Authorship, each author certifies that:

i. the candidate's stated contribution to the publication is accurate (as detailed above);
ii. permission is granted for the candidate in include the publication in the thesis; and
iii. the sum of all co-author contributions is equal to 100% less the candidate's stated contribution.

Name of Co-Author	Prof. Eva Bezak		
Contribution to the Paper	Initial idea, general guidance and supervision, and manuscript revision.		
Overall percentage (%)	15%		
Signature		Date	24/06/2016

Name of Co-Author	Dr. Wendy Harris-Phillips		
Contribution to the Paper	Manuscript revision and editing.		
Overall percentage (%)	5%		
Signature		Date	24/06/2016

Moghaddasi, L., Bezak, E. & Harriss-Phillips, W. (2016). Monte-Carlo model development for evaluation of current clinical target volume definition for heterogeneous and hypoxic glioblastoma.
Physics in Medicine and Biology, 61(9), 3407-3426.

6.3 Conclusion

The cellular modelling platform developed in chapter 5 allowed further refinement to a more realistic version of GBM treatment. The two main findings as suggested by the results are:

1. X-ray therapy for glioblastoma of the brain may only offer an extension of survival time rather than a cure, as x-ray therapy does not seem to result in severe enough radiobiological damage to GBM cells required to kill or sterilize them. This is due to extensive transient hypoxia, that is more severe in the original tumour bed (the GTV), and to large variations in intrinsic radioresistance of the GBM cells. The tumour may relapse within the beam area even before migrating cells have a chance to form a tumour mass in marginal regions.
2. The quantification tool for hypoxic and heterogeneous GBM enabled us to predict the reduction in SF as a result of the CTV margin extension by 0.5 cm. It was demonstrated that while the incorporation of genetic radiosensitivities and hypoxia complexities reduced the benefit of the CTV extension as compared to homogeneous-normoxic scenario, the choice of a larger CTV margin still may be beneficial to the extend time to recurrence for GBM patients. The extension of the CTV margin resulted in a SF reduction compared to 2.0 cm CTV margin, by approximately 3.5 - 4.5 times depending on the type of microscopic extension distribution (i.e. MEP model).

Considering that the GBM model at its current stage is fairly comprehensive, we are confident to draw conclusions based on simulation results. As outlined in item 1, the calculated SF showed a peak in the GTV region, despite the 10 Gy boost delivered to this region, indicating that x-ray EBRT is unable to overcome GBM cells using the current treatment protocols and tumour will relapse in the treatment area, and in the GTV in particular. As a result, other treatment modalities such as high LET targeted radiotherapy needs to investigated for use in GBM treatment.

Chapter 7

Development and verification of a Geant4 beam model for Boron Neutron Capture Therapy

The publication [P5] forms the basis of this chapter.

7.1 Introduction and motivation

As concluded in chapter 6, x-ray therapy using the current treatment protocols cannot induce sufficient radiobiological damage to glioblastoma cells to kill tumour cells and it will most likely relapse within the treatment region even prior to colony growth by cells that survived in the microscopic regions. Hence other treatment techniques needs be investigated. Boron Neutron Capture Therapy (BNCT) is a biochemically-targeted type of radiotherapy and is an alternative therapy for high grade gliomas (Barth et al., 2004, Van Dyk, 1999).

From this point the focus of this thesis will be on the use of an integrated GBM radiation treatment modelling framework to evaluate cell kill efficacy following BNCT treatment. In this chapter, development and verification of a computational model of an epithermal neutron beam for BNCT will be described. In addition, a sensitivity analysis will be performed to determine the optimal boron concentration and the optimal neutron energy spectrum to achieve an efficacious BNCT treatment.

7.2 Statement of Contribution

7.2.1 Conception

The initial idea of investigation of the efficacy of targeted therapies, and BNCT in particular, for the treatment/management of GBM was first conceptualised by Leyla Moghaddasi. The method to design a Geant4 MC code to simulate BNCT beam system was conceptualised by Leyla Moghaddasi.

7.2.2 Realisation

The literature review to identify model parameters and suitable reactor-produced BNCT spectrum was performed by Leyla Moghaddasi. The Geant4 code development to simulate the beam model and MATLAB code development for data analysis were undertaken by Leyla Moghaddasi. The model verification and sensitivity analyses were performed by Leyla Moghaddasi. General supervision and guidance, particularly in regards to physics of nuclear reactions and cross-sections involved, was provided by Eva Bezak. The manuscript was evaluated by Eva Bezak in terms of accuracy and interpretation of calculated results, conclusions reached, and general structure and flow.

7.2.3 Documentation

This paper was primarily written by Leyla Moghaddasi. Editing was performed by all authors.

Statement of Authorship

Title of Paper	**Development and verification of a Geant4 beam model for Boron Neutron Capture Therapy**
Publication Status	☐ Published ☐ Accepted for Publication ☑ Submitted for Publication ☐ Publication Style
Publication Details	Moghaddasi, L., E. Bezak, submitted to *Computational and Mathematical Methods in Medicine*

Principal Author

Name of Principal Author (Candidate)	Leyla Moghaddasi		
Contribution to the Paper	Developed the model, analysed the results of calculations, and wrote the manuscript and acted as corresponding author.		
Overall percentage (%)	80%		
Signature		Date	07/09/2016

Co-Author Contributions

By signing the Statement of Authorship, each author certifies that:

i. the candidate's stated contribution to the publication is accurate (as detailed above);

ii. permission is granted for the candidate in include the publication in the thesis; and

iii. the sum of all co-author contributions is equal to 100% less the candidate's stated contribution.

Name of Co-Author	Prof. Eva Bezak		
Contribution to the Paper	Initial idea, general guidance and supervision, and manuscript revision.		
Overall percentage (%)	20%		
Signature		Date	07/09/2016

Development and validation of a Geant4 beam model for Boron Neutron Capture Therapy

Leyla Moghaddasi[a,b,*], Eva Bezak[a,c,d]

[a]School of Physical Sciences, University of Adelaide, Adelaide, Australia
[b]Department of Medical Physics, Adelaide Radiotherapy Centre, Adelaide, Australia
[c]International Centre for Allied Health Evidence, University of South Australia, Adelaide, Australia
[d]Sansom Institute for Health Research, University of South Australia, Adelaide, Australia

Abstract

Aim. Boron Neutron Capture Therapy (BNCT) is a biochemically-targeted type of radiotherapy which selectively delivers localized dose to tumour cells diffused in normal tissue, while minimizing normal tissue toxicity. BNCT is based on thermal neutron capture by stable ^{10}B nuclei resulting in emission of a short-ranged alpha particle and a recoil ^{7}Li nuclei. The purpose of the current work was to develop and validate a Monte Carlo BNCT beam model.

Method. A neutron beam model was developed in Geant4 and validated against published data. The neutron beam spectrum was obtained from literature for a cyclotron-produced beam. The beam was fired at a water phantom with boron concentrations of 100 μg/g. The calculated percentage depth dose curves (PDDs) in the phantom were compared with published data to validate the beam model in terms of total and boron depth dose deposition. Subsequently, two sensitivity analyses were conducted to investigate the impact of: 1) neutron beam spectrum , and 2) various boron concentrations on the boron dose component

Results and Conclusion. Good agreement was achieved between the calculated and measured neutron beam PDDs (within 1%). The resulting boron depth dose deposition was also in agreement with measured data. The neutron beam spectrum sensitivity analysis confirmed that successful implementation of a BNCT treatment cannot be achieved unless low-energy neutrons outnumber high-energy neutrons in the BNCT spectrum. Also, enhancement tumour boron concentration was found to result in increased boron dose. However, the calculated boron dose results gradually converged beyond 100 μg/g boron concentration.

Keywords: BNCT, Thermal neutron, Epithermal neutron, Geant4, Monte Carlo

---

[*]Corresponding author
Email address: leyla.moghaddasi@adelaide.edu.au (Leyla Moghaddasi)

1. Introduction

Boron Neutron Capture Therapy (BNCT) is a biochemically-targeted type of radiotherapy designed to selectively target malignant cells in a tumour with high Linear Energy Transfer (LET) charged particles. BNCT is based on neutron capture occurring when a thermal neutron is captured by stable ^{10}B, resulting in a compound nucleus ^{11}B which immediately disintegrates into an energetic alpha particle ($\sim$ 1.47-1.77 MeV), a recoiling ^{7}Li nucleus ($\sim$ 0.84 MeV) and a 478 keV gamma ray according to the following fission reaction (equation 1) Van Dyk (1999):

$$^{1}n +^{10} B \rightarrow^{7} Li +^{4} He + \gamma \tag{1}$$

The alpha particle and ^{7}Li deposit their energy along a track of approximately between 4 to 7 μm, resulting in localised energy deposition, due to the high LET ($\sim$ 240 keV μm^{-1}) Van Dyk (1999); Allen (2006). The clustered irradiation damage, resulting in formation of DNA double strand and single strand breaks, induced by such high LET radiation makes the repair of sublethal and potentially lethal damages less efficient. BNCT is particularly advantageous for tumours with extensive hypoxia, as the cell killing process is less sensitive to cellular oxygen level as opposed to x-ray therapy Barth et al. (2004). This is because high LET charged particle radiation predominantly produces chemical DNA damage directly rather than through free radicals. As a consequence, BNCT offers a higher tumour kill/sterilization compared to photon therapy. In addition, as the BNCT is a binary modality in which a suitable ^{10}B agent is taken up preferentially by malignant cells following administration of a boron pharmaceutical, it has the potential to selectively deliver localized dose to tumour cells dispersed in normal tissue, while minimizing normal tissue toxicity. The cell kill efficacy despite hypoxia and the capability of targeting tumour cells (containing ^{10}B compound), makes BNCT an appropriate modality for tumours with diffusive and aggressive traits (e.g. hypoxia) such as Glioblastoma Multiforme (GBM) which is characterized by a very poor prognosis following conventional External x-ray Beam Radio Therapy (EBRT). However, the success of BNCT rests on two important factors: sufficient load of ^{10}B in tumour cells (at least 20 μg/g or 10^{9} atoms/cell Barth et al. (2012)) with a relatively large ratio of tumour to normal cell boron concentration; and sufficient number of thermal neutrons delivered to the site of the tumour.

The initiation of clinical studies on BNCT dates back to 1951 at the Brookhaven National Laboratory (BNL) using fission reactor-produced thermal neutron beams Slatkin (1991). Thereafter, a BNCT facility was developed at Massachusetts Institute of Technology (MIT) in 1958. The short penetration of thermal neutron beams forced the MIT research team to employ an intra-operative technique with a gas filled balloon inserted into surgical cavity. Following a large pause in BNCT research due to failure to show a considerable improvement in survival times at MIT and BNL trials Slatkin (1991), a new approach was taken in clinical trials using intermediate energy neutron (epithermal) beams which enabled the treatment of deep-seated tumours due to superior penetration as compared to thermal neutron beam without the need for intra-operative technique Fairchild et al. (1990). Encouraging results in terms of improvement of lifespan for patients receiving this treatment have been reported since. In 2009, Yamamoto *et al.* Yamamoto et al. (2009) reported a 2-year survival rate of 53.3% for a series of 15 GBM patients Class III which was superior to that observed in RTOG trial using EBRT Curran et al. (1993) being 35% for the same Class. Kawabata *et al.* Kawabata et al. (2009) investigated the survival benefit of BNCT by comparison of survival times for 21 patients treated with BNCT against 27 patient treated by x-ray EBRT. An improved survival time, from 48.2 to 76.2% and 14.8 to 25.0% for 1 year and 2 year survival, respectively, was observed for patients treated by BNCT.

1.1. Boron delivery agents.

Two common boron delivery agents currently used are: sodium mercapto-undecahydro-*closo*-dodecaborate ($Na_2B_{12}H_{11}SH$) or commonly named BSH; and (L)-4-dihydroxy-borylphenylalanine or BPA Barth et al. (2012). Boron concentrations in normal brain and glioma cells using these agents have been investigated in several studies in literature and the ratio of tumour-to-normal cell boron concentration was found to be approximately 3.5 (approximately 13 and 45 μg/g in normal and tumour cells, respectively) for high grade gliomas Barth et al. (2005, 1997); Joensuu et al. (2003); Diaz (2003); Capala et al. (2003); Palmer et al. (2002); Coderre et al. (2004). An enhanced ratio of tumour-to-normal cell boron concentration (above 10) has also been reported in the literature as a result of L-DOPA pretreatment Capuani et al. (2008).

1.2. Neutron spectrum for boron neutron capture therapy.

An optimal neutron spectrum for BNCT should contain high thermal (E $< 0.25\ eV$) and epithermal ($0.25\ eV\ - 100\ keV$) and minimal fast neutron (E $>\ 100\ keV$) components Palmer et al. (2002). The cross section for the ^{10}B(n,α)^{7}Li neutron capture reaction is very high in the thermal energy range of neutrons, see figure 1. However, the penetration depth for thermal neutrons is limited. Consequently, epithermal neutrons are more useful for clinical purposes as they lose energy while traversing the medium and will undergo boron neutron capture at larger depths. Epithermal neutron beams designed for BNCT are predominantly produced by fission reactors and accelerators, and therefore have broad spectra and contain unwanted fast neutrons and gamma contamination. Four major dose components should be considered when such spectra interact with biological medium (the terminology has been adopted from IAEA-TECDOC-1223 BNCT treatment planning protocol Coderre et al. (2001)):

1. Boron dose from thermal neutron capture through ^{10}B(n,α)^{7}Li reaction (which is the sum of the dose from ^{7}Li and alpha particles);
2. Thermal neutron dose as a result of thermal neutron capture by nitrogen atoms in biological tissue in the reaction ^{14}N(n,p)^{14}C;
3. Gamma dose from neutron capture by hydrogen atom and also from gamma contamination through the incident neutron beam;

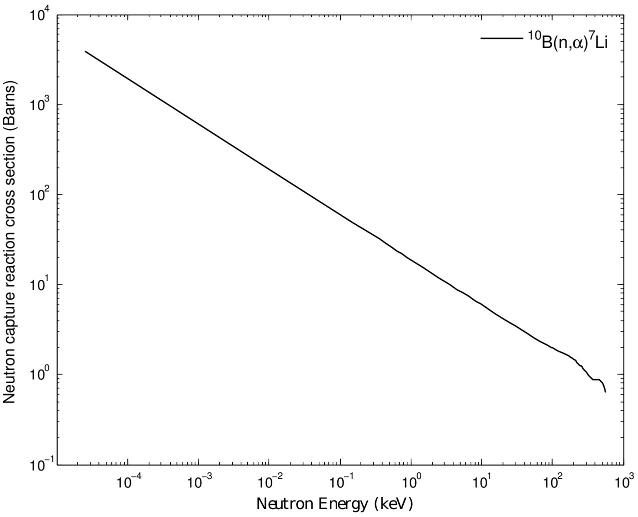

Figure 1: Boron neutron capture reaction cross section versus energy of incident neutron (reproduced from the data presented in the International Atomic Energy Agency (IAEA) website IAEA (2015)).

Table 1: Relative biological effectiveness factors and CBE factor (only for boron dose) for four principal dose components Van Dyk (1999).

	Photon w_γ	Fast neutron w_F	Thermal neutron w_T	Boron w_B
Brain tissue	0.5	3.2	3.2	1.3
Tumour tissue	0.5	3.2	3.2	3.8

4. Fast neutron dose which is due to elastic and inelastic scattering (e.g. $^{1}H(n,n')^{2}H$) and several possible nuclear reactions (e.g. $^{16}O(n,\alpha)^{13}C$); Palmer et al. (2002).

In current BNCT practices, to account for the variability of radiobiological effects of different physical dose components arising from a neutron beam spectrum, each physical dose component is weighted by its respective Relative Biological Effectiveness (RBE) factor, as listed in table 1 Van Dyk (1999). The concept of RBE was introduced to quantitatively evaluate the quality of a radiation beam in terms of biological damage it produces. RBE is the ratio doses from a reference x-ray beam and a test radiation beam, where both beams result in the same biological endpoint Marcu et al. (2012). The correction factor used for the dose arising from boron related reaction products is called Compound Biological Effectiveness (CBE) because it depends on the boron carrier used to put boron in the cell Coderre et al. (2001).

Computational and biomathematical modelling are widely used in the field of radiation dosimetry and radiobiological modelling. Monte Carlo (MC), in particular, is a suitable method to model complex probabilistic phenomena with significant uncertainty such as radiation interactions with biological systems. Several MC codes, for example, EGSnrc Kawrakow (2000) for the simulation of photon and electron electromagnetic processes, and GEANT4 Agostinelli et al. (2003) and MCNP/MCNPX Briesmeister (2000) which also include hadronic processes, have been developed. MCNP has been used for MC calculation of absorbed dose versus depth for four dose components in an ellipsoidal phantom irradiated by an epithermal neutron beam spectrum Palmer et al. (2002). Nigg *et al.* simulated a BNCT-enhanced Fast Neutron Therapy (FNT) experiment set-up using MCNP MC particle transport code. In their study, measured physical depth-dose curve and depth-boron dose curves corresponding to BNCT-enhanced FNT spectrum were also reported Nigg et al. (2000). The MC calculations were found to be in reasonable agreement with measured data (given the large error bars in measured data). The MCNP MC code was used to simulate a BNCT radiation transport facility by Nava *et al.* to investigate the effect of boron concentration on tumour to normal tissue dose and determine the optimal boron concentration as a consequence Nava et al. (2005).

Geant4 is a flexible (provided by the object-oriented technology (C++) which facilitates the extension and modification of the toolkit) and powerful MC toolkit capable of simulating complicated experimental set-ups. This MC toolkit, which is the result of an ongoing worldwide collaboration, has been developed to precisely track the passage of radiation through matter for a wide range of particles, processes (e.g. electromagnetic, hadronic, radioactive decay) over an extended energy range. The diverse functionality, inclusion of hadronic processes and performance optimization features make Geant4 a suitable MC software/tool for BNCT simulation.

1.3. Overview of Geant4 physics models.

To simulate the transportation of a hadron beam, which is required for BNCT simulation, a hadronic physics list and an electromagnetic (EM) physics list are required. Geant4 often provides several models for each type of hadronic (fission, radiative capture, elastic scattering, and inelastic scattering) or EM processes for which default cross sections are provided and can be overridden if required by the user. Several packaged physics lists are provided to select from according to the case under consideration. To transport a BNCT beam including neutrons down to thermal energies two packages can be used: QGSP_BERT_HP and QGSP_BIC_HP.

Cross section libraries are categorized based on their derivation: purely theoretical; experimental based on large data bases; and empirical parametrization. QGSP, standing for Quark Gluon String-Precompound, is a theory-driven two-component model with each component handling one part of a hadron-nucleon collision. Quark-gluon string (QGS) models high energy projectiles (this part of the package is not applicable to the BNCT application), and precompound model is used to handle de-excitation of the residual nucleus down to equilibrium at lower energies (0-100 MeV). In order to expand the applicability of these packages to a wider hadron energy range, QGSP is combined with Bertini Cascade (BERT) or Binary Cascade (BIC) which is a theory-driven model that propagates primary and secondary particles in nuclear fields of nuclei by numerical evaluation state function of quantum mechanical equation of motion Collaboration (2012). The High Precision data-driven neutron package (HP) are used to track neutrons from 20 MeV down to thermal energies. The HP neutron model is based on Geant4-supplied evaluated nuclear data bases, G4NDL data library, for cross sections, angular distributions and final state statuses Collaboration (2012). The G4NDL database is, however, incomplete. Low energy parameterized neutron models are used when the data cannot be found in the HP database for any element. In these packaged physics lists, the standard EM model is adopted to model electromagnetic processes. To avoid infrared divergence leading to substantial increase in CPU time, a secondary production threshold/range cut-off (this range is converted to energy depending on the material and particle) is required for some electromagnetic processes below which no secondary particle is generated. It should be noted that range cut-off is not tracking cut and particles are tracked down to zero energy regardless. Other user limits, such as step limit, should be defined by a user to ensure that the correct level of precision is being achieved. In Geant4 a step contains delta information of a particle track which is updated upon the end of each step. A particle's track is deleted if the particle disappears as a result of a decay or an inelastic scattering process (as is the case for fission and nuclear reactions). Therefore a maximum step size, assumed to be sufficiently small with respect to the size of the sensitive volume, should be defined to calculate the energy deposition Zahra et al. (2010).

The use of Geant4 in MC characterization (e.g. calculating individual dose profiles versus distance) and optimization of BNCT facilities in published literature is limited or non-existent to author's knowledge. Ma Ma et al. (2006) estimated the mean absorbed dose in the framework of the Medical Internal Radiation Dose Committee (MIRD) schema Sgouros et al. (2010). This was achieved using Geant4 to calculate the Dose Point Kernel (DPK) ("the average absorbed dose per unit activity in a spherical shell placed around the point source at origin" Ma et al. (2006)) corresponding to ^{7}Li and alpha particles within a single cell and consequently estimate the "S" value (the absorbed dose to a target volume per disintegration in the source region) for a number of cellular radii. In this study, the dose profile in a single cell was obtained, however, the dose distribution in a population of cells was not addressed. Also MIRD scheme developed to assist in the estimation of dose from internal radiation which is not particularly applicable for the BNCT modality.

The purpose of the current work was to develop a Geant4 beam model for a BNCT epithermal neutron beam. The BNCT beam model was then validated against measured and calculated data in literature Nigg et al. (2000). In addition, a sensitivity analysis was performed to investigate the effect of the neutron energy spectrum on the boron dose component. Finally, the sensitivity of boron dose to the concentration of boron agent in cells as compared to normal brain tissue was investigated. The sensitivity analyses were performed

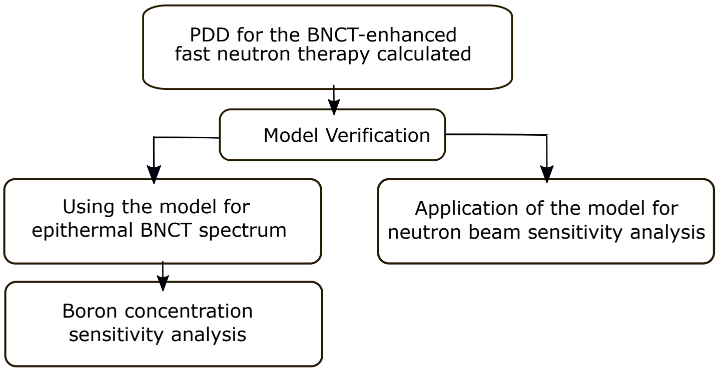

Figure 2: After Geant4 simulation of a neutron beam fired into a water phantom, the following steps were taken to complete this study, as illustrated in this flowchart showing the structure of the current work. Note that, BNCT-enhanced FNT beam was obtained from Niggs study Nigg et al. (2000) and the epithermal BNCT spectrum was adopted from Mareks study Marek et al. (2014).

to determine an optimal boron concentration and neutron energy spectrum to achieve a clinically optimal BNCT treatment.

2. Methods and Materials

Figure 2 summarizes the outline of the mathematical model development and sensitivity analyses undertaken in this work.

2.1. Beam model development and validation

The published cyclotron-produced neutron spectrum for BNCT-enhanced Fast Neutron Therapy (FNT) at the University of Washington (UW) Nigg et al. (2000) was used for the beam model in the current work. The rationale to choose the BNCT-enhanced FNT beam, having a higher fast neutron component than epithermal beams, was that at this stage of simulation the purpose was to develop a beam model and validate the model (in terms of physics processes and cross sections accuracy) against published measured and calculated results. Before the date this work was done, no other published data, including reference Nigg et al. (2000), contained a complete set of required data, that is, the energy spectrum and its corresponding measured and calculated Percentage Depth Dose (PDD) profiles, individually for total and boron dose, to be used for model validation in the current work. However, the study of Nigg *et al.*Nigg et al. (2000) provided their data in terms of total and boron absolute dose versus depth which allowed PDDs to be obtained by normalizing to the maximum dose.

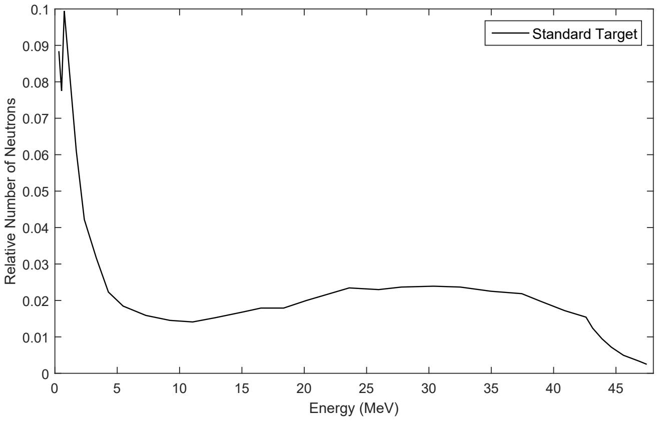

Figure 3: Free-field neutron spectrum for the University of Washington Fast-Neutron Therapy Facility produced by standard target (reproduced from the data of Nigg *et al.* Nigg et al. (2000)).

The Geant4 MC particle tracking toolkit Agostinelli et al. (2003) was used to develop the neutron beam model. The simulation set-up was designed to represent the measurement/calculation set-up in the study of Nigg *et al.*Nigg et al. (2000). A mathematical model representing a treatment technique should consist of a beam model as the source for external radiation therapy, a detector/phantom, and an appropriate list of processes and cross section libraries to model interactions of radiation with matter.

BNCT beam. The neutron beam spectrum was modelled using Geant4 General Particle Source (GPS) as the primary radiation particle generator. GPS has a large degree of flexibility to allow implementation of sophisticated sources, particularly poly-energetic beams, relatively simply. The UW BNCT-enhanced FNT neutron spectrum produced by the standard target (10.5 mm thick beryllium target) Nigg et al. (2000) was reproduced using the Plot Digitizer java program (http://plotdigitizer.sourceforge.net/), see figure 3. This energy distribution was implemented in the form of an energy histogram using linear interpolation. A 10 cm radius conical beam, with 150 cm Source to Surface Distance (SSD) and isotropic angular distributions was modelled. Photon contamination was not taken into account in the neutron beam model.

Phantom geometry description,material specification, and tracking. The neutron beam was fired into a $20 \times 20 \times 20$ cm^3 *in-silico* phantom made of water with 100 μg/g ^{10}B concentration and the dose components were scored in the mid-plane along beam axis, divided into 1 mm^3 voxels, see figure 4. Boron concentration was chosen to replicate the phantom material in Nigg's experimental set-up Nigg et al. (2000). The sensitive detector technique was implemented to score the dose in this scoring plane. The scoring plane was divided into 1 mm cubic voxels, resulting in an array of 200×200 voxels. The tracks of ^{7}Li and alpha

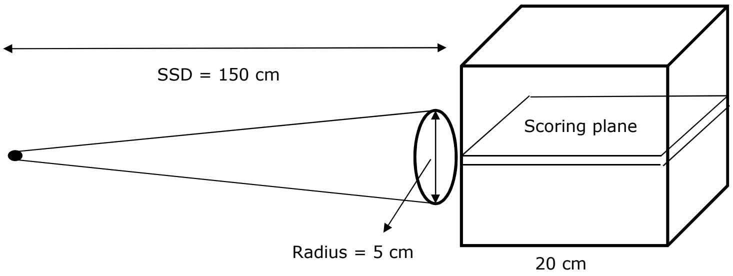

Figure 4: A schematic diagram showing the simulation set-up: a conical neutron spectrum of neutron beam, 150 cm SSD, a $20 \times 20 \times 20$ cm^3 phantom and and central axis dose scoring slice ($20 \times 20 \times 0.1$ cm^3) along the beam axis.

particles from the boron capture reaction (^{10}B(n,α)^{7}Li), gammas resulting from the neutron capture reaction (^{1}H(n,γ)^{2}H), and all other particles and nuclear fragments from fast neutron and thermal neutron capture (^{14}N(n,p)^{14}C) were individually tracked in the simulation. Three different dose matrices were calculated and several output files related to each dose component were generated: 1) Boron dose which is the dose deposited by ^{7}Li and alpha particles from the boron capture reaction; 2) Gamma dose from the neutron capture reaction; 3) Fast and thermal neutron dose as described in subsection 1.2. The reason these two dose components were combined was that the RBE for these components are identical, see table 1.

Physics processes. For this application the packaged physics list, Quark-Gluon String Precompound Binary Cascade High Precision Neutron (QGSP_BIC_HP), provided by Geant4 was implemented. Particles were assigned appropriate processes and cross sections along their passage. To ensure a more accurate calculation of the energy deposition, the maximum step was fixed to 4 μm, corresponding to the minimum range of the alphas and ^{7}Li nuclei. In order to be able to score and differentiate the dose from alphas and ^{7}Li nuclei (broron dose component) the step size had to be kept 4 μm despite the fact 1 mm^3 voxels were used. The production threshold/cut off-value was set to 4 μm for e^-, e^+ and proton particles and 0.01 mm for gamma particles.

Parallel simulation on an 20-CPU Linux computer clusters of supercomputers was performed for a total of 8×10^6 incident neutrons. The dose distribution along the central plane along the beam direction was obtained for boron dose (combined alpha and ^{7}Li doses), fast and thermal dose and gamma dose (residual dose). In order to validate the validity of the beam model, the calculated results were compared with both experimental and calculated PDD data from the literature Nigg et al. (2000). The total absorbed dose as well as boron only dose contributions were obtained by averaging of 3 and 5 voxels at depths around the region where the peak was observed, respectively. As a result, the

BNCT beam model was validated in terms of the accuracy of physics processes, cross sections and particle tracking.

2.2. Neutron beam sensitivity analysis

In this section the dependence of the boron dose component on different neutron beam energies as well as different neutron spectra was investigated. Following validation of the neutron beam model, the beam spectrum implemented in the previous section (i.e BNCT-enhanced FNT neutron spectrum) was replaced by two monoenergetic neutron beams and different beam spectra to evaluate the boron dose from each beam with respect to other dose components. This was performed to qualitatively investigate the impact of the neutron beam on the boron to residual dose ratio. A 5.0 cm radius conical beam, with 100 cm SSD and isotropic angular distributions was modelled. For all neutron beam energies/spectra of energies considered, simulations were run on parallel 4-CPU Linux clusters for a total number of 4×10^6 particles. The remainder of the set-up including material composition of the phantom and the physics remained the same as initial simulation set up (section**??**). First, the MC code was used for two monoenergetic neutron beams, 1.0 and 10.0 eV. As the epithermal neutron energy range is commonly defined from 0.5 eV to 10 keV Coderre et al. (2001), these two energies were selected in the present work to investigate the dose components at the two extremes of the epithermal neutron range. The boron dose and residual dose (the total dose excluding the boron dose) profiles were calculated for both energies and compared.

Subsequently, a published epithermal neutron beam spectrum suitable for BNCT, containing a significantly higher proportion of thermal and epithermal neutrons compared to those in the BNCT-enhanced FNT neutron spectrum (as used in the previous section), was identified in literature Marek et al. (2014). The spectrum of the neutron beam was reproduced using Plot Digitizer. This neutron data which was in terms of neutron fluence rate ($cm^{-2}s^{-1}$) versus neutron energy was used to calculate the relative number of neutrons (the number of neutrons in each energy bin/total number of neutrons (integral under the curve)) versus energy, see figure 5. The boron dose profile calculated for the epithermal spectrum was compared with that obtained using the BNCT-enhanced FNT Spectrum. Finally, the Geant4 code was set up for two hypothetical scenarios: irradiating the system with part of the epithermal spectrum from 0-10 keV, called the low energy tail; and another part of the epithermal spectrum from 10 keV to 10 MeV, called the high energy tail. This was to evaluate the extent that the high energy tail alters the ratio of boron to residual dose compared to the ratio produced by the low energy tail.

2.3. Boron concentration sensitivity analysis

In this sensitivity analysis, the impact of boron concentration on the boron dose component was investigated. The boron concentrations in normal brain and tumour cells were assumed to be 13 and 45 μg/g, respectively. The epithermal spectrum reported on by Marek Marek et al. (2014) (figure 5) was used to

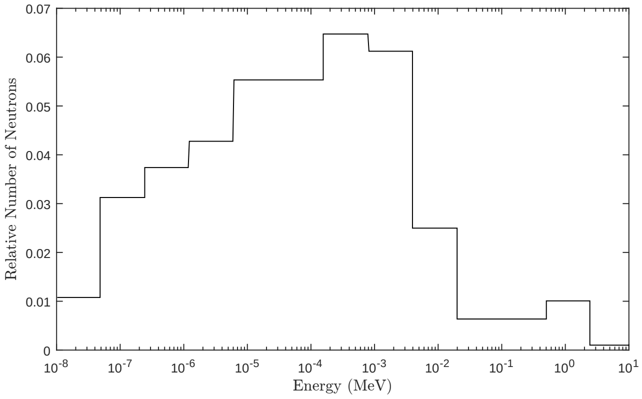

Figure 5: The free-in-air epithermal neutron spectrum for the LVR-15 reactor at Research Centre Rez, Czech Republic (reproduced from the data of Marek *et al.* Marek et al. (2014)).

model the beam. A 5.0 cm radius conical beam, with 100 cm SSD and isotropic angular distributions was modelled. As for phantom material specification, the MC code was used for several boron dose concentrations, namely, 13, 45, 130 and 1300 μg/g, distributed homogeneously in the water phantom. Simulations were run for each boron concentration for a total of 4×10^6 primary neutrons. Calculated boron doses from four simulation were compared and analysed.

3. Results

3.1. Beam model validation

Figure 6 shows a comparison of Geant4 calculated absorbed dose, obtained in the current work, with measured data from the study of Nigg *et al.* Nigg et al. (2000). Relative total absorbed dose as a function of depth in the phantom is presented in figure 6 (a). Calculated absorbed doses at different depths were found to be within 1.5% of measured data. The average relative error in the relative total absorbed dose was 4.8% in this calculation.

The results of calculated absorbed dose only from the boron neutron capture reaction, called boron dose (calculated by tracking alpha and ^{7}Li particles and their respective secondary particles and scoring absorbed dose of these particles), as compared to measured data, is shown in figure 6 (b). Figure 6 (b) shows a maximal dose at 40 mm for both the calculated and literature data (for 100 ug/g concentration) in the phantom with 100 $\mu g/g$ boron concentration, which coincides with that of measured data Nigg et al. (2000) for the same configuration. These results provide confidence that the developed beam model, and the selected physics list in particular, accurately models the correct nuclear reactions for incident neutrons and properly track emitted particles and fragments until they come to rest.

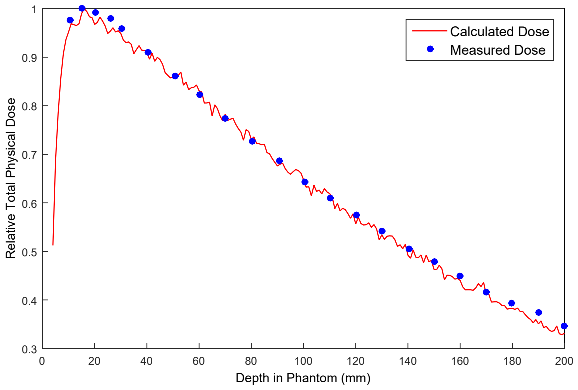

(a) Total Physical dose

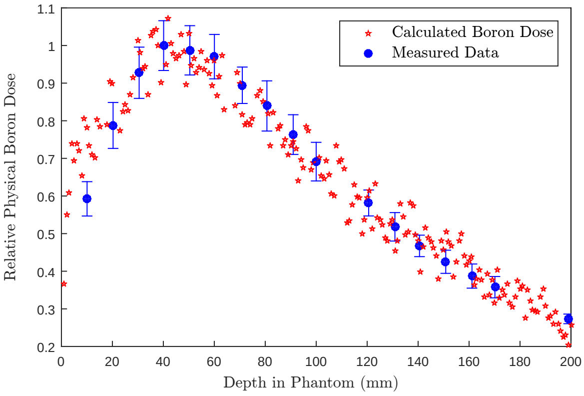

(b) Physical Boron dose

Figure 6: Geant4 calculated physical total and boron dose as compared to measured data obtained by Nigg *et al.* Nigg et al. (2000) using a BNCT-enhanced FNT spectrum. The error bars were reproduced from experimental data presented by Nigg Nigg et al. (2000). The statistical uncertainty of the calculated results was on average $\sim \pm 3\%$.

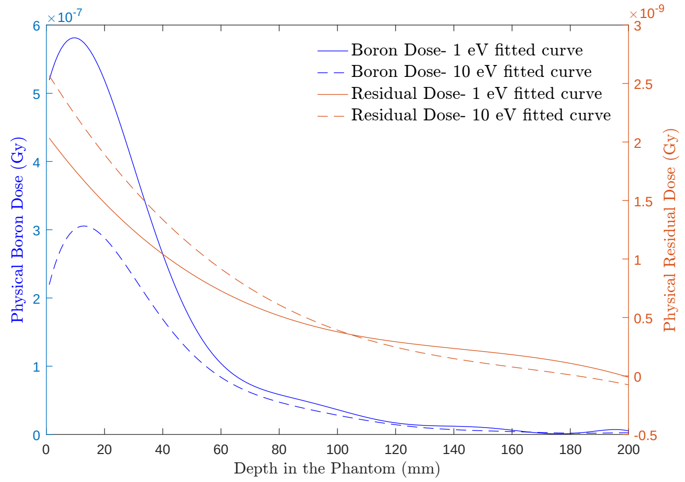

Figure 7: A comparison of boron dose and residual dose (fast, thermal neutron, and gamma dose) using two mono-energetic, 1 and 10 eV, diverging neutron beams with 5.0 cm diameter at the phantom surface.

3.2. Neutron beam sensitivity analysis

Figure 7 shows Geant4 calculated depth-dose curves of boron (the boron curves are fits to the calculated data) and residual dose components produced by diverging 5.0 cm diameter mono-energetic neutron beams: 1.0 eV and 10.0 eV. The residual dose components produced by both beams, however, were essentially the same and were found to be lower than boron dose components by $\sim$ 2.0 and 2.5 orders of magnitude for 10.0 and 1.0 eV neutron beams, respectively.

The depth-dose curves calculated using the epithermal spectrum Marek et al. (2014) and the BNCT-enhanced FNT spectrum Nigg et al. (2000) are compared in figure 8. Residual depth dose curve for the BNCT-enhanced FNT spectrum was found to be considerably larger than that calculated for the epithermal spectrum, figure 8 (a). Figure 8 (a) shows that the shapes of the curves were not similar and the gradient of BNCT-enhanced FNT residual depth-dose curve was lower than that of the epithermal curve. Further, the absorbed dose was above 30% of maximum dose at 20.0 cm depth in the phantom. The absorbed dose at 20.0 cm depth in the phantom corresponding to the epithermal spectrum, valued $\sim$ 8% of the maximum absorbed dose, was considerably lower than that for BNCT-enhanced FNT spectrum.

Boron dose shown in figure 8 (b) for both spectra appeared to be approximately similar in shape reaching a maximum at $\sim$ 4.0-4.5 cm depth in the phantom. As expected, the boron dose was found to be larger using the epithermal/BNCT spectrum as compared to the BNCT-enhanced spectrum for the entire depth range. This is due to the fact that, compared to the BNCT-

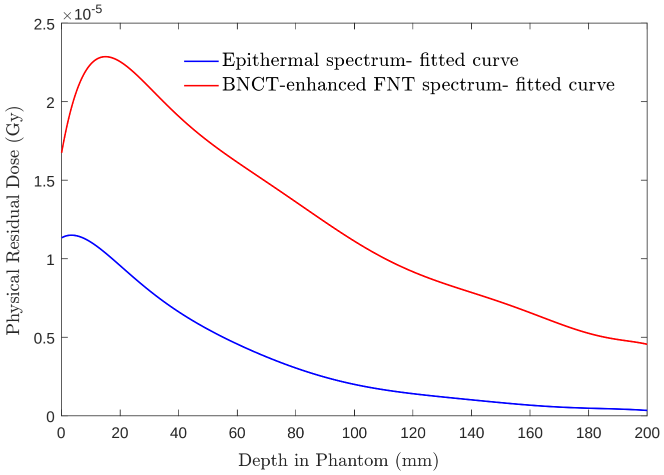

(a) Residual dose (fast, thermal neutron, and gamma dose)

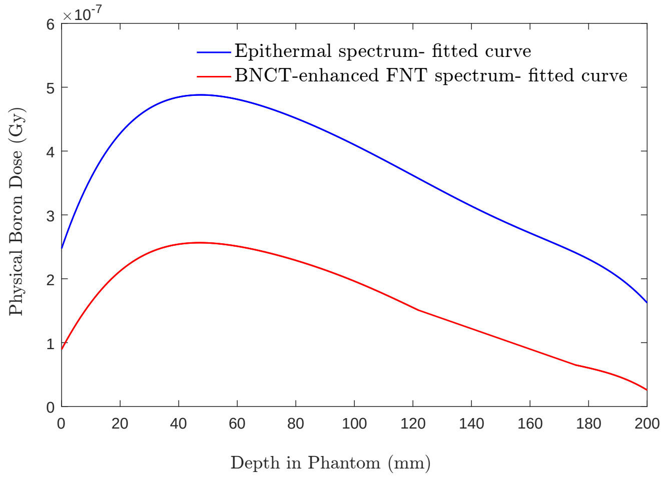

(b) Boron dose

Figure 8: Geant4 calculated physical dose using the epithermal/BNCT spectrum Marek et al. (2014) as compared to BNCT-enhanced FNT spectrum Nigg et al. (2000).

enhanced beam, the proportion of low energy neutrons was larger in the epithermal beam resulting in an increased number of boron neutron capture reactions and subsequently increased boron dose.

The comparison of boron dose with residual dose profiles, using two halves of the epithermal spectrum, below 10 keV and above 10 keV (figure 5), are shown in figure 9. Boron dose component produced by the low energy tail of the spectrum markedly dominated the residual dose which was lower by at least two orders of magnitude up to 2.0 cm depth, figure 9 (a). On the other hand, the dose profiles resulting from the high energy tail of the spectrum ($>$ 10 keV) showed an opposite trend with boron dose being lower than residual dose for the entire depth range and approximately lower by one order of magnitude for up to 2.0 cm depth, figure 9 (b).

Figure 10 compares boron dose profiles, figure 10(a), and residual dose profiles, figure 10(b), generated by the two tails of the epithermal spectrum. Figure 10(a) shows the boron dose profile for low energy tail of the spectrum reached a maximum at a shallower depth as compared to the profile produced by high energy tail of spectrum. While the low energy tail of the spectrum produced a boron dose profile which was not considerably higher than that produced by the high energy tail half, it is theoretically more desirable for BNCT treatment for which the ratio of boron dose component to the residual dose is of importance in order to deliver selective/targeted treatment to the tumour cells. As shown in figure 10(b) (note that the vertical axis is on logarithmic scale), residual dose generated by the low energy tail of the spectrum is minimal compared to that produced by the high energy tail of the spectrum (four orders of magnitude difference). This results in a boron dose to residual dose ratio of $\sim$ 0.05 and 150 at the depth of maximum boron dose for the high tail and the low tail of the epithermal/BNCT spectrum, respectively. It was also noted that the residual dose for the low energy tail splits up at about half way through phantom depth. This was attributed to the residual dose including fast neutron, thermal neutron capture and gamma dose. The fast neutron and thermal neutron dose contributions are represented by top side and down side (split down) of blue scatter curve, respectively. This is because the cross section for thermal neutron capture by nitrogen atoms in tissue reduces markedly beyond a few eV energy of incident neutron Auxier and Brown (1968) and at larger depths neutrons in this energy range have been mostly absorbed.

3.3. Boron concentration sensitivity analysis

Calculated boron dose as a function of depth in the phantom for different boron concentrations are shown in figure 11(a). The maximum boron dose as a function of boron concentration is shown in the figure 11(b). A non linear relationship between maximum boron dose and boron concentration was observed and the maximum boron dose gradually saturated. In other words, as suggested by this simulation results, increasing cellular boron concentration do not result in the boron dose increasing at the same rate.

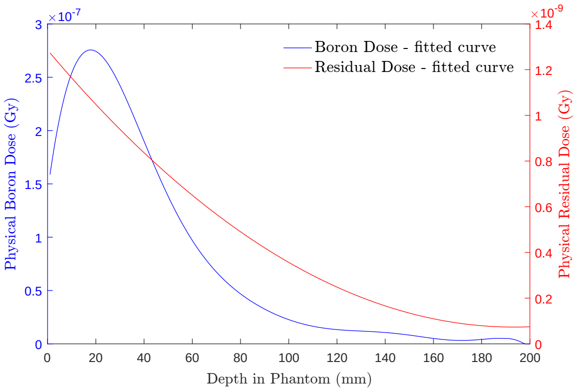

(a) Low energy tail of the epithermal spectrum

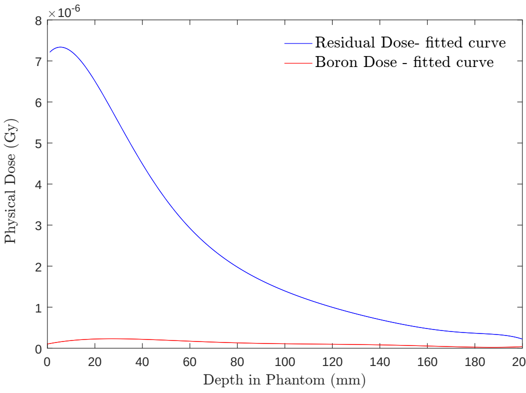

(b) High energy tail of the epithermal spectrum

Figure 9: Boron dose and residual dose for two halves of the epithermal spectrum (figure5): 1) Low energy tail of the spectrum (< 10 keV); and 2) High energy tail of the spectrum (> 10 keV).

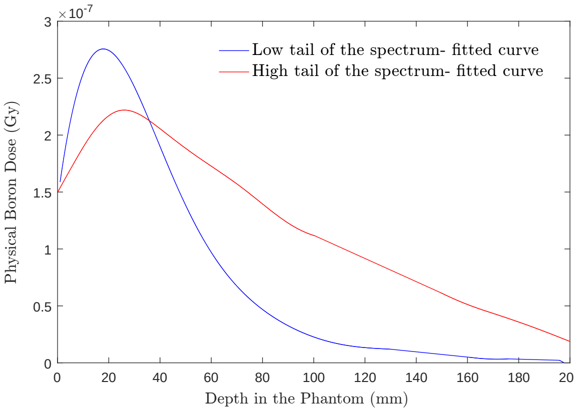

(a) Boron dose

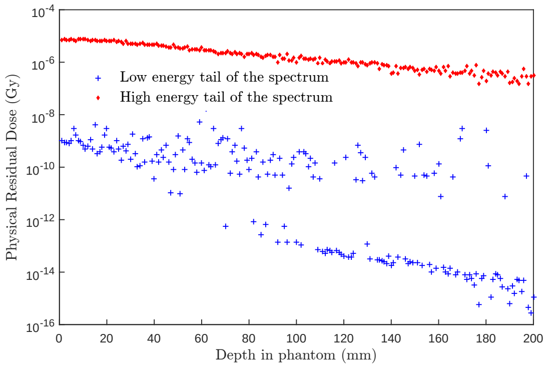

(b) Residual dose (fast, thermal neutron, and gamma dose)

Figure 10: A comparison of boron dose and residual dose using the two tails of the epithermal spectrum (figure5): a)The low energy tail of the spectrum (< 10 keV); and b) The high energy tail of the spectrum (> 10 keV).

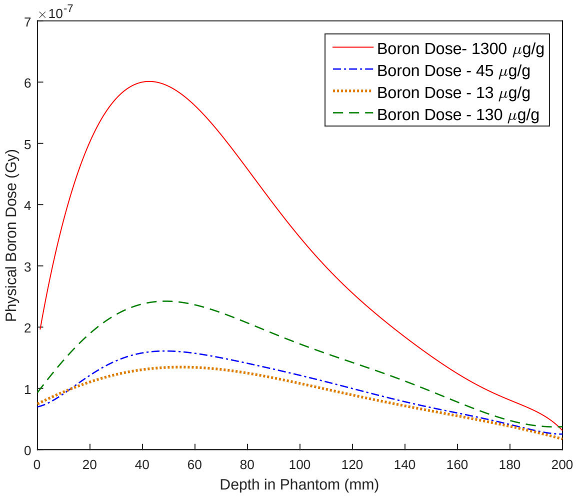

(a) Boron dose versus depth in the phantom for different boron concentrations.

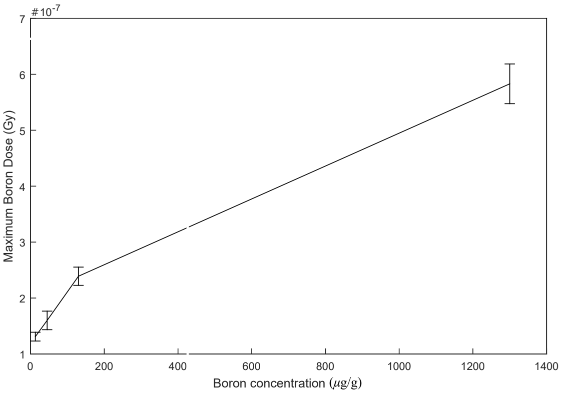

(b) Maximum boron dose versus boron concentrations in the phantom.

Figure 11: Boron dose versus boron concentration in the phantom using the epithermal spectrum Marek et al. (2014) and 4×10^6 incident neutrons.

4. Discussion

The rationale for BNCT treatment is the potential ability to deliver localized high LET absorbed dose to tumour cells containing sufficient number of boron atoms while minimizing the dose to normal tissue cells which contain fewer number of boron atoms (by a about 3.5 times using current boron delivery agents available). Therefore, the efficacy of BNCT depends upon two factors which increase the ratio of boron to residual dose component (which is not selective and the same dose is delivered to both tumour and normal cells): 1) the number of thermal neutrons arriving at the tumour site, and 2) the number of boron atoms in the cells.

A Monte Carlo BNCT beam model was developed using the Geant4 particle tracking package and was against published data in the current work. In addition, the beam model was used to investigate the sensitivity of BNCT dose delivery, in terms of the boron dose component ratio, to different neutron beam energy spectra as well as boron concentration in the cells.

Calculated values for total absorbed dose using a BNCT-enhanced FNT spectrum showed good agreement, within 1.5%, with published measured data Nigg et al. (2000). Calculated boron dose from Geant4 was also found in accordance with measured data. These findings, shown in figure 6, demonstrated that the developed beam model and selected physics cross sections could accurately track specific particles and score their respective absorbed dose.

The results of the neutron beam energy sensitivity analysis demonstrated a strong dependence of boron dose component ratio to the beam energy/spectrum. The boron dose component decreased to half when the energy of mono energetic neutron beam was increased from 1.0 to 10.0 eV, while the residual dose did not change considerably. The change from 1.0 to 10 eV neutron energy also caused a slight shift in the boron dose maximum depth which was due to the fact that neutrons with higher than thermal energies need to lose their energies through elastic or inelastic collisions prior being captured in a boron neutron capture fission reaction, see figure 7.

The boron dose produced by the epithermal spectrum, which contained a larger proportion of thermal and epithermal neutrons, was higher than that for the BNCT-enhanced FNT spectrum, whereas residual dose showed an opposite trend with that of the epithermal spectrum being up to 2.5 times lower than that produced by the BNCT-enhanced FNT spectrum, see figure 8. As a result, boron dose to residual dose ratio increased by $\sim$ 5 times at depth 4.0 cm when the BNCT-enhanced FNT spectrum was switched to the epithermal/BNCT spectrum. It is also worth noting that, with respect to normal tissue toxicity, given that fast neutrons have a very large radiobiological effect, compared to the epithermal spectrum, the BNCT-enhanced FNT beam is undesirable for BNCT treatment as the fast and thermal neutron dose profile showed a shallower gradient exposing deep-seated normal tissue to a substantial radiation dose ($\sim$ 30% of its maximum).

Investigation of dose profiles produced by the hypothetical low-energy tail and high-energy tail of the epithermal/BNCT spectrum (see figures 9 and 10) demonstrated that for successful implementation of BNCT, it is of high importance that the neutrons in the low-energy tail outnumbers neutrons in the high-energy tail in the spectrum. This is based on the observation that while for the low-energy tail the boron dose profile is dominant (delivering dose selectively to tumour cells) and residual dose (delivering dose to both tumour and normal tissue and contributing to normal tissue toxicity) is negligible, profiles corresponding to the high-energy tail completely inverted.

Other interesting findings of the current work were the results of boron concentration sensitivity analysis. As it can be seen in figure 11, boron dose does not increase at the same rate as boron concentration increases. While boron dose was increased by ~ 3.5 times as a result of changing from normal to tumour cell (from 13.0 to 45.5 $\mu g/g$), it did not improve at the same rate when boron concentration was further enhanced and a convergent boron dose results were obtained. For the boron neutron capture reaction to occur, both thermal neutrons and boron atoms are needed and if only the number of boron atoms is increased, it may not translate to an increased number of boron capture reactions unless there are sufficient number of thermal neutrons available.

The rationale to conduct this research arose from the conclusion derived from the previous research from the group. A comprehensive microscopic-scale GBM treatment modelling structure was previously developed and expanded to incorporate radiobiological characteristics of GBM (heterogeneous radiosensitivity and hypoxia) for external x-ray therapy. The model was used for evaluation and quantification of cell kill efficacy depending on various radiobiological parameters (e.g. genetic phenotype and hypoxia) Moghaddasi et al. (2016). It was demonstrated that x-ray external therapy may not be able to control GBM and tumour most probably relapses within the treatment region prior to formation of colonies by migrating cell survived in the marginal regions. In the future study, the beam model developed in this work will be incorporated into a GBM framework Moghaddasi et al. (2015, 2016) to build a comprehensive BNCT treatment modelling code to investigate and quantify GBM cell survival fraction following BNCT treatment.

5. Conclusion and Future Work

A neutron beam model with realistic energy spectrum was developed and was tested successfully against published data. The beam model developed was used to conduct two sensitivity analyses: neutron beam spectrum and boron concentration impact on boron to residual dose ratios. The results of the neutron beam sensitivity analysis suggested that the efficacy of BNCT (which is dependant on the ratio of boron dose relative to residual dose) strongly depends on the number of low energy neutrons in the incident spectrum which should be ideally dominating the number of neutrons with higher energies. Should this relationship not exist, substantial normal brain tissue toxicity may be incurred. In addition, it was demonstrated that enhancement of tumour cell to normal tissue boron concentration above a standard value (~ 10) may not translate to improved treatment outcome. An important area of future development of the present work will be to model nuclear reactor hardware which will affect the angular distribution of neutron beam (which is isotropic in the current model). This will result in gamma contamination being introduced into the simulated neutron beam model (the neutron beam currently include only a spectrum of neutrons).

References

Agostinelli S, Allison J, Amako Ka, Apostolakis J, Araujo H, Arce P, Asai M, Axen D, Banerjee S, Barrand G, et al. Geant4a simulation toolkit. Nuclear instruments and methods in physics research section A: Accelerators, Spectrometers, Detectors and Associated Equipment 2003;506(3):250–303.

Allen BJ. Internal high linear energy transfer (let) targeted radiotherapy for cancer. Physics in medicine and biology 2006;51(13):R327.

Auxier J, Brown M. Neutron cross-sections and reaction products for h, c, n, and o for the energy range from thermal to 15 mev. In: Proceedings. Pergamon Press; 1968. p. 853.

Barth RF, Coderre JA, Vicente MGH, Blue TE. Boron neutron capture therapy of cancer: current status and future prospects. Clinical Cancer Research 2005;11(11):3987–4002.

Barth RF, Grecula JC, Yang W, Rotaru JH, Nawrocky M, Gupta N, Albertson BJ, Ferketich AK, Moeschberger ML, Coderre JA, K RE. Combination of boron neutron capture therapy and external beam radiotherapy for brain tumors. International Journal of Radiation Oncology* Biology* Physics 2004;58(1):267–77.

Barth RF, Vicente M, Harling OK, Kiger III W, Riley KJ, Binns PJ, Wagner FM, Suzuki M, Aihara T, Kato I, Kawabata S. Current status of boron neutron capture therapy of high grade gliomas and recurrent head and neck cancer. Radiat Oncol 2012;7(146):1–21.

Barth RF, Yang W, Rotaru JH, Moeschberger ML, Joel DD, Nawrocky MM, Goodman JH, Soloway AH. Boron neutron capture therapy of brain tumors: enhanced survival following intracarotid injection of either sodium borocaptate or boronophenylalanine with or without blood-brain barrier disruption. Cancer Research 1997;57(6):1129–36.

Briesmeister JF. MCNPTM-A general Monte Carlo N-particle transport code; 2000. .

Capala J, Britta H, Sköld K, af Rosenschöld PM, Giusti V, Persson C, Wallin E, Brun A, Franzen L, Carlsson J, Salford L, Ceberg C, Persson B, Pellettieri L, Henriksson R. Boron neutron capture therapy for glioblastoma multiforme: clinical studies in sweden. Journal of neuro-oncology 2003;62(1):135–44.

Capuani S, Gili T, Bozzali M, Russo S, Porcari P, Cametti C, D'Amore E, Colasanti M, Venturini G, Maraviglia B, Lazzarino G, Pastore FS. L-dopa preloading increases the uptake of borophenylalanine in c6 glioma rat model: a new strategy to improve bnct efficacy. International Journal of Radiation Oncology* Biology* Physics 2008;72(2):562–7.

Coderre J, Hopewell J, Turcotte J, Riley K, Binns P, Kiger W, Harling O. Tolerance of normal human brain to boron neutron capture therapy. Applied radiation and isotopes 2004;61(5):1083–7.

Coderre J, et al. Current status of neutron capture therapy. Technical Report; IAEA-TECDOC-1223. ISSN 1011–4289, Annex 6, IAEA; 2001.

Collaboration G. Physics reference manual. Version geant4960 2012;9.

Curran WJ, Scott CB, Horton J, Nelson JS, Weinstein AS, Fischbach AJ, Chang CH, Rotman M, Asbell SO, Krisch RE, Nelson DF. Recursive partitioning analysis of prognostic factors in three radiation therapy oncology group malignant glioma trials. Journal of the National Cancer Institute 1993;85(9):704–10.

Diaz AZ. Assessment of the results from the phase i/ii boron neutron capture therapy trials at the brookhaven national laboratory from a clinicians point of view. Journal of neuro-oncology 2003;62(1-2):101–9.

Fairchild R, Saraf S, Kalef-Ezra J, Laster B. Comparison of measured parameters from a 24–kev and a broad spectrum epithermal neutron beam for neutron capture therapy: An identification of consequential parameters. Medical physics 1990;17(6):1045–52.

IAEA . Neutron cross-section standards (2006) and references (2015). 2015. URL: `https://www-nds.iaea.org/standards/`.

Joensuu H, Kankaanranta L, Seppälä T, Auterinen I, Kallio M, Kulvik M, Laakso J, Vähätalo J, Kortesniemi M, Kotiluoto P, Seren T, Karila J, Brander A, Jaärviluoma E, Ryynaänen P, Paetau A, Ruokonen I, Minn H, Tenhunen M, Jaäaäkelaäinen J, Faärkkilaä M, Savolainen S. Boron neutron capture therapy of brain tumors: clinical trials at the finnish facility using boronophenylalanine. Journal of neuro-oncology 2003;62(1-2):123–34.

Kawabata S, Miyatake SI, Nonoguchi N, Hiramatsu R, Iida K, Miyata S, Yokoyama K, Doi A, Kuroda Y, Kuroiwa T, Michiue H, Kumada H, Kirihata M, Imahori Y, Maruhashi A, Sakurai Y, Suzuki M, Masunaga I, Ono K. Survival benefit from boron neutron capture therapy for the newly diagnosed glioblastoma patients. Applied Radiation and Isotopes 2009;67(7):S15–8.

Kawrakow I. Accurate condensed history monte carlo simulation of electron transport. i. egsnrc, the new egs4 version. Medical physics 2000;27(3):485–98.

Ma Y, Geng J, Gao S, Bao S. Dose point kernel for boron-11 decay and the cellular s values in boron neutron capture therapy. Medical physics 2006;33(12):4739–43.

Marcu L, Bezak E, Allen BJ. Biomedical physics in radiotherapy for cancer. Csiro publishing, 2012.

Marek M, Vins M, Lahodova Z, Viererbl L, Koleska M. Extended set of activation monitors for nct beam characterization and spectral conditions of the beam after reactor fuel conversion. Applied Radiation and Isotopes 2014;88:157–61.

Moghaddasi L, Bezak E, Harriss-Phillips W. Evaluation of current clinical target volume definitions for glioblastoma using cell-based dosimetry stochastic methods. The British journal of radiology 2015;88(1053):20150155.

Moghaddasi L, Bezak E, Harriss-Phillips W. Monte-carlo model development for evaluation of current clinical target volume definition for heterogeneous and hypoxic glioblastoma. Physics in Medicine and Biology 2016;61(9):3407.

Nava E, Burn K, Casalini L, Petrovich C, Rosi G, Sarotto M, Tinti R. Monte carlo optimisation of a bnct facility for treating brain gliomas at the tapiro reactor. Radiation protection dosimetry 2005;116(1-4):475–81.

Nigg DW, Wemple CA, Risler R, Hartwell JK, Harker YD, Laramore GE. Modification of the university of washington neutron radiotherapy facility for optimization of neutron capture enhanced fast-neutron therapy. Medical Physics 2000;27(2):359–67.

Palmer MR, Goorley JT, Kiger W, Busse PM, Riley KJ, Harling OK, Zamenhof RG. Treatment planning and dosimetry for the harvard-mit phase i clinical trial of cranial neutron capture therapy. International Journal of Radiation Oncology* Biology* Physics 2002;53(5):1361–79.

Sgouros G, Roeske JC, McDevitt MR, Palm S, Allen BJ, Fisher DR, Brill AB, Song H, Howell RW, Akabani G, et al. Mird pamphlet no. 22 (abridged): radiobiology and dosimetry of α-particle emitters for targeted radionuclide therapy. Journal of Nuclear Medicine 2010;51(2):311–28.

Slatkin DN. A history of boron neutron capture therapy of brain tumours. Brain 1991;114(4):1609–29.

Van Dyk J. The modern technology of radiation oncology: a compendium for medical physicists and radiation oncologists. Medical Physics Pub Corp, 1999.

Yamamoto T, Nakai K, Kageji T, Kumada H, Endo K, Matsuda M, Shibata Y, Matsumura A. Boron neutron capture therapy for newly diagnosed glioblastoma. Radiotherapy and oncology 2009;91(1):80–4.

Zahra N, Frisson T, Grevillot L, Lautesse P, Sarrut D. Influence of geant4 parameters on dose distribution and computation time for carbon ion therapy simulation. Physica Medica 2010;26(4):202–8.

7.3 Discussion and conclusion

The epithermal neutron beam developed in this chapter was tested successfully against published data (agreement within 1% beyond the build up region was achieved). The epithermal neutron beam model was used to conduct two comprehensive sensitivity studies, which quantified the impact of two important factors related to BNCT efficacy and toxicity:

- Delivery of BNCT with limited toxicities depends on the ratio of boron dose relative to residual dose, and therefore the proportion of low energy neutrons in a BNCT neutron spectrum. It was demonstrated that if the low energy neutron population does not dominate the fast neutrons and gamma radiation, the boron to residual dose ratio inverts, and more dose will be delivered to healthy brain tissue compared to GBM.
- The boron to residual dose ratio versus tumour to normal cell boron concentration ratio was found to be non-linear and the boron to residual dose ratio saturated above 10. It indicates that enhancement of tumour to normal cell boron concentration ratio above a standard value (~ 10) may not translate to improved treatment outcome (i.e. in terms of both normal tissue toxicity and tumour cell kill) with the same rate.

The BNCT beam model developed in this chapter will be incorporated in the GBM treatment modelling framework presented in chapters 8 and 9.

Chapter 8

Development of an integrated Monte Carlo model for glioblastoma multiforme treated with Boron Neutron Capture Therapy

8.1 Introduction and motivation

This chapter describes the use and development of an integrated radiation treatment modelling framework to evaluate the efficacy of Boron Neutron Capture Therapy (BNCT) treatment of glioblastoma consisting of a homogeneous population of cells in terms of radiosensitivity (i.e. α & β values). The codes developed in chapters 5 and 7, to simulate GBM and its infiltration into normal tissue, and an epithermal neutron beam for BNCT are incorporated in the simulation performed in this chapter.

The model will be used to investigate the Survival Fractions (SFs) in several treatment regions using 2.0 and 2.5 CTV margin extensions. The results will be compared with the SFs obtained for x-ray EBRT, discussed in chapter 5, and the differences will be discussed.

8.2 Statement of Contribution

8.2.1 Conception

The initial idea of investigation of the efficacy BNCT for the treatment/management of GBM and integration of a MC model with semi-analytical cellular-based cell-survival model (radiobiological model) was first conceptualised by Leyla Moghaddasi. The method to design the architecture of the integrated model to simulate BNCT treatment of GBM was conceptualised by Leyla Moghaddasi.

8.2.2 Realisation

The Geant4 code development to obtain cell-based dosimetry in *in silico* GBM infused with a boron agent, and related MATLAB codes to simulate bio-distribution of the boron agent and for data analysis were undertaken by Leyla Moghaddasi. The model verification and data analyses were performed by Leyla Moghaddasi. General supervision and guidance on the work development was provided by Eva Bezak. The manuscript was evaluated by Eva Bezak in terms of accuracy and interpretation of calculated results, conclusions reached, and general structure and flow.

8.2.3 Documentation

This paper was primarily written by Leyla Moghaddasi. Editing was performed by all authors.

Statement of Authorship

Title of Paper	**Development of an integrated Monte Carlo model for glioblastoma multiforme treated with Boron Neutron Capture Therapy**
Publication Status	☐ Published ☐ Accepted for Publication ☑ Submitted for Publication ☐ Publication Style
Publication Details	Moghaddasi, L., E. Bezak, submitted to *Physics in Medicine and Biology*

Principal Author

Name of Principal Author (Candidate)	Leyla Moghaddasi		
Contribution to the Paper	Conceptualized the initial idea, developed the model, analysed the results of calculations, and wrote the manuscript and acted as corresponding author.		
Overall percentage (%)	80%		
Signature		Date	07/09/2016

Co-Author Contributions

By signing the Statement of Authorship, each author certifies that:

i. the candidate's stated contribution to the publication is accurate (as detailed above);
ii. permission is granted for the candidate in include the publication in the thesis; and
iii. the sum of all co-author contributions is equal to 100% less the candidate's stated contribution.

Name of Co-Author	Prof. Eva Bezak		
Contribution to the Paper	General guidance and supervision, and manuscript revision.		
Overall percentage (%)	20%		
Signature		Date	07/09/2016

Development of an integrated Monte Carlo model for glioblastoma multiforme treated with boron neutron capture therapy

Leyla Moghaddasi
School of Physical Sciences, University of Adelaide, Adelaide, Australia
Department of Medical Physics, Adelaide Radiotherapy Centre, Adelaide, Australia
E-mail: `leyla.moghaddasi@adradcentre.com.au`

Eva Bezak
School of Physical Sciences, University of Adelaide, Adelaide, Australia
International Centre for Allied Health Evidence, University of South Australia, Adelaide, Australia
Sansom Institute for Health Research, University of South Australia, Adelaide, Australia

July 2016

Abstract.

Introduction. Glioblastomas of the brain are notorious for their extensive diffusion and high fatality rate. Boron Neutron Capture Therapy (BNCT) is a biochemically-targeted type of radiotherapy where thermal neutrons are captured by ^{10}B, resulting in the emission of high LET α-particles and recoiling ^{7}Li atoms. The aim of the current work is to develop a BNCT treatment modelling framework for a GBM model, taking into account cellular composition of brain with addition of appropriate ^{10}B concentrations, to determine optimal Clinical Target Volume (CTV) margins for BNCT. It also aims to investigate the effectiveness of GBM cell death following BNCT as compared to conventional x-ray therapy (XRT), reported previously.

Methods. The GBM BNCT modelling framework, developed in this work, integrated a cell-based dosimetry model (i.e. to calculate the dose deposited in individual GBM/normal cells) using GEANT4.9.6.p02, with previously-developed Microscopic Extension Probability (MEP) model by the current group (i.e. to predict tumour spread using clinical data) and an in-house developed epithermal neutron beam model. The system was defined as a cubic phantom divided to 20 μm side voxels (the average size of glioma cells) and irradiated with the epithermal neutron beam. Typical ^{10}B concentrations in GBM and normal brain cells were obtained from literature. Each cell was then assigned a material composed of a brain (ICRP-based NIST database) material and a ^{10}B concentration depending on its MEP status (i.e. the probability that the cell was a tumour clonogen). Results from the cell-based dosimetry model and the MEP models were combined to evaluate survival fractions (SF) for typical CTV margins of 2.0 & 2.5cm.

Results and Conclusion. Compared to conventional XRT, SF within the beam decreased by five orders of magnitudes and the total SF was reduced approximately four times for the simulated model by BNCT. CTV extension by 0.5 cm reduced the

SF by $61.7 \pm 0.2\%$ for this modality which are inferior to those calculated for XRT. In conclusion, BNCT results in a more efficient cell kill and the extension of the CTV margin may not increase the treatment outcome significantly.

Keywords: Glioblastoma, Monte Carlo, BNCT, Geant4
Submitted to: *Phys. Med. Biol.*

1. Introduction

Glioblastoma Multiforme (GBM) is the most malignant astrocytic glioma (i.e. grade IV) (P. & K. 2000) and is known for its aggressive proliferation and extensive invasion to normal tissue before any symptoms are presented. Biochemical features allow the tumour cells to invade extracellular matrix of the normal brain (Barth et al. 2005). GBMs present clinically with extensive hypoxia (i.e. both transient and acute), high intrinsic radioresistance with genetic heterogeneity and complexity. GBMs are associated with very poor prognosis and currently there is no curative treatment for this malignancy (Moghaddasi et al. 2012). Despite aggressive treatment regimens, including concomitant x-ray therapy and chemotherapy, less than 5% of patients are expected to survive more than two years (Mehrian Shai et al. 2015).

Determination of an optimal Clinical Target Volume (CTV) for x-ray radiotherapy can be difficult, as current imaging modalities are not able to detect the entire extent of microscopic extension of the tumour (ICRU 1999). The infiltrative growth pattern of GBM and its rapid peripheral expansion cause the CTV delineation of this type of tumour to be even more problematic. In addition, histopathological studies on the extent of tumour cell infiltration into normal tissue, beyond the Gross Tumour Volume (GTV), shows large discrepancies for this tumour type (Moghaddasi et al. 2012). Marginal and distant GBM recurrences reported in literature (Trépanier et al. 2012, Lee et al. 1999) could be attributed to the microscopic extension (ME) uncertainty while the high rate of local relapse (Gunjur et al. 2012, Chan et al. 2002, Oppitz et al. 1999) could be explained by intrinsic radioresistance of GBM stem cells and their other aggressive features.

1.1. Alternative treatment modalities - Boron Neutron Capture Therapy

Developments in x-ray External Beam Radiation Therapy (EBRT) in terms of increased precision of dose delivery over the last two decades have failed to offer improved prognosis for GBM patients. Recent technological advances have enabled other treatment modalities to be developed which could represent alternative therapies for high grade gliomas. Boron Neutron Capture Therapy (BNCT) is a biochemically-targeted type of radiotherapy based on fission nuclear reactions which occur when a thermal neutron is captured by a stable ^{10}B atom, resulting in emission of an energetic alpha particle (i.e. $\sim$ 2.06 MeV), a recoiling ^{7}Li nucleus (i.e. $\sim$ 0.84 MeV) and a 478 keV gamma ray, see equation 1. The alpha particles and ^{7}Li nuclei deposit their energy along the range approximately between 4 to 7 μm with a high Linear Energy Transfer (i.e. LET) of approximately 240 keV/μm (Van Dyk 1999, Allen 2006). This is a binary modality in which a suitable ^{10}B agent is taken up preferentially by malignant cells following administration of a boron pharmaceutical.

$$^{1}n +^{10} B \rightarrow^{7} Li +^{4} He + \gamma \tag{1}$$

Clinical trials of BNCT for malignant glioma were undertaken at Brookhaven National Laboratory (BNL) and Massachusetts Institute of Technology (MIT) between

1959 and 1961 (Slatkin 1991). The BNCT research encountered a large pause due to failure to show a considerable improvement of survival times (Slatkin 1991). Following the production of epithermal neutron beams (i.e. intermediate energy neutron beam enabling the treatment of deep-seated tumours) (Fairchild et al. 1990) and more suitable radio-pharmaceuticals containing ^{10}B, BNCT studies re-emerged in the 1980s (Diaz 2003) and encouraging results in terms of improvement in lifespan for GBM patients receiving this treatment were reported. Yamamoto *et al.* (Yamamoto et al. 2009) reported a 2-years survival rate of 53.3% for a series of 15 GBM patients which was superior to that observed in RTOG trial using EBRT (i.e. 35%) (Curran et al. 1993). Kawabata *et al.* (Kawabata et al. 2009) investigated the survival benefit of BNCT by comparison of survival times for 21 patients treated with BNCT against 27 patients treated with x-ray EBRT. An improved survival time, from 48.2 to 76.2% and 14.8 to 25.0% for 1 year and 2 year survival, respectively, was observed for patients treated with BNCT.

The BNCT modality has several physical and biological advantages over megavoltage x-rays for the radiotherapy of GBM with its inherent complexities:

(i) The treatment is delivered by high LET particles. The clustered damage, in form of DNA double strand and single strand breaks, produced by high LET radiation beam makes the repair of sublethal and potentially lethal damages less efficient. This increases the possibility to overcome GBM intrinsic radioresistance and aggressive features and offers a higher tumour kill/strelization compared to x-ray radiotherapy.

(ii) As BNCT is a binary modality, it has the potential to selectively deliver localized dose to tumour cells (i.e. those cells containing ^{10}B compound) dispersed in normal tissue, while minimizing normal tissue toxicity. This makes BNCT an appropriate modality for GBM which grows infiltratively rather than forming a solid tumour (Unkelbach et al. 2014).

(iii) Charged particulate radiation interacts with biological tissue predominantly through direct interaction of incident particles or secondary electrons from ionized atoms with DNA, rather than producing free radicals which in return cause chemical damage to the DNA. As a result, the cell killing process in BNCT is less sensitive to oxygen pressure compared to x-ray radiotherapy (Barth et al. 2004), which makes it advantageous for tumours with extensive hypoxia such as GBM (Barendsen et al. 1966).

Although BNCT theoretically appears very suitable for GBM and other tumours with aggressive features, the success of this technique depends on two important factors: the ratio of boron concentration in tumour and normal cells, a sufficient amount of ^{10}B in tumour cells (i.e. at least 20 μg/g or 10^9 atoms/cell (Barth et al. 2012)); and sufficient number of thermal neutrons delivered to the site of the tumour. Two common boron delivery agents currently used are: sodium mercaptoundecahydro-*closo*-dodecaborate ($Na_2B_{12}H_{11}SH$) or commonly named BSH; and (L)-4-dihydroxy-borylphenylalanine or BPA (Barth et al. 2012).

Boron concentration. Boron concentrations in normal brain and glioma cells using these agents have been investigated in several studies in literature. In an animal study, Barth *et al.* (Barth et al. 1997) reported a ^{10}B concentration of 11.8 ± 3.5 and 94.5 ± 69.1 μg/g in normal brain and tumour cells respectively, using BPA with induced Blood-Brain Barrier Disruption (BBB-D), and 4.4 ± 1.8 and 48.6 ± 17.2 μg/g in normal brain and tumour cells respectively, using BSH with BBB-D. As listed in the table 1, other studies suggest a smaller ratio of tumour to normal tissue ^{10}B concentrations (Capala et al. 2003, Joensuu et al. 2003, Diaz 2003, Coderre et al. 2004, Palmer et al. 2002, Riley et al. 2003). Capuani *et al.* (Capuani et al. 2008) investigated the effect of preloading L-DOPA prior to BPA infusion and concluded that L-DOPA had a potential use as BPA accumulation enhancer, increasing tumour ^{10}B concentration from 33.5 ± 7.5 μg/g without preloading to 88.3 ± 12.1 μg/g with preloading.

Table 1. A summary of ^{10}B concentrations in normal tissue and tumour cells

Author	Dose (mg/Kg)	Drug	^{10}B concentration (μg/g)	
			Normal brain (NB)	Tumour cell
Barth (Barth et al. 2012)	500	BPA	11.8 ± 3.5	94.5 ± 69.1
Barth (Barth et al. 2012)	65	BSH	4.4 ± 1.8	48.6 ± 17.2
Capala (Capala et al. 2003)	900	BPA	15-34	3.7 × NB
Joensuu (Joensuu et al. 2003)	290	BPA	12-15	3.5 × NB
Diaz (Diaz 2003)	250-330	BPA		3.5 × NB
Coderre (Coderre et al. 2004)	250-330	BPA	12-16	3.5 × NB
Palmer (Palmer et al. 2002)	250-330	BPA	10-15	3.5 × NB
Riley (Riley et al. 2003)		BPA	18	65

Neutron spectrum for boron neutron capture therapy. An optimal neutron spectrum for BNCT should contain high thermal (E < 0.5 eV) and epithermal (0.5 eV - 10 keV) and minimal fast neutron (E > 10 keV) components. The cross section for the ^{10}B(n,α)^{7}Li neutron capture reaction is very high in the thermal energy range of neutrons. However, the penetration for thermal neutrons is limited. Consequently, epithermal neutrons are more useful for clinical purposes as they lose energy while traversing the medium and will undergo boron neutron capture at larger depths.

1.2. Monte Carlo particle simulations

Bio-mathematical and computational modelling has been recognized as a valuable tool to simulate biological systems and to provide predictions of the probable response of a tumour to radiotherapy for a variety of circumstances, including different therapeutic regimens (e.g. different CTV margins) and treatment modalities.

Geant4 (Agostinelli et al. 2003) is a flexible and powerful MC toolkit capable of simulating complicated experimental set-ups. This MC toolkit, which is the result of an ongoing worldwide collaboration, has been developed to precisely track the passage of radiation through matter for a diverse range of particles, processes over an extended energy range. The diverse functionality, inclusion of hadronic processes and performance optimization features make Geant4 a suitable MC software/tool for BNCT simulation. Nevertheless, the use of Geant4 for to simulate a BNCT radiation treatment framework is limited to our understanding and therefore on the input parameters and geometries simulated.

Previously, a comprehensive and flexible GBM x-ray radiation treatment modelling framework was developed by our group (Moghaddasi et al. 2015). Using Geant4 and MATLAB® (Mathworks, Natick, MA), GBM and its surroundings, containing both normal and clonogenic cells, was modelled. The model was used to evaluate current CTV practices applied in external radiotherapy (Moghaddasi et al. 2015), in terms of the surviving fraction of GBM tumour cells after treatment with 6 MV photon beam for several types of clonogenic infiltration distributions. The model was further developed to incorporate GBM heterogeneous radiosensitivity and hypoxia.

The purpose of the current work was to develop a BNCT treatment modelling framework for evaluation of current CTV margin extensions using the previously-developed GBM model. Preceding this work, a BNCT beam model was developed and verified against published data to replace the 6 MV x-ray beam model (Moghaddasi et al. 2015). The following sections briefly outline the architecture of the GBM model and the BNCT beam model designed previously.

1.3. Review of previously-developed microscopic scale GBM treatment model

The comprehensive GBM treatment modelling framework developed consisted of a microscopic extension GBM model, a tumour irradiation model, and a Survival Fraction (SF) algorithm (Moghaddasi et al. 2015, **?**). Figure 1 shows the genearal structure of the GBM treatment modelling developed in the previous work.

The cell-based dosimetry module was developed using Geant4 (version 4.9.6.p01) particle tracking toolkit (Agostinelli et al. 2003) to calculate the absorbed dose in each cell within a spatial brain glioblastoma model. The scale of the geometry was chosen to cover the entire extension of GBM microscopic disease in all directions. To enable cellular based dosimetry, the volume was divided into 20 μm cubic voxels (i.e. the average size of glioma cells (Nafe et al. 2005)), so that each voxel represented a cell.

Models of GBM Microscopic Extension Probability (MEP) with various distributions were developed in MATLAB® . The invasion of tumour cells within normal brain tissue was simulated using a probability distribution function, assigning each cell with a probability of being a tumour cell as a function of distance from the GTV. This probability distribution function was obtained by collecting and combining (i.e. a weighted average to the number of patients in each study) the published data reporting on recurrence pattern of GBM (Aydın et al. 2001, Burger et al. 1988, Trépanier et al. 2012, Wallner et al. 1989), see figure 2 (Moghaddasi et al. 2016*b*). The function

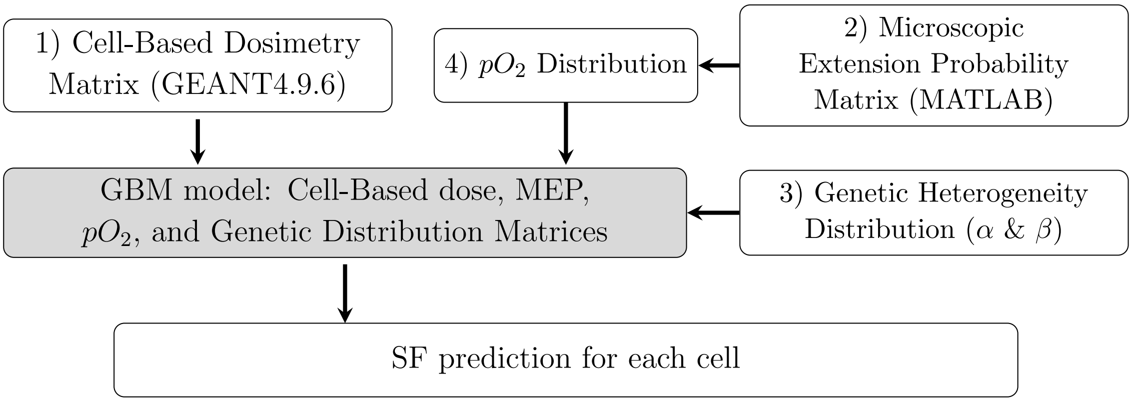

Figure 1. Schematic diagram showing the structure of the model components designed in the previous work (Moghaddasi et al. 2015).

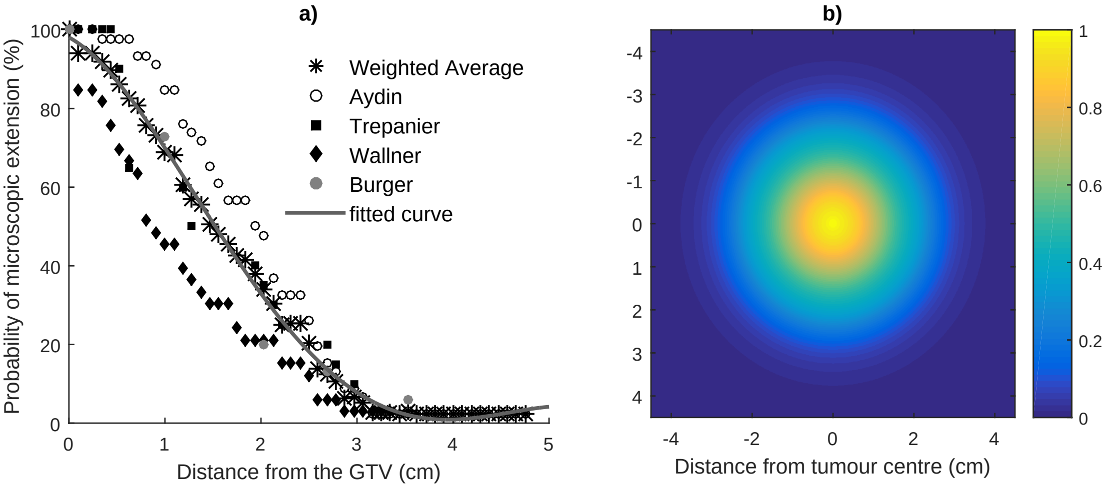

Figure 2. a) Clinical studies investigating the extent of microscopic extension in GBM patients. The function fitted to combined results (i.e. a three-term Gaussian function) was considered as the basis for the MEP models; b) Isotropic circular MEP distribution. As illustrated some part of the microscopic disease is not encompassed (i.e. falls beyond the beam and receives $< 90\%$ dose) in the PTV (i.e. 2.5 cm related to 2.0 cm CTV margin); courtesy of Moghaddasi *et al.* (Moghaddasi et al. 2016*b*).

fitted to combined data was considered as the basis for MEP models and was called the clinical function. An isotropic circular MEP (i.e. 2D distribution of ME) was modelled as this assumption is made in clinics for delineation of CTV margins. For this pattern (i.e. circular-clinical MEP), both the tumour and its ME were considered spherical where the MEP reduced isotropically in all directions based on the clinical function.

Finally, the dose matrices calculated in Geant4 were exported into MATLAB® and were combined with the MEP models to obtain cell-based survival fractions. The code initially consisted of a homogeneous population of GBM cells with normal oxygen pressure. The GBM model could incorporate other biological characteristics of GBM cells including heterogeneous radiosensitivity and hypoxia (Moghaddasi et al. 2016*b*). Cell Survival probabilities (SPs) for each cell were then calculated using Linear Quadratic (LQ) theory for each cell, and were used to calculate SFs for any specific region (e.g. within the beam, and penumbra).

1.4. Review of the BNCT beam model

Previously we reported on a BNCT epithermal neutron beam was developed using Geant4.9.6, to be used for development of a BNCT treatment modelling framework (Moghaddasi et al. 2016*a*), which is the objective of the current work. The BNCT beam model was verified against published measured and calculated data. A thorough sensitivity study was conducted on the effect of tumour to normal tissue boron concentration on the ratio of resulting boron to residual (i.e. non-selective dose including thermal, and fast neutron and gamma dose) dose. The dependence of this ratio on the proportion of thermal energy neutron the epithermal neutron spectrum was investigated.

2. Methods and Materials

Similar to the previously-developed models for x-ray therapy, the GBM treatment modelling platform using BNCT consisted of a cell-based dosimetry system for BNCT treatment, a microscopic-scale GBM model (i.e. combination of MEP, radiosensitivity), and a SF algorithm. For the BNCT treatment, however, the cell-based dosimetry module is not independent of the GBM model as the dose deposited in the cells depends on cellular boron concentration which is in itself dependant on whether the cell is a tumour or normal cells. These components are discussed in following sections.

2.1. Cell-based dosimetry for BNCT treatment

2.1.1. Geometry design The architecture of the geometry designed for cell-based dosimetry is shown in figure 3. The simulated geometry was a $9\ cm \times 9\ cm \times 2.2\ cm$ brain phantom consisting of a spherical GTV (i.e. 1 mm diameter) and a ME region (i.e. spanning up to 4.1 cm from the GTV) and a 0.4 cm PTV. This enclosed a volume of $9\ cm \times 9\ cm \times 0.9\ cm$ with initially assigned brain material (the volume in checked print in figure 4). This volume was divided into $20\ \times 20\ \times 20\ \mu m^3$ voxels to each represent a cell. While the Geant4 particle tracking was performed in the entire geometry, the dose was scored in a single slice with $9\ cm \times 9\ cm \times 20\ \mu m$ dimensions located at 2.0 cm from the phantom surface, perpendicular to the beam direction.

Bio-distribution of boron distribution and brain material. In order to simulate the brain which is injected by a ^{10}B agent in Geant4, each cell was assigned a brain material and a boron concentration (see steps 2 and 3 in the figure 3). The required fields to specify and construct the brain material (i.e. name, density, and atomic constituents) in Geant4 were taken from National Institute of Standards and Technology

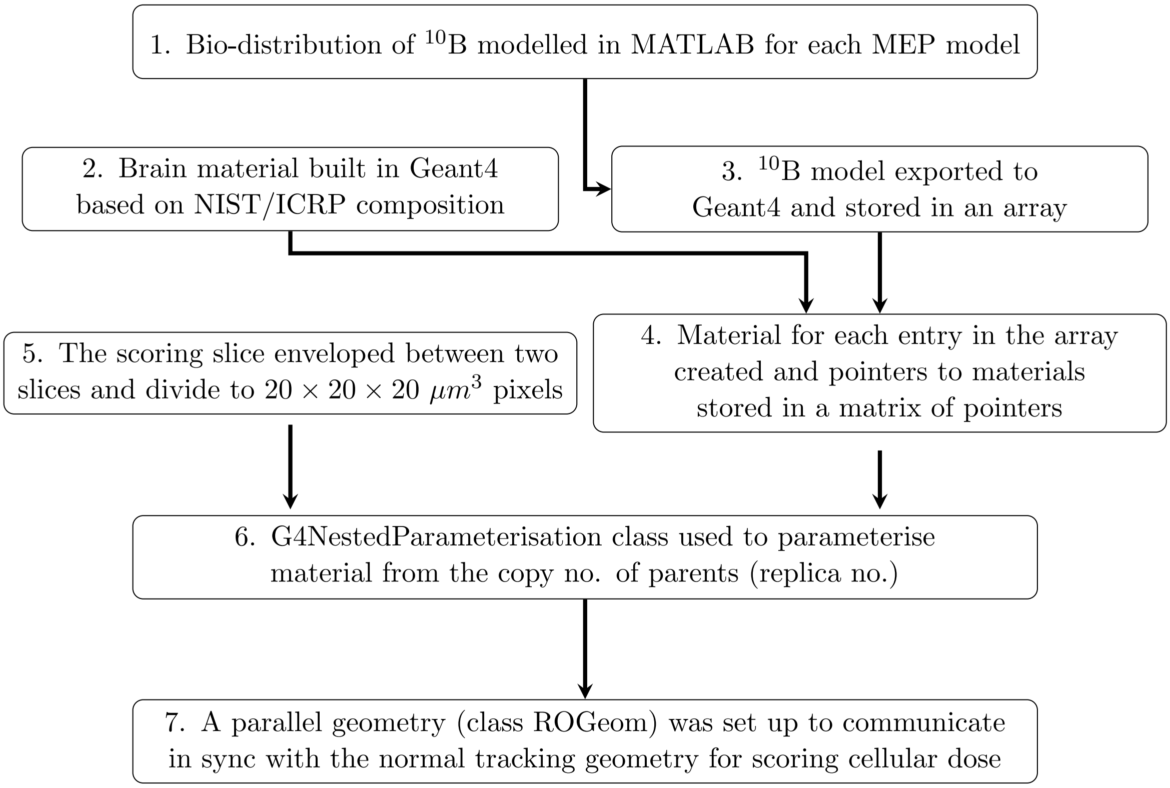

Figure 3. Schematic diagram showing the architecture of the geometry of Geant4 cell-based dosimetry system in the current work.

(NIST) Listings, Compositions of Materials used in STAR Databases webpage: *http://physics.nist.gov/cgi-bin/Star/compos.pl?matno=123*, and listed in table 2.

Table 2. Atomic constituents of brain material taken from National Institute of Standards and Technology (NIST) Listings, Compositions of Materials used in STAR Databases webpage.

source by:*http://physics.nist.gov/cgi-bin/Star/compos.pl?matno=123*

Symbol	Fraction Mass	Symbol	Fraction Mass
H	0.110667	S	0.001770
C	0.125420	Cl	0.002360
N	0.013280	K	0.003100
O	0.737723	Ca	0.000090
Na	0.001840	Fe	0.000050
Mg	0.000150	Zn	0.000010
P	0.003540		

Based on the data summarized in table 1, boron concentrations of 13 and 45.5 (normal brain boron concentration ×3.5) $\mu g/g$ were assumed in normal brain and GBM cells, respectively. Using these concentrations a linear function was derived to determine cellular boron concentration as a function of the probability that the cell is a tumour clonogen (i.e. MEP), equation 2:

$$B\_concentration_{ij} = \ 32.5 \times MEP_{ij} + 13 \tag{2}$$

where $B\_concentration_{ij}$ is the boron concentration in the cell (voxel) ij with MEP_{ij} probability that the cell is a tumour cell. The linear function was then converted to a step function with twelve steps. The bio-distribution of boron (i.e. the step #1 in the flowchart 1) developed in Matlab was exported to Geant4 and stored in an array. Using the brain material and boron concentration array, twelve composite materials, corresponding to each boron concentrations, were simulated using G4Element class. The pointers to each material were stored in a array of pointers to enable parametrization of the geometry.

Volume division to the size of GBM cells and material allocation. In order to distribute corresponding boron concentration to cells, the brain volume of of 9 $cm \times 9$ $cm \times$ 0.9 cm dimensions was divided into 20 μm side voxels, so that each voxel represented a cell. The divisions have been made in three layers. Firstly, using *G4Replica*, the brain volume was divided in x and y direction to 3 × 3 × 9 mm^3 voxels. As each replicated volume is indistinguishable from each other, another method, called nested parametrisation, was implemented for second-layer division (i.e. 9 mm to be divided by 3 to give 3 mm voxel size in z direction) as well as material parametrisation. Using *G4NestedParameterization* class, the material for each voxel was selected from the array of pointers (i.e. to materials) based on replica numbers of each voxel to relate to its corresponding material. Finally, the central slice was divided into 20 μm side voxels to allow cell-based dosimetry. As the parametrized volumes have the limitation that they cannot have daughter volumes, this division was implemented using Readout (RO) geometry method provided by Geant4. RO geometry is a parallel geometry which acts as a virtual tracking geometry, through which the real geometry is scanned. In RO geometry the scoring plane was divided to $20 \times 20 \times 20$ μm^3 voxels (i.e. the scoring plane is the central plane in dark colour on the right side of figure 4).

Given the potentially large amount of memory required for such a geometry, CPU time and RAM optimization methods were implemented: To parametrize the geometry to heterogeneous material composition, rather than direct three-dimensional parametrized volume method, nested parametrisation method was utilized which requires much less memory for geometry optimization, resulting in faster navigation for systems with large number of voxels; The brain volume was defined as a sub-detector "region", using G4Region, to allow a more detailed simulation to occur only in this region where it is actually required. As a result the processing speed was markedly increased.

2.1.2. Particle tracking and dose scoring Our previously-reported BNCT beam model (Moghaddasi et al. 2016*a*), simulating the epithermal spectrum from the LVR-15 reactor at Research Centre Rez (Marek et al. 2014) with its realistic energy distribution was

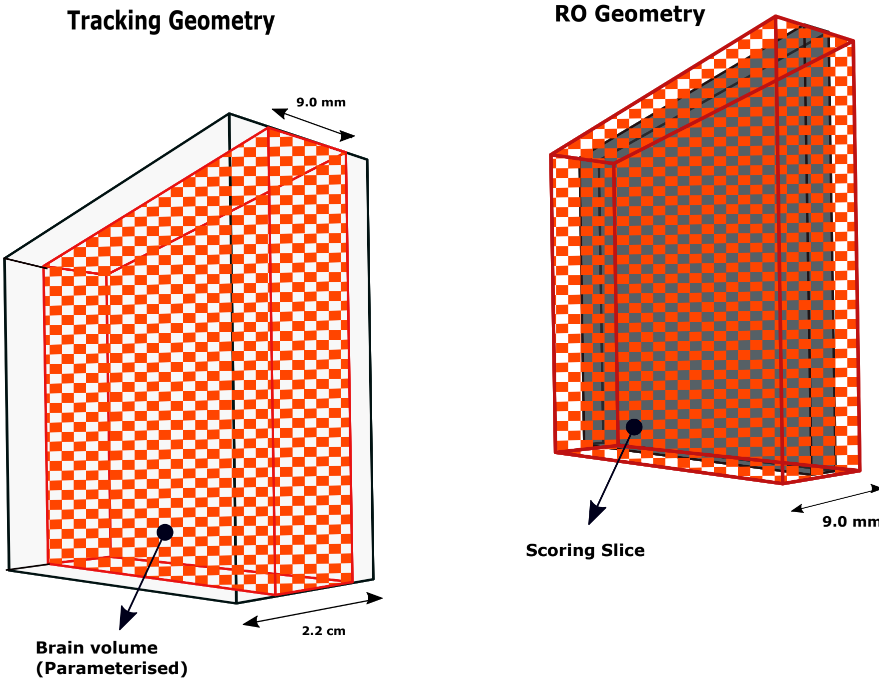

Figure 4. The real tracking geometry is shown on the left. A 9 $cm\times$ 9 $cm\times$ 2.2 cm box enclosed the brain volume (9 $cm\times$ 9 $cm\times$ 9 mm) which was divided to 3 $\times$ 3 $\times$ 3 mm^3 and the material parametrisation was implemented for all voxels within. On the right, the RO geometry is shown which consisted of the brain volume enclosing the scoring plane located in the middle of the volume and divided into 20 $\times$ 20 $\times$ 20 μm^3 (i.e. the size of glioma cells). The RO geometry communicates in sync with tracking geometry to score the dose in the cells defined in the scoring plane. It should be noted that this diagram is not to scale to allow illustration of details.

used in this work. The system (i.e. geometry described above) was irradiated with the conical epithermal neutron beam model. Two beam sizes were considered, 2.5 and 3.0 cm corresponding to 2.0 and 2.5 CTV margin extensions, respectively at 100 cm Source to Surface Distance (SSD). The model was designed to deliver the treatment in one fraction with a mean maximum tumour dose of 73.4 RBE-Gy, according to the reported mean maximum tumour dose in literature (Kawabata et al. 2013, Yamamoto et al. 2009, Kageji et al. 2014, Morris et al. 1997).

Dose conventions. Epithermal neutron beams designed for BNCT, predominantly produced by fission reactors and accelerators, have broad spectra and contain unwanted fast neutron and gamma contaminations. Four major dose components should be considered when such spectra interacts with biological medium (the terminology has been adopted from Harvard-MIT BNCT treatment planning protocol (Zamenhof et al. 1996)):

(i) Boron dose from thermal neutron capture through ^{10}B(n,α)^{7}Li reaction (which is the addition of the dose from ^{7}Li and alpha particles);

Table 3. Relative biological effectiveness factors and CBE factor (i.e. only for boron dose) for four principal dose components (Van Dyk 1999).

	Photon w_γ	Fast neutron w_F	Thermal neutron w_T	Boron w_B
Brain tissue	0.5	3.2	3.2	1.3
Tumour tissue	0.5	3.2	3.2	3.8

(ii) Thermal neutron dose as a result of thermal neutron capture by nitrogen atom in biological tissue in the reaction ^{14}N(n,p)^{14}C;

(iii) Gamma dose from neutron capture by hydrogen atom and also from gamma contamination in the incident neutron beam;

(iv) Fast neutron dose which is due to elastic and inelastic scattering (e.g. ^{1}H(n,n$'$)^{2}H) and several possible nuclear reactions (e.g. ^{16}O(n,α)^{13}C) (Palmer et al. 2002).

To account for the variability of radiobiological effects of different physical dose components of a neutron beam spectrum incident on biological tissue, current convention in clinical BNCT practices was adopted. Each physical dose component was weighted by its respective Relative Radiobiologic Effectiveness (RBE) factor (i.e. RBE is the ratio of the dose of a reference x-ray beam and the dose of the test radiation producing the same biological endpoint), as listed in table 3 (Van Dyk 1999). The correction factor used for boron products reaction is called Compound Biological Effectiveness (CBE) because it depends on the boron carrier used to put boron in the cell (Coderre et al. 2001).

Therefore, the total RBE-Gy dose, d_{wij}, was calculated as:

$$d_{wij} = w_\gamma d_{\gamma ij} \ + w_F d_{Fij} \ + w_T d_{Tij} \ + w_B d_{Bij} \tag{3}$$

where $d_{\gamma ij}$, d_{Fij}, d_{Tij}, and d_{Bij} were gamma dose, fast neutron dose, thermal neutron dose, and boron dose (i.e sum of lithium and alpha dose) in voxel/cell ij, respectively.

For this application packaged physics list, Quark-Gluon String Precompound Binary Cascade High Precision Neutron (QGSP_BIC_HP), provided by Geant4 was implemented to simulate particle tracking by assigning particles with appropriate processes and cross sections. To ensure that nuclear emissions and fragments, particularly alphas and ^{7}Li particles from boron capture reaction with minimum range of approximately 4 μm, are individually tracked and their corresponding deposited doses are scored, the production threshold/cut off-value was set to 4 μm for particles other than gammas and a 0.01 mm for gamma particles. The step size was set to 4 μm. These production thresholds were assigned only to the volume specified as "region" (i.e. the brain volume). Default thresholds (i.e. 0.7 mm) were used for the rest of geometry.

Several techniques have been provided by Geant4 to retrieve information through particle tracking (e.g. absorbed dose). In this simulation a sensitive detector technique was implemented to score the dose from individual particles in the scoring plane. A dummy sensitive detector associated with the RO geometry/parallel geometry was built and was linked to the sensitive detector (i.e. associated with real geometry) to enable synchronized communication of parallel and real geometries for scoring the absorbed dose in each cell.

Parallel simulations on 96-CPU 64-bit Linux clusters (i.e. South Australia (SA) Tizard supercomputer, the University of Adelaide) were performed for a total number of 5.8×10^9 particles, running for ~ 7 days. As a result, four dose matrices (i.e. ^{7}Li, alpha, gamma and residual dose consisting of fast neutron and thermal neutron doses) were calculated for each core and the results were combined.

2.2. Cell survival probability calculation

Four dose matrices calculated in Geant4 were exported into MATLAB. Using equation 3, the total RBE-Gy dose was calculated and was combined with the circular MEP model to obtain cell survival probability for each cell using equation 4. In the current work, the code consisted of a homogeneous population of GBM cells in terms of gene type with radiosensitivity equal to: $\alpha = 0.281$ and $\beta = 0.02$. These values were the mean of Gaussian distribution of α and β values for several GBM cell lines reported in the previous work (Moghaddasi et al. 2016*b*).

$$SP_{ij} = MEP_{ij} e^{-(\alpha d_{ij} + \beta d_{ij}^2)} \tag{4}$$

where MEP_{ij} is the probability that the cell ij is a tumour clonogen, and d_{ij} is the absorbed dose in the cell ij. SP_{ij} denotes the survival probability of the cell ij. It was postulated that Oxygen Enhancement Ratio (OER) (i.e. the radiobiological quantity to determine The effect of different pO_2 levels on cellular radiosensitivity and is expressed as the ratio of the radiation doses in a certain oxygen condition and in anoxic conditions required to produce the same radiobiological effect) is one for high LET, particulate radiation (Barendsen et al. 1966). Equation 6 was used to calculate number of surviving cells and SF for regions of interest:

$$\text{surviving cells in the ''region''} = \sum_{i,j} SP_{ij}(i,j \in \text{''}region\text{''}) \tag{5}$$

$$SF_{\text{region}} = \frac{\text{surviving cells in the ''region''}}{\text{total number of tumour cells before treatment}} \tag{6}$$

The SF within the beam region (i.e. the PTV), the SFs within the penumbra region (defined in this study as the region extending 5.0 mm beyond the PTV) and the total SFs (i.e. including in-beam, penumbra region, and out of field (< 1% dose coverage)) were first calculated/predicted for a 2.0 cm CTV margin. SF calculations were repeated four times using only four dose matrices from Geant4. The results were compared with those calculated for homogeneous-hypoxic GBM tumour model for x-ray therapy published previously (Moghaddasi et al. 2015).

$$SF_{within\ the\ beam} = 100 \times \frac{\text{surviving cells within the PTV}}{\text{total number of tumour cells before treatment}} \tag{7a}$$

$$SF_{penumbra\ region} = 100 \times \frac{\text{surviving cells in the penumbra region}}{\text{total number of tumour cells before treatment}} \tag{7b}$$

$$SF_{total} = 100 \times \frac{\text{surviving cells within the PTV, penumbra region, and out-of-field}}{\text{total number of tumour cells before treatment}} \tag{7c}$$

To further examine the pattern of SF within the beam and beyond, the differential SF was calculated in 0.5 mm steps and plotted versus distance from the tumour centre for 2.0 cm CTV margin. The differential SF was defined as the ratio of the number of surviving tumour clonogens to the initial number of tumour cells before treatment in 0.5 mm rim at each distance from the tumour centre. A comparison of these results were made with differential SF for photon therapy using the previous model.

To obtain a quantitative measure of SF reduction with increased treatment margins, the CTV margin was extended to 2.5 cm from 2.0 cm. The radius of the GTV, and the PTV margins remained 0.1 cm and 0.4 cm, respectively. The Geant4 simulation was run on parallel cores 96 CPU Linux clusters for 3.0 cm beam size. The change in SFs, as a result of the CTV increase by 0.5 cm, was calculated using equation 8.

$$SF_{change} = 100 \times \frac{SF_{2.0\ cm} - SF_{2.5\ cm}}{SF_{2.0\ cm}} \tag{8}$$

3. Results

3.1. Geant4 cell-based dosimetry for BNCT treatment

Figure 5 shows the axial profile of the calculated boron dose (i.e. combined ^{7}Li and alpha dose matrices). It is evident that the dose from boron is maximum within the GTV region (i.e. 1 mm radius) and reduces at larger distances from the GTV as the result of reduced boron concentrations in cells.

The distribution of the total RBE dose matrix in the scoring plane is shown in the figure 6 (a). It was demonstrated that there was considerable scattered beyond the PTV.

The axial profile of the total RBE dose in the scoring plane is presented in figure 6 (b). As expected, the axial profile for BNCT was shown to be curving down in the PTV region, which is in contrast to the axial profile of conventional radiation treatment, being reasonably flat in the PTV region.

3.2. Assessment of survival fractions for 2.0-cm clinical target volume margin

The results in this section are presented in terms of (a) SF within the beam (i.e. the PTV), (b) SF within the penumbra region (i.e. 5.0 mm beyond the PTV), (c) total SF (i.e. including out of beam (i.e. $< 1\%$), within the beam and penumbra region) utilizing circular MEP model with for a GBM consisting of homogeneous population of cells with radiosensitivity expressed in terms of LQ model parameters of $\alpha = 0.281$ and

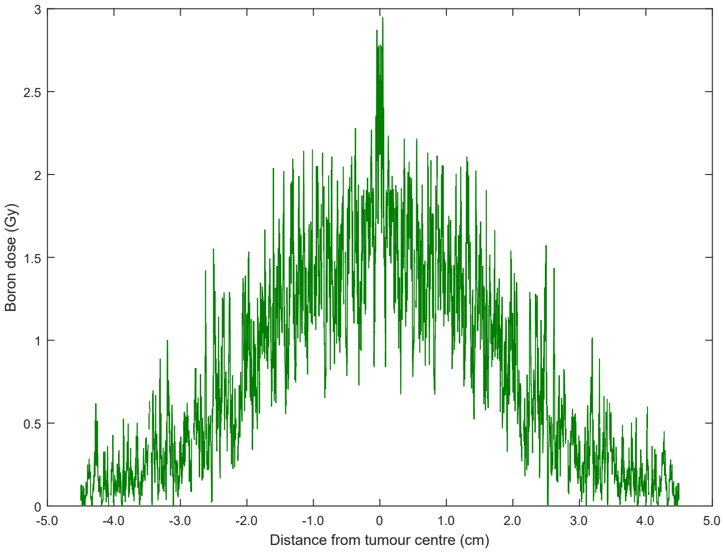

Figure 5. Axial profile of the calculated cell-based boron dose distribution (i.e. combined ^{7}Li and alpha dose matrices) in the scoring plane versus distance from the tumour centre. The statistical uncertainty of the calculated results was ~ ±12.5%.

Table 4. Survival fractions (SFs) in different regions for homogeneous-hypoxic circular MEP model for BNCT and conventional photon modalities.

	BNCT modality	X-ray conventional modality
SF within the beam (%)	$(4.13 \pm 5.82) \times 10^{-7}$	$(3.22 \pm 0.18) \times 10^{-3}$
SF within the penumbra region (%)	2.74 ± 0.49	6.71 ± 0.88
Total SF (%)	3.92 ± 0.68	12.79 ± 0.97

$\beta = 0.02$. The results for conventional x-ray therapy have also been presented using the previously-developed model (Moghaddasi et al. 2015) for efficiency comparison purpose.

Table 4 summarizes SF in the regions of interest and total SF. The SF within the beam has reduced by about four orders of magnitude for BNCT modality as opposed to conventional x-ray therapy. While not at the same magnitude, SF in penumbra region also showed a marked improvement using BNCT as compared to photon therapy. The results indicate a reduction in total SF of four orders of magnitude between BNCT and conventional photon therapy. It is worth to note that for circular MEP model, the total number of tumour clonogens and the number of tumour clonogens in the penumbra region before treatment were 2908500 and 299420, respectively.

Figure 7 shows differential SF curves in 0.5 mm steps using homogeneous-hypoxic GBM model treated by BNCT technique. The results with conventional x-ray therapy has also been presented to allow comparison and analysis of the pattern of SF at any distance. Considering the logarithmic scale on the vertical axis (i.e. differential SF), a marked decrease in the SF within the beam was observed for BNCT as compared

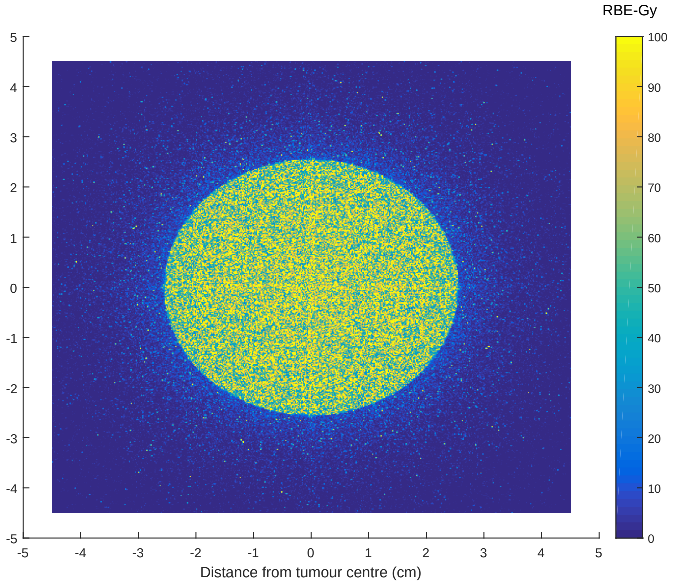

(a) RBE dose distribution in the scoring plane versus distance from the tumour centre.

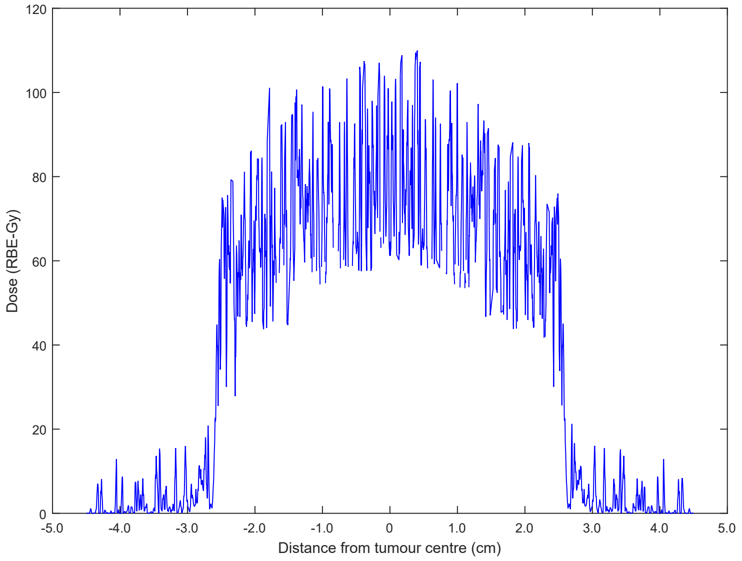

(b) Axial RBE dose in the scoring plane versus distance from tumour centre.

Figure 6. Cell-based RBE dose using equation 3 and four Geant4-calculated cellular dose matrices. The statistical uncertainty of the calculated results was $\sim \pm 10\%$.

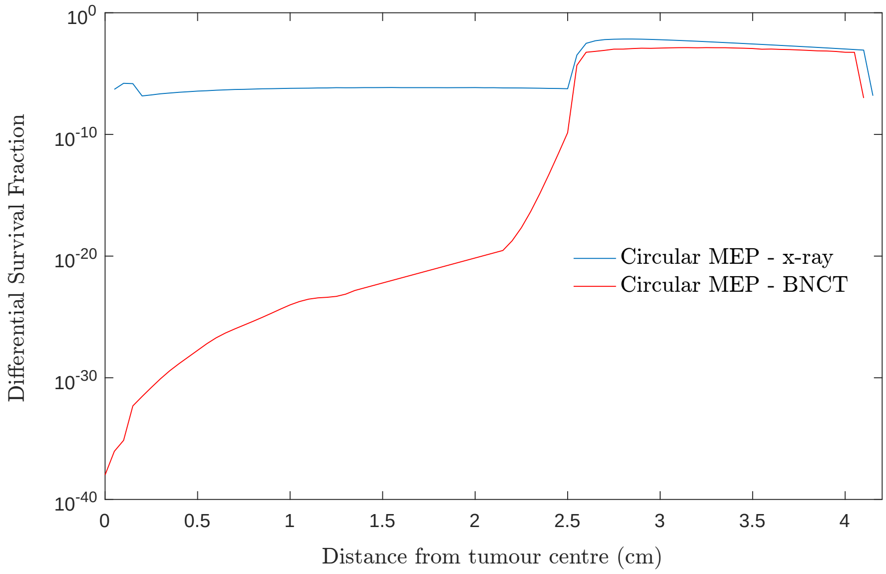

Figure 7. Comparative representation of differentiated SF versus distance from tumour centre for two scenarios: homogeneous-hypoxic GBM models treated by 1) BNCT; and 2) conventional x-ray therapy. These graphs are obtained applying circular MEP model and 2.0 cm CTV (i.e. 2.5 cm beam radius).

to x-ray modality. The SF within the beam for BNCT treatment gradually increased by distance from the tumour centre prior it showed a rise in the penumbra region. Nevertheless, the SF remained almost the same throughout of the beam area for the GBM model treated with x-ray. This can be attributed to the dose gradient within the beam for BNCT treatment, see figure 6 (b).

3.3. Quantification of survival fraction reduction following clinical target volume margin extension

A comparison of the cumulative survival fractions corresponding to a 2.0 cm CTV margin (i.e. 5.0 cm PTV) and 2.5 cm CTV margin (i.e. 6.0 cm PTV) for the clinical MEP model for genetically homogeneous-hypoxic GBM model are shown in figure 8. As illustrated, BNCT treatment results in significantly lower SF for both 2.0 and 2.5 cm radii beams.

Calculated SF_{change} data, as a result of the CTV increase by 0.5 cm, are summarized in table 5. As suggested by these results, the SFs for homogeneous-hypoxic GBM treated by BNCT was reduced by 53.83 ± 0.31% assuming circular MEP. The reduction in SF as a result of the CTV extension (i.e. by 72.93 ± 0.06%) was more pronounced for homogeneous-hypoxic GBM treated by conventional x-ray therapy.

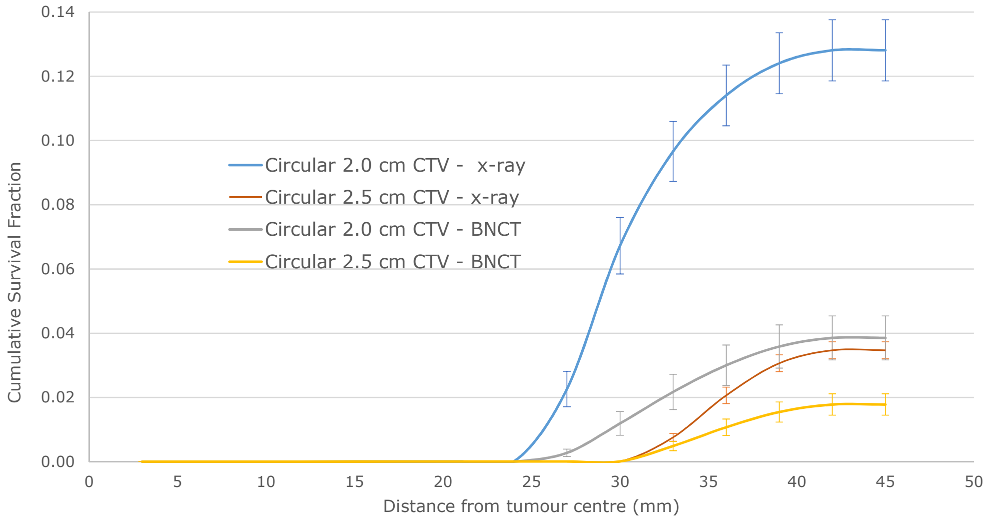

Figure 8. Cumulative SF versus distance from tumour centre for 2.0 and 2.5 cm CTVs applying the circular microscopic extension distribution model for a homogeneous-hypoxic GBM treated by BNCT as compared to conventional x-ray therapy.

Table 5. Changes in SFs as a result of the CTV extension (from 2.0 to 2.5 cm)

Treatment modality	SF- 2.0 cm CTV (%)	SF- 2.5 cm CTV (%)	$SF_{change}(\%)$
BNCT	3.85 ± 0.68	1.78 ± 0.33	53.83 ± 0.31
Conventional x-ray therapy	12.81 ± 0.95	3.47 ± 0.26	72.93 ± 0.06

4. Discussion

In the previous report an integrated MC quantification tool was developed for evaluation of survival fraction depending on GBM tumour clonogenic microscopic distributions (i.e. MEP distributions) (Moghaddasi et al. 2015, Moghaddasi et al. 2016*b*) and different CTV margin extensions (i.e. 2.0 and 2.5 cm) using photon EBRT. The establishment of a cell-based simulation platform allowed for application of different radiation sources/modalities and different radiobiological and physical (e.g. cellular material composition) cell properties. In the current work, the GBM model was utilized to develop a BNCT GBM treatment modelling platform for a homogeneous population of GBM cells with cellular oxygen pressure obtained from clinical oxygenation distributions.

The rationale for BNCT treatment is the ability to deliver localized high LET absorbed dose to tumour cells containing sufficient number of boron atoms while minimizing the dose to normal tissue cells which contain fewer number of boron atoms. Therefore an effective and non toxic BNCT depends on selective tumour cell uptake of boron compound or ratio of tumour to normal tissue boron concentration. In the previous report (Moghaddasi et al. 2016*a*), the sensitivity of boron dose to this ratio was investigated. It is known, however, that glioblastoma multiforme tumours present with low uptake due to their necrotic and hypoxic nature (Mallesch et al. 1994) as compared to other tumours (e.g. melanoma). Ongoing research is addressing this issue by investigating how the tumour uptake can be enhanced. An encouraging tumour to blood boron concentration ratio of 8.3 ± 0.7 was obtained using L-DOPA administration prior treatment (Capuani et al. 2008). In this study, however, a ratio of 3.5 was considered as this ratio is the most commonly assumed in literature, see table 1.

The calculated boron dose showed a peak within the GTV region and was followed by a sharp gradient reduction and reached to ~ 30 % of its maximum at 2.5 cm from the tumour centre, see figure 5. This caused an arch-shaped curve within the beam region (i.e. which is normally flat for conventional EBRT) as shown in axial profile of total RBE (figure 6 (b)). A beam with such a profile allows to escalate the dose within the GTV as the absorbed dose reduces at larger distances due to reduced boron concentration which is in itself dependant on the probability that the cell is a tumour cell. A hypothetical high ratio of tumour to normal tissue boron concentration could result in a profile with a higher-raised arch which could deliver a more selective and less toxic treatment.

Following BNCT treatment the calculated SF within the beam region decreased by four orders of magnitude as compared to conventional photon EBRT for homogeneous hypoxic GBM (table 4). The calculated number of surviving cells within the beam (i.e. $SF_{\text{within the beam}} \times$ total number of tumour cells before treatment) was ~ 0.01 which suggest that BNCT should be able to provide local tumour control for GBM. Given, in the current work a simplified model of GBM with homogeneous population and isotropic infiltration distribution has been simulated, this finding should be considered with care. Nevertheless, published clinical reports, while scarce, are supportive of this result. Miyatake (Miyatake et al. 2006) presented a case report of the recurrence pattern of a gliosarcoma patient after BNCT and it was demonstrated that gliosarcoma responded well to BNCT and the recurrence occurred in the periphery of the tumour outside the field. Likewise, an evidence of favourable local tumour control of high-grade meningiomas using BNCT was demonstrated in a cohort of 20 patients studied by Kawabata (Kawabata et al. 2013). Only three out of twenty patients had local treatment failure (Kawabata et al. 2013). It should be noted that, high-grade meningiomas show a slightly higher ratio of tumour to normal brain boron concentration (3.7 ± 0.8) (Kawabata et al. 2013) compared with malignant gliomas and as a result the local control for GBM should be slightly inferior to that of meningiomas. Matsuda (Matsuda et al. 2009) analysed the failure pattern of 8 GBM patients treated by BNCT. None of the patients recurred within the GTV and 6 out of 8 patients showed failure in low dose region of CTV-2 (i.e. GTV + 2 cm). The low dose regions were attributed to low boron concentration and insufficient delivery of thermal neutrons. An improved local control for GBM should be expected if these two factors are conquered. These factors were also identified in the previous report of our group.

Survival fraction in the penumbra region was also investigated to quantify the contribution of local invasion/microscopic disease, which could be eliminated by selecting a slightly larger CTV margin, to total SF. The SF in penumbra using BNCT was lower than that using photon EBRT by approximately 3 times. This could be attributed to scatter nature of neutron interactions as well as boron dose produced by neutrons which have thermalized through scattering laterally and undergone boron neutron capture fission. The total SF was also significantly lower (i.e. by ~ 3 times) for BNCT as compared to photon therapy.

The differentiated curves presented in figure 7 allowed analysis of SF at any distance. Given the logarithmic scale on the vertical axis, it can be observed that SF within the beam is significantly lower using BNCT as compared to photon therapy. Unlike photon EBRT, SF for BNCT gradually increases as a function of distance from the tumour centre as a result of boron dose reduction. This trend can explain the observed failure pattern in the study of Matsuda (Matsuda et al. 2009) where 6 out of 8 patients recurred within CTV-2 (i.e. GTV + 2 cm) and none had failure within the GTV. As widely reflected in the literature (Aydın et al. 2001, Chan et al. 2002, Lee et al. 2009), tumour relapse for photon therapy shows a different trend, with GBM recurring locally and particularly in the GTV region containing cells with severe hypoxia. It is interesting to note that this clinical observation is evident in the current work results. SF for photon therapy showed a local peak within the GTV (i.e. 1.0 mm radius), figure 7, despite a 10 Gy boost dose delivered to this region, suggesting that the tumour most likely relapse in the GTV or beam region before migrating cells have a chance to form a colony in marginal regions. The SF in penumbra, while lower using BNCT, is high in both treatment modalities which increase the risk of preferential recurrence, as also demonstrated in published clinical studies (Kawabata et al. 2013, Miyatake et al. 2006).

It is clearly evident that increasing the beam size will reduce the SF, and of course, simultaneously increase normal tissue toxicity. However, a quantification of the reduction of SF when the CTV is extended by 0.5 cm could be a valuable guidance in adjusting prescriptions. In order to investigate the impact of the extent of the CTV margin, the beam size was increased by 0.5 cm in radius (i.e. resulting in 2.5-cm CTV margin), and cumulative SFs were calculated and plotted vs distance from the tumour centre. As indicated in table 5 and shown in figure 8, total SF both for 2.0 and 2.5 cm CTV margins were markedly lower using BNCT as compared to conventional x-ray therapy. However, compared to photon therapy, the change in SF as a result of CTV extension by 0.5 cm showed a considerable reduction using BNCT, table 5. In other words, while the CTV extension could be beneficial for GBM patients treated by x-ray EBRT, it does not seem to be efficacious for patients treated by BNCT, particularly considering the toxicity induced to normal tissue by scattered neutron having a much higher detrimental effect than photons.

5. Conclusion and Future Work

An integrated radiobiological framework was developed using the Geant4 Monte Carlo toolkit and MATLAB® to evaluate current CTV margin extensions in terms of cell kill efficacy for glioblastoma of the brain using BNCT. The cellular GBM response to BNCT was also investigated and was compared with photon EBRT.

The main outcomes of this study were: 1) according to these simulations, while radiobiological damage caused by photon beams may not be sufficient to kill or sterilize GBM cell populations and tumour is most likely to relapse in the treatment volume, BNCT could provide local control for GBM patients; 2) A quantification tool was developed to estimate the reduction in survival fraction due to extension of the CTV. Although SF is sensitive to the extent of CTV margin in BNCT treatment and decreases by ~ 2 times, this reduction may not justify the radiation injury caused by high LET BNCT beam in its current status of its development. The efficacy of BNCT strongly depends on the number of low energy neutrons in a spectrum which should be dominating the number of neutrons with higher energies as well as a good ratio of tumour to normal brain boron concentration. Should these factors be optimized, BNCT could be a potent modality for GBM.

We acknowledge that this study has utilized a simplified model of GBM and its microscopic extension. It is generally agreed that cancer systems, particularly GBM, are complex and dynamic systems and progression through carcinogenesis is influenced by factors such as the micro-environmental changes, immune system response, and cellular phenotype conversions.The GBM model in this work consisted only of population of cells with homogeneous radio-sensitivities and an isotropic infiltration distribution (i.e. Circular MEP) was considered. In future, genetic heterogeneity of GBM will be incorporated in the BNCT treatment modelling and anisotropic infiltration distributions will be investigated. Another important area of future development of the present work is to use more accurate models, utilizing particle track structure parameters, to translate physical dose to radiobiological effect.

References

Agostinelli S, Allison J, Amako K a, Apostolakis J, Araujo H, Arce P, Asai M, Axen D, Banerjee S, Barrand G, Behnel F, Bellagamba L, J B, Broglia L, Brunengo A, Burkharda H, Chauvie S, Chumah J, Chytracek R, Cooperman G, Cosmo G, Degtyarenko P, DellAcqua A, Depaola G, Dietrich D, Enami R, Feliciello A, Ferguson C, Fesefeldt H, Folger G, Foppiano F, Forti A, Garelli S, Giani S, Giannitrapani R, Gibin D, Cadenas G J J, Gonzalez I, Abriln G G, Greeniaus G, Greiner W, Grichine V, A G, Guatelli S, Gumplinger P, Hamatsu R, Hashimoto K, Hasui H, Heikkinen A, Howard A, Ivanchenko V, Johnson A, Jones F, Kallenbach J, Kanay N, Kawabata M, Kawabata Y, Kawaguti M, Kelner S, Kent P, Kimura A, Kodama T, Kokoulin R, Kossov M, Kurashige H, Lamanna E, Lampen T, Lara V, Lefebure V, Lei F, Liendl M, Lockman W, Longo F, Magn S, Maire M, Medernach E, Minamimoto K, Mora de Freitasap P, Morita Y, Murakami K, Nagamatu M, Nartallo R, Nieminen P, Nishimura T, Ohtsubo K, Okamura M, ONeales S, Oohata Y, Paech K, Perl J, Pfeiffer A, Pia M G, Ranjard F, Rybin A, Sadilov S, Di Salvo E, Santin G, Sasaki T, Savvas N, Sawada Y, Scherer S, Sei S, Sirotenko V, Smith D, Starkov N, Stoecker H, Sulkimo J, Takahata M, Tanaka S, Tcherniaev E, Safai Tehrani E, Tropeano M, Truscott P, Uno H, Urban L, Urban P, Verderi M, Walkden A, Wander W, Weber H, Wellisch J P, Wenaus T, Williams D C, Wright D, Yamada T, Yoshida H & Zschiesche D 2003 Geant4a simulation toolkit *Nuclear instruments and methods in physics research section A: Accelerators, Spectrometers, Detectors and Associated Equipment* **506**(3), 250–303.

Allen B J 2006 Internal high linear energy transfer (let) targeted radiotherapy for cancer *Physics in medicine and biology* **51**(13), R327.

Aydın H, Sillenberg I & von Lieven H 2001 Patterns of failure following ct-based 3-d irradiation for malignant glioma *Strahlentherapie und Onkologie* **177**(8), 424–431.

Barendsen G, Koot C, Van Kersen G, Bewley D, Field S & Parnell C 1966 The effect of oxygen on impairment of the proliferative capacity of human cells in culture by ionizing radiations of different let *International Journal of Radiation Biology and Related Studies in Physics, Chemistry and Medicine* **10**(4), 317–327.

Barth R F, Coderre J A, Vicente M G H & Blue T E 2005 Boron neutron capture therapy of cancer: current status and future prospects *Clinical Cancer Research* **11**(11), 3987–4002.

Barth R F, Grecula J C, Yang W, Rotaru J H, Nawrocky M, Gupta N, Albertson B J, Ferketich A K, Moeschberger M L, Coderre J A & Rofstad E K 2004 Combination of boron neutron capture therapy and external beam radiotherapy for brain tumors *International Journal of Radiation Oncology* Biology* Physics* **58**(1), 267–277.

Barth R F, Vicente M, Harling O K, Kiger 3rd W, Riley K J, Binns P J, Wagner F M, Suzuki M, Aihara T, Kato I & Kawabata S 2012 Current status of boron neutron capture therapy of high grade gliomas and recurrent head and neck cancer *Radiat Oncol* **7**(146), 1–21.

Barth R F, Yang W, Rotaru J H, Moeschberger M L, Joel D D, Nawrocky M M, Goodman J H & Soloway A H 1997 Boron neutron capture therapy of brain tumors: enhanced survival following intracarotid injection of either sodium borocaptate or boronophenylalanine with or without blood-brain barrier disruption *Cancer Research* **57**(6), 1129–1136.

Burger P C, Heinz E R, Shibata T & Kleihues P 1988 Topographic anatomy and ct correlations in the untreated glioblastoma multiforme *Journal of neurosurgery* **68**(5), 698–704.

Capala J, Britta H, Sköld K, af Rosenschöld P M, Giusti V, Persson C, Wallin E, Brun A, Franzen L, Carlsson J, Salford L, Ceberg C, Persson B, Pellettieri L & Henriksson R 2003 Boron neutron capture therapy for glioblastoma multiforme: clinical studies in sweden *Journal of neuro-oncology* **62**(1), 135–144.

Capuani S, Gili T, Bozzali M, Russo S, Porcari P, Cametti C, D'Amore E, Colasanti M, Venturini G, Maraviglia B, Lazzarino G & Pastore F S 2008 L-dopa preloading increases the uptake of borophenylalanine in c6 glioma rat model: a new strategy to improve bnct efficacy *International Journal of Radiation Oncology* Biology* Physics* **72**(2), 562–567.

Chan J L, Lee S W, Fraass B A, Normolle D P, Greenberg H S, Junck L R, Gebarski S S & Sandler H M 2002 Survival and failure patterns of high-grade gliomas after three-dimensional conformal radiotherapy *Journal of clinical oncology* **20**(6), 1635–1642.

Coderre J, Hopewell J, Turcotte J, Riley K, Binns P, Kiger W & Harling O 2004 Tolerance of normal human brain to boron neutron capture therapy *Applied radiation and isotopes* **61**(5), 1083–1087.

Coderre J et al. 2001 Current status of neutron capture therapy Technical report IAEA-TECDOC-1223. ISSN 1011–4289, Annex 6, IAEA.

Curran W J, Scott C B, Horton J, Nelson J S, Weinstein A S, Fischbach A J, Chang C H, Rotman M, Asbell S O, Krisch R E & Nelson D F 1993 Recursive partitioning analysis of prognostic factors in three radiation therapy oncology group malignant glioma trials *Journal of the National Cancer Institute* **85**(9), 704–710.

Diaz A Z 2003 Assessment of the results from the phase i/ii boron neutron capture therapy trials at the brookhaven national laboratory from a clinicians point of view *Journal of neuro-oncology* **62**(1-2), 101–109.

Fairchild R, Saraf S, Kalef-Ezra J & Laster B 1990 Comparison of measured parameters from a 24–kev and a broad spectrum epithermal neutron beam for neutron capture therapy: An identification of consequential parameters *Medical physics* **17**(6), 1045–1052.

Gunjur A, Bressel M & Ryan G 2012 The addition of temozolomide does not change the pattern of progression of glioblastoma multiforme post-radiotherapy *Journal of medical imaging and radiation oncology* **56**(5), 567–573.

ICRU 1999 International commission of radiation units and measurements,prescribing, recording and reporting photon beam therapy, (supplement to icru report 50), icru report 62.

Joensuu H, Kankaanranta L, Seppälä T, Auterinen I, Kallio M, Kulvik M, Laakso J, Vähätalo J, Kortesniemi M, Kotiluoto P, Seren T, Karila J, Brander A, Järviluoma E, Ryynänen P, Paetau A, Ruokonen I, Minn H, Tenhunen M, Jääskeläinen J, Färkkilä M & Savolainen S 2003 Boron neutron capture therapy of brain tumors: clinical trials at the finnish facility using boronophenylalanine *Journal of neuro-oncology* **62**(1-2), 123–134.

Kageji T, Mizobuchi Y, Nagahiro S, Nakagawa Y & Kumada H 2014 Correlation between radiation dose and histopathological findings in patients with gliblastoma treated with boron neutron capture therapy (bnct) *Applied Radiation and Isotopes* **88**, 20–22.

Kawabata S, Hiramatsu R, Kuroiwa T, Ono K & Miyatake S I 2013 Boron neutron capture therapy for recurrent high-grade meningiomas: Clinical article *Journal of neurosurgery* **119**(4), 837–844.

Kawabata S, Miyatake S I, Nonoguchi N, Hiramatsu R, Iida K, Miyata S, Yokoyama K, Doi A, Kuroda Y, Kuroiwa T, Michiue H, Kumada H, Kirihata M, Imahori Y, Maruhashi A, Sakurai Y, Suzuki M, Masunaga S I M & Ono K 2009 Survival benefit from boron neutron capture therapy for the newly diagnosed glioblastoma patients *Applied Radiation and Isotopes* **67**(7), S15–S18.

Lee I H, Piert M, Gomez-Hassan D, Junck L, Rogers L, Hayman J, Ten Haken R K, Lawrence T S, Cao Y & Tsien C 2009 Association of 11 c-methionine pet uptake with site of failure after concurrent temozolomide and radiation for primary glioblastoma multiforme *International Journal of Radiation Oncology* Biology* Physics* **73**(2), 479–485.

Lee S W, Fraass B A, Marsh L H, Herbort K, Gebarski S S, Martel M K, Radany E H, Lichter A S & Sandler H M 1999 Patterns of failure following high-dose 3-d conformal radiotherapy for high-grade astrocytomas: a quantitative dosimetric study *International Journal of Radiation Oncology* Biology* Physics* **43**(1), 79–88.

Mallesch J L, Moore D E, Allen B J, McCarthy W H, Jones R & Stening W A 1994 The pharmacokinetics of p-boronophenylalanine. fructose in human patients with glioma and metastatic melanoma *International Journal of Radiation Oncology* Biology* Physics* **28**(5), 1183–1188.

Marek M, Vins M, Lahodova Z, Viererbl L & Koleska M 2014 Extended set of activation monitors for nct beam characterization and spectral conditions of the beam after reactor fuel conversion *Applied Radiation and Isotopes* **88**, 157–161.

Matsuda M, Yamamoto T, Kumada H, Nakai K, Shirakawa M, Tsurubuchi T & Matsumura A 2009 Dose distribution and clinical response of glioblastoma treated with boron neutron capture therapy *Applied Radiation and Isotopes* **67**(7), S19–S21.

Mehrian Shai R, Yalon M, Simon A, Eyal E, Pismenyuk T, Moshe I, Constantin i S & Toren A 2015 High metallothionein predicts poor survival in glioblastoma multiforme *BMC Medical Genomics* **8**(1), 68.

Miyatake S I, Kuwabara H, Kajimoto Y, Kawabata S, Yokoyama K, Doi A, Tsuji M, Mori H, Ono K & Kuroiwa T 2006 Preferential recurrence of a sarcomatous component of a gliosarcoma after boron neutron capture therapy: case report *Journal of neuro-oncology* **76**(2), 143–147.

Moghaddasi L, Bezak E & Harriss-Phillips W 2015 Evaluation of current clinical target volume definitions for glioblastoma using cell-based dosimetry stochastic methods *The British journal of radiology* **88**(1053), 20150155.

Moghaddasi L, Bezak E & Harriss-Phillips W 2016*a* Development and verification of a geant4 beam model for boron neutron capture therapy *Submitted to Physica Medica* .

Moghaddasi L, Bezak E & Harriss-Phillips W 2016*b* Monte-carlo model development for evaluation of current clinical target volume definition for heterogeneous and hypoxic glioblastoma *Physics in Medicine and Biology* **61**(9), 3407.
URL: *http://stacks.iop.org/0031-9155/61/i=9/a=3407*

Moghaddasi L, Bezak E & Marcu L G 2012 Current challenges in clinical target volume definition: tumour margins and microscopic extensions *Acta Oncologica* **51**(8), 984–995.

Morris G, Coderre J, Micca P, Fisher C, Capala J & Hopewell J 1997 Central nervous system tolerance to boron neutron capture therapy with p-boronophenylalanine. *British journal of cancer* **76**(12), 1623.

Nafe R, Franz K, Schlote W & Schneider B 2005 Morphology of tumor cell nuclei is significantly related with survival time of patients with glioblastomas *Clinical cancer research* **11**(6), 2141–2148.

Oppitz U, Maessen D, Zunterer H, Richter S & Flentje M 1999 3d-recurrence-patterns of gliobastomas after ct-planned postoperative irradiation *Radiotherapy and Oncology* **53**(1), 53–57.

P. K & K. C W 2000 *Pathology and genetics of tumours of the nervous system* International Agency for Research on Cancer.

Palmer M R, Goorley J T, Kiger W, Busse P M, Riley K J, Harling O K & Zamenhof R G 2002 Treatment planning and dosimetry for the harvard-mit phase i clinical trial of cranial neutron capture therapy *International Journal of Radiation Oncology* Biology* Physics* **53**(5), 1361–1379.

Riley K, Binns P & Harling O 2003 Performance characteristics of the mit fission converter based epithermal neutron beam *Physics in medicine and biology* **48**(7), 943.

Slatkin D N 1991 A history of boron neutron capture therapy of brain tumours *Brain* **114**(4), 1609–1629.

Trépanier P Y, Fortin I, Lambert C & Lacroix F 2012 A monte carlo based formalism to identify potential locations at high risk of tumor recurrence with a numerical model for glioblastoma multiforme *Medical physics* **39**(11), 6682–6691.

Unkelbach J, Menze B H, Konukoglu E, Dittmann F, Ayache N & Shih H A 2014 Radiotherapy planning for glioblastoma based on a tumor growth model: implications for spatial dose redistribution *Physics in medicine and biology* **59**(3), 771.

Van Dyk J 1999 *The modern technology of radiation oncology: a compendium for medical physicists and radiation oncologists* Medical Physics Pub Corp.

Wallner K E, Galicich J H, Krol G, Arbit E & Malkin M G 1989 Patterns of failure following treatment for glioblastoma multiforme and anaplastic astrocytoma *International Journal of Radiation Oncology* Biology* Physics* **16**(6), 1405–1409.

Yamamoto T, Nakai K, Kageji T, Kumada H, Endo K, Matsuda M, Shibata Y & Matsumura A 2009 Boron neutron capture therapy for newly diagnosed glioblastoma *Radiotherapy and oncology* **91**(1), 80–84.

Zamenhof R, Redmond E, Solares G, Katz D, Riley K, Kiger S & Harling O 1996 Monte carlo-based treatment planning for boron neutron capture therapy using custom designed models automatically generated from ct data *International Journal of Radiation Oncology* Biology* Physics* **35**(2), 383–397.

8.3 Conclusion

The GBM modelling framework has been successfully extended in this chapter to incorporate BNCT. The GBM model in this chapter consisted only of population of cells with homogeneous radiosensitivities and isotropic infiltration distribution. The two main achievements of the model developed in this chapter were:

- Survival Fractions (SFs) within the PTV was reduced by more than four orders of magnitude using BNCT as compared to x-ray EBRT for GBM. This promising result obtained for homogeneous GBM (i.e. simplified conditions), indicates that GBM may be responsive to BNCT.
- The quantitative tool developed in this chapter enables evaluation of CTV margins of 2.0 and 2.5 cm. It was demonstrated that the reduction in SF as a result of the CTV margin extension by 0.5 cm (from 2.0 to 2.5 cm) is less than in the case of 0.5 cm CTV margin extension in x-ray EBRT (i.e. by $\sim$ 2 times less) in BNCT treatment.

The model developed in this chapter will be further enhanced in the next chapter.

Chapter 9

An integrated Monte Carlo model for heterogeneous glioblastoma multiforme treated with Boron Neutron Capture Therapy

9.1 Introduction and motivation

In this chapter we expand upon the model developed in chapter 8 by incorporating heterogeneous radiosensitivities of individual cells and two anisotropic infiltration distributions into the normal brain tissue in the cellular structure of *in silico* GBM. The code developed in chapter 8 was used to assess the efficacy of cell kill in BNCT treatment and compared with x-ray EBRT in terms of cellular survival probabilities for glioblastoma of the brain. However, a simplified model of GBM with homogeneous radiosensitivity and microscopic extension isotropic in all direction was considered which is of limited clinical relevance. This shortcoming will be addressed in the current chapter.

9.2 Statement of Contribution

9.2.1 Conception

The initial idea for investigation of the efficacy BNCT for the treatment/management of GBM and integration of a MC model with semi-analytical cellular-based cell-survival model (radiobiological model) was first conceptualised by Leyla Moghaddasi. The method to design the architecture of the integrated model to simulate BNCT of GBM was conceptualised by Leyla Moghaddasi.

9.2.2 Realisation

The Geant4 code development to obtain cell-based dosimetry matrices for each MEP model in *in silico* GBM infused with a boron agent, and related MATLAB codes to simulate bio-distributions of the boron agent and for all data analyses were undertaken by Leyla Moghaddasi. The model verification and data analyses were performed by Leyla Moghaddasi. General supervision and guidance on the development of the work was provided by Eva Bezak. The manuscript was evaluated by Eva Bezak in terms of accuracy and interpretation of calculated results, conclusions reached, and general structure and flow.

9.2.3 Documentation

This paper was primarily written by Leyla Moghaddasi. Editing was performed by all authors.

Statement of Authorship

Title of Paper	**An integrated Monte Carlo model for heterogeneous glioblastoma multiforme treated with Boron Neutron Capture Therapy**		
Publication Status	☐ Published ☐ Submitted for Publication	☐ Accepted for Publication ☑ Publication Style	
Publication Details	Moghaddasi, L., E. Bezak, M. Douglass, to be submitted to *Medical Physics*		

Principal Author

Name of Principal Author (Candidate)	Leyla Moghaddasi		
Contribution to the Paper	Developed the model, analysed the results of calculations, and wrote the manuscript and acted as corresponding author.		
Overall percentage (%)	75%		
Signature		Date	07/09/2016

Co-Author Contributions

By signing the Statement of Authorship, each author certifies that:

i. the candidate's stated contribution to the publication is accurate (as detailed above);

ii. permission is granted for the candidate in include the publication in the thesis; and

iii. the sum of all co-author contributions is equal to 100% less the candidate's stated contribution.

Name of Co-Author	Prof. Eva Bezak		
Contribution to the Paper	General guidance and supervision and manuscript revision.		
Overall percentage (%)	20%		
Signature		Date	07/09/2016
Name of Co-Author	Dr. Michael Douglass		
Contribution to the Paper	Manuscript revision and editing.		
Overall percentage (%)	5%		
Signature		Date	07/09/2016

An integrated Monte Carlo model for heterogeneous glioblastoma multiforme treated with boron neutron capture therapy

Leyla Moghaddasi
School of Physical Sciences, University of Adelaide, Adelaide, Australia and
Department of Medical Physics, Adelaide Radiotherapy Centre, Adelaide, Australia

Eva Bezak
School of Physical Sciences, University of Adelaide, Adelaide, Australia
International Centre for Allied Health Evidence,
University of South Australia, Adelaide, Australia and
Sansom Institute for Health Research,
University of South Australia, Adelaide, Australia

Michael Douglass
School of Physical Sciences, University of Adelaide, Adelaide, Australia and
Department of Medical Physics, Royal Adelaide Hospital, Adelaide, Australia

Abstract

Introduction. Glioblastomas (GBM) of the brain are are highly resistant to radiotherapy and are characterized by extensive infiltration into the brain. Boron Neutron Capture Therapy (BNCT), a biochemically-targeted type of radiotherapy based on thermal neutron capture by ^{10}B atoms resulting in emission of short-ranged high Linear Energy Transfer (LET) particles, represents an alternative radiotherapy technique for GBM. Previously, an integrated BNCT modelling framework was developed for a simplified model of GBM consisting only of cells with heterogeneous radiosensitivities and isotropic microscopic extension. The model integrated a cell-based dosimetry model (i.e. to calculate the dose deposited in individual GBM/normal cells) using GEANT4.9.6.p02, previously-developed Microscopic Extension Probability (MEP) models by the current group and an in-house developed epithermal neutron beam model developed.

Methods. The current work expanded on the previous model by developing a more realistic *in silico* GBM model with heterogeneous radiosensitivity and anisotropic microscopic extensions. The genetic heterogeneity was modelled using a range of α/β values (linear-quadratic model parameters) associated with different GBM cell lines, which were distributed among the cells randomly, taken from a Gaussian-weighted sample of α/β values. Bio-distribution of cellular ^{10}B concentrations were generated in Matlab for each MEP model and were exported to Geant4. Each cell within the GBM and its surrounding normal tissue was then assigned a material composed of a brain material and a ^{10}B concentration. As a result, 3 sets of dosimetry matrices corresponding to three MEP models were calculated. Results from the cell-based dosimetry model, MEP, and heterogeneous radiosensitivity matrices were combined to evaluate survival fractions (SF) for typical CTV margins of 2.0 & 2.5 cm and several regions of interest. Calculated SFs were compared with those obtained for x-ray radiotherapy (XRT).

Results and Conclusion. Following BNCT treatment of heterogeneous hypoxic GBM, the calculated SFs within the beam region, varied slightly between MEP models, and decreased by more than two orders of magnitude as compared to XRT. It was demonstrated that BNCT results in a markedly reduced SFs for both CTV extensions for all three MEP models as compared to XRT. However, the reduction in SF as a result of the CTV margin extension using BNCT was on average ~ 2.4 times compared to x-ray EBRT (~ 4 times). In conclusion, BNCT results in a more efficient cell kill and the extension of the CTV margin may not increase the treatment outcome significantly.

I. INTRODUCTION

Malignant gliomas are the most common primary intracranial neoplasms arising from glial cells that provide critical support to the central nervous system (CNS) [1]. Glioblastoma multiforme (GBM) is the most aggressive form of glioma (grade IV), notorious for aggressive proliferation and diffusive growth rather than forming a solid tumour mass with defined boundaries [2]. The infiltrative growth pattern and high mobility of GBM cells makes the determination of Clinical Target Volume (CTV) for this tumour particularly difficult. While the uncertainty in its microscopic extension (ME) could result in marginal and distant recurrences, the observed high rate of GBM local relapse [3–5] can be attributed to intrinsic radioresistance, hypoxia and other aggressive features of GBM. GBMs present clinically with extensive intra-tumour and inter-tumour heterogeneities in terms of genetic expressions and cytogenetic aberrations resulting in varying radiosensitivities. GBMs present with severe intratumoural and peritumoural hypoxia that are major factors in tumour aggressiveness and radioresistance [6]. These characteristics of GBM have rendered the current treatment regimens ineffective and the prognosis for GBM patients remains severe, despite major advances in x-ray External Beam Radiation Therapy (EBRT) in the last two decades. According to a recent report, the median overall survival for GBM patients was found to be 9.2 months using concurrent chemoradiotherapy [7].

Recent technological advances have allowed development of other radiotherapy modalities, such as proton and heavy ion therapy and targeted therapies. These techniques have several physical and biological advantages over x-ray radiotherapy as the treatment is delivered using high Linear Energy Transfer (LET) particles. High LET particles offer the advantage of delivering localized dose to the tumour volume while the radiation dose to normal tissue surrounding the tumour is reduced. In addition, the radiobiological damage caused by charged particles is predominantly through direct DNA damage (i.e. double strand breaks), rather than due to free radical production. As a result, the cell killing process is less sensitive to cellular oxygen level as compared to x-ray radiotherapy.

Boron Neutron Capture Therapy (BNCT) is a binary type of radiotherapy based on a nuclear reaction in which a thermal neutron is captured by a stable ^{10}B nucleus, resulting in an emission of an energetic alpha particle ($\sim 1.47 - 1.77$ MeV), a recoiling ^{7}Li nucleus ($\sim 0.84 - 1.02$ MeV), and a 478 keV gamma ray (equation 1). The alpha particles and the

^{7}Li nuclei deposit their energy along their trajectory approximately from 4 to 7 μm with a high LET rate of about 240 keV/μm [8, 9]. This is a binary modality in which a suitable ^{10}B agent is taken up preferentially by malignant cells following administration of an appropriate boron agent.

$$^1n +^{10} B \rightarrow^7 Li +^4 He + \gamma \tag{1}$$

BNCT has potential to be effective in treatment of GBM for three main reasons: 1) better management of intrinsic radioresistance and heterogeneous radiosensitivities of GBM, as the treatment is delivered by high LET radiation, resulting in densely clustered ionization damages; 2) the process of cell killing in BNCT is not very susceptible to oxygen status; 3) BNCT, being a biochemical type of radiotherapy, can selectively deliver localized dose to tumour cells while minimizing normal tissue toxicity. This is particularly advantageous for GBMs with infiltrative growth pattern and rapid peripheral expansion as it potentially enables the targeting of subclinical disease spread in normal brain tissue. Encouraging results in terms of lifespan increase for GBM patients receiving this treatment have been reported [10–13]. The median Overall Survival (OS) time following BNCT treatment for a group of 5 GBM patients was found 23.2 months in the study of Yamamoto [10]. This is comparable to the report from a cohort of 89 GBM patients treated with BNCT achieving a median OS of 22.9 months [12]. These survival rates are superior compared to those reported for GBM patients in RTOG trial (10.7 months) [14] and EORTC 26981/22981-NCIC CE3 trial (10 months) [15] using EBRT. Kawabata *et al.* [13] investigated the survival benefit of BNCT by comparing the survival times for 21 patients treated with BNCT against 27 patients treated with x-ray EBRT. An improved survival rate, from 48.2 to 76.2% and 14.8 to 25.0% for 1 year and 2 year survival, respectively, was observed for patients treated with BNCT.

Although BNCT seems to be a suitable modality for GBM patients, a successful BNCT treatment depends on two major factors [16]: a) an adequate tumour-to-normal cell ratio of boron concentration, and sufficient amount of ^{10}B in tumour cells (i.e. at least 20 μg/g or 10^9 atoms/cell [17]) to ensure sufficient dose delivery to tumour cells; b) a neutron beam with large proportion of thermal and epithermal neutrons relative to fast neutrons, as the dose delivered by fast neutrons is not targeted and imposes risk to normal brain tissue.

Boron agents. Two commonly used boron delivery agents are: $Na_2B_{12}H_{11}SH$ or commonly named BSH; and (L)-4-dihydroxy-borylphenylalanine or BPA [17]. In a previous report of our group, several studies investigating boron concentrations in normal brain and glioma cells using these agents were reviewed and summarized. It was concluded that while this ratio varies between different studies, a tumour-to-normal cell ratio of boron concentration of ~ 3.5 is a common assumption/finding.

Neutron spectrum. An optimal neutron spectrum for BNCT should contain high thermal (E $< 0.25\ eV$), epithermal ($0.25\ eV\ - 100\ keV$) and minimal fast neutron (E $>\ 100\ keV$) components [18]. The cross section for the $^{10}B(n,\alpha)^7Li$ neutron capture reaction is high in the thermal energy range. However, the penetration of thermal neutrons is limited. Consequently, epithermal neutrons are more useful for clinical purposes as they thermalize at larger depths where they undergo capture reactions.

BNCT dosimetry. Epithermal neutron beams designed for BNCT produced by fission reactors and accelerators have broad spectra and contain unwanted fast neutron and gamma contaminations. As a result the dose delivered by this mixed radiation beam to tissue during BNCT is composed of four main components [19]:

1. Boron dose from thermal neutron capture through $^{10}B(n,\alpha)^7Li$ reaction (which is the sum of the dose from ^7Li and alpha particles);

2. Thermal neutron dose resulting from thermal neutron capture by ^{14}N in biological tissue in the reaction $^{14}N(n,p)^{14}C$;

3. Gamma dose from neutron capture by ^{1}H and also from gamma contamination in the incident neutron beam;

4. Fast neutron dose due to elastic and inelastic scattering (e.g. $^1H(n,n')^2H$) and several possible nuclear reactions (e.g. $^{16}O(n,\alpha)^{13}C$) [18].

These physical dose components do not result in the same biological effect as particles of different types and energies interact differently with tissue. Therefore, the variability of radiobiological effects of different physical doses needs be taken into account upon calculating the dose delivered.

Bio-mathematical and computational modelling, especially Monte Carlo (MC) techniques are a useful tool for simulating biological systems and enable predictions of the probable radiobiological effects for a variety of therapeutic scenarios (e.g. different CTV margins) and treatment modalities.

Geant4 [20] is a powerful MC toolkit capable of simulating complicated experimental setups. The passage of radiation through matter can be tracked for a diverse range of particles over an extensive energy range. The diverse functionality including hadronic processes and performance optimization features make Geant4 a suitable MC software/tool for BNCT simulation [21].

A. An overview of the progression of GBM treatment modelling

The GBM treatment modelling framework was developed for a GBM composed of a population of cells with individual radiosensitivities and oxygenation levels (including hypoxia) treated with 6 MV x-ray EBRT [22]. The GBM model was designed as a matrix consisting of cells (containing both clonogenic tumour and normal brain cells), with each cell being assigned a tumour clonogen probability, oxygen status, radiation sensitivity, and the calculated absorbed dose.

The cell-based dosimetry module was developed using Geant4 (version 4.9.6.p01) to calculate the absorbed dose in each cell within a spatial GBM model. The scale of the geometry was chosen to cover the entire extension of the GBM microscopic disease in all directions and the volume was divided into 20 μm size cubic voxels (i.e. the average size of glioma cells [23]).

The Microscopic extension probability (MEP) models used in this work were developed in MATLAB ® (Mathworks, Natick, MA) to simulate the infiltration of tumour cells into the healthy brain using a probability distribution function, assigning each cell with a probability of being a tumour clonogen as a function of distance from the gross tumour. The probability distribution function was obtained from published clinical data addressing recurrence patterns of GBM (figure 1(d)). Using this clinical function, three 2D distributions of MEP models were developed: (1) circular MEP where microscopic infiltration occurred isotropically in all directions according to the clinical function (figure 1(a)); (2) elliptical MEP which simulated the preferential diffusion of GBM histological disease along the white matter fibre tracts [2] (figure 1(b)); and (3) irregular MEP developed by using two random number generators to determine the radial infiltration extension and a polar angle (figure

1(c)).

The individual matrices (i.e. calculated absorbed dose, MEP, radiosensitivity, and hypoxia) can be combined to predict cell survival probabilities, and therefore, cell survival fractions. The details were described in reference [24]. Figure 2 schematically shows the individual components of the integrated model.

BNCT treatment modelling for GBM: Previously we reported on a BNCT treatment modelling framework for a simplified GBM model consisting of cells with homogeneous radiosensitivities and isotropic distribution of histological infiltration (i.e. circular MEP model) [21]. As for the source of radiation, the model utilized a Geant4 BNCT epithermal neutron beam, developed and verified by our group against published measured and calculated data [16].

The aim of the current work is to apply the BNCT treatment modelling to a a semi-realistic model of GBM with heterogeneous radiosensitivity and anisotropic infiltration distributions and to estimate the treatment efficacy in terms of the number fo surviving tumour clonogens.

II. MATERIALS AND METHODS

A. Cell-based dosimetry

The geometry architecture designed for the cell-based dosimetry module, described in detail in our previous report [21], was used in this work for a heterogeneous GBM with anisotropic MEPs. The simulated geometry was a 9 $cm \times 9\ cm \times 2.2\ cm$ brain phantom consisting of a spherical GTV (i.e. 1 mm diameter) and a ME region (i.e. spanning up to 4.1 cm from the GTV) and a 0.4 cm PTV. The size of the GTV was intentionally considered small as the main aim of this study is to investigate the effect of the CTV margin extension on the SF and the larger size of the GTV only increases CPU time.

To simulate the brain injected by a ^{10}B agent in Geant4 each cell was assigned a brain material and a boron concentration. The brain material was built in Geant4 using brain elemental composition according to the National Institute of Standards and Technology (NIST) Listings, compositions of materials used in STAR Databases webpage: *http://physics.nist.gov/cgi-bin/Star/compos.pl?matno=123*. The distribution of boron concentrations is de-

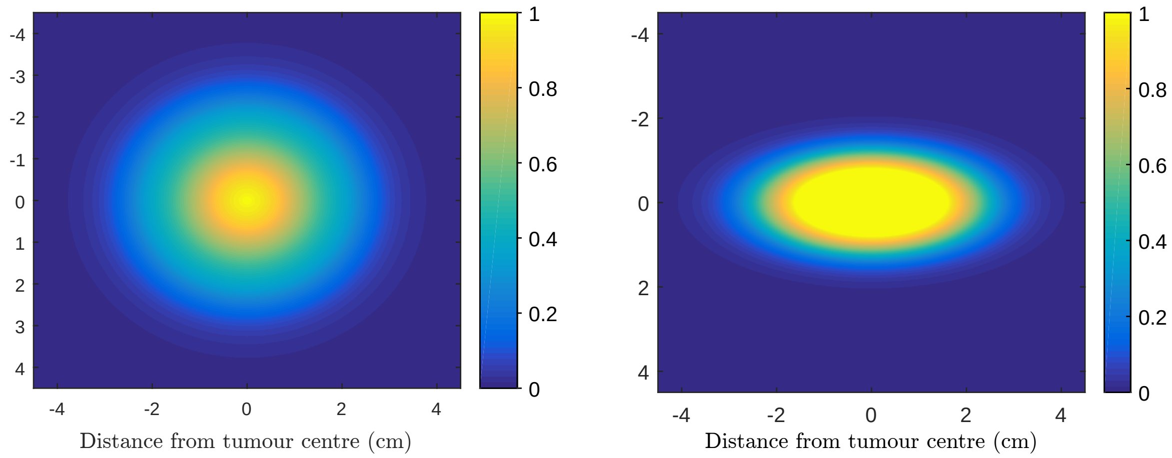

(a) Circular MEP

(b) Elliptical MEP

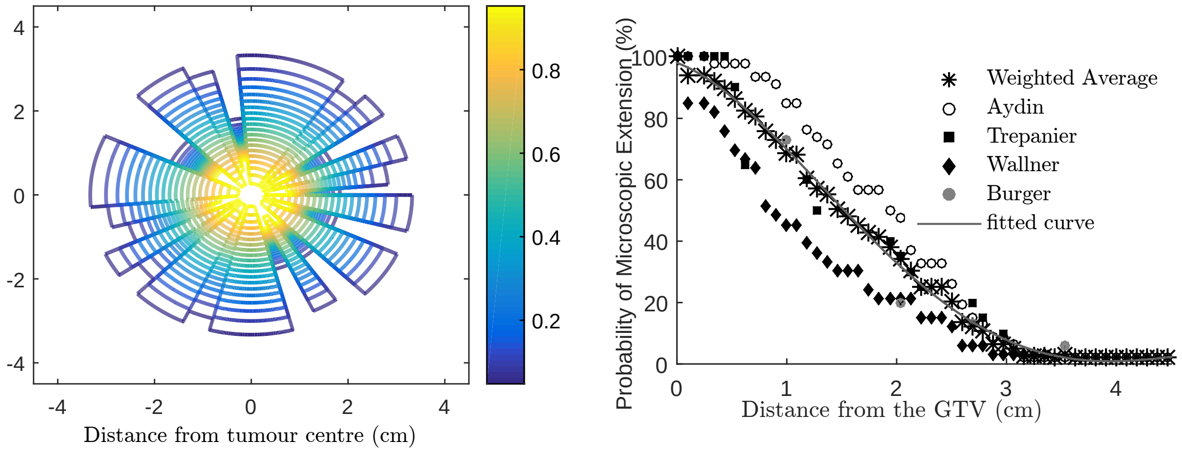

(c) Irregular MEP

(d) Microscopic extension in clinical studies

FIG. 1: Microscopic extension probability (MEP) distribution models: a) isotropic circular; and anisotropic b) elliptical; and c) irregular models. Dark blue colour (number 0) indicates that the cell is a normal brain cell and the yellow colour (number 1) refers to a cell with 100% probability to be a tumour cell. Colours from blue to yellow (numbers from 0-1) indicate an increasing probability that a cell is a tumour cell. Clinical studies investigating the extent of microscopic extension in GBM patients are shown in (d). The function fitted to the combined results (i.e. a three-term Gaussian function) was considered as the basis for the MEP models [24].

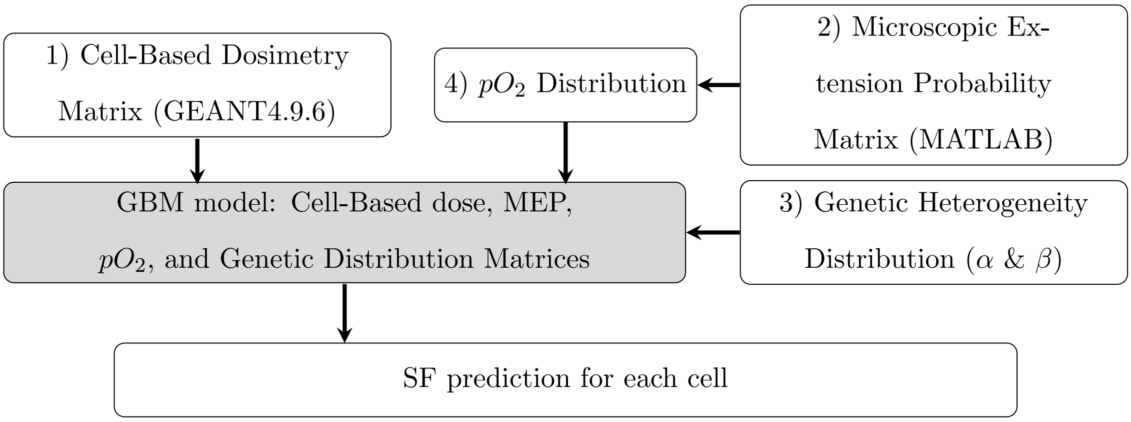

FIG. 2: Schematic diagram showing the structure of the model components designed in the previous work [22].

pendent on whether a cell was a tumour cell or a normal brain cell. Boron concentrations of 13 and 45.5 $\mu g/g$ (3.5 times bigger than normal brain boron concentration) were assumed in normal brain and GBM cells, respectively [21]. Subsequently, a linear function was derived to determine cellular boron concentration as a function of the probability that the cell is a tumour cell (i.e. MEP):

$$B_{c,ij} = \ 32.5 \times MEP_{ij} + 13 \tag{2}$$

where $B_{c,ij}$ is the boron concentration in the ij voxel/cell with MEP_{ij} probability that the cell is a tumour cell. For each MEP model, the corresponding boron bio-distribution was exported to Geant4 to parametrize the irradiated GBM volume (using Geant4 nested parametrization method) in which each cell consisted of brain material and boron concentration as specified by the distribution.

The system was irradiated by our previously-reported BNCT beam model [16], simulating the epithermal spectrum from the LVR-15 reactor at the Rez Research Centre [25]. Two conical beam sizes of 2.5 and 3.0 cm radii were considered to cover PTVs with 2.0 and 2.5 CTV margins respectively at 100 cm Source to Surface Distance (SSD). The model was designed to deliver the treatment in one fraction with a mean maximum tumour dose of 73.4 RBE-Gy, according to the reported mean maximum tumour doses in literature [11, 26–28].

In this work, the current convention in clinical BNCT practices, e.g. IAEA-TECDOC-1223 BNCT treatment planning protocol [19], was adopted to account for the variability of

TABLE I: Relative biological effectiveness factors, w, and CBE factor (i.e. only for boron dose) for four principal dose components [8].

	Photon w_γ	Fast neutron w_F	Thermal neutron w_T	Boron w_B
Brain tissue	0.5	3.2	3.2	1.3
Tumour tissue	0.5	3.2	3.2	3.8

radiobiological effects of different physical dose components. Each physical dose component was weighted by its respective Relative Radiobiological Effectiveness (RBE) factor (i.e. RBE is the ratio of the dose delivered by a reference x-ray beam (typically ^{60}Co) and the dose deposited by the test radiation producing the same biological endpoint), as listed in table I [8]. The correction factor used for boron products reaction is called Compound Biological Effectiveness (CBE) because it depends on the boron carrier used to put boron in the cell [19].

Therefore, the total RBE-Gy dose, d_{wij}, was calculated as:

$$d_{wij} = w_\gamma d_{\gamma ij} \ + w_F d_{Fij} \ + w_T d_{Tij} \ + w_B d_{Bij} \tag{3}$$

where $d_{\gamma ij}$, d_{Fij}, d_{Tij}, and d_{Bij} are gamma dose, fast neutron dose, thermal neutron dose, and boron dose (i.e. sum of lithium and alpha doses) in the ij voxel/cell respectively. w_B, w_F, w_T, w_γ are CBE for boron dose and RBE values for fast neutron, thermal and gamma doses respectively.

Geant4 packaged physics list, Quark-Gluon String Precompound Binary Cascade High Precision Neutron (QGSP_BIC_HP) was implemented to simulate particle tracking by assigning particles with appropriate processes and cross sections. To ensure that nuclear emissions and fragments, particularly alpha and ^{7}Li particles from boron capture reaction with minimum range of approximately 4 μm, were individually tracked and their corresponding deposited doses were scored, the tracking step size was set to 4 μm. The production threshold/cut off value for secondary particles was set to 4 μm for e^-, e^+ and proton particles and a 0.01 mm for gamma rays. These production thresholds were assigned only to the volume of 9 $cm \times 9$ $cm \times 0.9$ cm size enclosing the scoring slice. Default thresholds of 0.7 mm were used for the rest of geometry.

While the Geant4 particle tracking was performed in the entire geometry, the dose was only scored in a single slice (i.e. scoring plane) with $9\ cm \times 9\ cm \times 20\ \mu m$ dimensions located at 2.0 cm from the phantom surface, perpendicular to the beam direction. In this simulation a sensitive detector technique was implemented to score the dose from individual particles in the scoring plane. A parallel geometry was built and was linked to the sensitive detector (i.e. associated with real geometry) to enable synchronized communication of parallel and real geometries for scoring the absorbed dose in each cell.

Parallel simulations on 47-CPU 64-bit Linux clusters (i.e. South Australia (SA) Tizard supercomputer, the University of Adelaide) were performed for a total number of 5.8×10^9 particles. Each was run for approximately $\sim$ 14 days for each MEP model and each beam size (i.e. six sets of simulations, three MEP models, two beam sizes). As a result, for each MEP model and beam size, the four dose matrices corresponding to different physical dose components (i.e. ^{7}Li, alpha, gamma and residual dose consisting of fast neutron and thermal neutron doses) were calculated.

B. Survival fraction calculation

The distribution of different cellular radiation sensitivities (i.e. different α and β parameters) were generated using a Gaussian-weighted distribution of α and β parameters adopted from the *in vitro* study of Taghian *et al.* [29] for 21 malignant glioma cell lines, see figure 3.

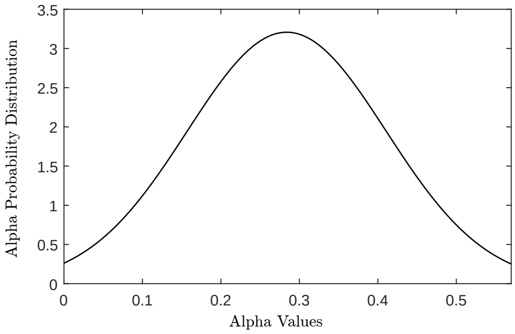

FIG. 3: The Gaussian distribution of α values measured for 21 malignant glioma cell lines in the study of [29].

For each MEP model, four dose matrices calculated in Geant4 were exported into MATLAB. Using equation 3, the total biological dose was calculated and was combined with the

MEP models and the radiation sensitivity matrices, representing genetic heterogeneity in terms of radiosensitivity, to obtain the cell survival probability for each cell using equation 4:

$$SP_{ij} = MEP_{ij}e^{-(\alpha_{ij}d_{ij}+\beta_{ij}d_{ij}^2)} \tag{4}$$

where MEP_{ij} is the probability that the ij cell is a tumour cell, and d_{ij} is the absorbed dose in the ij cell with radiosensitivity described by α_{ij} and β_{ij}. SP_{ij} denotes the survival probability of the ij cell. The Oxygen Enhancement Ratio (OER) (i.e. the radiobiological quantity to determine the effect of different pO_2 levels on cellular radiosensitivity and is expressed as the ratio of the radiation doses in a certain oxygen condition and in anoxic conditions required to produce the same radiobiological effect) is assumed to be one for high LET particle radiation [30]. As a result, the OER value of 1 was adopted in this work. Equation 5 was used to calculate number of surviving cells and SF for regions of interest (POI):

$$\begin{aligned} \text{surviving cells in the region} &= \sum_{i,j} SP_{ij}(i,j \in ROI) \\ SF_{\text{region}} &= \frac{\text{surviving cells in the ROI}}{\text{total number of tumour cells before treatment}} \end{aligned} \tag{5}$$

The diagram in figure 4 outlines the SF analysis performed in this work. Heterogeneous-hypoxic GBM treated with BNCT is shown in scenario 3 on the left of figure 4. The results of this analysis were compared with SFs for heterogeneous-hypoxic GBM using x-ray EBRT [22] (scenario 1), and homogeneous-hypoxic GBM using BNCT [21] (scenario 2).

Using a 2.0 cm CTV margin, SFs were calculated for each of three MEP models in several regions, using equation 6: 1) within the beam region (i.e. the PTV); 2) within the penumbra region (defined in this study as the region extending 5.0 mm beyond the PTV); and 3) the total SFs (i.e. including the in-beam, penumbra and the out of field regions):

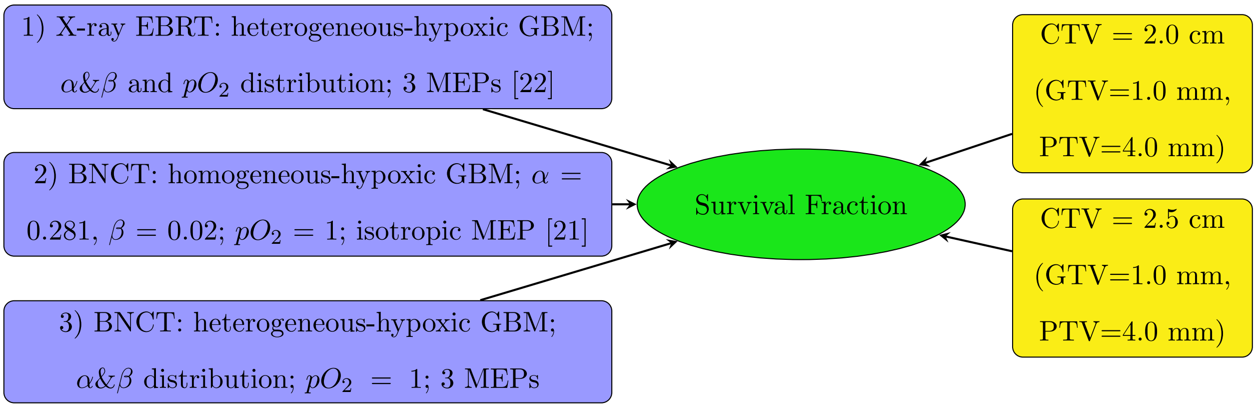

FIG. 4: Schematic diagram showing the SF analysis structure. SFs were investigated for three GBM tumour types (left) using two CTV margin extensions (right). In this work the investigation was conducted for heterogeneous-hypoxic GBM treated with BNCT (number 3 on the left) for both CTV margins on the right and three MEP models. The results were compared with previously reported SFs for heterogeneous-hypoxic GBM using x-ray EBRT [22], and homogeneous-hypoxic GBM using BNCT [21].

$$
\begin{aligned}
SF_{within\ the\ beam} &= 100 \times \frac{\text{surviving cells within the PTV}}{\text{total number of tumour cells before treatment}} \\
SF_{penumbra\ region} &= 100 \times \frac{\text{surviving cells in the region extending 5.0 mm beyond the PTV}}{\text{total number of tumour cells before treatment}} \\
SF_{total} &= 100 \times \frac{\text{surviving cells within the PTV, penumbra, and out-of-field regions}}{\text{total number of tumour cells before treatment}}
\end{aligned}
\tag{6}
$$

The results were compared with those calculated for heterogeneous-hypoxic GBM tumour model and all three MEP models, using x-ray therapy published previously [22].

Using a 2.0 cm CTV margin, the differential SFs, defined as the ratio of the number of surviving tumour clonogens to the initial number of tumour cells before the treatment in 0.5 mm sphere shells at each distance from the tumour centre were calculated and plotted for the three MEP models. This was to investigate the pattern of SF within the beam and beyond in more details.

To obtain a quantitative measure of SF reduction as a result of CTV margin extension by 0.5 cm, the Geant4-calculated cell-based dosimetry matrices corresponding to 6.0 cm diameter beam (i.e. corresponding to 2.5 cm CTV margin) were imported to MATLAB and were analysed similarly to obtain SF for each MEP model for the extended CTV margin. The change in SFs, as a result of the CTV increase by 0.5 cm, was quantified using equation 7:

$$SF_{change} = 100 \times \frac{SF_{2.0\ cm} - SF_{2.5\ cm}}{SF_{2.0\ cm}} \tag{7}$$

III. RESULTS

A. Assessment of survival fractions for a 2.0 cm CTV margin

The results in this section are presented in terms of (a) SF within the beam (i.e. the PTV), (b) SF within the penumbra region (i.e. 5.0 mm beyond the PTV), (c) total SF (i.e. including within the beam, penumbra and out of the beam regions) calculated for circular, elliptical and irregular MEP models and for a heterogeneous GBM. The results for conventional x-ray therapy are also presented using the previously-developed model [22] for comparison.

1. Survival fractions in various regions - 2.0 cm CTV margin

Table II summarizes the SFs in the regions of interest and the total SFs for the three MEP models. The SF within the beam was reduced by more than two orders of magnitude for different MEP distributions for BNCT modality as opposed to conventional x-ray therapy [22]. The results indicate a reduction of up to $\sim$ 5 and 3.5 times (for elliptical infiltration distribution) in the SF within the penumbra region and the total SF, respectively, following BNCT as compared to x-ray EBRT.

2. Differential survival fraction - 2.0 cm CTV margin

Figure 5 shows differential SF curves in 0.5 mm steps using heterogeneous-hypoxic GBM models for the three MEP distributions treated with BNCT. Previously reported results for conventional x-ray therapy [22] and the homogeneous-hypoxic model using BNCT [21]

TABLE II: Survival fractions (SFs) in different regions for heterogeneous-hypoxic GBM model, using three MEP distributions, for BNCT and conventional x-ray EBRT [22].

Modality	BNCT		
MEP	SF within the beam (%)	SF within the penumbra region (%)	Total SF (%)
Circular	$(1.8 \pm 2.6) \times 10^{-4}$	2.7 ± 0.3	3.9 ± 0.4
Elliptical	$(3.2 \pm 3.5) \times 10^{-4}$	0.6 ± 0.2	1.5 ± 0.3
Irregular	$(2.9 \pm 2.3) \times 10^{-4}$	1.3 ± 0.4	3.8 ± 0.6
	Conventional x-ray EBRT		
Circular	$(4.3 \pm 0.2) \times 10^{-2}$	6.3 ± 0.9	12.9 ± 1.0
Elliptical	$(4.8 \pm 0.2) \times 10^{-2}$	3.0 ± 0.4	5.5 ± 0.5
Irregular	$(4.5 \pm 0.2) \times 10^{-2}$	5.4 ± 0.7	11.1 ± 0.8

are also presented to allow comparison and analysis of the SF pattern at any distance. Considering the logarithmic scale on the vertical axis used in figure 5, a marked decrease in the SF within the beam was observed for BNCT as compared to x-ray EBRT, irrespective of the pattern of microscopic extension distribution (i.e. MEP model). For all three MEP models, the SF within the beam for BNCT gradually increased with distance from the tumour centre prior to reaching the penumbra region, while the SF remained almost constant throughout the beam area for the GBM model treated with x-rays. This can be attributed to the dose gradient within the irradiated volume for BNCT treatment due to the negative gradient of boron concentration (see figure 6 [21]), and the boron dose component as a consequence. For the heterogeneous GBM model, the in-beam SFs show similar trend with a slight variation in values between different MEP models, and are considerably larger than those for the homogeneous GBM.

B. Quantification of survival fraction reduction following clinical target volume margin extension

Figures 7 (a), (b), and (c) show a comparison of the total survival fractions corresponding to a 2.0 cm CTV margin (i.e. 5.0 cm PTV) and a 2.5 cm CTV margin (i.e. 6.0 cm PTV) for the circular, elliptical and irregular MEP models and for the heterogeneous-hypoxic GBM

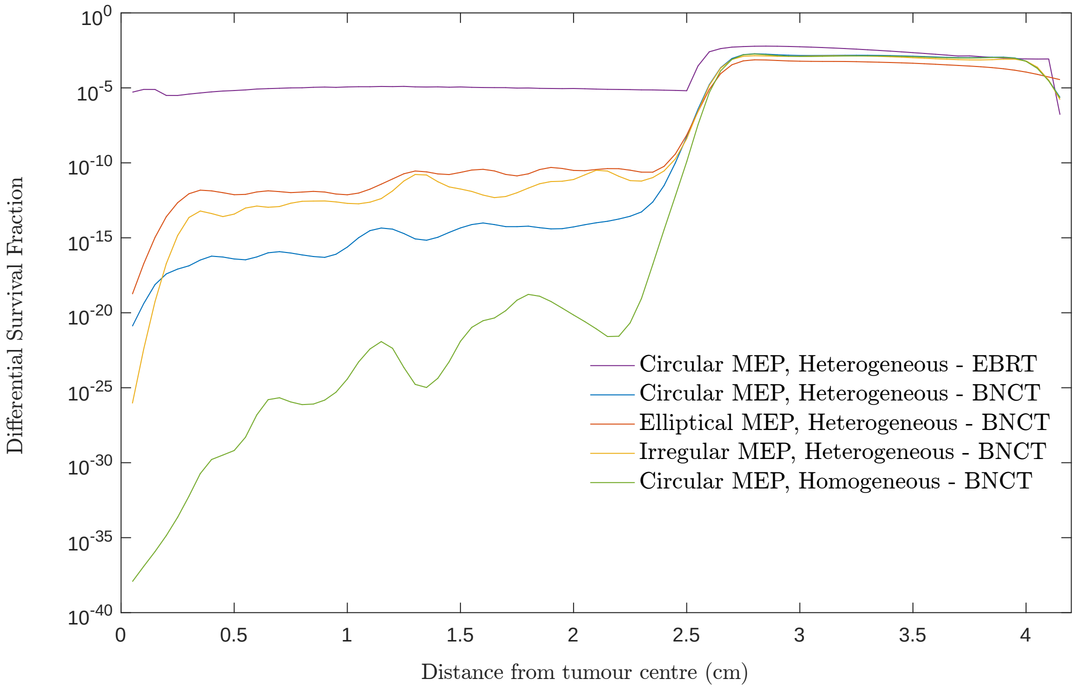

FIG. 5: Comparative representation of differential SFs versus distance from the tumour centre for three scenarios: heterogeneous-hypoxic GBM models treated with 1) BNCT applying circular, elliptical, and irregular MEP distributions; and 2) conventional x-ray therapy for a circular MEP model [22]; and 3) homogeneous-hypoxic GBM model treated with BNCT for a circular MEP model [21]. The graphs were obtained using 2.0 cm CTV margin (corresponding to 2.5 cm beam radius).

model, respectively.

The calculated SF_{change} data, as a result of the CTV margin increase by 0.5 cm, are summarized in table III. As suggested by these results, the SFs for heterogeneous-hypoxic GBM treated with BNCT and 2.5 cm CTV margin were reduced between (61.7 ± 0.2)% and (55.7 ± 0.2)% for irregular and circular MEPs, respectively compared to 2.0 cm CTV margin. The reduction in the SF as a result of the CTV extension was, however, more pronounced for heterogeneous-hypoxic GBM treated by conventional x-ray therapy ranging from (72.6 ± 3.6)% to (77.7 ± 3.1)% for circular and elliptical MEP models respectively.

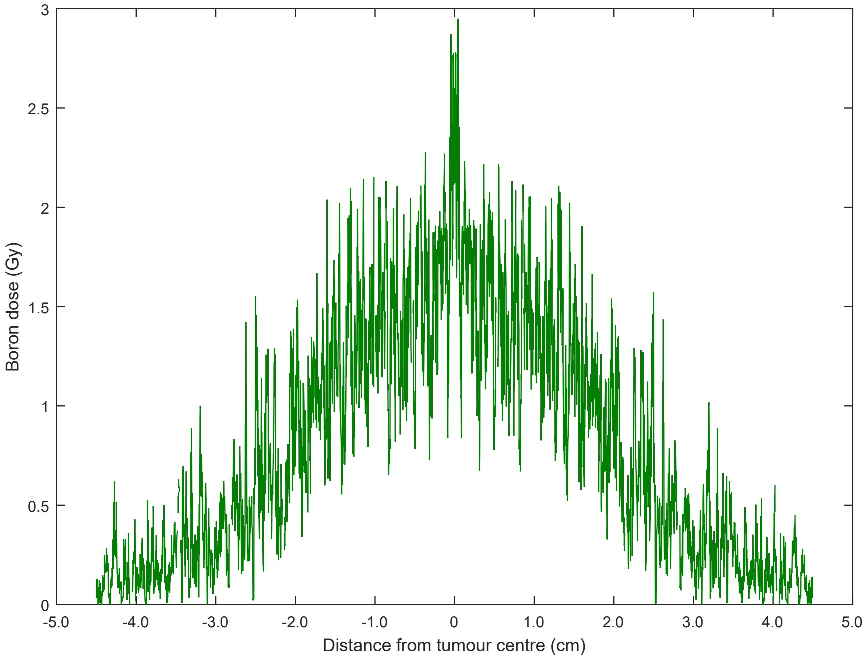

FIG. 6: Axial profile of the calculated cell-based boron dose distribution in the scoring plane versus distance from the tumour centre using circular MEP [21]. The statistical uncertainty in the calculated results was on average ±12.5%.

TABLE III: Changes in the SFs (equation 7) as a result of the CTV extension (from 2.0 to 2.5 cm) for a heterogeneous-hypoxic GBM model and the three MEP models treated with BNCT. The previously-reported results for x-ray EBRT [22] are also presented for comparison purposes.

Treatment modality	BNCT		
MEP model	SF with 2.0 cm CTV (%)	SF with 2.5 cm CTV (%)	SF_{change}(%)
Circular	3.9 ± 0.4	1.7 ± 0.3	55.7 ± 0.2
Elliptical	1.5 ± 0.3	0.6 ± 0.2	56.2 ± 0.3
Irregular	3.8 ± 0.6	1.5 ± 0.3	61.7 ± 0.2
	Conventional x-ray therapy		
Circular	12.9 ± 1.0	3.5 ± 0.3	72.6 ± 3.6
Elliptical	5.5 ± 0.5	1.2 ± 0.1	77.7 ± 3.1
Irregular	11.1 ± 0.8	2.9 ± 0.2	73.5 ± 3.4

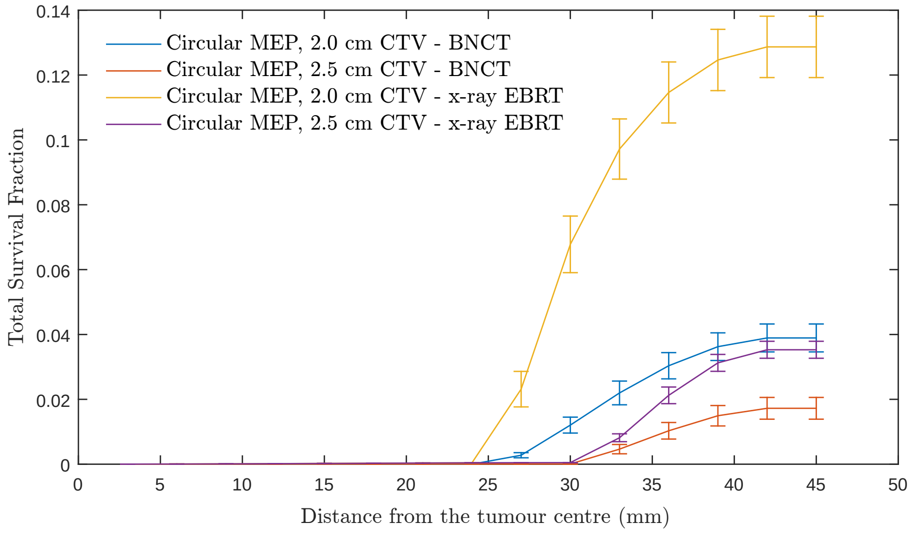

(a) Circular MEP.

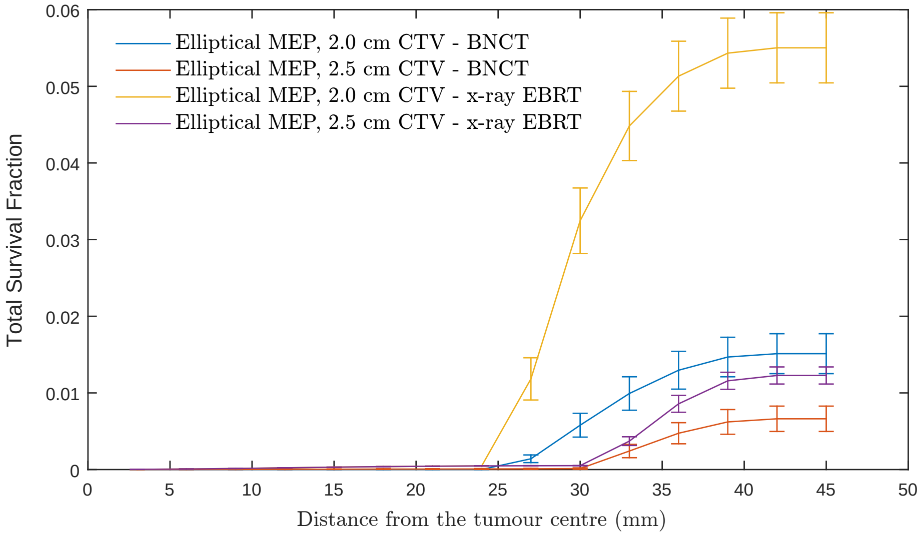

(b) Elliptical MEP.

FIG. 7

IV. DISCUSSION

The model developed in this work is an expansion on the BNCT simulation of the *in silico* cellular GBM model described in our previous report [21]. In the current work, genetic het-

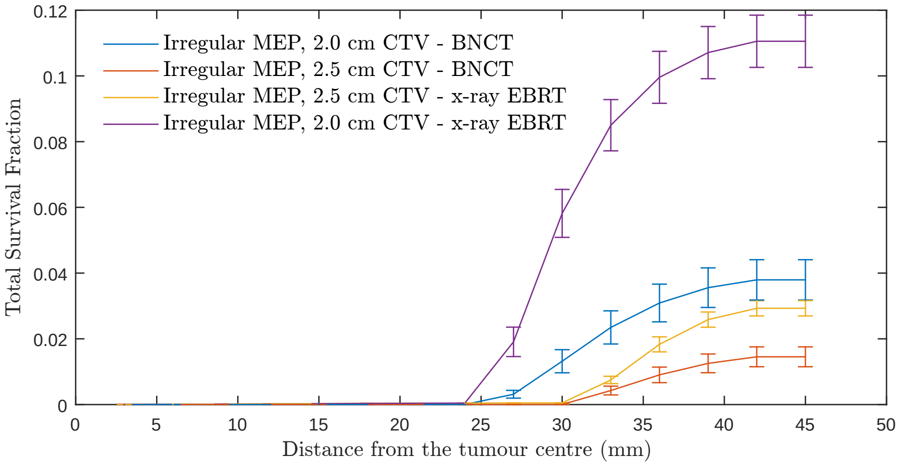

(c) Irregular MEP.

FIG. 7: Total SF versus distance from the tumour centre for 2.0 and 2.5 cm CTVs applying three microscopic extension distribution models for a heterogeneous-hypoxic GBM treated by BNCT as compared to conventional x-ray therapy.

erogeneity in terms of radiosensitivity was incorporated into the cellular platform of the GBM model and three different infiltration distributions (i.e. circular, elliptical and irregular MEPs) were investigated. The model aimed to evaluate the cell kill efficacy following BNCT and the results were compared with those for x-ray EBRT reported previously by our group [22]. Additionally, the effect of the CTV margin extension on cell survival was also investigated.

BNCT could potentially be a suitable modality for GBM treatment compared to x-ray EBRT as BNCT has the ability to deliver localized absorbed dose deposited by high LET particles to tumour cells containing a sufficient number of boron atoms while minimizing the dose to normal tissue cells which contain fewer number of boron atoms. The efficacy of BNCT depends on the ratio of tumour to normal tissue boron concentration to deliver a treatment with reduced side effects. Ongoing research is performed to enhance the ratio of tumour to normal brain boron concentration [17, 31–33]. In this study, a ratio of 3.5 was considered as this is the most commonly assumed value in literature [21].

Following the BNCT treatment of heterogeneous hypoxic GBM, the calculated SFs within the beam region varied slightly between the MEP models, and decreased by more than two orders of magnitude as compared to conventional photon EBRT (table II). As reported in the previous work [21] for homogeneous-hypoxic GBM, this reduction was found to be four orders of magnitude. The calculated number of surviving cells within the beam (i.e. $SF_{\text{within the beam}}$ × total number of tumour cells before treatment) was on average ~ 6, suggesting that BNCT should be able to provide some local tumour control. Moreover, published clinical data, while being scarce for BNCT failure patterns, are in agreement with this simulation finding. In a cohort of 8 GBM patients treated by BNCT with the median follow-up duration of 20.3 months in the study of Matsuda *et al.* [34], none of the patients recurred within the GTV and 6 out of 8 patients recurred in the low dose regions of CTV (i.e. where the average minimum dose dropped to about half of that in the GTV region) and the failure was attributed to low or heterogeneous boron concentration and insufficient thermal neutron delivery to the CTV. Similarly, the local tumour progression occurred only in three cases in a cohort of 20 high-grade meningioma patients with the median follow-up duration of 13 months [26].

The SFs in the penumbra region were also evaluated in this work to quantify the contribution of histological disease to total SFs for various microscopic extension distributions. The ratio of the SF in penumbra region to total SF, which is an approximate measure of the ME contribution to SF, following BNCT, ranged $\sim\ 0.3 - 0.7$ between MEP models, while it was almost the same ($\sim\ 0.5$) for all MEP models using x-ray EBRT. The large variation between MEP models in terms of the SF in penumbra region in BNCT modality could be attributed to neutron scatter. Fast neutrons that have scattered laterally into the penumbra region and thermalized through multiple scattering, could undergo boron neutron capture reaction which depends on the boron concentration in the tumour periphery and therefore the MEP model. As summarized in table II, the SF in penumbra and the total SF for BNCT were significantly lower compared to corresponding SFs following x-ray EBRT. Additionally, the simulation results suggest that BNCT may be the most efficacious for tumours with elliptical (i.e. elongated) microscopic extension.

Differential SF curves presented in figure 5 allowed for the analysis of the SF within the beam area and beyond in more detail. Following BNCT, the differential SF trended similarly for all MEP models and heterogeneous GBM. SF gradually increased as a function of distance from the tumour centre as a result of boron dose reduction. Compared with heterogeneous

GBM, homogeneous GBM showed a larger SF gradient within the beam, suggesting superior response of a GBM with homogeneous cell population to BNCT, which unfortunately is not realistic in most cases. The incorporation of heterogeneity and anisotropic microscopic extension did not alter the pattern of SF considerably but still suggests reduced efficacy of BNCT as compared to homogeneous scenarios. Following EBRT, however, the SF trend changed completely, showing a plateau within the beam with a local peak within the GTV, which received an additional boost of 10 Gy in x-ray EBRT (30 fractions of 2 Gy to the PTV plus a 10 Gy boost to the GTV) [22]. This suggests that the tumour most likely relapses in the GTV. It is difficult to directly compare these simulation results with clinical findings due to the fact that the data addressing post-treatment failure analysis for BNCT is limited in literature. However, the differences between calculated SF patterns in this work explain the varying failure patterns for BNCT and x-ray therapy reflected in published literature. For example, as reported by Aydin [35] and Lee [36], following x-ray EBRT, GBM tumour relapsed locally and particularly in the GTV region with severe hypoxia (consistent with the local peak in figure 5). The SF gradient within the beam following BNCT indicates that the tumour is likely to recur at farther distances from the GTV, which is in agreement with the observation in the study of Matsuda *et al.* [34]. Although the SF in penumbra is lower for all three MEP models using BNCT as compared to x-ray EBRT, it is still considerable and could increase the risk of marginal recurrence, as also demonstrated in published clinical studies [26, 37].

Quantification of SF reduction as a result of the CTV margin extension by 0.5 cm could be useful in deciding whether the reduction in SF as a result of the CTV extension is sufficiently large to justify increased toxicity of normal tissue. As shown in figures 7 (a), (b), and (c), BNCT results in a markedly reduced SFs for both CTV extensions for all three MEP models as compared to conventional x-ray therapy for heterogeneous-hypoxic GBM. As shown, the response of GBM to BNCT is the best for elliptical infiltration distribution (figure 7 (b)) and the least favourable for circular microscopic extension (figure 7 (a)). The reduction in SF as a result of the CTV margin extension using BNCT was on average (between the three MEP models) $\sim$ 2.4 times which is less compared to x-ray EBRT ($\sim$ 4 times), see table III). This indicates that while the extension of the CTV margin could be beneficial and prolong the survival of GBM patients treated by x-ray EBRT by reducing the risk of marginal recurrence, it may not benefit as much the GBM patients treated by BNCT.

V. CONCLUSION AND FUTURE WORK

In this work, we investigated the response of heterogeneous GBM of various infiltration geometries to BNCT. The results in terms of surviving tumour cells were compared with those obtained previously for x-ray EBRT.

The main outcomes of this study were:

1. Unlike x-ray therapy, which cannot overcome radioresistance and complexities of GBM, BNCT could potentially be a promising modality for this malignancy under these conditions: 1) there is sufficient enhancement of tumour to normal tissue boron concentration; and 2) availability of a suitable neutron beam with high proportion of thermal neutrons while minimizing fast neutron components.
2. A quantification tool was developed to estimate the reduction in survival fraction due to extension of the CTV for three MEP distributions. It was concluded that the reduction in SF, which was considerably lower than that for x-ray therapy for all MEP models, may not justify the increased normal brain exposure to high LET radiation.
3. It was demonstrated that BNCT is efficacious for GBM within the beam in terms of cell kill efficacy. Any increase in the dose and the CTV margin extension should be subject to further improvement of boron microdistribution and the neutron beam spectrum and should be evaluated with care.

A potential extension of this model is to take a microdosimetry approach to translation of physical dose to radiobiological endpoints (e.g. cell death) by using more accurate representation of cellular radiobiology and the cell survival probability based on microscopic parameters. These parameters can be obtained by Monte Carlo modelling of BNCT beam particles track structures which could be further fed into the radiobiological model.

REFERENCES

[1] Dale Purves, George J Augustine, David Fitzpatrick, William C Hall, Anthony-Samuel LaMantia, James O McNamara, and Leonard E White, "Neuroscience. 4th," Sunderland, MA: Sinauer Associates (2007).

[2] Jan Unkelbach, Bjoern H Menze, Ender Konukoglu, Florian Dittmann, Nicholas Ayache, and Helen A Shih, "Radiotherapy planning for glioblastoma based on a tumor growth model: implications for spatial dose redistribution," Physics in medicine and biology **59**, 771 (2014).

[3] Ashray Gunjur, Mathias Bressel, and Gail Ryan, "The addition of temozolomide does not change the pattern of progression of glioblastoma multiforme post-radiotherapy," Journal of medical imaging and radiation oncology **56**, 567–573 (2012).

[4] June L Chan, Susan W Lee, Benedick A Fraass, Daniel P Normolle, Harry S Greenberg, Larry R Junck, Stephen S Gebarski, and Howard M Sandler, "Survival and failure patterns of high-grade gliomas after three-dimensional conformal radiotherapy," Journal of clinical oncology **20**, 1635–1642 (2002).

[5] Ulrich Oppitz, Dirk Maessen, Hildegard Zunterer, Susanne Richter, and Michael Flentje, "3d-recurrence-patterns of gliobastomas after ct-planned postoperative irradiation," Radiotherapy and Oncology **53**, 53–57 (1999).

[6] Yuan Rong, Donald L Durden, Erwin G Van Meir, and Daniel J Brat, "'pseudopalisading'necrosis in glioblastoma: a familiar morphologic feature that links vascular pathology, hypoxia, and angiogenesis," Journal of Neuropathology & Experimental Neurology **65**, 529–539 (2006).

[7] AJ Kole, HS Park, DN Yeboa, CE Rutter, CD Corso, S Aneja, NH Lester-Coll, BR Mancini, JP Knisely, and JB Yu, "Concurrent chemoradiotherapy versus radiotherapy alone for "biopsy-only" glioblastoma multiforme," Cancer (2016).

[8] Jake Van Dyk, *The modern technology of radiation oncology: a compendium for medical physicists and radiation oncologists* (Medical Physics Pub Corp, 1999).

[9] Barry J Allen, "Internal high linear energy transfer (let) targeted radiotherapy for cancer," Physics in medicine and biology **51**, R327 (2006).

[10] T Yamamoto, A Matsumura, K Nakai, Y Shibata, K Endo, F Sakurai, T Kishi, H Kumada, K Yamamoto, and Y Torii, "Current clinical results of the tsukuba bnct trial," Applied radiation and isotopes **61**, 1089–1093 (2004).

[11] Tetsuya Yamamoto, Kei Nakai, Teruyoshi Kageji, Hiroaki Kumada, Kiyoshi Endo, Masahide Matsuda, Yasushi Shibata, and Akira Matsumura, "Boron neutron capture therapy for newly diagnosed glioblastoma," Radiotherapy and oncology **91**, 80–84 (2009).

[12] Yoshinobu Nakagawa, Kyonghon Pooh, Toru Kobayashi, Teruyoshi Kageji, Shinichi Uyama, Akira Matsumura, and Hiroaki Kumada, "Clinical review of the japanese experience with boron neutron capture therapy and a proposed strategy using epithermal neutron beams," Journal of neuro-oncology **62**, 87–99 (2003).

[13] Shinji Kawabata, Shin-Ichi Miyatake, Naosuke Nonoguchi, Ry Hiramatsu, Kyoko Iida, Shiro Miyata, Kunio Yokoyama, Atsushi Doi, Yuzo Kuroda, Toshihiko Kuroiwa, *et al.*, "Survival benefit from boron neutron capture therapy for the newly diagnosed glioblastoma patients," Applied Radiation and Isotopes **67**, S15–S18 (2009).

[14] Walter J Curran, Charles B Scott, John Horton, James S Nelson, Alan S Weinstein, A Jennifer Fischbach, Chu H Chang, Marvin Rotman, Sucha O Asbell, Robert E Krisch, *et al.*, "Recursive partitioning analysis of prognostic factors in three radiation therapy oncology group malignant glioma trials," Journal of the National Cancer Institute **85**, 704–710 (1993).

[15] René-Olivier Mirimanoff, Thierry Gorlia, Warren Mason, Martin J Van den Bent, Rolf-Dieter Kortmann, Barbara Fisher, Michele Reni, Alba A Brandes, Jüergen Curschmann, Salvador Villa, *et al.*, "Radiotherapy and temozolomide for newly diagnosed glioblastoma: recursive partitioning analysis of the eortc 26981/22981-ncic ce3 phase iii randomized trial," Journal of Clinical Oncology **24**, 2563–2569 (2006).

[16] L Moghaddasi, E Bezak, and W Harriss-Phillips, "Development and verification of a geant4 beam model for boron neutron capture therapy," Medica Physica (2016b).

[17] Rolf F Barth, MG Vicente, Otto K Harling, WS Kiger 3rd, Kent J Riley, Peter J Binns, Franz M Wagner, Minoru Suzuki, Teruhito Aihara, Itsuro Kato, *et al.*, "Current status of boron neutron capture therapy of high grade gliomas and recurrent head and neck cancer," Radiat Oncol **7**, 1–21 (2012).

[18] Matthew R Palmer, J Timothy Goorley, WS Kiger, Paul M Busse, Kent J Riley, Otto K Harling, and Robert G Zamenhof, "Treatment planning and dosimetry for the harvard-mit

phase i clinical trial of cranial neutron capture therapy," International Journal of Radiation Oncology* Biology* Physics **53**, 1361–1379 (2002).

[19] JA Coderre *et al.*, *Current status of neutron capture therapy*, Tech. Rep. (IAEA-TECDOC-1223. ISSN 1011–4289, Annex 6, IAEA, 2001).

[20] Sea Agostinelli, John Allison, K al Amako, J Apostolakis, H Araujo, P Arce, M Asai, D Axen, S Banerjee, G Barrand, *et al.*, "Geant4a simulation toolkit," Nuclear instruments and methods in physics research section A: Accelerators, Spectrometers, Detectors and Associated Equipment **506**, 250–303 (2003).

[21] L Moghaddasi, E Bezak, and W Harriss-Phillips, "Development of an integrated monte-carlo model for glioblastoma multiforme treated with boron neutron capture therapy," (2016c).

[22] L Moghaddasi, E Bezak, and W Harriss-Phillips, "Monte-carlo model development for evaluation of current clinical target volume definition for heterogeneous and hypoxic glioblastoma," Physics in Medicine and Biology **61**, 3407 (2016).

[23] Reinhold Nafe, Kea Franz, Wolfgang Schlote, and Berthold Schneider, "Morphology of tumor cell nuclei is significantly related with survival time of patients with glioblastomas," Clinical cancer research **11**, 2141–2148 (2005).

[24] Leyla Moghaddasi, Eva Bezak, and Wendy Harriss-Phillips, "Evaluation of current clinical target volume definitions for glioblastoma using cell-based dosimetry stochastic methods," The British journal of radiology **88**, 20150155 (2015).

[25] Milan Marek, Miroslav Vins, Zdena Lahodova, Ladislav Viererbl, and Michal Koleska, "Extended set of activation monitors for nct beam characterization and spectral conditions of the beam after reactor fuel conversion," Applied Radiation and Isotopes **88**, 157–161 (2014).

[26] Shinji Kawabata, Ryo Hiramatsu, Toshihiko Kuroiwa, Koji Ono, and Shin-Ichi Miyatake, "Boron neutron capture therapy for recurrent high-grade meningiomas: Clinical article," Journal of neurosurgery **119**, 837–844 (2013).

[27] T Kageji, Y Mizobuchi, S Nagahiro, Y Nakagawa, and H Kumada, "Correlation between radiation dose and histopathological findings in patients with gliblastoma treated with boron neutron capture therapy (bnct)," Applied Radiation and Isotopes **88**, 20–22 (2014).

[28] GM Morris, JA Coderre, PL Micca, CD Fisher, J Capala, and JW Hopewell, "Central nervous system tolerance to boron neutron capture therapy with p-boronophenylalanine." British journal of cancer **76**, 1623 (1997).

[29] Alphonse Taghian, Herman Suit, Francisco Pardo, Danielle Gioioso, Kathleen Tomkinson, Willem DuBois, and Leo Gerweck, "In vitro intrinsic radiation sensitivity of glioblastoma multiforme," International Journal of Radiation Oncology* Biology* Physics **23**, 55–62 (1992).

[30] GW Barendsen, CJ Koot, GR Van Kersen, DK Bewley, SB Field, and CJ Parnell, "The effect of oxygen on impairment of the proliferative capacity of human cells in culture by ionizing radiations of different let," International Journal of Radiation Biology and Related Studies in Physics, Chemistry and Medicine **10**, 317–327 (1966).

[31] Silvia Capuani, Tommaso Gili, Marco Bozzali, Salvatore Russo, Paola Porcari, Cesare Cametti, Emanuela D'Amore, Marco Colasanti, Giorgio Venturini, Bruno Maraviglia, Giuseppe Lazzarino, and Francesco S Pastore, "L-dopa preloading increases the uptake of borophenylalanine in c6 glioma rat model: a new strategy to improve bnct efficacy," International Journal of Radiation Oncology* Biology* Physics **72**, 562–567 (2008).

[32] WS Kiger, III, MR Palmer, KJ Riley, RG Zamenhof, and PM Busse, "A pharmacokinetic model for the concentration of 10b in blood after boronophenylalanine-fructose administration in humans," Radiation research **155**, 611–618 (2001).

[33] Shin-Ichi Miyatake, Shinji Kawabata, Yoshinaga Kajimoto, Atsushi Aoki, Kunio Yokoyama, Makoto Yamada, Toshihiko Kuroiwa, Motomu Tsuji, Yoshio Imahori, Mitsunori Kirihata, *et al.*, "Modified boron neutron capture therapy for malignant gliomas performed using epithermal neutron and two boron compounds with different accumulation mechanisms: an efficacy study based on findings on neuroimages," Journal of neurosurgery **103**, 1000–1009 (2005).

[34] M Matsuda, T Yamamoto, H Kumada, K Nakai, M Shirakawa, T Tsurubuchi, and A Matsumura, "Dose distribution and clinical response of glioblastoma treated with boron neutron capture therapy," Applied Radiation and Isotopes **67**, S19–S21 (2009).

[35] Halim Aydın, Ina Sillenberg, and Harald von Lieven, "Patterns of failure following ct-based 3-d irradiation for malignant glioma," Strahlentherapie und Onkologie **177**, 424–431 (2001).

[36] Irwin H Lee, Morand Piert, Diana Gomez-Hassan, Larry Junck, Lisa Rogers, James Hayman, Randall K Ten Haken, Theodore S Lawrence, Yue Cao, and Christina Tsien, "Association of 11 c-methionine pet uptake with site of failure after concurrent temozolomide and radiation for primary glioblastoma multiforme," International Journal of Radiation Oncology* Biology* Physics **73**, 479–485 (2009).

[37] Shin-Ichi Miyatake, Hiroko Kuwabara, Yoshinaga Kajimoto, Shinji Kawabata, Kunio Yokoyama, Atsushi Doi, Motomu Tsuji, Hiroshi Mori, Koji Ono, and Toshihiko Kuroiwa, "Preferential recurrence of a sarcomatous component of a gliosarcoma after boron neutron capture therapy: case report," Journal of neuro-oncology **76**, 143–147 (2006).

9.3 Conclusion

A comprehensive radiobiological BNCT modelling tool for an *in silico* GBM with three different microscopic extension distribution patterns was developed. The model simulates a semi-realistic GBM, including major characteristics of this malignancy affecting cellular response to BNCT: intrinsic radiosensitivity, genetic heterogeneity, hypoxia, and varying boron concentration depending on whether the cell is a tumour clonogen or a normal cell. The simulation results can be summarized into two main findings:

- The surviving fraction within the beam region (i.e. the PTV) varied slightly between the GBM with different MEP models and was reduced by ~ 2 orders of magnitude using BNCT as compared to x-ray EBRT for heterogeneous GBM. These results, while not as promising as those obtained for homogeneous GBM (the SF within the beam was lower by two orders of magnitude compared to the heterogeneous case), still indicates that GBM may be responsive to BNCT in the PTV.
- Predictions of the quantitative tool developed in this chapter for the evaluation of CTV margins of 2.0 and 2.5 cm, indicated a marked decrease in SF for both 2.0 and 2.5 cm CTV margins using BNCT as opposed to x-ray EBRT. However, it was demonstrated that compared to x-ray EBRT, the reduction in SF as a result of the CTV margin extension was reduced by $\sim 20\%$ using BNCT for all three MEP models. Therefore, further expansion of the CTV margin may not be warranted in BNCT at its current status of development. Given the high radiobiological effect of neutrons, any adjustments in BNCT delivery including dose escalation/margin extension should be subject to two major improvements: 1) enhancement of tumour to normal tissue boron concentration; and 2) sufficient delivery of thermal neutron while minimizing fast neutron components in epithermal beam production.

Chapter 10

Conclusion and future work

10.1 Conclusion

The main objective of the current work has been to develop a radiobiological Monte Carlo (MC) model to address clinically important issues in radiotherapy of Glioblastoma Multiforme (GBM). GBM of the brain possesses aggressive characteristics which have caused all current treatment regimens to be inefficient, and as a result GBM patients have consistently poor prognosis. These features include high mobility (i.e. diffusive infiltration), presence of microenvironmental cells other than neoplastic gliomas, high intrinsic radioresistance with genetic heterogeneity and complexity, and extensive hypoxia. Determination of an optimal Clinical Target Volume (CTV) margin is generally problematic since the exact extent of microscopic disease to be encompassed by the CTV cannot be fully visualized using current imaging techniques and therefore remains uncertain.The diffusive characteristics of GBM cells and their rapid peripheral expansion cause the CTV delineation of this type of tumour to be even more problematic. This issue has been widely reflected in literature indicating a high discrepancy/uncertainty in the CTV margin definition for GBM (see chapter 2).

A wide range of mathematical and computational models have been developed over the last three decades to provide prediction of patterns of GBM infiltration (chapter 3). Recent deterministic models have incorporated several biological mechanisms such as hypoxia, haptotaxis and more, and are capable to anticipate tumour behaviour at a macroscopic level (Unkelbach et al., 2014, Martínez-González et al., 2012). Stochastic models (e.g. Monte Carlo) have also shown a progressive improvement by moving from a macroscopic to a microscopic scale, and can accurately predict absorbed dose and radiobiological effects of radiation (e.g. cell death) (e.g. (Incerti et al., 2009)). Despite these developments, to our knowledge, there is no published work reporting an integrated stochastic tumour model with MC cell-based dosimetry application to evaluate radiotherapy treatment outcome for glioblastoma of the brain.

Consequently, the primary goal of this research work was to establish a micro-scale GBM treatment modelling framework for the evaluation of current CTV practices in terms of survival fraction of tumour clonogens following the External Beam Radiotherapy (EBRT). The computational model was initially developed for a 6 MV x-ray EBRT for a simplified homogeneous GBM model and gradually expanded to take into account more radiobiological parameters to perform a more realistic radiobiological simulation. The predictions of the model directed this research to investigate another treatment modality, namely, Boron Neutron Capture Therapy (BNCT). BNCT is designed to target cancer cells and to deliver localized dose deposited by high Linear Energy Transfer (LET) particles preferentially to tumour cells and to provide superior normal tissue sparing as compared to conventional EBRT. Consequently, the second phase of this work focused on developing a BNCT to be incorporated into the GBM modelling framework and on investigating whether this modality could overcome the limitations of x-ray EBRT.

The literature was thoroughly reviewed (see chapters 2 and 3) to identify appropriate model parameters (e.g. the extension and pattern of microscopic extension for GBM) to establish a model based on clinical data. An innovative approach was taken to establish a cellular-scale modelling framework for GBM treatment using a 6 MV x-ray beam and to evaluate its outcome in terms of cell Survival Fraction (SF). The MC model integrated three components: 1) an *in silico* GBM tumour model with diffusions of tumour cells beyond the CTV margin, called Microscopic Extension Probability (MEP) models developed in MATLAB®, 2) a dosimetry module for GBM model irradiation using the Geant4 MC toolkit; and 3) a cell survival probability algorithm developed in MATLAB®. The main achievements in the development of the model are:

1. A Geant4 6 MV x-ray beam model with realistic energy spectrum was developed, and comprehensively verified against experimental data. The beam model was used as the source of EBRT in the MC irradiation module (chapter 4).

2. Three models of GBM microscopic extensions (i.e. MEP models), namely, isotropic, elongated/elliptical, and irregular patterns, were simulated to reflect clinical infiltration patterns published in literature (chapter 5).

3. A cell SF algorithm was developed for the GBM model. The SF algorithm was used to combine all of the above-mentioned components for SF calculation. The cellular platform established allowed for incorporation of other biological characteristics affecting cellular radiosensitivity (chapter 5).

4. The model was further expanded to incorporate genetic heterogeneity in terms of radiosensitivity of individual cells, and cellular oxygenation (i.e hypoxia) to calculate GBM cell SFs and evaluate the impact of CTV margins of 2.0 and 2.5 cm on cell survival fraction in x-ray EBRT (chapter 6).

5. In the second phase of the study the GBM treatment modelling framework was used to simulate BNCT modality for GBM.

6. The literature was reviewed to identify a clinically relevant BNCT spectrum. An epithermal BNCT neutron beam model was developed using Geant4 MC toolkit and was tested against published literature. Two sensitivity analyses were performed using the code developed for the BNCT beam model to investigate optimal neutron beam and cellular boron concentrations. (chapter 7).

7. A novel MC BNCT modelling platform for an *in silico* GBM was constructed utilizing the codes developed in chapters 7 and 5 (MEP models). Simulation of BNCT, at this level of accuracy and complexity has never been performed, to our knowledge, inside a MC particle tracking toolkit before. Unlike the x-ray EBRT model, for the BNCT, the cell-based dosimetry module is not independent of the GBM model as the dose deposited in individual cells depends on the cellular boron concentration which is in itself dependent on whether the cell is a tumour or a normal cell.

This required a cellular boron concentration for each MEP model to be generated, imported to Geant4 and assigned to corresponding cells.

8. A MC BNCT treatment modelling platform for GBM was constructed utilizing the codes developed in chapters 7 and 5 (MEP models). A simplified GBM model consisting only of a population of cells with homogeneous radiosensitivities and isotropic infiltration distribution was initially used.
9. The model was expanded to simulate a semi-realistic GBM, including major characteristics of this malignancy affecting cellular response to BNCT, e.g. intrinsic radiosensitivity, genetic heterogeneity, hypoxia. At this point the final goal of the current work, to perform a comprehensive radiobiological BNCT simulation for an *in silico* GBM with three different microscopic extension distribution patterns was achieved.
10. The SF algorithm (chapter 6) was used to calculate cell survival fraction following BNCT to evaluate the efficacy of BNCT for the treatment/management of GBM as compared to x-ray EBRT. The SFs were calculated using CTV margins of 2.0 and 2.5 cm to quantitatively evaluate the impact of CTV margins on cell suvival in BNCT.

The main findings of the model are outlined as follows:

1. The quantification tool developed for hypoxic and heterogeneous GBM enabled to predict the reduction in SF as a result of the CTV margin extension by 0.5 cm (from 2.0 to 2.5 cm). While it is evident that increasing the margin will decrease the SF, quantification of this reduction can be a useful guidance for clinicians on their decision to choose an optimal CTV margin. It was determined that the choice of a larger CTV margin in x-ray EBRT may be beneficial to extend the time to recurrence for GBM patients, as it resulted in the reduction of the SF by approximately 3.5- 4.5 times depending on the type of microscopic extension distribution.
2. X-ray EBRT, using the current treatment protocols, does not seem to produce the required radiobiological damage to GBM cells to kill or sterilize them. Even dose

escalation to 70 Gy (in the GTV region) does not result in an improved control. This is attributed to the intrinsic radioresistance and heterogeneity and extensive hypoxic nature of GBM that cannot be overcome by low LET x-ray EBRT.

3. For BNCT, the SF within the beam region varied slightly between semi-realistic *in silico* GBM model with different MEP models and was reduced by ∼ 2 orders of magnitude using BNCT as compared to x-ray EBRT. This indicates that BNCT may be more efficacious therapy for GBM than x-ray EBRT within the treatment field (i.e. the PTV).
4. The total SF was reduced up to 4 times (depending on the type of MEP distribution) using BNCT compared to x-ray EBRT. As determined by the quantitative tool developed, the reduction in SF as a result of the CTV margin extension using BNCT was on average (for all three MEP models) ∼ 2.4 times compared to x-ray EBRT (∼ 4 times). In other words, in terms of total tumour control, GBM patients treated by BNCT will benefit less from the CTV margin extension compared to those treated with x-ray EBRT. Furthermore, considering the high radiobiological effect of neutrons, while not investigated in this work, the impact of the larger CTV margin on the normal brain toxicity would be more severe for BNCT as compared to conventional EBRT. Additionally, any dose escalation or CTV margin extension will further improve BNCT efficacy subject to: 1) enhancement of tumour to normal tissue boron concentration; and 2) delivery of sufficient numbers of thermal neutrons while minimizing fast neutron components in the epithermal beam composition.

10.2 Future Work

The flexibility and robustness of this radiobiological model, capable of modelling a wide range of experimental conditions, treatment modalities, and other cancer sites, has been manifested throughout the thesis. However, this model still has limitations which should be addressed in future research.

Cancer systems are complex and dynamic systems and progression through cell death is influenced by a large number of microscopic biological and chemical mechanisms which are merged into two parameters in the Linear Quadratic (LQ) model used in this work. The focus in modern radiobiology modelling has moved towards using stochastic Monte Carlo methods (i.e. describing a macroscopic tumour behaviour by simulation of microscopic scale interactions in individual cells) rather than an analytical mathematical equation (i.e. predicting the behaviour of a group of cells as a whole). Hybrid modelling approaches, a combination of Monte Carlo and analytical based modelling, could be equally useful to translate physical interactions into radiobiological endpoints.

Recently, a hybrid methodology was designed by Douglass *et al.* (Douglass, 2014) in their radiobiological package using the Two Lesion Kinetics (TLK) model (Stewart, 2001), adapted to the cellular level. The model enabled prediction of radiation damage produced by physical processes at a nano-scale level. This required the simulation of particle track structures (i.e. using Geant4-DNA (Incerti et al., 2010)) to calculate the number and location of ionization events in each cell. The clustering algorithm, developed in the same work, was used to calculate the number of simple and complex DNA double strand breaks as an input to TLK model. The TLK model was solved to calculate the number of surviving cells, to subsequently obtain the cell survival curve.

The model developed in this work is also a hybrid model, integrating the MC dose calculation with an analytical cell survival algorithm by improving the LQ model, which was adapted to study the radiation effects in individual cells rather than the average over the entire tumour. Potential areas of the code development include:

1. Utilizing a more advanced mathematical cell death model using microscopic or molecular level parameters, e.g. Lethal and Potentially Lethal (LPL) (Curtis, 1986) or TLK models, to replace the LQ model used in the software package developed in this work. Nevertheless, at present the application of these models to this particular project is not possible as the available MC software (capable to simulate particle track structure) do not support boron material and neutron interactions. Therefore, the development of more accurate cell survival models is subject to further developments of Geant4-DNA or RITRACKS (Plante and Cucinotta, 2011).
2. Application of the model for charged particle therapy modalities, e.g. proton and carbon ion therapy or targeted alpha therapy where an alpha emitting radioisotope

is labelled with an antibody or protein which targets the antigens expressed by cancer cells.

3. Using the model for other tumour sites. This can be achieved by inputting physical and biological parameters corresponding to the tumour site to be modelled.

Appendix A

Microscopic Extension Probability (MEP) model

The code shown below simulates an irregular anisotropic extension of microscopic GBM cells into normal brain tissue.

```
 %% creating a matrix of ones encompassing tumour and microscopic extension
 myworld = ones(4500,4500,'single');  % 9cm*9cm surface so each element 20 micro meter
 % Initialization
   for i =1:4500
       for j = 1:4500
            if (i-2250)^2+(j-2250)^2 >((50)^2)
                                 myworld(i,j) = 0;
                        else

                                 myworld(i,j) = 1;
            end
       end
   end
 %% custom decay of ME (Mean Of the 4 data sets)
 r = ones(4500,4500,'single');
for i = 1:4500
 for j = 1:4500
  if (i-2250)^2+(j-2250)^2 >=((50)^2) && (i-2250)^2+(j-2250)^2 <= ((2050)^2)
   r(i,j) = ((((i-2250)^2+(j-2250)^2)^(1/2))-50)*(20*(10^-4));
   myworld(i,j)=(-0.5986*r(i,j)^4+7.043*r(i,j)^3-21.36*r(i,j)^2-13.22*r(i,j)+98.09)/100;
  elseif (i-2250)^2+(j-2250)^2 > ((2050)^2)
   myworld(i,j) = 0;
  end
 end
end


  for i = 1:4500
         for j = 1:4500
                 if myworld(i,j)<0
                         myworld(i,j)=0;
                 end
```

```
         end
  end

%% Obtain a randomely irregular probability distribution
% from circular isotropic distribution

         ME_irre = myworld;
         samp_vec = [200,250,400,500,1000];
         shrink_samp = randsample(samp_vec,16,true);

  % Obtain probability vector for 0 degree, to be used as the basis for shrinkage
         dir_vec = zeros(2050,1);
         slope = tand(0);
  for j = 2250:-1:200
         for k = 2251:4300
                 if (2250-j)/(k-2250) == slope
                         dir_vec(k-2250) = ME_irre(j,k);

                 end
         end
  end
  nnz(dir_vec)

 %% Shrink dir_vec for random shrinkages

 shrink_vec = cell(16,1);
 % distance from GTV to be used for polynomial coefficient
 distance = (0:1999).*(20*(10^-4));

 %% Work on top right quarter

 angle_samp = randsample(0:10:80,4);
  for i = 1:4
         n = shrink_samp(i);
         o = 2000/n;
         prob_vec = dir_vec;

         for m = 1:(2000/o)
           myvec = dir_vec((50+(m-1)*o):(49+ m*o));
           myprob = (sum(myvec))/(o-1);

                 if myprob > 1
                         myprob = 1;
                 end

           for q = 1:(o-1)
                 prob_vec(50 + (q-1) +(o-1)*(m-1)) = myprob;
           end
  end


  for x = (2050-n):2050
         prob_vec(x) = 0;
  end

 % substitute the created shrunk vector in cell storage

  shrink_vec{i} = prob_vec;

 % Obtain the Gaussian associated with the shrink_vec

  func = transpose(prob_vec(51:2050));
  coef = fit(transpose(distance),transpose(func),'gauss3');

 % Get the angle at which the probability is shrunk to shrink_vec

if angle_samp(i) ~= 90

for j = 2250:-1:200
 for k = 2251:4300
  if (j-2250)^2+(k-2250)^2 >=((50)^2) && (j-2250)^2+(k-2250)^2 <= ((1850)^2)
```

```
   r(j,k) = ((((j-2250)^2+(k-2250)^2)^(1/2))-50)*(20*(10^-4));
   if (2250-j)/(k-2250)<=tand(angle_samp(i)+ 5)&&(2250-j)/(k-2250)>=tand(angle_samp(i)-5)
         ME_irre(j,k) = feval (coef,r(j,k));
         if ME_irre(j,k) > 1
                 ME_irre(j,k) = 1;
         elseif ME_irre(j,k) < 0
                 ME_irre(j,k) = 0;
         end
   end
  end
end
end

else

for j = 2250:-1:200
 for k = 2000:4300
  if (j-2250)^2+(k-2250)^2 >=((50)^2) && (j-2250)^2+(k-2250)^2 <= ((2050)^2)
         r(j,k) = ((((j-2250)^2+(k-2250)^2)^(1/2))-50)*(20*(10^-4));
         if (2250-j)/(k-2250)<=11.4 && (2250-j)/(k-2250)>=-11.4 || (2250-j)/(k-2250)==Inf
                 ME_irre(j,k) = feval (coef,r(j,k));
         end
  end
 end
end
end
end

 %% Work on top left quarter

 angle_samp = randsample(100:10:180,4);
  for i = 5:8
   n = shrink_samp(i);
   o = 2000/n;
   prob_vec = dir_vec;
         for m = 1:(2000/o)
                 myvec = dir_vec((50+(m-1)*o):(49+ m*o));
                 myprob = (sum(myvec))/(o-1);
                         if myprob > 1
                                 myprob = 1;
                         end
                 for q = 1:(o-1)
                         prob_vec(50 + (q-1) +(o-1)*(m-1)) = myprob;
                 end
         end

  for x = (2050-n):2050
         prob_vec(x) = 0;
  end

 % substitute the created shrunk vector in cell storage

  shrink_vec{i} = prob_vec(51:2050);

 % Obtain the Gaussian associated with the shrink_vec

  func = transpose(shrink_vec{i});
  coef = fit(transpose(distance),transpose(func),'gauss3');

 % Get the angle at which the probability is shrunk to shrink_vec
 %substitute irregular pattern in ME_irre

for j = 2250:-1:200
 for k = 2249:-1:200
 if (j-2250)^2+(k-2250)^2 >=((50)^2) && (j-2250)^2+(k-2250)^2 <= ((2050)^2)
  r(j,k) = ((((j-2250)^2+(2250-k)^2)^(1/2))-50)*(20*(10^-4));
  if(2250-j)/(k-2250)>=tand(angle_samp(i-4)-5)&&(2250-j)/(k-2250)<=tand(angle_samp(i-4)+5)
   ME_irre(j,k) = feval (coef,r(j,k));
    if ME_irre(j,k) > 1
          ME_irre(j,k) = 1;
    elseif ME_irre(j,k) < 0
```

```
          ME_irre(j,k) = 0;
    end
  end
 end
 end
end

end

 %% Work on bottom left quarter
 .....

 %% Work on bottom right quarter
 .....

 %% Plot the results
 x = -2250:2249;
 y = -2250:2249;
 imagesc(myX,myY,ME_irre)
 colormap('default')
 colorbar
 az = 0;
 el = 90;
 %% plot isoline contour
 x = -2250:2249;
 y = -2250:2249;
 dis_x = x.*(20*10^-4);
 dis_y = y.*(20*10^-4);
 contour(dis_x,dis_y,ME_irre,20)
 colormap('default')
 colorbar
```

Appendix B

BNCT code- Geometry

This code, which is developed from scratch in this work, simulates the geometry in the BNCT treatment modelling code.

```
// DetectorConstruction

//

// Build the geometry and sensitive elements of our model

//


#include "DetectorConstruction.hh"

#include "G4NistManager.hh"
#include "G4Material.hh"
#include "G4UserLimits.hh"

#include "G4Box.hh"
#include "G4LogicalVolume.hh"
#include "G4PVPlacement.hh"

#include "G4PVParameterised.hh"
#include "NestedPhantomParameterisation.hh"
#include "G4PVReplica.hh"
#include "G4Region.hh"
#include "G4ProductionCuts.hh"

#include "G4VisAttributes.hh"
#include "G4Colour.hh"

#include "G4SDManager.hh"
#include "VoxelScoring.hh"
#include "ROGeom.hh"


#include <fstream>
#include <math.h>
#include <globals.hh>
#include "G4ThreeVector.hh"
#include <G4UnitsTable.hh>


// Constructor
```

```
DetectorConstruction::DetectorConstruction()

{

//initialize the dynamic arrays

num_voxels = 30;

B_den = new G4double[11];
B_fra = new G4double[11];
Br_fra = new G4double[11];
den = new G4double[11];
B_density = new G4float[(num_voxels)*(num_voxels)];

}


DetectorConstruction::~DetectorConstruction()

{

delete B_fra;
delete Br_fra;
delete den;

}

// Construct


G4VPhysicalVolume *DetectorConstruction::Construct()

{

//Zero the arrays at the beginning

for(G4int i=0;i<11;i++){

        B_den[i]=0;
        B_fra[i]=0;
        Br_fra[i]=0;
        den[i]=0;
}

for(G4int i=0;i<(num_voxels)*(num_voxels);i++){
        B_density[i]=0;
}

//Read "B_density.dat" file and store it in an array (B_density)

        ReadDensityData();

//....oooOO0OOooo........oooOO0OOooo........oooOO0OOooo........oooOO0OOooo......

// Define materials from the Geant4 database

G4NistManager* man = G4NistManager::Instance();
G4Material* air  = man->FindOrBuildMaterial("G4_AIR");

// Define composite materials (brain+ boron)

// Creating elements :

G4double z, a, density, ncomponents, fractionmass;
G4String name, symbol;


G4Element* boron = new G4Element( name = "Boron",symbol = "B",z = 5.0,
        a = 10.013 * g/mole );
G4Element* elH = new G4Element(name ="Hydrogen",symbol="H" , z= 1.0,
        a= 1.01*g/mole);
```

```
G4Element* elC  = new G4Element(name ="Carbon"  ,symbol="C" , z= 6.0,
         a= 12.01*g/mole);
G4Element* elN  = new G4Element(name ="Nitrogen",symbol="N" , z= 7.0,
        a= 14.01*g/mole);
G4Element* elO  = new G4Element(name ="Oxygen"  ,symbol="O" , z= 8.0,
        a= 16.00*g/mole);
G4Element* elNa = new G4Element( name = "Sodium",symbol = "Na",z= 11.0,
        a = 22.98977* g/mole);
G4Element* elMg = new G4Element( name = "Magnesium",symbol = "Mg",z = 12.0,
         a = 24.3050* g/mole );
G4Element* elP = new G4Element( name = "Phosphorus",symbol = "P",z = 30.0,
        a = 30.973976* g/mole );
G4Element* elS = new G4Element( name = "Sulfur",symbol = "S",z = 16.0,
        a = 32.065* g/mole );
G4Element* elCl = new G4Element( name = "Chlorine",symbol = "P",z = 17.0,
        a = 35.453* g/mole );
G4Element* elK = new G4Element( name = "Potassium",symbol = "P",z = 19.0,
        a = 30.0983* g/mole );
G4Element* elCa = new G4Element( name="Calcium",symbol = "Ca",z = 20.0,
        a = 40.078* g/mole );
G4Element* elFe = new G4Element( name = "Iron",symbol = "Fe",z = 26,
        a = 56.845* g/mole );
G4Element* elZn = new G4Element( name = "Zinc",symbol = "Zn",z = 30,
        a = 63.929* g/mole );


// Creating Materials :

G4int numberofElements;
G4Material* brain = new G4Material( "Brain", density = 1.03*g/cm3,
numberofElements = 13 );


brain->AddElement(elH,0.110667);
brain->AddElement(elC,0.12542);
brain->AddElement(elN,0.01328);
brain->AddElement(elO,0.737723);
brain->AddElement(elNa,0.00184);
brain->AddElement(elMg,0.00015);
brain->AddElement(elP,0.00354);
brain->AddElement(elS,0.00177);
brain->AddElement(elCl,0.00236);
brain->AddElement(elK,0.0031);
brain->AddElement(elCa,0.00009);
brain->AddElement(elFe,0.00005);
brain->AddElement(elZn,0.00001);


// Create an array of boron concentration


for(G4int i=0;i<11;i++){
        G4double b; // to round the decimal to double precision
        G4int a;
        b = 100*(0.65 + i*0.1625);
        a = b + 0.5;
        b = (G4double)a/100;
        B_den[i]= b;

}

// Define parameters to determine fraction masses

G4double m1 , m2;

m1 = 8.24*pow(10.0,-9.0)*g;  // brain mass in a voxel(gram)
m2 = 16.6*pow(10.0,-14.0)*g;  // mass of 10^9 boron atom (gram)


// Determine fractionmasses for brain and boron for each boron concentration
// and store them in two arrays
```

```
G4double B_d, Br_d;
B_d = 2.37*g/cm3;           // Boron density
Br_d = 1.03*g/cm3;          // Brain density

for(G4int i=0; i<11; i++){
B_fra[i] = 10000*(B_den[i]*m2/(B_den[i]*m2+m1))*100;  // Boron fractionmass array
}


for(G4int i=0; i<11; i++){
Br_fra[i] = 100-B_fra[i];//(m1/(B_den[i]*m2+m1))*100; // Brain fractionmass array
}


for(G4int i=0; i<11; i++){
den[i] = (Br_fra [i]*Br_d + B_fra [i]*B_d)/100;   // density of composite material array
}

// Build eleven materials corresponding to 11 boron concentrations


G4Material* mat1 =
new G4Material("mat1", density= den[0], ncomponents=2);
mat1->AddMaterial(brain, fractionmass= Br_fra[0]*perCent);
mat1->AddElement (boron  , fractionmass= B_fra[0]*perCent);

G4Material* mat2 =
new G4Material("mat2", density= den[1], ncomponents=2);
mat2->AddMaterial(brain, fractionmass=Br_fra[1]*perCent);
mat2->AddElement (boron  , fractionmass= B_fra[1]*perCent);

G4Material* mat3 =
new G4Material("mat3", density= den[2], ncomponents=2);
mat3->AddMaterial(brain, fractionmass=Br_fra[2]*perCent);
mat3->AddElement (boron , fractionmass= B_fra[2]*perCent);

G4Material* mat4 =
new G4Material("mat4", density= den[3], ncomponents=2);
mat4->AddMaterial(brain, fractionmass=Br_fra[3]*perCent);
mat4->AddElement (boron  , fractionmass= B_fra[3]*perCent);

G4Material* mat5 =
new G4Material("mat5", density= den[4], ncomponents=2);
mat5->AddMaterial(brain, fractionmass=Br_fra[4]*perCent);
mat5->AddElement (boron  , fractionmass= B_fra[4]*perCent);

G4Material* mat6 =
new G4Material("mat6", density= den[5], ncomponents=2);
mat6->AddMaterial(brain, fractionmass=Br_fra[5]*perCent);
mat6->AddElement (boron  , fractionmass= B_fra[5]*perCent);

G4Material* mat7 =
new G4Material("mat7", density= den[6], ncomponents=2);
mat7->AddMaterial(brain, fractionmass=Br_fra[6]*perCent);
mat7->AddElement (boron  , fractionmass= B_fra[6]*perCent);

G4Material* mat8 =
new G4Material("mat8", density= den[7], ncomponents=2);
mat8->AddMaterial(brain, fractionmass=Br_fra[7]*perCent);
mat8->AddElement (boron  , fractionmass= B_fra[7]*perCent);

G4Material* mat9 =
new G4Material("mat9", density= den[8], ncomponents=2);
mat9->AddMaterial(brain, fractionmass=Br_fra[8]*perCent);
mat9->AddElement (boron  , fractionmass= B_fra[8]*perCent);

G4Material* mat10 =
new G4Material("mat10", density= den[9], ncomponents=2);
mat10->AddMaterial(brain, fractionmass=Br_fra[9]*perCent);
mat10->AddElement (boron  , fractionmass= B_fra[9]*perCent);
```

```
G4Material* mat11 =
new G4Material("mat11", density= den[10], ncomponents=2);
mat11->AddMaterial(brain, fractionmass=Br_fra[10]*perCent);
mat11->AddElement (boron  , fractionmass= B_fra[10]*perCent);

// Store these materials in a vector of type pointers


mat_array.push_back(mat1);
mat_array.push_back(mat2);
mat_array.push_back(mat3);
mat_array.push_back(mat4);
mat_array.push_back(mat5);
mat_array.push_back(mat6);
mat_array.push_back(mat7);
mat_array.push_back(mat8);
mat_array.push_back(mat9);
mat_array.push_back(mat10);
mat_array.push_back(mat11);


//****************************************************************************//

//*********Begin Geometry*****************************************************//

//****************************************************************************//

// Build our mother volume, the "lab", the object that holds
// the lab apparatus.

// (We don't want a lab that is too big, since this determines how
// far particle travel and effects visualization).

G4double lab_half_x = 5.00*cm;
G4double lab_half_y = 5.00*cm;
G4double lab_half_z = 5.00*cm;


G4VSolid *labSolid = new G4Box( "labSolid",lab_half_x,lab_half_y,lab_half_z );
G4LogicalVolume *labLogical = new G4LogicalVolume( labSolid,air,"labLog", 0, 0,0);
G4VPhysicalVolume *lab = new G4PVPlacement( 0,G4ThreeVector(0,0,0),
                 labLogical,"labPhys",0,false,0 );

// We generally don't want to include the lab in any pictures

labLogical->SetVisAttributes( G4VisAttributes::Invisible );

// Build our Brain box

G4double box_half_x = 4.5*cm;
G4double box_half_y = 4.5*cm;
G4double box_half_z = 1.1*cm;

G4VSolid *brainSolid = new G4Box( "brainSolid", box_half_x, box_half_y, box_half_z);
G4LogicalVolume *brainLogical = new G4LogicalVolume( brainSolid,brain,
         "brainLogical",0, 0,0 );
//G4VPhysicalVolume *brainPhysical =
        new G4PVPlacement( 0, G4ThreeVector(0,0,0),brainLogical,
                 "brainPhys", labLogical, false,0);

// Build our sensitive volume (to be voxelised in ROGeom);
//This volume is located on the top-left quarter, and 0.5 cm offset along z

G4double phantom_half_x = 2.25*cm;
G4double phantom_half_y = 2.25*cm;
G4double phantom_half_z = 4.5*mm;

G4VSolid *phantomSolid = new G4Box( "phantomSolid",
                phantom_half_x, phantom_half_y,phantom_half_z );
```

```
G4LogicalVolume *phantomLogical = new G4LogicalVolume( phantomSolid,brain,
        "phantomLogical", 0, 0, 0 );
//G4VPhysicalVolume *phantomPhysical =
new G4PVPlacement( 0, G4ThreeVector(-2.25*cm,-2.25*cm,0.5*cm),
                phantomLogical, "phantomPhys",brainLogical,false,0 );

// Segmentation of brain phantom into voxels
// Number of segmentation.

fNx = num_voxels/2;
fNy = num_voxels/2;
fNz = 3;

G4int nxCells = fNx;
G4int nyCells = fNy;
G4int nzCells = fNz;

G4ThreeVector sensSize;
sensSize.setX(2*phantom_half_x/nxCells);
sensSize.setY(2*phantom_half_y/nyCells);
sensSize.setZ(2*phantom_half_z/nzCells);

// Replication of brain Phantom Volume.

// Y Slice

G4String yRepName("RepY");
G4VSolid* solYRep =
        new G4Box(yRepName,phantom_half_x,sensSize.y()/2.,phantom_half_z);
G4LogicalVolume* logYRep =
        new G4LogicalVolume(solYRep,brain,yRepName);
//G4PVReplica* yReplica =
        new G4PVReplica(yRepName,logYRep,phantomLogical,kYAxis,fNy,sensSize.y());

// X Slice

G4String xRepName("RepX");
G4VSolid* solXRep =
        new G4Box(xRepName,sensSize.x()/2.,sensSize.y()/2.,phantom_half_z);
G4LogicalVolume* logXRep =
        new G4LogicalVolume(solXRep,brain,xRepName);
//G4PVReplica* xReplica =
        new G4PVReplica(xRepName,logXRep,logYRep,kXAxis,fNx,sensSize.x());

//.................................

// Voxel solid and logical volumes

//.................................

// Z Slice

G4String zVoxName("phantomSens");
G4VSolid* solVoxel =
        new G4Box(zVoxName,sensSize.x()/2.,sensSize.y()/2.,sensSize.z()/2.);
G4LogicalVolume* logicPhantomSens = new G4LogicalVolume(solVoxel,brain,zVoxName);

//  Nested parameterisation handles material and transfomation of voxels.

// Create a matrix of materials based on boron concentration in B_density

        BuildMaterialMatrix(B_density, B_den, mat_array);

NestedPhantomParameterisation* paramPhantom
        = new NestedPhantomParameterisation(sensSize/2.,nzCells, phantomMat);
//G4VPhysicalVolume * physiPhantomSens =
        new G4PVParameterised("PhantomSens",     // their name
                logicPhantomSens,  // their logical volume
                logXRep,           // Mother logical volume
                kUndefined,        // Are placed along this axis
                nzCells,           // Number of cells
```

```
                paramPhantom);     // Parameterisation.

//    Optimization flag is avaiable for,
//    kUndefined, kXAxis, kYAxis, kZAxis.

//    Checking overlaps

G4cout <<"checking overlaps ";
G4bool  CheckOverlaps(G4int res=1000, G4double tol=0.1, G4bool verbose=true);

G4cout << "There are " << nzCells << " Slices in the scoring region in z direction."
        << "The width of slices are " << sensSize.z()/um << " um  "
        << G4endl;

// **************

// Cut per RegionphantomLogical->SetSensitiveDetector( voxelScoring );

// **************
// A smaller cut is fixed in the phantom to calculate the energy deposit with the
// required accuracy

G4Region* aRegion = new G4Region("DetectorLog");
phantomLogical -> SetRegion(aRegion);
aRegion -> AddRootLogicalVolume(phantomLogical);
G4ProductionCuts* fVertexDetectorCuts = new G4ProductionCuts();
aRegion->SetProductionCuts(fVertexDetectorCuts);

//**************

// Pass the voxel to the sensitive manager

//**************

G4SDManager *sensitiveManager = G4SDManager::GetSDMpointer();
ROGeom *voxelROgeom = new ROGeom( "voxelROgeom" );
voxelROgeom->BuildROGeometry();

VoxelScoring *voxelScoring = new VoxelScoring( "voxelScoring" );
sensitiveManager->AddNewDetector( voxelScoring );
logicPhantomSens->SetSensitiveDetector( voxelScoring );
phantomLogical->SetSensitiveDetector( voxelScoring );

voxelScoring->SetROgeometry( voxelROgeom );

// User Limits

// Sets a max step length in the tracker region, with G4StepLimiter


G4double maxStep = 3.0*um;
fStepLimit = new G4UserLimits(maxStep);
phantomLogical->SetUserLimits(fStepLimit);
logicPhantomSens->SetUserLimits(fStepLimit);

//////////////////////////////////////////////////////////////////////////////

// Visualisations


G4VisAttributes* brainAttributes= new G4VisAttributes(G4Colour(1.0,0.0,0.0));//red
brainAttributes -> SetVisibility(true);
brainAttributes -> SetForceWireframe(true);
brainLogical  ->SetVisAttributes(brainAttributes);



// Mother volume of brainPhantom to be parameterised

G4VisAttributes* phantomVisAtt = new G4VisAttributes(G4Colour(1.0,1.0,0.0));//yellow
phantomVisAtt -> SetVisibility(true);
```

```
phantomVisAtt -> SetForceWireframe(true);
phantomLogical->SetVisAttributes(phantomVisAtt);


// Replica

G4VisAttributes* yRepVisAtt = new G4VisAttributes(G4Colour(0.0,1.0,0.0));//green
logYRep->SetVisAttributes(yRepVisAtt);
G4VisAttributes* xRepVisAtt = new G4VisAttributes(G4Colour(0.0,1.0,0.0));
logXRep->SetVisAttributes(xRepVisAtt);


// This method returns the mother volume

return lab;

}

//....oooOOOOOooo........oooOOOOOooo........oooOOOOOooo........oooOOOOOooo.

//....oooOOOOOooo........oooOOOOOooo........oooOOOOOooo........oooOOOOOooo.


void DetectorConstruction::SetMaxStep(G4double maxStep)

{

if ((fStepLimit)&&(maxStep>0.)) fStepLimit->SetMaxAllowedStep(maxStep);

}


///////////////////////////////////////////////////////////////////////////

void DetectorConstruction::ReadDensityData()

{

std::ifstream inFile ("B_density_test.dat");
if(inFile.fail()) {
                G4cout << "ERROR, can't open the file!" << G4endl;

        } else {

           G4cout<< " inFile was successfully opened"<< G4endl;
        for(G4int i = 0; i < (num_voxels)*(num_voxels); i++) {
            inFile >> B_density[i];
        }
}
inFile.close();

// Print B_density into dat file for verification

char doseFileName[50];
sprintf(doseFileName, "B_density_confirm.dat");


// Print the arrays to file
std::ofstream outFile(doseFileName);


// Print the data to a 2D for external visualization

for(G4int i=0;i<(num_voxels/2);i++){
        for(G4int j=0;j<(num_voxels/2);j++){
                outFile << B_density[i*(num_voxels/2)+j] << " ";
}

outFile << std::endl;
}
```

```
outFile.close();

}


//....oooOOOOOooo........oooOOOOOooo........oooOOOOOooo........oooOOOOOooo......

void DetectorConstruction::BuildMaterialMatrix(G4float B_density[],
                                 G4double B_den[], std::vector<G4Material*> mat_array)

{


G4Material* tmat = 0;

for(G4int i=0; i<(num_voxels)*(num_voxels);i++){
        for (G4int j = 0; j<11; j++){
                G4double densityDif = B_density[i]- B_den[j];
                        if ( densityDif> -0.1 && densityDif < 0.1){
                                tmat = mat_array[j];
                                phantomMat.push_back(tmat);

                                break;
                                }
                }
}


G4cout<< "The size of material matrix is:"<< phantomMat.size()<< G4endl;

}
```

Follwoing code is used to parametrize the geometry to assign cells with their corresponding material (i.e. brain plus their corresponding boron concentration).

```

#include "NestedPhantomParameterisation.hh"
#include "G4VPhysicalVolume.hh"
#include "G4VTouchable.hh"
#include "G4ThreeVector.hh"
#include "G4Box.hh"
#include "G4LogicalVolume.hh"
#include "G4Material.hh"
#include <fstream>
#include <iostream>


//=========================================================================
// (NestedPhantomParameterisation)
//  (Description)
//     Class for nested parameterisation.
//     This parameterisation handles material and transfomation of voxles.
//////////////////////////////////////////////////////////////////////

//....oooOOOOOooo........oooOOOOOooo........oooOOOOOooo........oooOOOOOooo......
NestedPhantomParameterisation
::NestedPhantomParameterisation(const G4ThreeVector& voxelSize,
G4int nz, std::vector<G4Material*>& mat): G4VNestedParameterisation(),
fdX(voxelSize.x()),fdY(voxelSize.y()),fdZ(voxelSize.z()), fNz(nz),fMat(mat)

{

// Position of voxels.
// x and y positions are already defined in DetectorConstruction
// by using replicated volume. Here only we need to define is z positions of voxles.

fpZ.clear();
```

```
G4double zp;
for ( G4int iz = 0; iz < fNz; iz++){
        zp = (-fNz+1+2*iz)*fdZ;
        fpZ.push_back(zp);
        }
}

//....oooOOOOOooo........oooOOOOOooo........oooOOOOOooo........oooOOOOOooo......
NestedPhantomParameterisation::~NestedPhantomParameterisation(){
fpZ.clear()
;}

//....oooOOOOOooo........oooOOOOOooo........oooOOOOOooo........oooOOOOOooo......


// Material assignment to geometry.
//
G4Material* NestedPhantomParameterisation
::ComputeMaterial(G4VPhysicalVolume* currentVol, const G4int copyNoZ,
const G4VTouchable* parentTouch)
{

if(parentTouch==0) return fMat[0]; // protection for initialization

// Copy number of voxels.
// Copy number of X and Y are obtained from replication number.
// Copy nymber of Z is the copy number of current voxel.

        G4int ix = parentTouch->GetReplicaNumber(0);
        G4int iy = parentTouch->GetReplicaNumber(1);
        G4int iz = copyNoZ;
        num_voxels = 30;

//  materials are chosen for every voxel.

G4Material* mat=0;

G4int copyNo = iy*(num_voxels)+ ix;
mat = fMat[copyNo];

// Set the material to the current logical volume

G4LogicalVolume* currentLogVol = currentVol->GetLogicalVolume();
currentLogVol->SetMaterial(mat);

return mat;
}
```

Lastly the code to simulate parallel geometry to score the dose in individual cells ($20 \times 20 \times 20\ \mu m^3$).

```

// ReadoutGeometry for course detector

#include "ROGeom.hh"
#include "G4NistManager.hh"
#include "G4Material.hh"
#include "G4Box.hh"
#include "G4LogicalVolume.hh"
#include "G4PVPlacement.hh"
#include "G4SDManager.hh"
#include "DummyVoxelScoring.hh"

// Constructor
//
ROGeom::ROGeom(G4String name)
        :G4VReadOutGeometry( name )
```

```
{;}

// Construct
//
// Do the actual work
//
G4VPhysicalVolume *ROGeom::Build()
{
        G4NistManager* man = G4NistManager::Instance();
        G4Material* water  = man->FindOrBuildMaterial("G4_WATER");
        G4Material* air   = man->FindOrBuildMaterial("G4_AIR");

        /**************************************************************/
        //******************************Begin Geometry*******************//
        //************************************************************//

        G4double lab_half_x = 4.5*cm;
        G4double lab_half_y = 4.5*cm;
        G4double lab_half_z = 1.1*cm;
        G4VSolid *labSolid = new G4Box( "ROlabCourse",
                lab_half_x,
                lab_half_y,
                lab_half_z );
        G4LogicalVolume *labLogical = new G4LogicalVolume( labSolid,
                air,
                "ROlabCourse",
                0,
                0,
                0 );
        G4VPhysicalVolume *ROlabCourse = new G4PVPlacement( 0,
        G4ThreeVector(0,0,0), "ROlabCourse", labLogical,
        0, false, 0 );

        // Build our course scoring box

        G4double box_half_x = 10*um;
        G4double box_half_y = 10*um;
        G4double box_half_z = 10*um;
        G4int num_voxels = 2500;

        G4VSolid *waterSolid = new G4Box( "waterSolid",
        box_half_x,
        box_half_y,
        box_half_z );

        G4LogicalVolume *waterLogical = new G4LogicalVolume( waterSolid,
        water,
        "waterLogical", 0, 0, 0 );

        // Place the copies of the volume
        //
        for(G4int i=0;i<num_voxels;i++){
                for(G4int j=0;j<(num_voxels);j++){

                        // Calculate where the centre of each voxel should be
                        G4double voxel_x = -lab_half_x + i*2*box_half_x + box_half_x;
                        G4double voxel_y = -lab_half_y + j*2*box_half_y + box_half_y;
                        G4double voxel_z = 0.5*cm;

                        new G4PVPlacement( 0,
                        G4ThreeVector(voxel_x,voxel_y,voxel_z),
                        "CourseScoringPhys",
                        waterLogical,
                        ROlabCourse,
                        false,
                        num_voxels*i+j);
                }
        }

        //
        // Create the sensitive volumes (these are not used)
```

```
        //
        G4SDManager *sensitiveManager = G4SDManager::GetSDMpointer();

        DummyVoxelScoring *dummyScoring = new DummyVoxelScoring( "dummyScoring" );
        sensitiveManager->AddNewDetector( dummyScoring );
        waterLogical->SetSensitiveDetector( dummyScoring );

        //
        // This method is supposed to return the mother volume

        return ROlabCourse;
}
```

Appendix C

BNCT Code-Tracking and Dose Scoring

A sample of the code, developed in this work to track particles and to score dose in individual cells, is presented below.

```
// VoxelScoring.cc

#include "VoxelScoring.hh"
#include "G4TouchableHistory.hh"
#include "G4Step.hh"
#include "RunAction.hh"
#include "G4RunManager.hh"

// Constructor

VoxelScoring::VoxelScoring(G4String name)
        :G4VSensitiveDetector( name )
{
        //initialize the dose scoring array

        num_voxels = 2500;
        total_energy_dep = new G4double[num_voxels*(num_voxels)];
        alpha_energy_dep = new G4double[num_voxels*(num_voxels)];
        li_energy_dep= new G4double[num_voxels*(num_voxels)];
        gamma_energy_dep= new G4double[num_voxels*(num_voxels)];

}

VoxelScoring::~VoxelScoring()
{

        delete gamma_energy_dep;
        delete alpha_energy_dep;
        delete li_energy_dep;
        delete total_energy_dep;

}

// Initialize

void VoxelScoring::Initialize( G4HCofThisEvent* )
{
```

```
//Zero the arrays at the beginning of ea,eventIDch event

for(G4int i=0;i<num_voxels*(num_voxels);i++){

        total_energy_dep[i]=0;
        alpha_energy_dep[i]=0;
        li_energy_dep[i]=0;
        gamma_energy_dep[i]=0;
        }
}

// Process hits

G4bool VoxelScoring::ProcessHits( G4Step *step, G4TouchableHistory *ROhist)
{

//Find which voxel we are in

G4int voxel = ROhist-> GetCopyNumber();

// Get the parent ID and track ID

G4int parentID=step->GetTrack()->GetParentID();
G4int trackID=step->GetTrack()->GetTrackID();

// Get the energy deposited in this voxel and density of each voxel

total_energy_dep[voxel] += step->GetTotalEnergyDeposit() /keV;

// Get particle name and find step size for that particle to make sure
// step size is as short as we want

G4String particle_name = step->GetTrack()->GetDefinition()->GetParticleName();


// Check if we have a neutron inelastic process

if(trackID>1){

G4double charge=step->GetTrack()->GetDynamicParticle()->GetDefinition()->GetPDGCharge();
G4String processName = step->GetTrack()->GetCreatorProcess()->GetProcessName();
        if(processName =="NeutronInelastic"){
         if (charge == 2){ //(particle_name=="alpha"){

                secondary_alphas.push_back(trackID);
                alpha_energy_dep[voxel] += step->GetTotalEnergyDeposit() /keV;
                }
         else if(charge==3){

                secondary_li.push_back(trackID);
                li_energy_dep[voxel] += step->GetTotalEnergyDeposit() /keV;
                }
         }
         else if (processName =="nCapture"){
           secondary_gamma.push_back(trackID);
           gamma_energy_dep[voxel] += step->GetTotalEnergyDeposit() /keV;
     }
        else{

        // Check if the parentID is derived from the above particles
        G4int num_alpha_tracks=secondary_alphas.size();
        for(G4int i=0;i<num_alpha_tracks;i++){
                if(parentID==secondary_alphas[i]){
                        secondary_alphas.push_back(trackID);
                        alpha_energy_dep[voxel] += step->GetTotalEnergyDeposit() /keV;
                        break;
                        }
                }
        G4int num_li_tracks=secondary_li.size();
        for(G4int i=0;i<num_li_tracks;i++){
                if(parentID==secondary_li[i]){
```

```
                        secondary_li.push_back(trackID);
                        li_energy_dep[voxel] += step->GetTotalEnergyDeposit() /keV;
                        break;
                        }
                }
        G4int num_gamma_tracks=secondary_gamma.size();
        for(G4int i=0;i<num_gamma_tracks;i++){
                if(parentID==secondary_gamma[i]){
                        secondary_gamma.push_back(trackID);
                        gamma_energy_dep[voxel] += step->GetTotalEnergyDeposit() /keV;
                        break;
                        }
                }
        }
}

return true;

}
```

Bibliography

Agostinelli, S., Allison, J., Amako, K. a., Apostolakis, J., Araujo, H., Arce, P., Asai, M., Axen, D., Banerjee, S., Barrand, G., et al. (2003). GEANT4—a simulation toolkit. *Nuclear instruments and methods in physics research section A: Accelerators, Spectrometers, Detectors and Associated Equipment*, 506(3):250–303.

Aguirre, A. R., Font, C. R., Guardia, M. B., García, D. C., Peinado, M. G., Fernández, A. R., and Elvira, J. L. (2007). Positron emission tomography with 18 F-fluorodeoxyglucose in patients with uterine sarcoma. *Revista española de medicina nuclear (English Edition)*, 26(4):189–195.

Allen, B. J. (2006). Internal high linear energy transfer (LET) targeted radiotherapy for cancer. *Physics in medicine and biology*, 51(13):R327.

Andreo, P., Burns, D., Hohlfeld, K., Saiful Huq, M., Kanai, T., Laitano, F., Smyth, V., and Vynckier, S. (2000). IAEA TRS-398. *Absorbed Dose Determination in External Beam Radiotherapy: An International Code of Practice for Dosimetry Based on Standards of Absorbed Dose to Water.*

Australian Institute of Health and Welfare (2015). *Australian Cancer Incidence and Mortality (ACIM) books: All cancers combined.* Canberra: AIHW.

Aydın, H., Sillenberg, I., and von Lieven, H. (2001). Patterns of failure following CT-based 3-D irradiation for malignant glioma. *Strahlentherapie und Onkologie*, 177(8):424–431.

Bar-Shalom, R., Yefremov, N., Guralnik, L., Gaitini, D., Frenkel, A., Kuten, A., Altman, H., Keidar, Z., and Israel, O. (2003). Clinical performance of PET/CT in evaluation of cancer: additional value for diagnostic imaging and patient management. *Journal of nuclear medicine*, 44(8):1200–1209.

Barth, R. F., Grecula, J. C., Yang, W., Rotaru, J. H., Nawrocky, M., Gupta, N., Albertson, B. J., Ferketich, A. K., Moeschberger, M. L., Coderre, J. A., and K, R. E. (2004). Combination of boron neutron capture therapy and external beam radiotherapy for brain tumors. *International Journal of Radiation Oncology* Biology* Physics*, 58(1):267–277.

Bentzen, S. M., Constine, L. S., Deasy, J. O., Eisbruch, A., Jackson, A., Marks, L. B., Ten Haken, R. K., and Yorke, E. D. (2010). Quantitative analyses of normal tissue effects in the clinic (QUANTEC): an introduction to the scientific issues. *International Journal of Radiation Oncology* Biology* Physics*, 76(3):S3–S9.

Berberat, J., McNamara, J., Remonda, L., Bodis, S., and Rogers, S. (2014). Diffusion tensor imaging for target volume definition in glioblastoma multiforme. *Strahlentherapie und Onkologie*, 190(10):939–943.

Bernal, M., Bordage, M.-C., Brown, J., Davídková, M., Delage, E., El Bitar, Z., Enger, S., Francis, Z., Guatelli, S., Ivanchenko, V., et al. (2015). Track structure modeling in liquid water: A review of the Geant4-DNA very low energy extension of the Geant4 Monte Carlo simulation toolkit. *Physica Medica*, 31(8):861–874.

Bondiau, P.-Y., Konukoglu, E., Clatz, O., Delingette, H., Frenay, M., and Paquis, P. (2011). Biocomputing: numerical simulation of glioblastoma growth and comparison with conventional irradiation margins. *Physica Medica*, 27(2):103–108.

Briesmeister, J. F. et al. (2000). MCNPTM-a general monte Carlo N-particle transport code. *Version 4C, LA-13709-M, Los Alamos National Laboratory.*

Burger, P. C., Heinz, E. R., Shibata, T., and Kleihues, P. (1988). Topographic anatomy and CT correlations in the untreated glioblastoma multiforme. *Journal of neurosurgery*, 68(5):698–704.

Carrasco, P., Jornet, N., Duch, M. A., Panettieri, V., Weber, L., Eudaldo, T., Ginjaume, M., and Ribas, M. (2007). Comparison of dose calculation algorithms in slab phantoms with cortical bone equivalent heterogeneities. *Medical physics*, 34(8):3323–3333.

Chadwick, K. and Leenhouts, H. (1973). Molecular theory of cell survival. Technical report, Instituut voor Toepassing van Atoomenergie in de Landbouw, Wageningen, Netherlands.

Chang, E. L., Akyurek, S., Avalos, T., Rebueno, N., Spicer, C., Garcia, J., Famiglietti, R., Allen, P. K., Chao, K. C., Mahajan, A., et al. (2007). Evaluation of peritumoral edema in the delineation of radiotherapy clinical target volumes for glioblastoma. *International Journal of Radiation Oncology* Biology* Physics*, 68(1):144–150.

Cherry, S. R., Sorenson, J. A., and Phelps, M. E. (2012). *Physics in nuclear medicine.* Elsevier Health Sciences.

Cheung, T., Butson, M. J., and Peter, K. (2006). Measurement of high energy x-ray beam penumbra with Gafchromic™ EBT radiochromic film. *Medical physics*, 33(8):2912–2914.

Cirrone, G., Cuttone, G., Di Rosa, F., Pandola, L., Romano, F., and Zhang, Q. (2010). Validation of the Geant4 electromagnetic photon cross-sections for elements and compounds. *Nuclear Instruments and Methods in Physics Research Section A: Accelerators, Spectrometers, Detectors and Associated Equipment*, 618(1):315–322.

Clatz, O., Sermesant, M., Bondiau, P.-Y., Delingette, H., Warfield, S. K., Malandain, G., and Ayache, N. (2005). Realistic simulation of the 3-D growth of brain tumors in MR images coupling diffusion with biomechanical deformation. *Medical Imaging, IEEE Transactions on*, 24(10):1334–1346.

Collaboration, G. (2012). Geant4 user's guide for application developers. *Accessible from the GEANT4 web page [1] Version geant4*, 9.

Collingridge, D. R., Piepmeier, J. M., Rockwell, S., and Knisely, J. P. (1999). Polarographic measurements of oxygen tension in human glioma and surrounding peritumoural brain tissue. *Radiotherapy and oncology*, 53(2):127–131.

Curtis, S. B. (1986). Lethal and potentially lethal lesions induced by radiation—a unified repair model. *Radiation research*, 106(2):252–270.

Dong, M.-J., Liu, Z.-F., Zhao, K., Ruan, L.-X., Wang, G.-L., Yang, S.-Y., Sun, F., and Luo, X.-G. (2009). Value of 18F-FDG-PET/PET-CT in differentiated thyroid carcinoma with radioiodine-negative whole-body scan: a meta-analysis. *Nuclear medicine communications*, 30(8):639–650.

Douglass, M., Bezak, E., and Penfold, S. (2012). Development of a randomized 3D cell model for Monte Carlo microdosimetry simulations. *Medical physics*, 39(6):3509–3519.

Douglass, M., Bezak, E., and Penfold, S. (2015a). Development of a radiation track structure clustering algorithm for the prediction of DNA DSB yields and radiation induced cell death in eukaryotic cells. *Physics in medicine and biology*, 60(8):3217.

Douglass, M., Penfold, S., and Bezak, E. (2015b). Preliminary investigation of microdosimetric track structure physics models in Geant4-DNA and RITRACKS. *Computational and mathematical methods in medicine*, 2015.

Douglass, M. J. J. (2014). *Development of an Integrated Stochastic Radiobiological Model for Electromagnetic Particle Interactions in a 4D Cellular Geometry.* PhD thesis, University of Adelaide.

Emami, B., Lyman, J., Brown, A., Cola, L., Goitein, M., Munzenrider, J., Shank, B., Solin, L., and Wesson, M. (1991). Tolerance of normal tissue to therapeutic irradiation. *International Journal of Radiation Oncology* Biology* Physics*, 21(1):109–122.

Engels, B., Soete, G., Verellen, D., and Storme, G. (2009). Conformal arc radiotherapy for prostate cancer: increased biochemical failure in patients with distended rectum on the planning computed tomogram despite image guidance by implanted markers. *International Journal of Radiation Oncology* Biology* Physics*, 74(2):388–391.

Fiorentino, A., Caivano, R., Pedicini, P., and Fusco, V. (2013). Clinical target volume definition for glioblastoma radiotherapy planning: magnetic resonance imaging and computed tomography. *Clinical and Translational Oncology*, 15(9):754–758.

Fippel, M. (2013). Monte Carlo techniques in radiation therapy.

Fix, M. K., Stampanoni, M., Manser, P., Born, E. J., Mini, R., and Rüegsegger, P. (2001). A multiple source model for 6 MV photon beam dose calculations using Monte Carlo. *Physics in medicine and biology*, 46(5):1407.

Friedland, W., Dingfelder, M., Kundrát, P., and Jacob, P. (2011). Track structures, DNA targets and radiation effects in the biophysical Monte Carlo simulation code PARTRAC. *Mutation Research/Fundamental and Molecular Mechanisms of Mutagenesis*, 711(1):28–40.

Friedrich, T., Durante, M., and Scholz, M. (2013). The local effect model–principles and applications. *URL http://three. usra. edu/articles/LEM_20130426. pdf.*

Gaspar, L. E., Fisher, B. J., Macdonald, D. R., Leber, D. V., Halperin, E. C., Schold, S. C., and Cairncross, J. G. (1992). Supratentorial malignant glioma: patterns of recurrence and implications for external beam local treatment. *International Journal of Radiation Oncology* Biology* Physics*, 24(1):55–57.

Gilbert, M. R., Dignam, J. J., Armstrong, T. S., Wefel, J. S., Blumenthal, D. T., Vogelbaum, M. A., Colman, H., Chakravarti, A., Pugh, S., Won, M., et al. (2014). A randomized trial of bevacizumab for newly diagnosed glioblastoma. *New England Journal of Medicine*, 370(8):699–708.

Gordin, A., Golz, A., Keidar, Z., Daitzchman, M., Bar-Shalom, R., and Israel, O. (2007). The role of FDG-PET/CT imaging in head and neck malignant conditions: impact on diagnostic accuracy and patient care. *Otolaryngology–Head and Neck Surgery*, 137(1):130–137.

Graeber, M. B. (2010). Changing face of microglia. *Science*, 330(6005):783–788.

Halperin, E. C., Bentel, G., Heinz, E. R., and Burger, P. C. (1989). Radiation therapy treatment planning in supratentorial glioblastoma multiforme: an analysis based on post mortem topographic anatomy with CT correlations. *International Journal of Radiation Oncology* Biology* Physics*, 17(6):1347–1350.

Han, T., Mikell, J. K., Salehpour, M., and Mourtada, F. (2011). Dosimetric comparison of Acuros XB deterministic radiation transport method with Monte Carlo and model-based convolution methods in heterogeneous media. *Medical physics*, 38(5):2651–2664.

Heemsbergen, W. D., Al-Mamgani, A., Witte, M. G., van Herk, M., and Lebesque, J. V. (2013). Radiotherapy with rectangular fields is associated with fewer clinical failures than conformal fields in the high-risk prostate cancer subgroup: results from a randomized trial. *Radiotherapy and Oncology*, 107(2):134–139.

Hess, C., Schaaf, J., Kortmann, R., Schabet, M., and Bamberg, M. (1994). Malignant glioma: patterns of failure following individually tailored limited volume irradiation. *Radiotherapy and Oncology*, 30(2):146–149.

Histed, S. N., Lindenberg, M. L., Mena, E., Turkbey, B., Choyke, P. L., and Kurdziel, K. A. (2012). Review of functional/anatomic imaging in oncology. *Nuclear medicine communications*, 33(4):349.

ICRP (1991). *ICRP Publication 60: 1990 Recommendations of the International Commission on Radiological Protection.* Number 60. Elsevier Health Sciences.

ICRU, R. . (1999). recording and reporting photon beam therapy (supplement to ICRU report 50). *International Commission on Radiation Units and Measurements, Bethesda, USA:(supplement to ICRU Report 50)*, 62.

Incerti, S., Baldacchino, G., Bernal, M., Capra, R., Champion, C., Francis, Z., Guèye, P., Mantero, A., Mascialino, B., Moretto, P., et al. (2010). The geant4-dna project. *International Journal of Modeling, Simulation, and Scientific Computing*, 1(02):157–178.

Incerti, S., Seznec, H., Simon, M., Barberet, P., Habchi, C., and Moretto, P. (2009). Monte Carlo dosimetry for targeted irradiation of individual cells using a microbeam facility. *Radiation protection dosimetry*, 133(1):2–11.

Jones, D. (1994). Icru report 50—prescribing, recording and reporting photon beam therapy. *Medical Physics*, 21(6):833–834.

Kawrakow, I. (2000). Accurate condensed history Monte Carlo simulation of electron transport. i. EGSnrc, the new EGS4 version. *Medical physics*, 27(3):485–498.

Lee, I. H., Piert, M., Gomez-Hassan, D., Junck, L., Rogers, L., Hayman, J., Ten Haken, R. K., Lawrence, T. S., Cao, Y., and Tsien, C. (2009). Association of 11 C-Methionine PET uptake with site of failure after concurrent temozolomide and radiation for primary glioblastoma multiforme. *International Journal of Radiation Oncology* Biology* Physics*, 73(2):479–485.

Levin, C. S. and Hoffman, E. J. (1999). Calculation of positron range and its effect on the fundamental limit of positron emission tomography system spatial resolution. *Physics in medicine and biology*, 44(3):781.

Li, W., Holsinger, R., Kruse, C., Flugel, A., and Graeber, M. (2013). The potential for genetically altered microglia to influence glioma treatment. *CNS & Neurological Disorders-Drug Targets (Formerly Current Drug Targets-CNS & Neurological Disorders)*, 12(6):750–762.

Liu, T., Xu, W., Yan, W.-L., Ye, M., Bai, Y.-R., and Huang, G. (2007). FDG-PET, CT, MRI for diagnosis of local residual or recurrent nasopharyngeal carcinoma, which one is the best? a systematic review. *Radiotherapy and Oncology*, 85(3):327–335.

Louvel, G., Metellus, P., Noel, G., Peeters, S., Guyotat, J., Duntze, J., Le Reste, P.-J., Hieu, P. D., Faillot, T., Litre, F., et al. (2016). Delaying standard combined chemoradiotherapy after surgical resection does not impact survival in newly diagnosed glioblastoma patients. *Radiotherapy and Oncology*.

Lyman, J. T. (1985). Complication probability as assessed from dose-volume histograms. *Radiation Research*, 104(2s):S13–S19.

Marcu, L., Bezak, E., and Allen, B. J. (2012). *Biomedical Physics in Radiotherapy for Cancer*. Csiro publishing.

Martínez-González, A., Calvo, G. F., Romasanta, L. A. P., and Pérez-García, V. M. (2012). Hypoxic cell waves around necrotic cores in glioblastoma: a biomathematical model and its therapeutic implications. *Bulletin of mathematical biology*, 74(12):2875–2896.

Matsuo, M., Miwa, K., Tanaka, O., Shinoda, J., Nishibori, H., Tsuge, Y., Yano, H., Iwama, T., Hayashi, S., Hoshi, H., et al. (2012). Impact of [11 C] methionine positron emission tomography for target definition of glioblastoma multiforme in radiation therapy planning. *International Journal of Radiation Oncology* Biology* Physics*, 82(1):83–89.

McDonald, M. W., Shu, H.-K. G., Curran, W. J., and Crocker, I. R. (2011). Pattern of failure after limited margin radiotherapy and temozolomide for glioblastoma. *International Journal of Radiation Oncology* Biology* Physics*, 79(1):130–136.

Moghaddasi, F. L., Bezak, E., and Marcu, L. (2012a). In silico modelling of tumour margin diffusion and infiltration: review of current status. *Computational and mathematical methods in medicine*, 2012.

Moghaddasi, L., Bezak, E., and Marcu, L. G. (2012b). Current challenges in clinical target volume definition: tumour margins and microscopic extensions. *Acta Oncologica*, 51(8):984–995.

Mosskin, M., Ericson, K., Hindmarsh, T., Von Holst, H., Collins, V., Bergström, M., Eriksson, L., and Johnström, P. (1989). Positron emission tomography compared with magnetic resonance imaging and computed tomography in supratentorial gliomas using multiple stereotactic biopsies as reference. *Acta radiologica*, 30(3):225–232.

Murakami, M., Tsukada, H., Shida, M., Watanabe, M., Maeda, H., Koido, S., Hirasawa, T., Muramatsu, T., Miyamoto, T., Nasu, S., et al. (2006). Whole-body positron emission tomography with F-18 fluorodeoxyglucose for the detection of recurrence in uterine sarcomas. *International journal of gynecological Cancer*, 16(2):854–860.

Murray, J. D. (2002). Mathematical biology I: An introduction, vol. 17 of interdisciplinary applied mathematics.

Niyazi, M., Brada, M., Chalmers, A. J., Combs, S. E., Erridge, S. C., Fiorentino, A., Grosu, A. L., Lagerwaard, F. J., Minniti, G., Mirimanoff, R.-O., et al. (2016). ESTRO-ACROP guideline “target delineation of glioblastomas”. *Radiotherapy and Oncology.*

Okamoto, H., Kohno, T., Kanai, T., Kase, Y., Matsumoto, Y., Furusawa, Y., Fujita, Y., Saitoh, H., and Itami, J. (2011). Microdosimetric study on influence of low energy photons on relative biological effectiveness under therapeutic conditions using 6 MV linac. *Medical physics*, 38(8):4714–4722.

Padma, M., Said, S., Jacobs, M., Hwang, D., Dunigan, K., Satter, M., Christian, B., Ruppert, J., Bernstein, T., Kraus, G., et al. (2003). Prediction of pathology and survival by FDG PET in gliomas. *Journal of neuro-oncology*, 64(3):227–237.

Patton, J. A., Delbeke, D., and Sandler, M. P. (2000). Image fusion using an integrated, dual-head coincidence camera with x-ray tube-based attenuation maps. *The Journal of Nuclear Medicine*, 41(8):1364.

Picard, J. (1999). [positron emission tomography in tumor pathology]. *Bulletin de l’Academie nationale de medecine*, 184(5):1023–9.

Plante, I. and Cucinotta, F. A. (2008). Ionization and excitation cross sections for the interaction of HZE particles in liquid water and application to Monte Carlo simulation of radiation tracks. *New Journal of Physics*, 10(12):125020.

Plante, I. and Cucinotta, F. A. (2011). Monte Carlo simulation of ionizing radiation tracks. *Application of Monte Carlo methods in biology, medicine and other fields of science. InTech, Rijeka, Croatia*, pages 315–356.

Podgorsak, E. B. (2005). External photon beams: physical aspects. *Radiation Oncology Physics: A handbook for teachers and students. Vienna: IAEA*, pages 161–217.

Purdy, J. A., Perez, C. A., and Poortmans, P. (2012). *Technical Basis of Radiation Therapy: Practical Clinical Applications.* Springer Berlin Heidelberg.

Rosenschold, P. M., Costa, J., Engelholm, S. A., Lundemann, M. J., Law, I., Ohlhues, L., and Engelholm, S. (2014). Impact of [18F]-fluoro-ethyl-tyrosine PET imaging on target definition for radiation therapy of high-grade glioma. *Neuro-oncology*, page nou316.

Schwenzer, N., Stegger, L., Bisdas, S., Schraml, C., Kolb, A., Boss, A., Müller, M., Reimold, M., Ernemann, U., Claussen, C., et al. (2012). Simultaneous PET/MR imaging in a human brain PET/MR system in 50 patients—current state of image quality. *European journal of radiology*, 81(11):3472–3478.

Sharma, P., Kumar, R., Singh, H., Jeph, S., Sharma, J. B., Jain, S. K., Sharma, D. N., Bal, C., and Malhotra, A. (2012). Role of FDG PET-CT in detecting recurrence in patients with uterine sarcoma: comparison with conventional imaging. *Nuclear medicine communications*, 33(2):185–190.

Siegel, R., Naishadham, D., and Jemal, A. (2013). Cancer statistics, 2013. *CA: a cancer journal for clinicians*, 63(1):11–30.

Stewart, R. D. (2001). Two-lesion kinetic model of double-strand break rejoining and cell killing. *Radiation Research*, 156(4):365–378.

Taghian, A., Suit, H., Pardo, F., Gioioso, D., Tomkinson, K., DuBois, W., and Gerweck, L. (1992). In vitro intrinsic radiation sensitivity of glioblastoma multiforme. *International Journal of Radiation Oncology* Biology* Physics*, 23(1):55–62.

Trépanier, P.-Y., Fortin, I., Lambert, C., and Lacroix, F. (2012). A Monte Carlo based formalism to identify potential locations at high risk of tumor recurrence with a numerical model for glioblastoma multiforme. *Medical physics*, 39(11):6682–6691.

Unkelbach, J., Menze, B. H., Konukoglu, E., Dittmann, F., Ayache, N., and Shih, H. A. (2014). Radiotherapy planning for glioblastoma based on a tumor growth model: implications for spatial dose redistribution. *Physics in medicine and biology*, 59(3):771.

Van Dyk, J. (1999). *The modern technology of radiation oncology: a compendium for medical physicists and radiation oncologists.* Medical Physics Pub Corp.

Van Herk, M. (2004). Errors and margins in radiotherapy. In *Seminars in radiation oncology*, volume 14, pages 52–64. Elsevier.

Van Herk, M. (2008). Will IGRT live up to its promise? *Acta Oncologica*, 47(7):1186–1187.

Wallner, K. E., Galicich, J. H., Krol, G., Arbit, E., and Malkin, M. G. (1989). Patterns of failure following treatment for glioblastoma multiforme and anaplastic astrocytoma. *International Journal of Radiation Oncology* Biology* Physics*, 16(6):1405–1409.

Wee, C. W., Sung, W., Kang, H.-C., Cho, K. H., Han, T. J., Jeong, B.-K., Jeong, J.-U., Kim, H., Kim, I. A., Kim, J. H., et al. (2015). Evaluation of variability in target volume delineation for newly diagnosed glioblastoma: a multi-institutional study from the korean radiation oncology group. *Radiation Oncology*, 10(1):1.

Wienhard, K., Eriksson, L., Grootoonk, S., Casey, M., Pietrzyk, U., and Heiss, W.-D. (1992). Performance evaluation of the positron scanner ECAT EXACT. *Journal of computer assisted tomography*, 16(5):804–813.

Witte, M. G., Heemsbergen, W. D., Bohoslavsky, R., Pos, F. J., Al-Mamgani, A., Lebesque, J. V., and van Herk, M. (2010). Relating dose outside the prostate with freedom from failure in the dutch trial 68 Gy vs. 78Gy. *International Journal of Radiation Oncology* Biology* Physics*, 77(1):131–138.

Yan, D., Yan, S., Lu, Z., Xie, C., Chen, W., Xu, X., Li, X., Yu, H., Zhu, X., and Zheng, L. (2014). Postoperative radiotherapy for glioma: Improved delineation of the clinical target volume using the geodesic distance calculation. *PloS one*, 9(6):e98616.

Yong, T., Yuan, Z., Jun, Z., Lin, Z., He, W., and Juanqi, Z. (2010). Sensitivity of PET/MR images in liver metastases from colorectal carcinoma. *Hellenic journal of nuclear medicine*, 14(3):264–268.

Zaider, M. and Hanin, L. (2011). Tumor control probability in radiation treatment. *Medical physics*, 38(2):574–583.